Volume Fraction Sensing of Multivariable Systems using Multi-Resonances of Planar Microwave Resonators

By

Navid Hosseini

A thesis submitted in partial fulfillment of the requirements of the degree of

Doctor of Philosophy

In

ELECTROMAGNETICS AND MICROWAVES

Department of Electrical and Computer Engineering
University of Alberta

Abstract

In recent years, sensing and selectivity have been the subject of many types of research due to their practical challenges. The main issue is the limited number of output data that confine the degree of freedom to solve the unknown problem. The majority of multi-variable experiments seek more assisting parameters and independent features for finalizing their solution.

Microwave resonators as detecting devices can help gather the required data from the material under test in different experiments. Their resonance shift is one of the features that is mainly utilized for sensing purposes. But, for the detection of multi-variable parameters like multi-subcomponent volumes in a solvent or mixture, more than one independent feature is required. For overcoming this bottleneck, a new material characteristic is required, generating and defining the new independent features. Having more independent features out of the sensor response enables unknown variables identification.

In this thesis, the term “harmonic” represents the resonance modes of the microwave resonator. One of the simplest forms of microwave resonators is the split ring resonator (SRR) and ring resonators. These kinds of structures are low-cost, non-invasive, and real-time devices making them a proper candidate for sensing applications. Like any other resonator, their microwave profile can be easily perturbed by introducing the external load and altering their Q-factor as a result. Generally, the rings are resonating structures that generate multiple resonant modes in their frequency response. These resonant mode frequencies are dependent features of the rings as they iterate themselves and their operational band. To make these elements change uniquely and independently, the variant permittivity profile of the materials under test can be considered as a new parameter. Developing the frequency shift of the resonances as a function of real relative

permittivity variations defines the multiple independent features and authorizes the multi-variable diagnosis along with material senses. This can be realized by forming the linear system of equations for each independent resonant mode and solving them for volumetric unknowns or sub-component concentrations.

Preface

This thesis includes the original work by Navid Hosseini submitted to accomplish the degree of Doctor of Philosophy in electromagnetics and microwaves. The subject is mainly focused on selective sensing of the multivariable sensors for volumetric analysis of the multi-variable mixtures.

Throughout this thesis, Prof. Mojgan Daneshmand, Prof. Masum Hossain, and Dr. Masoud Baghelani gave significant supervisory counsel and support during the work. Prof. Ashwin K. Iyer, and Prof. Vien Van assisted with some of the tasks. The format of the thesis is paper-based with the following details:

Chapter 1 and 2 present the introduction and the literature review on the different methods of mixture sensing and characterization using the microwave sensors.

Chapter 3 is a compilation of two published papers. In the first paper, the model-based approach for multivariable systems was published as N. Hosseini, M. Baghelani, and M. Daneshmand, “Selective Volume Fraction Sensing Using Resonant- Based Microwave Sensor and its Harmonics,” in IEEE Transactions on Microwave Theory and Techniques, vol. 68, no. 9, pp. 3958-3968, Sept. 2020. The second one, which proposes the model-free approach, was published as M. Baghelani, N. Hosseini and M. Daneshmand, "Artificial Intelligence Assisted Non-Contact Microwave Sensor for Multivariable Biofuel Analysis," in IEEE Transactions on Industrial Electronics, Oct. 2020.

Chapter 4 is a combination of published papers as N. Hosseini, S. S. Olokede, and M. Daneshmand, “A Novel Miniaturized Asymmetric CPW Split Ring Resonator with Extended Field Distribution Pattern for Sensing Applications,” in Sensors and Actuators A: Physical. 2020 Apr 1;304:111769, and M. Baghelani, N. Hosseini, and M. Daneshmand, “Non-Contact Real-Time Water and Brine Concentration Monitoring in Crude Oil Based on Multi-Variable Analysis of Microwave Resonators,” in Measurement. 2021.

Chapter 5 is a published paper as N. Hosseini, M. Baghelani, “Selective Real-Time Non-Contact Alcohol Concentration Measurement during Fermentation Process using Microwave Split-Ring Resonator Based Sensor,” in Sensors and actuators A journal.

Chapter 6 will have a brief review of the achievements and limitations of the work, together with potential future works.

To the memory of Mojgan Daneshmand

my love, Arezoo

and my dear parents

Acknowledgment

Its a genuine pleasure to express my immeasurable appreciation and a deep sense of thanks to Prof. Mojgan Daneshmand, my initial advisor, for her kind support, wisdom, thoughts, management, and supporting me fulfill the significant part of my academic adventures. She meant a lot to the whole group, may she rest in peace. Deep gratitude and sincere appreciation go to Prof. Masum Hossain for his support, guidance, and precious suggestions in the competition and success of this study. I am incredibly grateful for his professional advice and the implementation of pathways to a higher level of technology.

My sincere thanks also go to Prof. Ashwin K. Iyer, and Vien Van for their insightful comments and their outstanding talents in their field, as seen in their method of leadership. Also, I would like to express my gratitude to my other committee members, Prof. Doug Barlage and Edmond Lou, who demonstrated that modern technology should always transcend the traditional academic borders. I owe a deep sense of thanks to Prof. Ashwin K. Iyer for his continued support during the last five years of my academic experience at the University of Alberta.

My special appreciation to Dr. Masoud Baghelani, Thomas Jones, and Mehdi Nosrati in providing relevant assistance to complete this research.

I would like to express my sincere gratitude to my parents, who I am deeply indebted for always being there with their tremendous support and patience in helping me survive all the difficulties during my academic life.

My appreciation extends to my colleagues for their collaborative attitudes, particularly Sameir Deif, who contributed to having a professional and peaceful laboratory atmosphere for fulfilling the projects.

And, finally, to my caring and supportive love, Arezoo. Your patience, encouragement, and astound support are greatly appreciated. That was a great relief to think that you were always supportive and immensely kind.

This work would not have been accomplished without the financial support provided by Future Energy Systems (FES), Mitacs, and the University of Alberta during the different phases of research and all awards and contributions toward the accomplishment of the project objectives.

Table of Contents

List of Figures

List of Tables

Abbreviations & Acronyms

GC-MS	Chromatography-Mass Spectroscopy
LC-MS	Liquid Chromatography-Mass Spectroscopy
RF CMOS	Radio Frequency Complementary Metal Oxide Semiconductor
CT-SRR	Circular tapped split ring resonator
SRR	Split Ring Resonator
CCSR	Complementary Circular Spiral Resonator
PDMS	Polydimethylsiloxane
LTCC	Low-Temperature Co-fired Ceramic
VFM	Volumetric Fraction Matrix
SCM	Sensor Calibration Matrix
MM	Mixture Matrix
ANN	Artificial Neural Network
ReLU	Rectified Linear Unit
MSE	Mean Square Error
SSRR	Symmetrical Split Ring Resonator
DI	Deionized Water
CPW-SRR	Coplanar Waveguide Split Ring Resonator
MUT	Material Under Test

Chapter 1 Introduction

1.1 Motivation

The volumetric fraction measurement of mixtures is crucial in the diagnosis and chemical analysis [1], [2]. Complicated and high-cost analytical chemistry procedures for mass spectroscopy have been proposed, like FTIR for quantitative analysis of the mixture, Gas Chromatography-Mass Spectroscopy (GC-MS) and Liquid Chromatography-Mass Spectroscopy (LC-MS) for gas and liquid materials and mixtures [3]–[5].

Conventionally, microwave spectroscopy is utilized for identifying material dispersion. One of the main classes of these methods is dielectric spectroscopy as an essential tool for extracting information regarding the permittivity profile of the materials. Most dielectric spectroscopy methods can be summarized and classified through curve fitting, circuit modelling and mapping [6], [7]. The fitting techniques can also be applied in regression analysis using a capacitive sensor [8] or a commercial dielectric probe [9]. For example, the transmission coefficient can be utilized to extract the complex permittivity of the mixture using curve fitting techniques [10]. Another research involved the fitting process for complex permittivity extraction based on the phase variation method using an interferometry-based sensor [11]. However, all these techniques suffer from a high degree of error, resulting in several types of research utilizing resonant-based sensors for minute and sensitive measurements.

Microwave resonator-based sensors have achieved a great deal of interest during the last decade with their applications expanded from biomedical to oil and gas, mainly due to their impressive characteristics such as high sensitivity, low power consumption, low-cost, being non-invasive inherently, and even distant sensing capability [12]–[16]. Much effort has been made to prosper the microwave sensors' functionality [17], [18]. Still, unfortunately, these sensors suffer from the lack of features addressing sensing capability in multi-variable environments. This problem has challenged the commercialization and widespread use of these sensors. All the magnificent

features of microwave resonator-based sensors motivated us to work through a solution for enabling multivariable sensing and ultimately selectivity of this kind of sensor.

1.2 Objectives

The main objectives of this thesis can be summarized as follows:

- Proposing and developing a novel resonant mode-based sensing technique for the multivariable mixture analysis by introducing the linearly independent parameters for the microwave sensors.
- Developing the artificial neural network process for analyzing the highly nonlinear problems by the multiple variables during the sensing procedure.
- Designing and fabricating a novel multi-resonant mode sensor with a uniform E-field profile for selective sensing.
- Developing the model-free multivariable selective algorithm for determining water concentration together with its salinity in oil.
- Designing and realizing the planar sensor with notch filter type response for non-contact determination of alcohol concentration during fermentation process.
- Performing the transient simulation and measurements for the realization of RF CMOS sensors for the industrialization of the proposed technology.

1.3 Thesis Organization

For developing the detailed background information over the proposed method and thesis materials, Chapter 2 presents a literature review on single and binary variable sensing methods, the theory of microwave spectroscopy methods, nonlinearity, and multivariable sensing parameters. Chapter 3 proposes a novel resonant mode-based nonlinear technique for solving the multivariable problem for more than two unknowns. The algorithm takes the benefit of nonlinearity to achieve multiple independent features for solving the final problem. The method is

going to be applied for measuring the volumetric fraction of multicomponent mixtures. For proof of concept, an ordinary planar ring resonator is designed and fabricated to operate in the desired frequency band that causes nonlinearity and yields independent resonant mode shifts. It is shown that by sampling the shifts in the variant profile of dispersion spectrum, Δf_n , as the shift of the n^{th} resonant mode becomes an independent feature of the single ring. As there is no closed-form formula for modelling the resonator behaviour, a compressive relation is developed and proposed for modelling the sensor calibration curve. Different fitting parameters of the proposed equation are then calculated through the intersection of dispersion and the sensor calibration curve. Then, a model-free analysis for the same approach using a feed-forward neural network is utilized. The proposed method avoids the curve fitting estimation errors that occur during the calculation of the sensor calibration curve. Using resonant mode frequency shifts and resonance amplitude variations of sample experiments as two independent parameters and quality factor as the partial dependent feature, the artificial neural network is trained and utilized for the target experiments. This capability is applied to detect biofuel impurities like several mixtures of gasoline, ethanol, and water with different volume fractions.

The first section in Chapter 4 provides the design details of a novel CPW split ring resonator for boosting sensing capabilities by enhancing the sensor's electrical field profile. The design is implemented on the TL-based equivalent circuit of SRR to miniaturize the sensor layout and achieve a uniform E-field pattern on the proposed prototype. The second part of the chapter presents a wide dynamic range sensor designed in the same regime to analyze the water concentration and its salinity in oil. The approach considers a model-free frequency-based method using the linearly independent parameters. The sensor calibration matrix is formed based only on resonance shift values instead of applying the complicated models and simplifying the problem. Chapter 5 investigates a new type of design with a notch type frequency response and its realization. The proposed sensor provides a multi-resonant mode response in the desired band. The implemented device is applied for measuring the alcohol concentration during the fermentation process using a model-free shift-based technique. Using transient impulse response of the multi-resonant mode module, the same calculation is feasible while having the whole system on a single

chip using CMOS technology. The pulse source is a pulse generator for implementing the desired signals. Chapter 6 includes both the conclusion part and future works and briefly discusses transient analysis as a significant step for the industrialization of the technique.

1.4 References

[1] H. F. Cook, "Dielectric behaviour of human blood at microwave frequencies," *Nature*, vol. 168, no. 4267, p. 247, 1951.

[2] H. Choi, J. Nylon, S. Luzio, J. Beutler, and A. Porch, "Design of continuous non-invasive blood glucose monitoring sensor based on a microwave split ring resonator," in *2014 IEEE MTT-S International Microwave Workshop Series on RF and Wireless Technologies for Biomedical and Healthcare Applications (IMWS-Bio2014)*, 2014, pp. 1–3.

[3] A. Rohman, D. L. Setyaningrum, and S. Riyanto, "FTIR spectroscopy combined with partial least square for analysis of red fruit oil in ternary mixture system," *Int. J. Spectrosc.*, vol. 2014, 2014.

[4] A. Kondyli and W. Schrader, "High-resolution GC/MS studies of a light crude oil fraction," *J. mass Spectrom.*, vol. 54, no. 1, pp. 47–54, 2019.

[5] J. J. Pitt, "Principles and applications of liquid chromatography-mass spectrometry in clinical biochemistry," *Clin. Biochem. Rev.*, vol. 30, no. 1, p. 19, 2009.

[6] D. Havelka, O. Krivosudský, and M. Cifra, "Grounded coplanar waveguide-based 0.5–50 GHz sensor for dielectric spectroscopy," in *2017 47th European Microwave Conference (EuMC)*, 2017, pp. 950–953.

[7] N. Bonanos, P. Pissis, and J. R. Macdonald, "Impedance spectroscopy of dielectrics and electronic conductors," *Charact. Mater.*, pp. 1–14, 2002.

[8] A. Fendri, H. Ghariani, and O. Kanoun, "Dielectric spectroscopy for assessment of water content in edible oils," in *2017 14th International Multi-Conference on Systems, Signals & Devices (SSD)*, 2017, pp. 728–732.

[9] M. Nakamura, T. Tajima, K. Ajito, and H. Koizumi, "Selectivity-enhanced glucose measurement in multicomponent aqueous solution by broadband dielectric spectroscopy," in *2016 IEEE MTT-S International Microwave Symposium (IMS)*, 2016, pp. 1–3.

[10] M. A. Suster, D. Maji, N. Vitale, U. Gurkan, and P. Mohseni, "An RF/microwave microfluidic sensor for miniaturized dielectric spectroscopy based on sensor transmission characteristics," in *2015 IEEE SENSORS*, 2015, pp. 1–4.

[11] A. P. Saghati, J. S. Batra, J. Kameoka, and K. Entesari, "A metamaterial-inspired wideband microwave interferometry sensor for dielectric spectroscopy of liquid chemicals," *IEEE Trans. Microw. Theory Tech.*, vol. 65, no. 7, pp. 2558–2571, 2017.

[12] M. Abdolrazzaghi, M. H. Zarifi, C. F. A. Floquet, and M. Daneshmand, "Contactless Asphaltene Detection Using an Active Planar Microwave Resonator Sensor," *Energy & Fuels*, vol. 31, no. 8, pp. 8784–8791, 2017.

[13] M. Nosrati, Z. Abbasi, M. Baghelani, S. Bhadra, and M. Daneshmand, "Locally Strong-Coupled Microwave Resonator Using PEMC Boundary for Distant Sensing Applications," *IEEE Trans. Microw. Theory Tech.*, 2019.

[14] M. A. Karimi, M. Arsalan, and A. Shamim, "Design and dynamic characterization of an orientation insensitive microwave water-cut sensor," *IEEE Trans. Microw. Theory Tech.*, vol. 66, no. 1, pp. 530–539, 2017.

[15] W.-T. S. Chen and R. R. Mansour, "Miniature gas sensor and sensor array with single-and dual-mode RF dielectric resonators," *IEEE Trans. Microw. Theory Tech.*, vol. 66, no. 8, pp. 3697–3704, 2018.

[16] Z. Abbasi, P. Shariaty, M. Nosrati, Z. Hashisho, and M. Daneshmand, "Dual-Band Microwave Circuits for Selective Binary Gas Sensing System," *IEEE Trans. Microw.*

Theory Tech., 2019.
[17] M. H. Zarifi, T. Thundat, and M. Daneshmand, "High resolution microwave microstrip resonator for sensing applications," *Sensors Actuators A Phys.*, vol. 233, pp. 224–230, 2015.
[18] M. Daneshmand and M. H. Zarifi, "Apparatus and method for high resolution complex permittivity sensing using high Q microwave sensors for lossy or non-lossy mediums and samples." Google Patents, Jan. 08, 2019.

Chapter 2 Literature Review and Technical Background

This chapter reviews different aspects of selective multivariable analysis like resonance-based sensing, independent feature definition, microwave spectroscopy, and mixture analysis. First, various resonance-based techniques are reviewed and reported. Second, the multi-feature microwave sensors and their capabilities in the multivariable analysis are presented. As will be shown later, microwave spectroscopy is another crucial parameter for multivariable mixture analysis. Here, various microwave spectroscopy techniques are investigated and reported. Finally, single material and multicomponent mixture properties and their modelling is presented.

2.1 Microwave Sensors

The majority of microwave sensors are operating based on their single resonant frequency perturbation. Working with a single feature or parameter during the experiment limits the measurement scope to the maximum of one or two variables.

2.1.1 Single Variable Sensing for Determination of Glucose Concentrations

Microwave biosensors are essential candidates for measuring the sub-components concentration in a mixture. A Circular tapped split ring resonator (CT-SRR) is one of the proposed techniques for the characterization of aqueous glucose solution [1]. Various glucose concentrations in deionized water were prepared and examined by measuring 20 uL samples that covered the gapping area of the sensor as the most sensitive region of the device. Fig. 2.1 refers to the design layout and the realized prototype under the test. The glucose concentration range in the solutions is between 0 to 0.2 g/mL. The only measuring parameter of the sensor is its resonant frequency defined by coupled SRR, which offers the frequency range from 1.5 to 2.5 GHz for different loading scenarios.

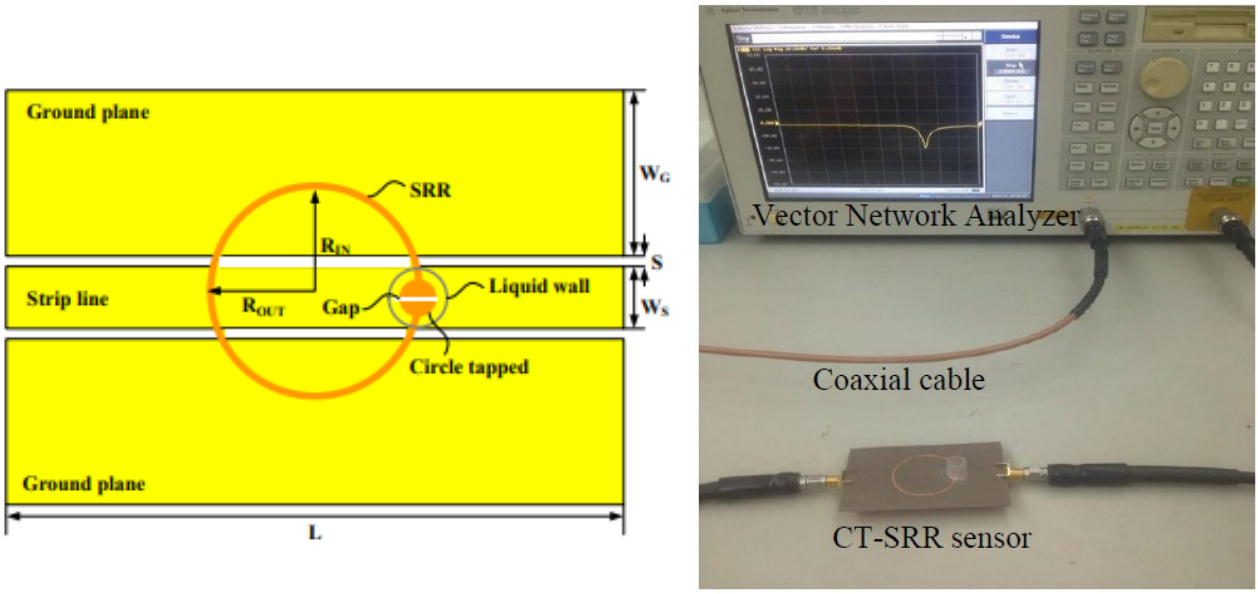

Fig. 2.1. CT-SRR sensor configuration and fabricated prototype under the test [1].

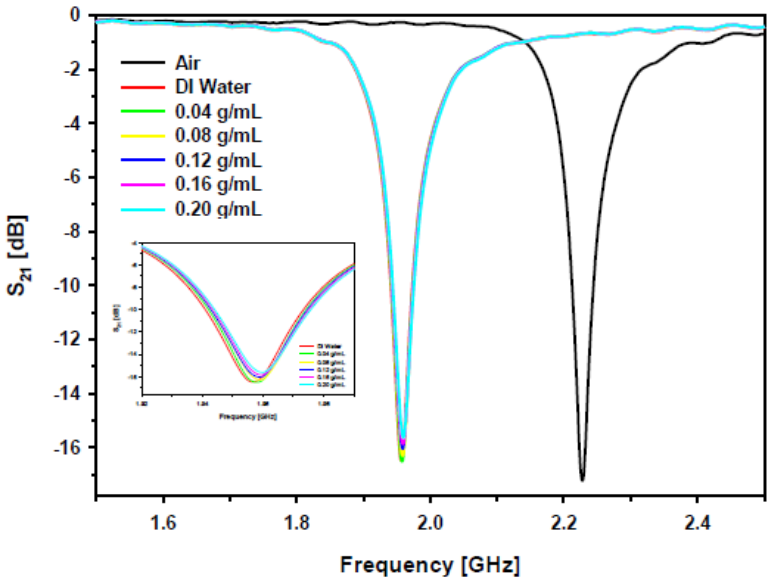

Fig. 2.2. The transmission coefficient of the sensor for different glucose concentrations in DI water [1].

The proposed technique has the maximum capability of binary mixture analysis due to its single independent feature. So only a single variable can be monitored and processed like glucose concertation in DI water. Fig. 2.2 shows the sensor response for various glucose concentrations.

2.1.2 A Planar Double-Sided Spiral Split-Ring Resonator for Mixture Characterizations

Another approach is using a double-sided spiral split-ring resonator (DSS-SRR) for real-time analysis of the fluid concertation [2]. The design specifications, together with its equivalent circuit, are shown in Fig. 2.3. As the sensing area of the device, the interdigital capacitor is exposed with different permittivities that perturb the resonator specifications and alter the resonant frequency. Considering the device's equivalent circuit, the sensor's input impedance can be analyzed as presented by Eq. 2.1.

$$Z_{in} = R_0 + j\omega L_0 + \frac{\omega^2 M^2}{j\omega L - j\frac{1}{\omega C}} \tag{2.1}$$

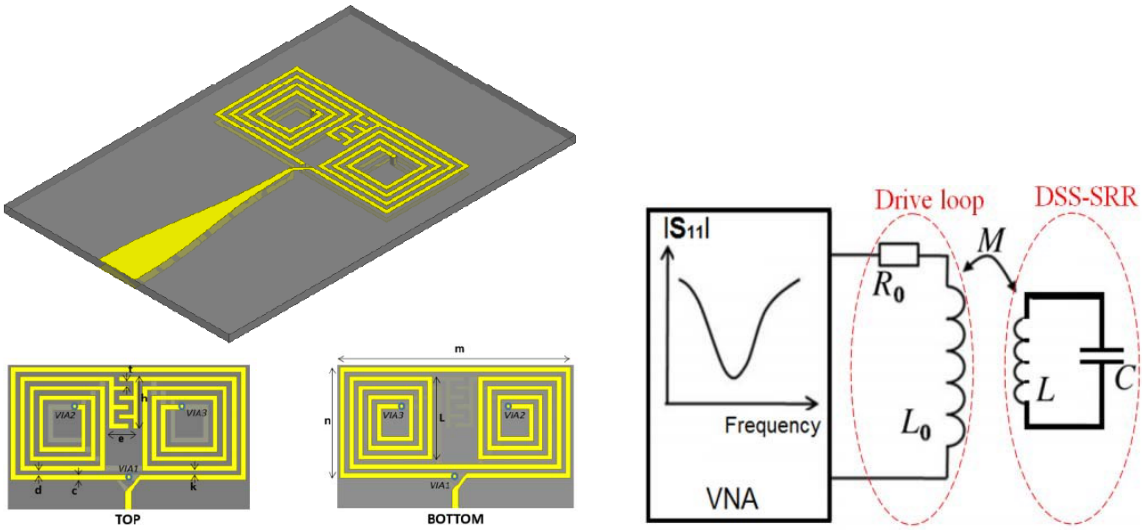

Fig. 2.3. Design geometry and equivalent circuit of the sensor [2].

The notch appears at the sensor's resonant frequency, shown in S_{11} of the single port resonator. This frequency is the measuring parameter for assessing the volume fraction of mixture components. In this work, different water-ethanol mixtures are prepared and tested using the single frequency values. Decreasing the ethanol concentration in the mixture shifts the resonance to lower

frequencies. Increasing the relative permittivity decreases the coupling coefficient, M, and reduces the notch depth correspondingly. The notch depth conveys the relationship between the complex permittivity and the resonant frequency. Considering the circuit model of the loaded sensor, increasing the ohmic loss reduces the notch depth.

The independent feature of the sensor is the notch changing for different loading cases. Here, a single variable specification can be detected, which is ethanol volume fraction in water. Fig. 2.4 exhibits the relative permittivity of the ethanol-water mixture for different ethanol concentrations together with sensor behaviour for various solution types.

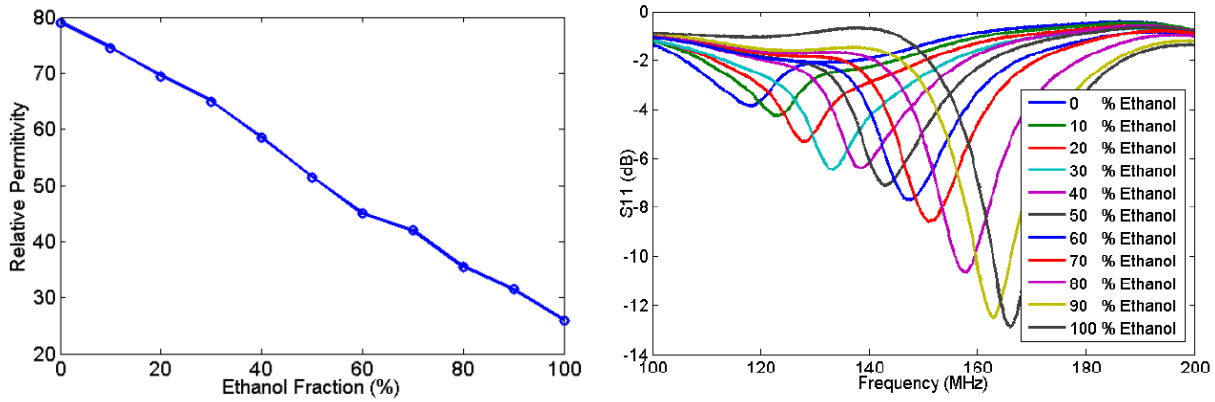

(a) (b)

Fig. 2.4. (a) Mixture relative permittivity and (b) S_{11} measurement results for different ethanol concentrations in water ranging from 0% to 100% [2].

2.1.3 Binary Mixture Sensing using Complementary Circular Spiral Resonator

A small size-sensitive microwave sensor is designed and fabricated to measure different mixtures [3]. The sensor type is a complementary circular spiral resonator (CCSR) with an operational frequency at 2.4 GHz to measure the ethanol concentrations in water. The shifts of the resonance are higher than the previous design due to the higher resonant frequency. The realized sensor structure and its functionality for detecting various ethanol concentrations in water are

reported in Fig. 2.5. The complementary ring is coupled to the transmission line at the resonant frequency and yields a notch response in the transmission coefficient of the sensor.

The maximum shifting range of the resonance is about 490 MHz while changing the ethanol concentration from 0% to 100% in water. The resonance variations are close to saturation while increasing the mixture permittivity and decreasing the ethanol concentration in the solution. The system exhibits the potential of a maximum of single variable detection as it utilizes a single independent sensor parameter. Considering the complex permittivity, the loss effect can be characterized by absorption curve values, which is a maximum of around 1 GHz for ethanol. This can be observed through different amplitudes of the resonant modes in Fig. 2.4 and Fig. 2.5.

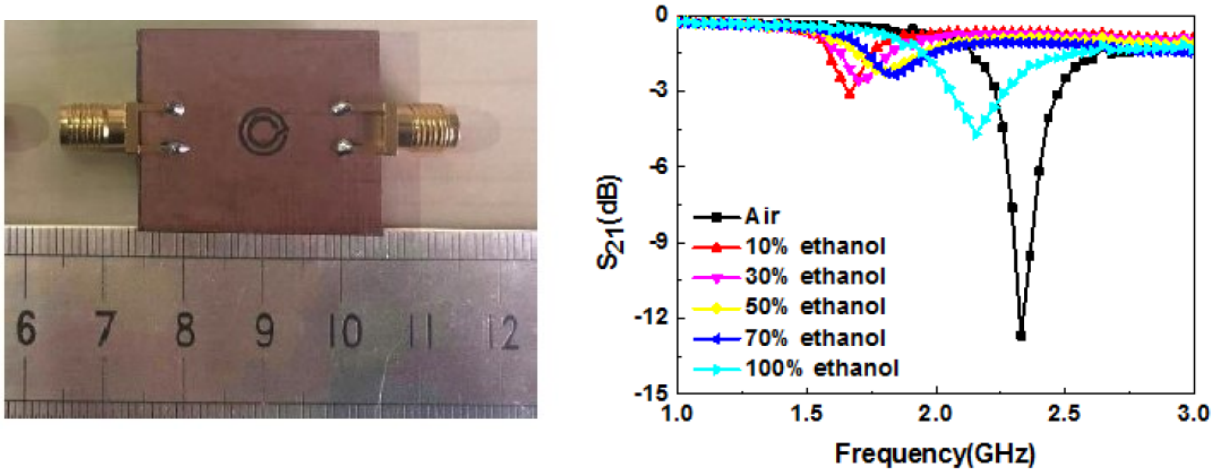

Fig. 2.5. Fabricated CCSR sensor for measuring the liquids and mixtures [3].

2.1.4 Complex Permittivity Characterization of Mixture Solutions

A stopband resonator is designed and implemented on a CPW line for measuring the DI water-ethanol solutions [4]. The sensor is matched to the 50 Ω impedance and operates at 20 GHz resonant frequency. A microfluidic channel is fabricated using a polydimethylsiloxane (PDMS) layer to convey the provided solution toward the sensor, as shown in Fig. 2.6. The

micro-scale dimensions of the sensor enable it to measure the nanoliter range solutions, which is appropriate for lab-on-chip applications. Since there is no closed-form formula for relating the complex permittivity components to the frequency shifts and resonance peak variations, a predictive model is derived using the simulation results as shown in Fig. 2.7. The defined relation between the resonant frequency shifts, ΔF_r, amplitude variations, ΔS_{21}, and complex permittivity components are presented in (2-2) and (2-3).

$$\Delta F_r = \frac{\partial F_r}{\partial \varepsilon'}\Delta\varepsilon' + \frac{\partial F_r}{\partial \varepsilon''}\Delta\varepsilon'' \tag{2-2}$$

$$\Delta S_{21} = \frac{\partial |S_{21}|}{\partial \varepsilon'}\Delta\varepsilon' + \frac{\partial |S_{21}|}{\partial \varepsilon''}\Delta\varepsilon'' \tag{2-3}$$

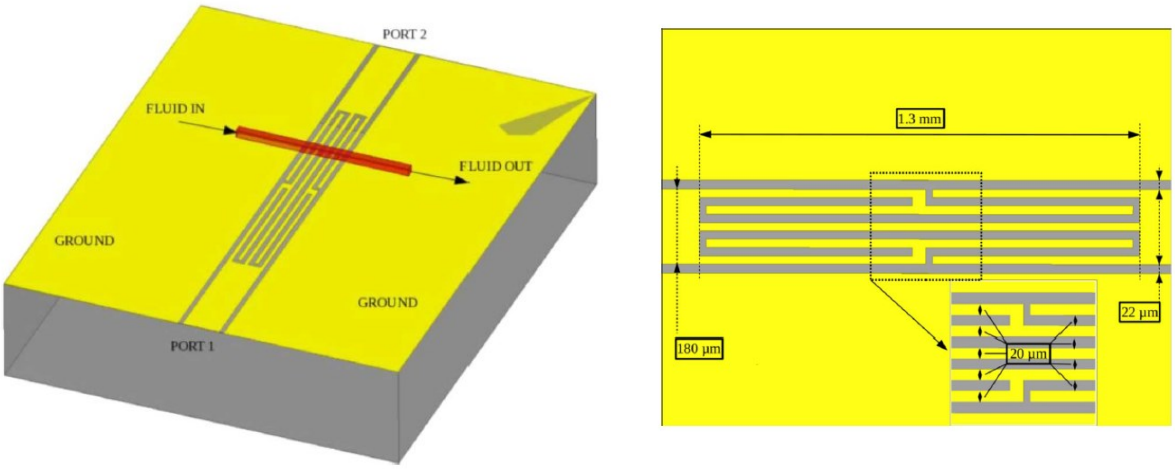

Fig. 2.6. Quarter wavelength resonator patterned on the CPW line and is integrated with PDMS type microfluidic on its top plane [4].

As can be seen in Fig. 2.7 (a) and (b), although resonance peak remains mostly constant for real relative permittivity changes and is more dependent on the imaginary part of the relative permittivity, and the resonant frequency depicts the evident variation for real relative permittivity values; still these formulas are not linearly independent from each other. Indeed, considering the relations and the problem uniqueness, the system can monitor single parameter variation, as shown in Fig. 2.7 (c). Increasing the ethanol concentration in DI water decreases the relative permittivity

of the mixture and increases the resonant frequency values. This frequency and amplitude variation can be used to map the ethanol volume fraction changes in the solution.

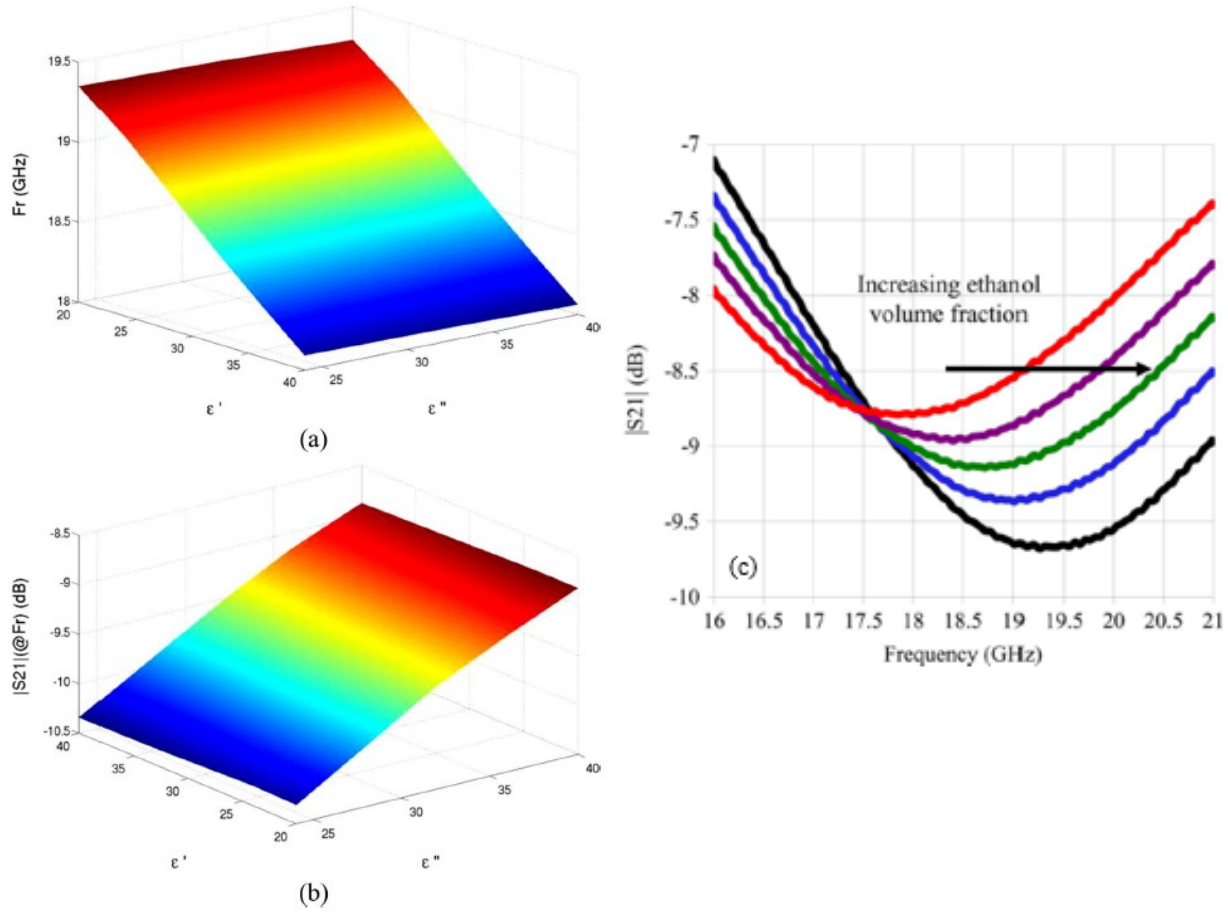

Fig. 2.7. (a) Resonance frequency and (b) peak attenuation variations versus real and imaginary parts of the relative permittivity. (c) S_{21} variations for different mixture types with various ethanol concentrations in DI water [4].

2.2 Multivariable Resonant Mode Based Analysis

2.2.1 Resonant mode Based Spectroscopy

Considering the resonant modes of the planar ring resonator, the variations in the permittivity profile of the martial under the test can directly affect the order of the resonant modes, which later will be used as one of the fundamental concepts in discrete spectroscopy [5]. Fig. 2.8 expresses the Low-Temperature Co-fired Ceramic (LTCC) based SRR integrated with the low-loss polymer as the container for measuring the spectrum of the resonant mode shifts.

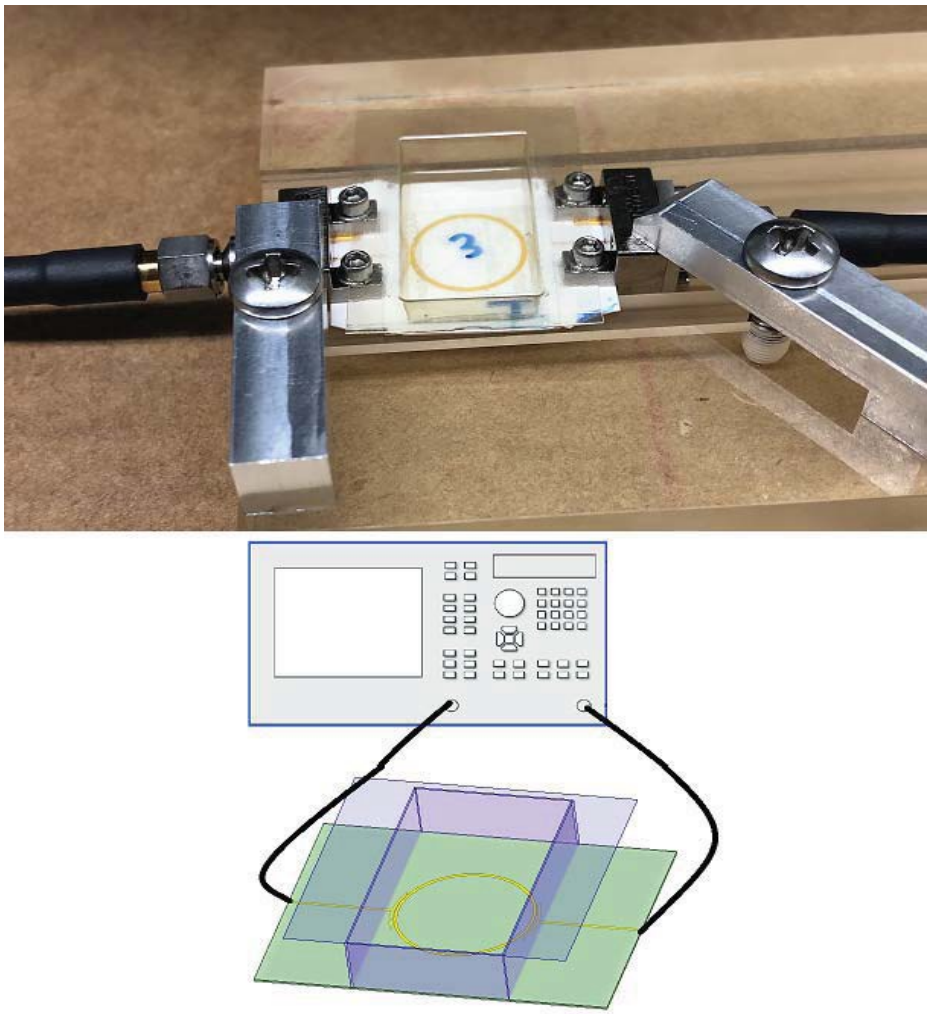

Fig. 2.8. The experimental setup for measuring the effect of permittivity variations [5].

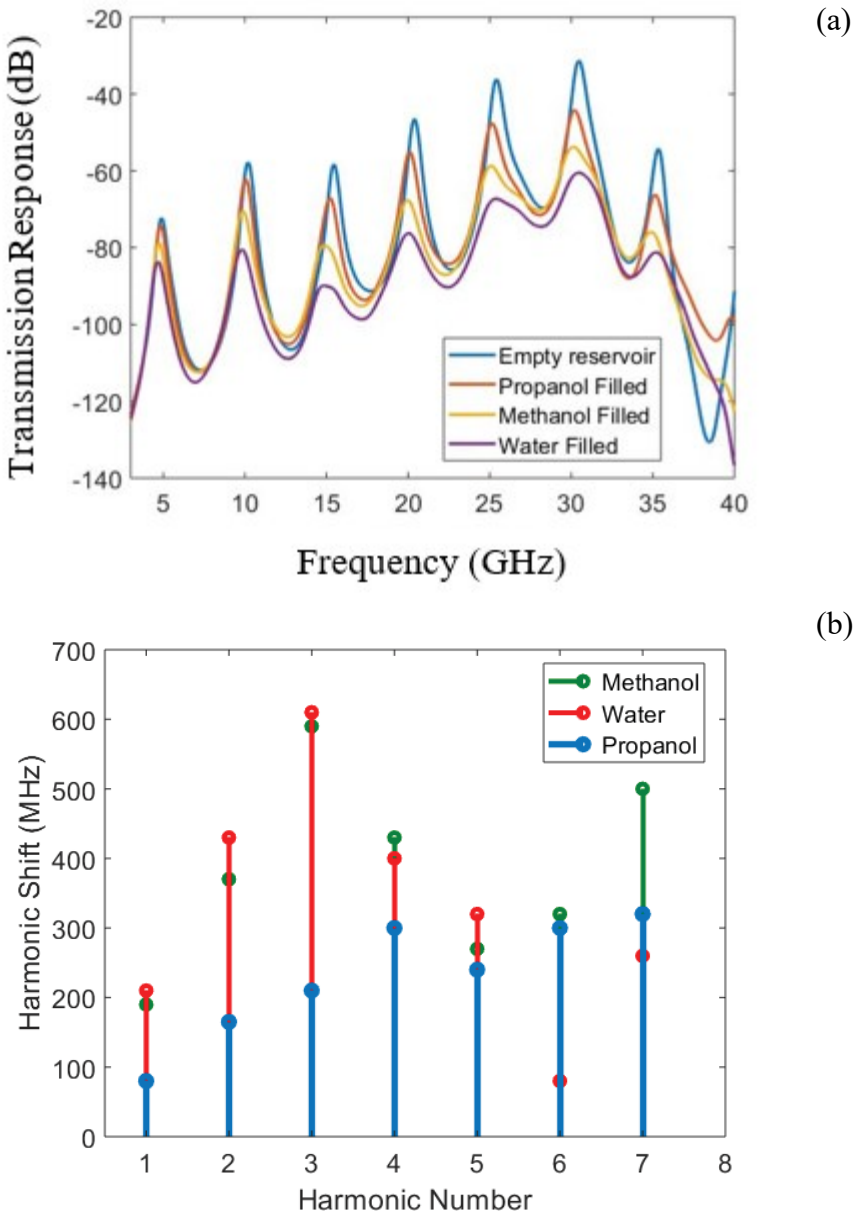

Fig. 2.9. (a) The device's frequency response together with the (b) corresponding resonant mode shifts [5].

The frequency response of the methanol, water, and propanol as permittivity variant materials, are exhibited in Fig. 2.9 together with the corresponding shifts, which are not in order. This can be interpreted through the dispersive spectrum of the permittivity, which will be used extensively in the next chapter.

2.2.2 Selective Measurement of Water Content in Multivariable Biofuel

The mixtures with more than binary components can only be measured and analyzed using multiple independent features. Here, a sensor with linearly independent parameters is introduced to detect multi-component changes like ethanol and gasoline in DI water [6]. Considering the Vx as the volume percentage of the subcomponent, the following volumetric ranges are assigned for the experiment. Since water is a lossy material, its concentration is limited to lower values

$$
\begin{aligned}
&51 < V\mathrm{E} < 85\\
&15 < V\mathrm{G} < 49\\
&0 < V\mathrm{W} < 6\\
&V\mathrm{E} + V\mathrm{G} + V\mathrm{W} = 100
\end{aligned}
\tag{2-4}
$$

where VE, VG, and VW are the ethanol, gasoline, and DI water volume fractions in different mixtures. The sum of all volumetric component percentages is 100, which can be used along two other linearly independent equations shown in Eq. (2-5). These equations derived from each subcomponent contribution in generating the final mixture impact the sensor behaviour. Each equation exhibits the linearly independent resonant mode in the system. As can be shown in Fig. 2.10(b), the sensor response presents four resonant modes, as independent parameters, in the investigated frequency range. Still, only two of these resonances are required to analyze the triple mixture considering what we have in relation (2-5).

$$
\begin{aligned}
&\Delta f_{1,\mathrm{E}} \times V\mathrm{E} + \Delta f_{1,\mathrm{G}} \times V\mathrm{G} + \Delta f_{1,\mathrm{W}} \times V\mathrm{W} = \Delta f_{1} \times 100\\
&\Delta f_{3,\mathrm{E}} \times V\mathrm{E} + \Delta f_{3,\mathrm{G}} \times V\mathrm{G} + \Delta f_{3,\mathrm{W}} \times V\mathrm{W} = \Delta f_{3} \times 100
\end{aligned}
\tag{2-5}
$$

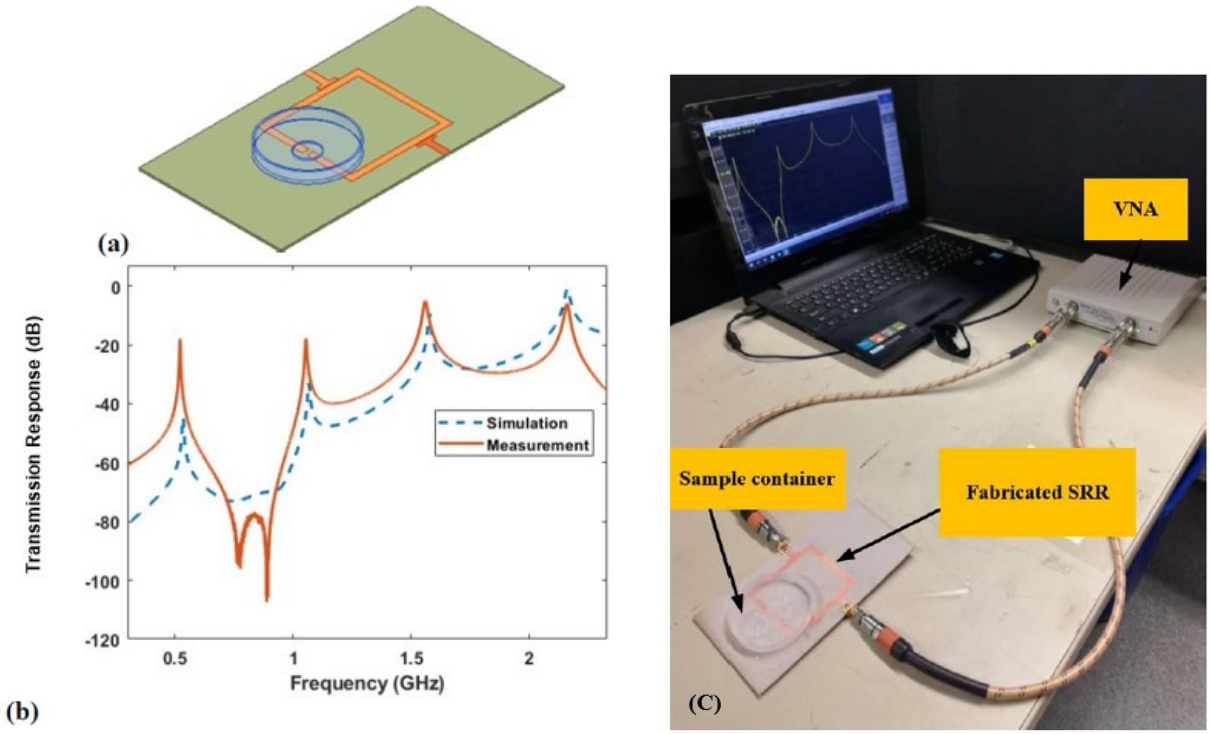

Fig. 2.10. (a) 3D schematic, (b) sensor response, and (c) experiment setup for volumetric analysis of the multivariable mixture [6].

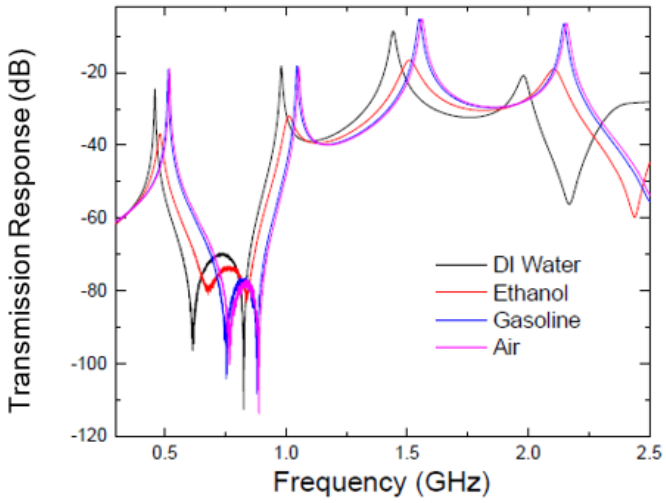

Fig. 2.11. The frequency repose of the sensor for different materials as the load [6].

Where $\Delta f_{i,j}$ is the shift of the ith resonant mode for material j. In the first part of the experiment, the sensor is calibrated for different subcomponents used in the solution, as presented in Fig. 2.11. Then different types of the mixtures are loading the sensing area as shown in Fig. 2.10 (c), and

their corresponding responses are processed using the relations in both Eq. 4 and 5. The measurement results and actual values of the mixture components are reported in Table 2.1

Table 2.1. The experiment and measurement results of the mixture component concentrations using the multivariable analysis.

Ethanol content		**Gasoline content**		**Water content**	
Actual value	*Calculated*	*Actual value*	*Calculated*	*Actual value*	*Calculated*
64	64.18	33	32.88	3	2.94
71	71.12	23	22.88	6	6.00
80	80.14	17	16.92	3	2.94
75	77.36	20	18.48	5	4.16
72	75.28	25	22.15	3	2.57
79	78.06	17	17.9	4	4.04
76	74.59	19	20.51	5	4.90
81	80.83	19	19.05	0	0.12

2.3 Microwave Spectroscopy

Microwave spectroscopy methods generally rely on the scattering parameter of the sensing system for the material characterization. One of the main classes of these methods is dielectric spectroscopy as an effective tool for extracting information regarding the permittivity profile of the materials. Most dielectric spectroscopy methods can be summarized and classified through curve fitting, circuit modelling and mapping [7], [8]. Dielectric spectroscopy also can be patterned through the resonant mode-based data fitting [9]. For getting the complex permittivity spectrum, the circuit can be as simple as an interdigital capacitor (IDC) embedded and modelled in the CPW transmission line [10].

The real and imaginary parts of the permittivity can be interpreted with circuit parameters. Then using the scattering parameters of the circuit, the permittivity spectrum can be traced. Fitting the simulation data with the measurements is also an alternative for spectrum analysis [11]. The complex permittivity components are deducted through mapping of the scattering parameters. The fitting techniques can also be applied in regression analysis using a capacitive sensor [12] or a commercial dielectric probe [13]. For example, the transmission coefficient can be utilized to extract of complex permittivity of the mixture using curve fitting techniques [14]. Another research

applied the fitting process for complex permittivity extraction based on the interferometry-based sensor's phase variation method [15]. Depending on formulation types, all mapping approaches may include approximation error.

2.3.1 Transmission Line-Based Dielectric Spectroscopy

For the broadband measurements, the characteristic impedance and propagation constant are the transmission line parameters that can be affected by any external perturbation. This fact helps to characterize the properties of the materials under the test while being integrated with the transmission line or waveguide structure [16]. The preferred material can partially fill the coaxial line structure, then measured scattering parameters can be post-processed to extract the dielectric properties of the specimen shown in Fig. 2.12.

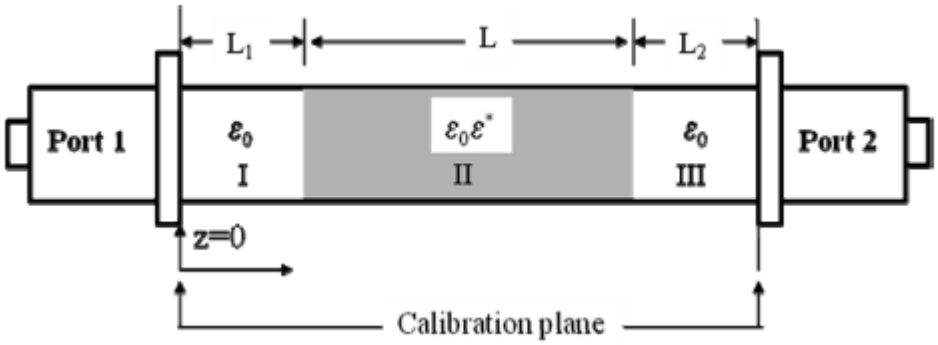

Fig. 2.12. The proposed setup for measuring of the scattering properties of the two-port line [17].

The complex scattering parameters like transmission and reflection coefficient are measured using VNA. The de-embedding process can assist in extracting the MUT properties of the material like the layout shown in Fig. 2.13.

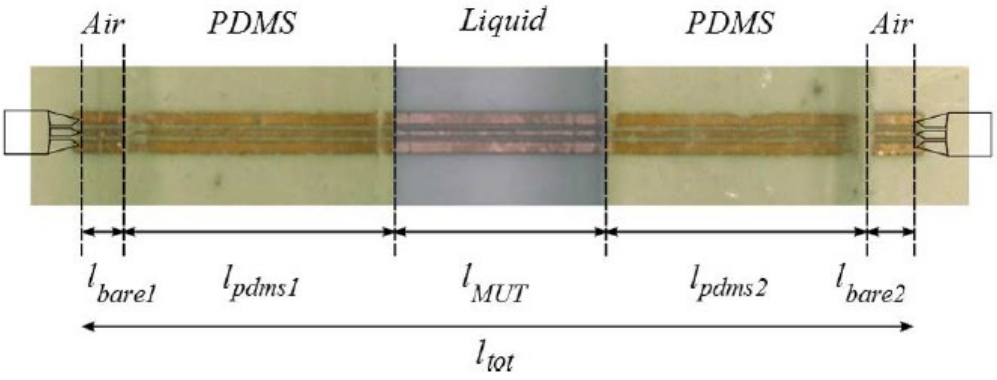

Fig. 2.13. The material under the characterization can be located in the middle part for getting the scattering parameters [18].

In some cases, the equivalent circuit of the line is used for modelling the permittivity effect into the line structure [19], [20]. Then, a fitting function can be utilized to extract the permittivity of the material by converging the model and measurements. The MUT can be characterized through the circuit parameters by de-embedding the air-filled sections as presented in Fig. 2.14.

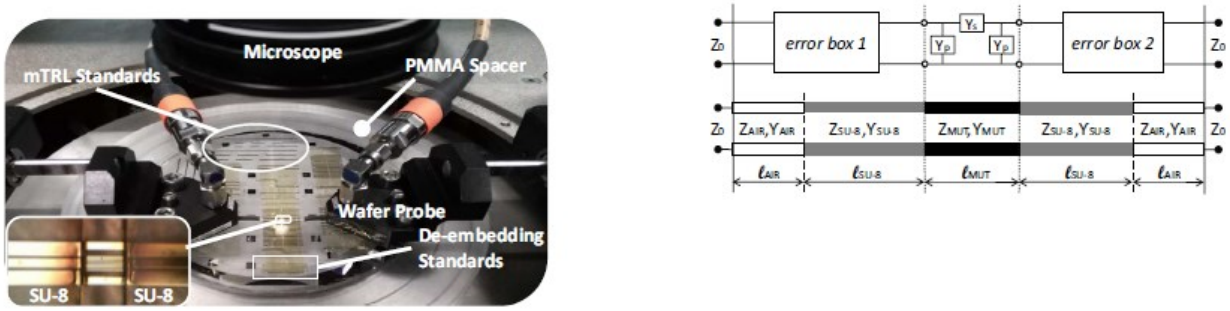

Fig. 2.14. Experimental setup and the equivalent circuit of the line under the test [10].

2.3.2 Radiation-Based Dielectric Spectroscopy

As shown in Fig. 2.15, the radiation or free-based method trusts on impedance mismatch between the free space and the material. This difference between the impedances creates reflected waves and different scattering parameters to extract the material properties. This method does not demand any sample modification; large-size samples can also be probed through the procedure and characterized for a wide range of frequencies.

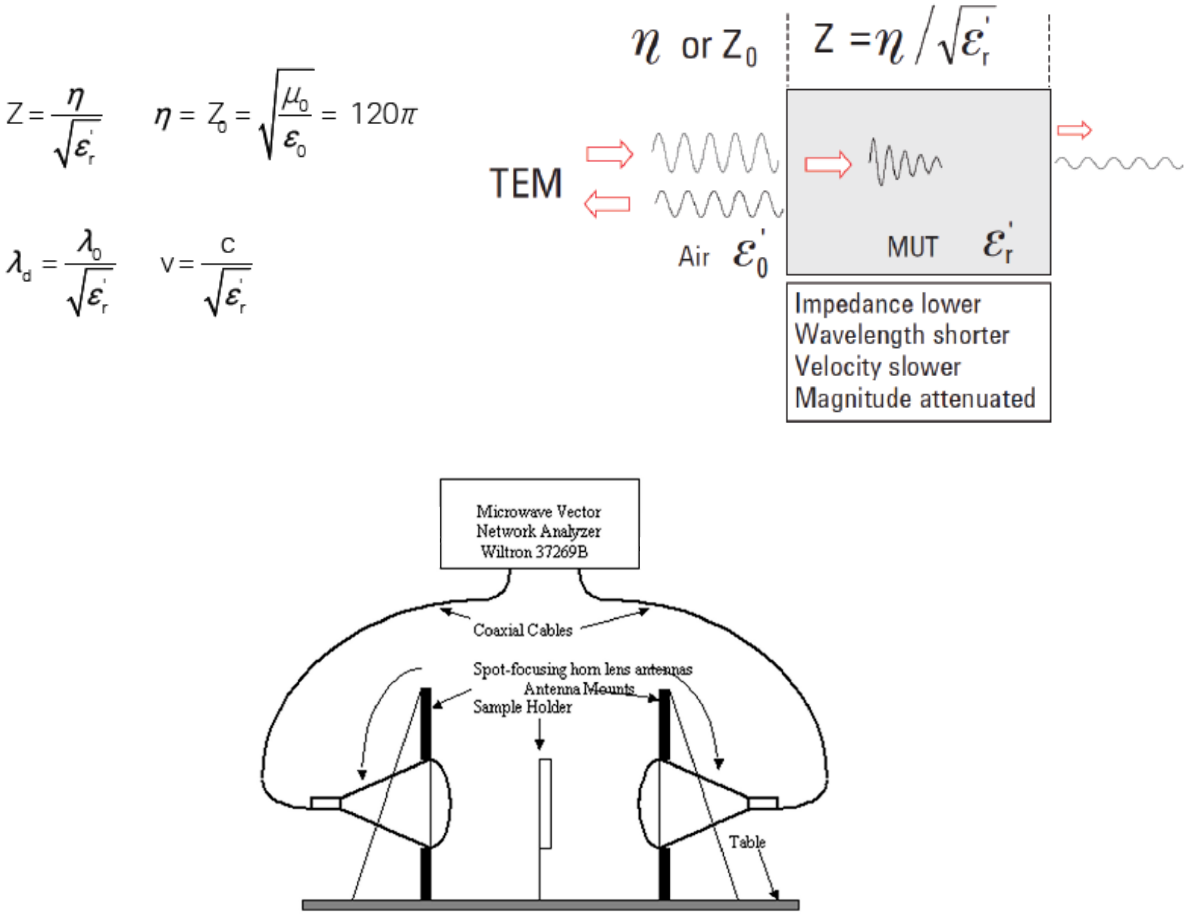

Fig. 2.15. Free space microwave measurement principle and setup [21].

2.3.3 Coaxial Probe System

In this method, the cutoff section of the probe is immersed into the sample or pressed into the specimen. In both scenarios, the fringing E-field has penetrated the material under the test. Through the impact of the perturbed E-field, the reflection coefficient of the open-ended probe is altered, and the dielectric constant is measurable [22]. Fig. 2.16 shows the coaxial probe prototype and the experimental setup, which can be used for wideband 500 MHz-110 GHz permittivity analysis. The following approach trusts high-quality contact between the open-ended probe and the specimen to minimize the effect of air gaps and air impact in the measurements, so the samples should be appropriately polished prior to the measurements.

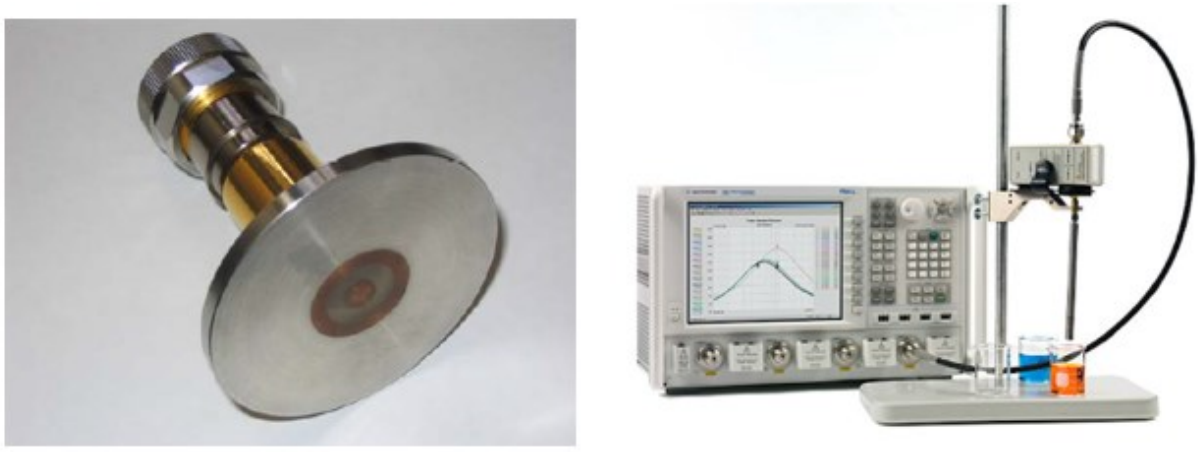

Fig. 2.16. The coaxial probe prototype and setup [23].

Considering a reference impedance for the line that lunches the TEM fields into the sample, the load impedance can affect this known impedance while contacting the probe. The integration of the sample with the probe and its equivalent circuit is shown in Fig. 2.17. The reference impedance can be evaluated by calibrating the system with a known sample prior to the main experiment.

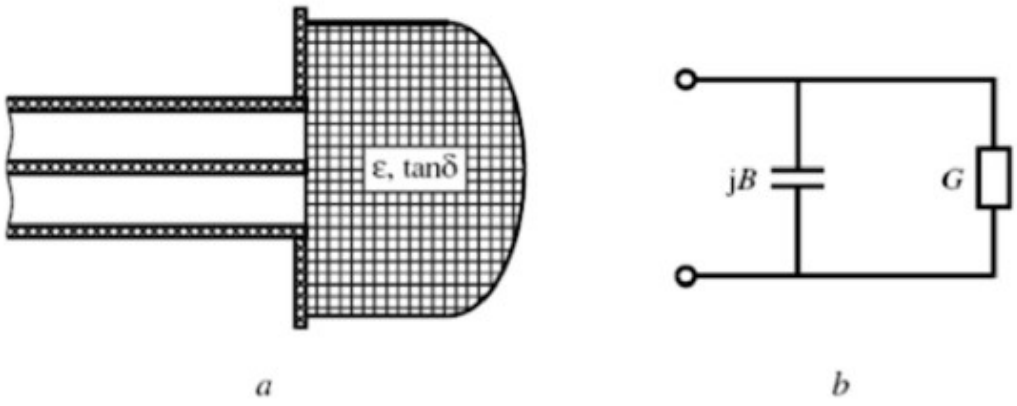

Fig. 2.17. The schematic and equivalent circuit of the dielectric probe with open end [24].

2.3.4 Resonance-Based Spectroscopy

The microwave resonators are considered low-cost, high convenience, and reliable devices for measuring and sensing the permittivity-based changes in the material under the test. The interaction of the electromagnetic fields around the sensor profile affects the microwave sensor's frequency response, which defines the distinct features for liquid and chemical sensing [25]–[27]. The sensitivity enhancement, through applying the new microfluidic techniques, on the planar resonator surface was performed, considering the most sensitive profile of the split ring resonator [28],

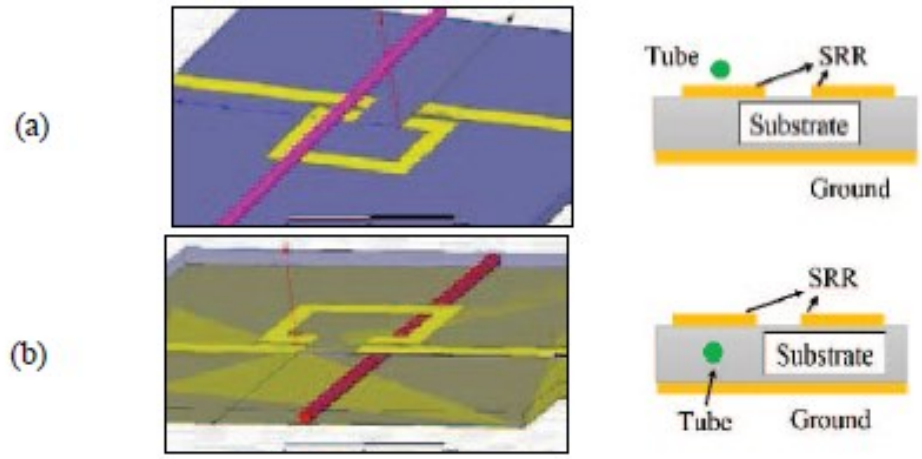

Fig. 2.18. Two configurations for the liquid sensing procedure on (a) above and (b) under the sensor [28].

The primary platform is based on embedding the microfluidic channel into the substrate area to effectively perturb the electric field profile between the coupling gap and the ground, as shown in Fig. 2.18. Fig. 2.19 presents the observed effect of different channel configurations on the sensor's performance,

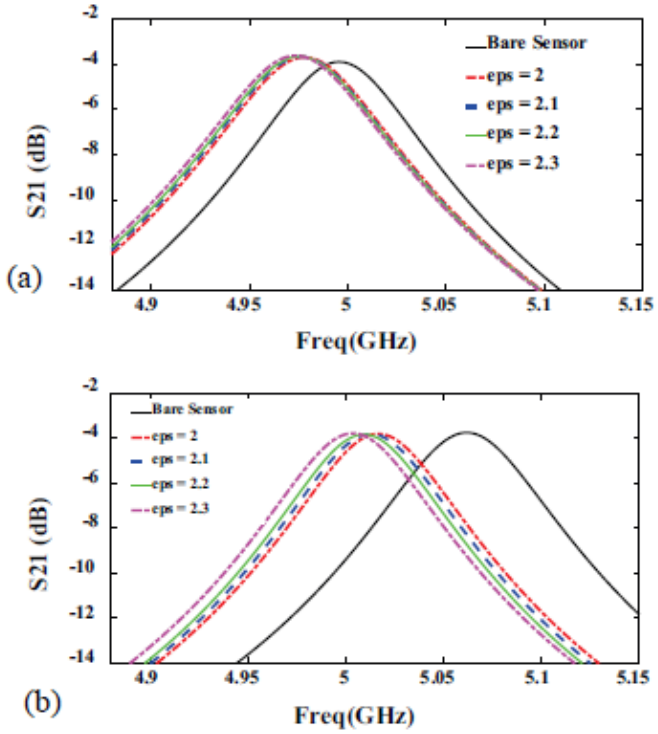

Fig. 2.19. The frequency response of the sensor for different scenarios; (a) above and (b) inside the substrate [28].

Sometimes, the host medium coated the sensing area, which absorbs the guest particles for the sensing procedure. This technique provides a convenient environment for measuring the materials or liquids with different concentrations [29].

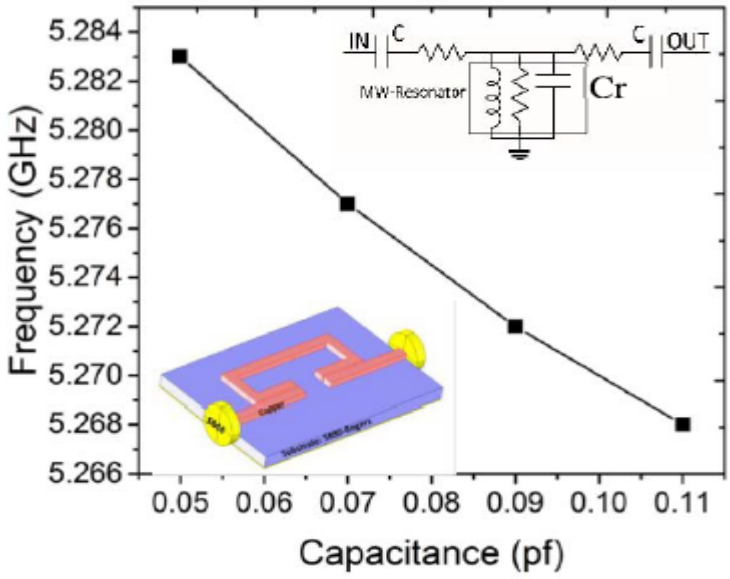

Fig. 2.20. A full-wave simulated model of the sensor and the equivalent circuit presenting the capacitance effect of the PDMS layer on the resonance [29].

2.4 Dielectric Dispersion and Modelling

2.4.1 Debye and Cole-Cole Models

Under the impact of the electrical field, electric polarization can happen for the dielectric material. This polarization can be altered for a different range of frequencies, modelled through various types of formulations. One of the basic and primary types of the formula is the Debye model. The initial Debye relaxation model was proposed in 1912 based on the relaxation time of the dipoles in the material structure [30]. The primary empirical formula was provided to explain the single relaxation materials covering alcohols, but not the more significant categories like polymers. Fig. 2.21 presents the plots of the real and imaginary permittivity for both the Debye and Cole-Cole diagrams.

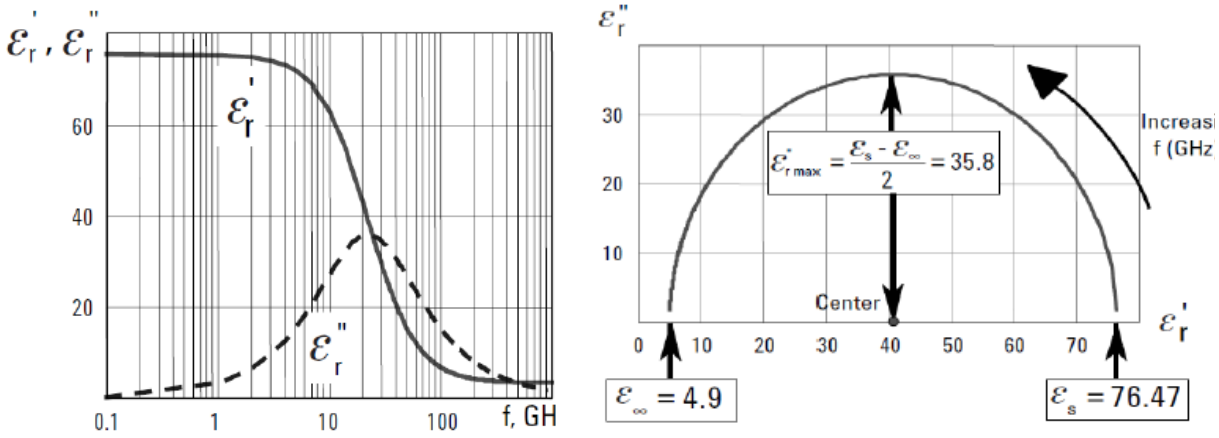

Fig. 2.21. Debye Relaxation for dispersion and absorption plots and corresponding Cole-Cole diagram [31].

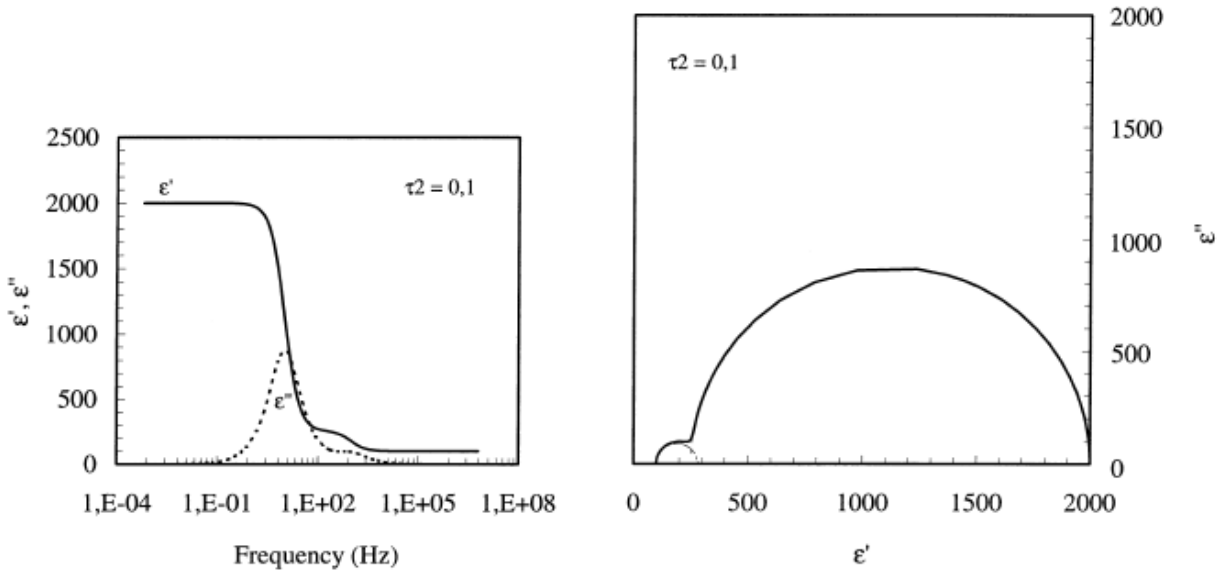

Fig. 2.22. Real and imaginary parts of the permittivity and Cole-Cole plots of the complex permittivity with different relaxation times [32].

The initial format of the Debye model does not satisfy the whole categories of the material like large molecule polymers or biological tissues [33]–[37]. As shown in Fig. 2.22, the broadness and asymmetry of dielectric profile demand to introduce the modified versions of the Debye model like Cole-Cole relaxation models [38], [39].

Debye equation defines the relation between the complex permittivity with the high, zero frequency and relaxation time as follow:

$$\varepsilon = \varepsilon_{\infty} + \frac{\varepsilon - \varepsilon_{\infty}}{1 + j\omega\tau} \tag{2-6}$$

where ε_{∞} is high-frequency permittivity, ε_s defines static permittivity and τ is the relaxation time of the dipoles. Considering the relation $\varepsilon_r = \varepsilon_r' - j\varepsilon_r''$, ε_r' and ε_r'' can be express as:

$$\varepsilon_r' = \varepsilon_{\infty} + \frac{\varepsilon_s - \varepsilon_{\infty}}{1 + \omega^2\tau^2} \tag{2-7}$$

$$\varepsilon_r'' = \frac{(\varepsilon - \varepsilon_{\infty})\omega\tau}{1 + \omega^2\tau^2} \tag{2-8}$$

Where

$\omega = 1/\tau$

For the big and log chain molecules like polymers, a broader dispersion curve is expected, which can be formularized through the Cole-Cole model [38],

$$\varepsilon^* = \varepsilon_{\infty} + \frac{\varepsilon - \varepsilon_{\infty}}{(1 + j\omega\tau)^{1-\alpha}} \tag{2-9}$$

The new parameter, α, defines the relaxation time's symmetric distribution, which can get the values between 0 and 1. The most general form of the Cole-Cole model, named Havriliak-Negami, is given as below [40]:

$$\varepsilon^* = \varepsilon_{\infty} + \frac{\varepsilon - \varepsilon_{\infty}}{[(1 + j\omega\tau)^{1-\alpha}]^{\beta}} \tag{2-10}$$

Which the new parameter, β, is defined. For the Cole-Cole model, β is considered one, and if α is zero, the general formula gives the Debye relaxation model.

2.5 Dielectric Mixture Analysis

2.5.1 Mixture Permittivity Approximation

Considering the background theory, various electromagnetic-based algorithms have developed and built the mixing rules and formulas. The use of electromagnetic (EM) theory combines the advantage of non-invasive and low-cost methods. Moreover, this theory has the main benefits of supporting real-time measurements. The concept aims to find the relation between the different inclusions as the mixture components and the effective properties of the final mixture. Maxwell-Garnett is one of the approaches to predicting the final mixture permittivity using sub-components volume fraction and relative permittivity [41]. The theory is based on macroscopic Maxwell's equations derived in many research areas [42]–[45]. The formulation can be extended into multiphase mixtures by defining one of the components as the host medium and the others as guests with distinct polarization effects [46]. One of the fundamental assumptions in Maxwell-Garnett approximation is the host and guest volume fraction ratios, and the theory is not accurate when the components volume fractions are comparable. This originates from the asymmetric nature of equations for the host medium.

2.6 References

[1] S. Harnsoongnoen, U. Charoen-In, and A. Wanthong, "Determination of glucose concentration with resonant coplanar microwave sensor," in *2017 International Electrical Engineering Congress (iEECON)*, 2017, pp. 1–3.

[2] L. Benkhaoua, M. T. Benhabiles, S. Mouissat, and M. L. Riabi, "Miniaturized quasi-lumped resonator for dielectric characterization of liquid mixtures," *IEEE Sens. J.*, vol. 16, no. 6, pp. 1603–1610, 2015.

[3] X. Zhang, C. Ruan, and K. Chen, "High-sensitivity microwave sensor for liquid characterization using a complementary circular spiral resonator," *Sensors*, vol. 19, no. 4, p. 787, 2019.

[4] T. Chretiennot, D. Dubuc, and K. Grenier, "A microwave and microfluidic planar resonator for efficient and accurate complex permittivity characterization of aqueous solutions," *IEEE Trans. Microw. Theory Tech.*, vol. 61, no. 2, pp. 972–978, 2012.

[5] N. Hosseini, M. Baghelani, and M. Daneshmand, "Discrete Microwave Spectroscopy using Planar Resonator," in *2019 IEEE Canadian Conference of Electrical and Computer Engineering (CCECE)*, 2019, pp. 1–4, doi: 10.1109/CCECE.2019.8861771.

[6] M. Baghelani, N. Hosseini, and M. Daneshmand, "Selective measurement of water content in multivariable biofuel using microstrip split ring resonators," in *IEEE MTT-S International Microwave Symposium Digest*, 2020, vol. 2020-Augus, doi: 10.1109/IMS30576.2020.9223908.

[7] G. Pandey, R. Kumar, and R. J. Weber, "Design and implementation of a self-calibrating, compact micro strip sensor for in-situ dielectric spectroscopy and data transmission," in IEEE Sensors*, 2013 IEEE*, 2013, pp. 1–4.

[8] C. Schröder and O. Steinhauser, "Using fit functions in computational dielectric spectroscopy," *J. Chem. Phys.*, vol. 132, no. 24, p. 244109, 2010.

[9] A. Talai, F. Steinhäußer, A. Bittner, U. Schmid, R. Weigel, and A. Koelpin, "A permittivity characterization method by detuned ring-resonators for bulk materials up to 110 GHz," in *2014 44th European Microwave Conference*, 2014, pp. 124–127.

[10] X. Bao, I. Ocket, J. Bao, D. Kil, L. Brancato, and B. Nauwelaers, "Broadband dielectric spectroscopy measurements of liquids combining interdigital capacitor and coplanar waveguide," in *2017 47th European Microwave Conference (EuMC)*, 2017, pp. 946–949.

[11] D. Havelka, O. Krivosudský, and M. Cifra, "Grounded coplanar waveguide-based 0.5–50 GHz sensor for dielectric spectroscopy," in *2017 47th European Microwave Conference (EuMC)*, 2017, pp. 950–953.

[12] A. Fendri, H. Ghariani, and O. Kanoun, "Dielectric spectroscopy for assessment of water content in edible oils," in *2017 14th International Multi-Conference on Systems, Signals & Devices (SSD)*, 2017, pp. 728–732.

[13] M. Nakamura, T. Tajima, K. Ajito, and H. Koizumi, "Selectivity-enhanced glucose measurement in multicomponent aqueous solution by broadband dielectric spectroscopy," in *2016 IEEE MTT-S International Microwave Symposium (IMS)*, 2016, pp. 1–3.

[14] M. A. Suster, D. Maji, N. Vitale, U. Gurkan, and P. Mohseni, "An RF/microwave microfluidic sensor for miniaturized dielectric spectroscopy based on sensor transmission characteristics," in IEEE Sensors, 2015, pp. 1–4.

[15] A. P. Saghati, J. S. Batra, J. Kameoka, and K. Entesari, "A metamaterial-inspired wideband microwave interferometry sensor for dielectric spectroscopy of liquid chemicals," *IEEE Trans. Microw. Theory Tech.*, vol. 65, no. 7, pp. 2558–2571, 2017.

[16] M. S. Venkatesh and G. S. V Raghavan, "An overview of dielectric properties measuring techniques," *Can. Biosyst. Eng.*, vol. 47, no. 7, pp. 15–30, 2005.

[17] Z. Lu, M. Lanagan, E. Manias, and D. D. Macdonald, "Two-port transmission line technique for dielectric property characterization of polymer electrolyte membranes," *J. Phys. Chem. B*, vol. 113, no. 41, pp. 13551–13559, 2009.

[18] S. Liu, I. Ocket, M. Cauwe, D. Schreurs, and B. Nauwelaers, "Sensitivity analysis of broadband on-wafer dielectric spectroscopy of yeast cell suspensions up to 110 GHz," *IEEE Microw. Wirel. Components Lett.*, vol. 25, no. 3, pp. 199–201, 2015.

[19] J. C. Booth *et al.*, "Quantitative permittivity measurements of nanoliter fluid volumes from 50 MHz to 40 GHz with microfluidic channels," in *CPEM 2010*, 2010, pp. 353–354.

[20] J. Mateu, N. Orloff, M. Rinehart, and J. C. Booth, "Broadband permittivity of liquids extracted from transmission line measurements of microfluidic channels," in *2007 IEEE/MTT-S International Microwave Symposium*, 2007, pp. 523–526.

[21] D. K. Ghodgaonkar, V. V Varadan, and V. K. Varadan, "Free-space measurement of complex permittivity and complex permeability of magnetic materials at microwave frequencies," *IEEE Trans. Instrum. Meas.*, vol. 39, no. 2, pp. 387–394, 1990.

[22] W. J. Ellison and J.-M. Moreau, "Open-ended coaxial probe: Model limitations," *IEEE Trans. Instrum. Meas.*, vol. 57, no. 9, pp. 1984–1991, 2008.

[23] I. M. Woodhead, I. Platt, J. H. Christie, and S. Krenek, "A broadband spectroscopic sensor probe," *Int. J. Smart Sens. Intell. Syst.*, vol. 1, no. 2, pp. 459–469, 2008.

[24] A. I. Mekhannikov, A. V Myl'nikov, and L. P. Maslennikova, "Calibration of a coaxial antenna-probe for microwave dielectric measurements," *Meas. Tech.*, vol. 50, no. 4, pp. 425–428, 2007.

[25] M. S. Boybay and O. M. Ramahi, "Material characterization using complementary split-ring resonators," *IEEE Trans. Instrum. Meas.*, vol. 61, no. 11, pp. 3039–3046, 2012.

[26] A. Ebrahimi, W. Withayachumnankul, S. Al-Sarawi, and D. Abbott, "High-sensitivity metamaterial-inspired sensor for microfluidic dielectric characterization," *IEEE Sens. J.*, vol. 14, no. 5, pp. 1345–1351, 2013.

[27] M. H. Zarifi and M. Daneshmand, "Liquid sensing in aquatic environment using high quality planar microwave resonator," *Sensors Actuators B Chem.*, vol. 225, pp. 517–521, 2016.

[28] M. Abdolrazzaghi, M. H. Zarifi, and M. Daneshmand, "Sensitivity enhancement of split ring resonator based liquid sensors," in *2016 IEEE SENSORS*, 2016, pp. 1–3.

[29] M. H. Zarifi, A. Sohrabi, P. M. Shaibani, M. Daneshmand, and T. Thundat, "Detection of volatile organic compounds using microwave sensors," *IEEE Sens. J.*, vol. 15, no. 1, pp. 248–254, 2014.

[30] P. Debye, "Zur theorie der spezifischen wärmen," *Ann. Phys.*, vol. 344, no. 14, pp. 789–839, 1912.

[31] K. M. Chew, R. Sudirman, N. Seman, and C. Y. Yong, "Relaxation frequency and relaxation time estimation for phantom modeling by proposed fitting linear models," in *2012 IEEE-EMBS Conference on Biomedical Engineering and Sciences*, 2012, pp. 911–915.

[32] P. Q. Mantas, "Dielectric response of materials: extension to the Debye model," *J. Eur.*

Ceram. Soc., vol. 19, no. 12, pp. 2079–2086, 1999.

[33] Y. Feldman, A. Puzenko, Y. Ryabov, W. T. Coffey, and Y. P. Kalmykov, "Dielectic Relaxation Phenomena in Complex Materials," *Adv. Chem. Phys.*, vol. 133, no. A, p. 1, 2006.

[34] C. Cametti, "Dielectric and conductometric properties of highly heterogeneous colloidal systems," *Riv. del Nuovo Cim. della Soc. Ital. di Fis.*, vol. 32, no. 5, pp. 185–260, 2009.

[35] R. Hilfer, "Analytical representations for relaxation functions of glasses," *J. Non. Cryst. Solids*, vol. 305, no. 1–3, pp. 122–126, 2002.

[36] A. Khamzin, R. Nigmatullin, and I. Popov, "Justification of the empirical laws of the anomalous dielectric relaxation in the framework of the memory function formalism," *Fract. Calc. Appl. Anal.*, vol. 17, no. 1, pp. 247–258, 2014.

[37] R. Metzler and J. Klafter, "The random walk's guide to anomalous diffusion: a fractional dynamics approach," *Phys. Rep.*, vol. 339, no. 1, pp. 1–77, 2000.

[38] K. S. Cole and R. H. Cole, "Dispersion and absorption in dielectrics I. Alternating current characteristics," *J. Chem. Phys.*, vol. 9, no. 4, pp. 341–351, 1941.

[39] K. S. Cole and R. H. Cole, "Dispersion and absorption in dielectrics II. Direct current characteristics," *J. Chem. Phys.*, vol. 10, no. 2, pp. 98–105, 1942.

[40] S. Havriliak and S. Negami, "A complex plane analysis of α-dispersions in some polymer systems," in *Journal of Polymer Science Part C: Polymer Symposia*, 1966, vol. 14, no. 1, pp. 99–117.

[41] V. A. Markel, "Introduction to the Maxwell Garnett approximation: tutorial," *JOSA A*, vol. 33, no. 7, pp. 1244–1256, 2016.

[42] B. Salski and M. Celuch, "On the equivalence between the Maxwell-Garnett mixing rule and the Debye relaxation formula," *IEEE Trans. Microw. Theory Tech.*, vol. 60, no. 8, pp. 2352–2358, 2012.

[43] A. H. Sihvola and I. V Lindell, "Chiral Maxwell-Garnett mixing formula," *Electron. Lett.*, vol. 26, no. 2, pp. 118–119, 1990.

[44] B. Salski and M. Celuch, "The debye rigorous equivalent of the Maxwell-Garnett mixing rule for effective modeling of carbon suspensions under MW irradiation," in *2011 IEEE MTT-S International Microwave Symposium*, 2011, pp. 1–4.

[45] M. H. Nisanci, F. de Paulis, M. Y. Koledintseva, J. L. Drewniak, and A. Orlandi, "From Maxwell Garnett to Debye model for electromagnetic simulation of composite dielectrics—PART II: Random cylindrical inclusions," *IEEE Trans. Electromagn. Compat.*, vol. 54, no. 2, pp. 280–289, 2011.

[46] A. Sihvola, "Mixing rules with complex dielectric coefficients," *Subsurf. Sens. Technol. Appl.*, vol. 1, no. 4, pp. 393–415, 2000.

Chapter 3 Selective Volume Fraction Sensing using Resonant Modes of Planar Resonator

This research proposes a new technique for enabling multivariable volume fraction analysis by microwave resonator-based sensors. We address this issue using material dispersion and its nonlinear impact on the resonant mode frequency shift. The concept is utilized to determine the volumetric fraction of multicomponent mixture selectively. Since the relaxation frequency of the permittivity spectrum is different for various materials, the resultant response from different material combinations can generate independent features. Debye model as a simplified presentation of the Cole-Cole relation plays a significant role in distinguishing the components in the mixture. For the proof of concept, a model-based technique for analyzing the mixtures of methanol, ethanol, and propanol is proposed. Next, as complementary research, the artificial intelligence-assisted (AI) method is applied to monitor the biofuel impurities. It is shown that the volume fraction of the components can be selectively distinguished. The concept in theory and experiment is verified, and the formulation is explained in detail.

3.1 Introduction

In diagnostic and chemical analysis, volumetric fraction measurement of mixtures is an important parameter [1], [2]. For mass spectroscopy, sophisticated and expensive analytical chemistry techniques such as FTIR for quantitative study of mixtures, Gas Chromatography-Mass Spectroscopy (GC-MS), and Liquid Chromatography-Mass Spectroscopy (LC-MS) for gas and liquid materials and mixes have been suggested [3]–[5].

Material dispersion is identified via microwave spectroscopy. Dielectric spectroscopy is an important technique for collecting information on the permittivity profile of materials, and it is one of the primary classes of these approaches. Curve fitting, circuit modelling, and mapping may be used to summarise and classify most dielectric spectroscopic approaches [6], [7]. Using a

capacitive sensor [8] or a commercial dielectric probe [9], the fitting approaches may also be used for regression analysis. The transmission coefficient also may be used to determine the mixture's relative complex permittivity [10]. Another study used an interferometry-based sensor and a fitting methodology for relative complex permittivity extraction based on the phase variation method [11]. All of these approaches have a significant error rate, which has led to numerous researchers using resonant-based sensors for minute and sensitive readings. Microwave resonator-based sensors have sparked a lot of interest in the last decade, with applications ranging from biomedical to oil and gas, owing to their impressive features like high sensitivity, low power consumption, low-cost, inherently non-invasiveness, and even distant sensing capabilities [12]–[16]. Developing the microwave sensors functionality was the main goal of many researches [17], [18].

In this work, we propose utilizing the information provided by the frequency shift of the resonant modes to obtain the information required for sensing in multivariable mixtures. The use of electromagnetic (EM) theory combines the advantage of non-invasive and low-cost methods. The concept aims to find the relation between the different inclusions as the mixture components and the practical impact on the properties of the final mixture and resonant frequency shifts of the sensors. The proposed technique enables selective sensing using resonant-based microwave sensors in multivariable multicomponent mixtures with known materials and paves the way for combining the sensitivity with selectivity.

The organization of the research is as follows: after an introduction in section 3.1, the operational concept of the proposed method is described briefly in section 3.2.

Section 3.2.1 shows the capability of the Debye model for exhibiting the relative permittivity spectrum of different materials. A discrete method of spectroscopy based on frequency shift deviations is described to characterize and detect the varying profile of the components as the primary step together with a comprehensive simulation response of the loaded sensor. In sections 3.2.2 and 3.2.3, the volumetric analysis framework and sensor performance are observed. Finally, the performed experiments are explained in section 3.2.4.

3.2 Model-Based Multi-Feature Technique

Resonant-based sensors have been chiefly utilized on binary solvents. For most of these methods, resonant frequency shift and transmission coefficient are the main criteria for evaluating the mixture contents and concentrations [19], [20].

Considering the transmission line theory, reflection-based analysis was also applied to formulate characterizing the binary solvent features [21]. Dispersion and absorption parameters of the pure material or binary mixtures were analyzed through resonance frequencies and amplitudes [22]. However, to our knowledge, no paper has utilized resonant-based sensors for selective volumetric mixture sensing.

The present work proposes a novel volumetric characterization method using microwave resonator-based sensors by introducing new orthogonal features which enable the microwave resonator sensors to determine the concentration of more than two materials in a known mixture. These new features are originated from frequency-dependent relative permittivity characteristics of materials, which provides a unique relative permittivity spectrum of each component. Fig. 3.1 summarizes the process flow of the proposed technique in a chart for selective sensing of a mixture volume fraction analysis.

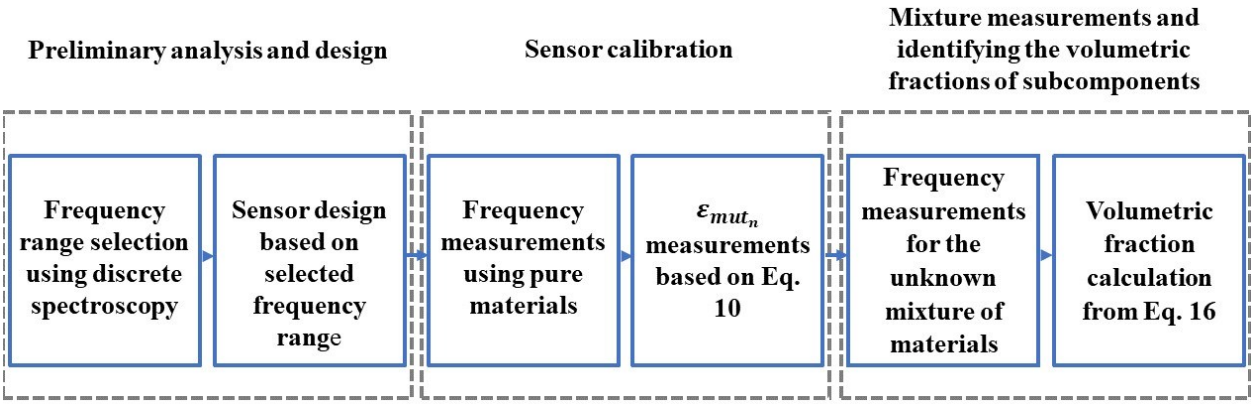

Fig. 3.1. The flowchart of the volumetric ratio extraction process [45].

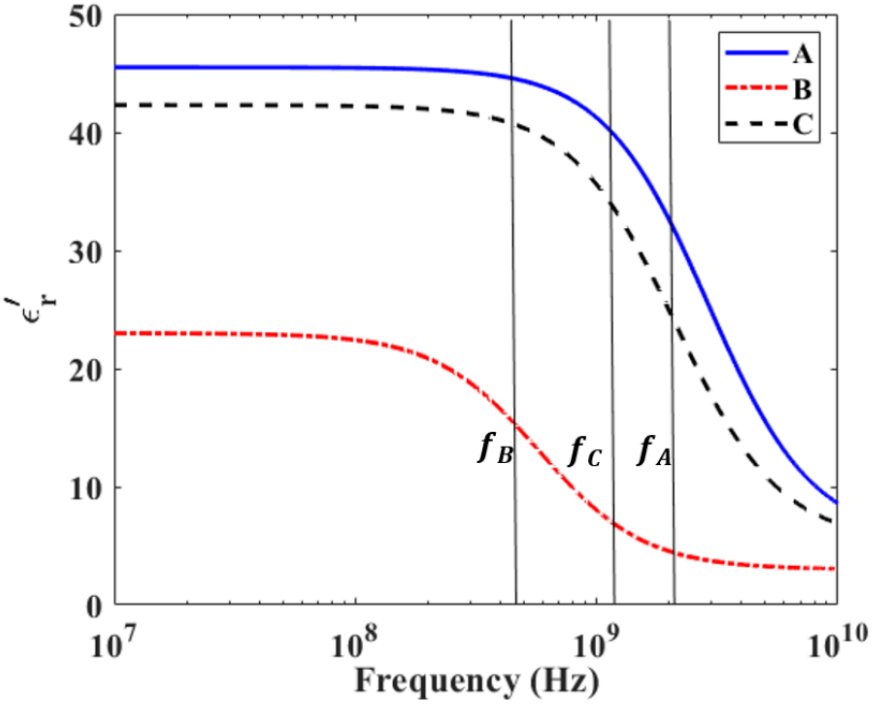

Fig. 3.2. The relative permittivity profile or dispersion plots of different materials with distinct relaxation time [45].

Generally, the proposed procedure requires sensor design, calibration, and measurement steps, as in any sensor. Considering a function between the resonant modes and their corresponding shifts, the variant permittivity profile of the subcomponents can define the nonlinearity into system. This nonlinearity generates the independently changing resonant modes that can be utilized as individual features of the sensor. So, the whole process starts by designing the sensors with operating frequencies in the variant section of the permittivity profile. These frequencies should be chosen so that the relative real permittivity of materials is not constant compared to each other.

Sensor calibration is then accomplished by combining resonance frequency shifts of all the resonant resonator modes due to the introduction of pure materials (methanol, ethanol, and propanol) to the resonator. This information is then used to form the Sensor Calibration Matrix (SCM) based on Eq. (3-9). The mixture matrix (MM) for the mixture of interest, which we would like to determine the volumetric fraction of each component in, is then created by introducing that mixture to the sensor using Eq. (3-9) with the calculated parameters given in Table 3.2. The

volumetric fraction matrix (VFM) containing the volume of each material in the mixture could be calculated using Eq. (3-15).

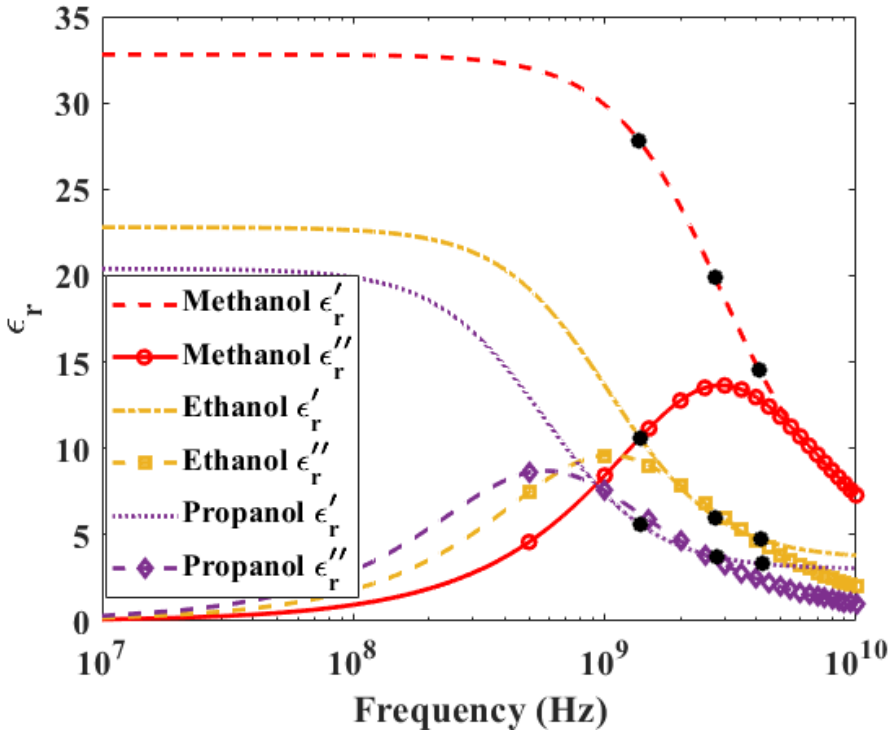

Fig. 3.3. The relative permittivity profile of the different types of alcohol at 23°C [45].

These steps were discussed in detail in sections 3.3-3.6. For example, we can consider different types of materials with discriminated molecular configurations that respond differently to the single driving force or E-field, creating relative permittivity dispersion with various molecular relaxations. Indeed, the different relaxation frequencies [23] yield the difference between the falling patterns of the A, B, and C relative permittivity, as shown in Fig. 3.2.

By designing the dominant resonator frequency and resonant modes to operate in the varying profile of the relative permittivity curves, the extracted frequency-based dataset forms resonant modes, or their frequency shifts are not linearly dependent anymore. This independence can be applied to generate the system of mixing equations on volumetric data of the mixture component. This is because the different resonant modes of a single resonator are exposed to different relative

permittivity values (in Fig. 3.2), so the related frequency shift to each of the resonant modes is different and follows the dispersion of the material relative permittivity. A detailed review of the phenomena is presented in the next section.

The next step is designing the sensor that can operate and perform the frequency-based sampling in the candidate frequency band. The functionality of the sensor should be characterized for different MUT loading scenarios. Then these achieved sensor responses are calibrated and interpreted in terms of the related MUT permittivity. For each resonance response, measured at sensor output, the corresponding MUT relative permittivity is demanded. For a mixture of known materials, related literature or even a dielectric measuring probe could be used for determining the required sample's relative permittivity.

During the experiment, each resonant mode or resonance is responsible for providing the necessary information to complete of the related mixing equation. So, the dataset extracted from a single resonance or resonant mode after different sensor loadings can be used to form the corresponding resonant mode-based mix equation. Writing the final mixing equations in matrix form, the sensor calibration matrix is obtained, which contains all the predicted relative permittivity values to form the linear equations. As for analyzing the mixture with i number of varying components, at least, $i-1$ number of resonant modes or resonances is demanded solving the equations.

Through the chapter, this concept is formulized, and a set of equations based on the Debye model and intensive electromagnetic simulations in HFSS are structured. Solutions of these equations will provide the volumetric fraction of different components in the mixture. The multicomponent analysis is feasible as microwave resonator-based sensors' most critical operational problem based on the achieved results and approach.

3.2.1 Relative Permittivity Profile and Sensor Design

3.2.1.1 Relative Permittivity Variation versus Frequency

Considering the Debye model of different subcomponents [24], the frequency dependencies of dispersion and absorption curves for methanol, ethanol, and propanol at 23°C are presented in Fig. 3.3 [25], [26]. Different dielectric relaxation times for the methanol, ethanol, and propanol yield different frequencies accompanying E-field attenuation in loss factor. Considering the mixture of these liquids, other relaxation times are involved in variant yield curves.

The altering relative permittivity profile of the materials under the test at different frequency ranges is detectable through the shift variations of a typical resonator assumed as the sensor. The corresponding dispersion relations and Debye presentation of the materials are shown in the appendix A.

3.2.1.2 Resonator Design

The microstrip ring structure shown in Fig. 3.4 is a ring resonator used to perform the measurements in this chapter. The simplicity of the layout and supporting the multiple frequencies introduce the ring resonator as a suitable candidate for the measures. The size of the sensor is the main parameter that should be confirmed for controlling the resonance-based sampling resolution and operational frequencies [27]. Technically, for each resonance, the standing wavelength follows the relation in equation (3-1) as follows.

$$n\lambda_g = 2\pi R, \quad \text{n} = 1, 2, 3, \tag{3-1}$$

where R is the mean radius of the ring and λ_g can be interpreted as the guided wavelength for each resonant mode as follows;

$$\lambda_g = \frac{c}{f_n\sqrt{\varepsilon_{eff}(f_n)}} \tag{3-2}$$

This equation shows the relationship between the perturbed resonance frequency, f_n, and the effective relative permittivity, $\varepsilon_{eff}(f_n)$, of the device integrated with the material under the test [28], [29]. The change in the relative permittivity profile of MUT can then be monitored using the sensor's resonant frequency shift or frequency response. As the resonator's main design parameter, the resonance frequency is selected because ratios of relative permittivity of the mixture's components vary at the frequencies related to resonant modes of the resonator. This guarantees to have orthogonal features, which increase the number of independent equations. This enables the capability of distinguishing between more than two variables in the mixture and consequently their volumetric calculations, as will be discussed in the succeeding sections.

3.2.1.3 Proposed Deviation-based Discrete Spectroscopy Concept

The permittivity-based spectroscopy is processed by observing the frequency shift of the resonant mode frequencies of the resonator. For mixture analysis, the frequency shift measurements are carried out as the main factor for accomplishing the mixing equations from volumetric fractions as the unknowns. These shifts are linearly increasing across the resonant modes when the effective relative permittivity remains constant during the corresponding range, so for monitoring the potential changes in the relative permittivity profile of the materials, a parameter named shift deviation is defined and derived based on effective relative permittivity changes for simplifying the permittivity-based spectroscopy. Using equation (3-2) we can easily relate the resonance frequency of each resonant mode to the overall effective relative permittivity of MUT and substrate as follows;

$$f_n = \frac{nC}{2\pi r\sqrt{\varepsilon_{eff}(f_n)}} \tag{3-3}$$

Each resonant mode frequency-shift due to the introduction of MUT to the system can be calculated by,

$$\Delta f_n = \frac{nC}{2\pi r}\left(\frac{1}{\sqrt{\varepsilon_{eff,Air}}} - \frac{1}{\sqrt{\varepsilon_{eff}(f_n)}}\right) \tag{3-4}$$

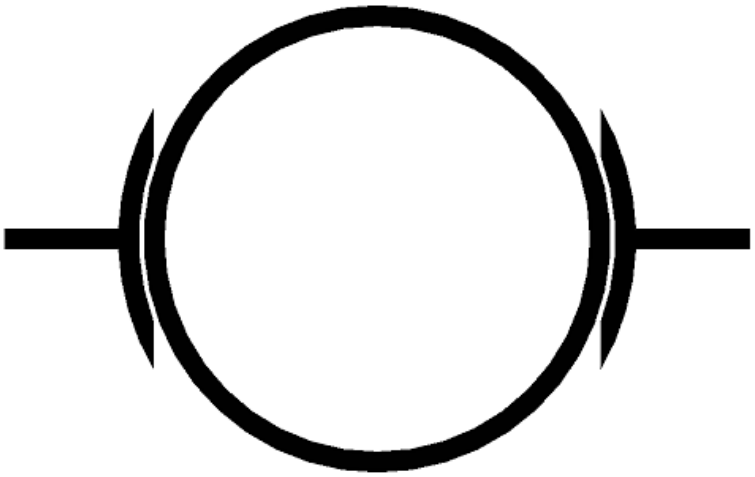

Fig. 3.4. The layout of the simple ring resonator was chosen as the multi-resonant mode sensor for performing the volumetric data analysis [45].

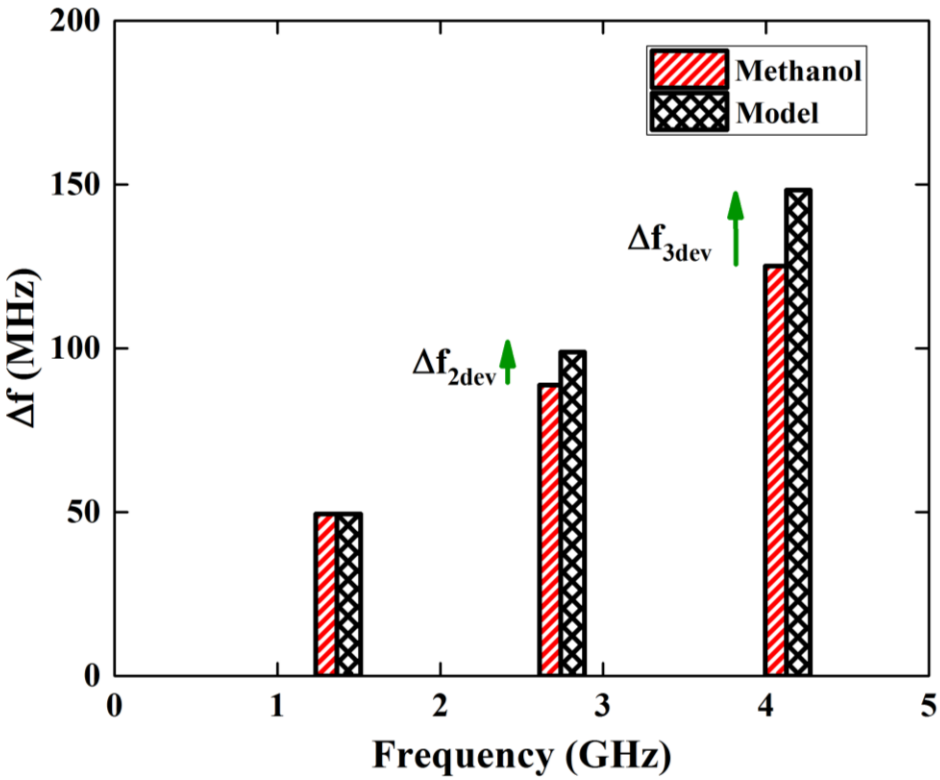

Fig. 3.5. The comparison between the measured resonant mode shift spectra of the methanol and a model with a non-variant relative permittivity model [45].

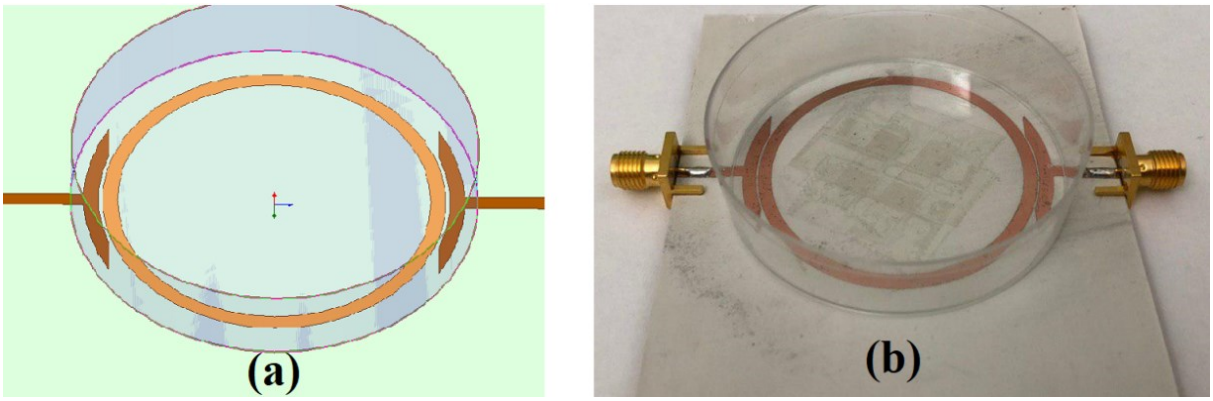

Fig. 3.6. The schematics of the (a) simulated and (b) fabricated ring resonator integrated with the cylinder polymer container on top [45].

If the relative permittivity were considered constant $\varepsilon_{eff}(f_n) = \varepsilon_{eff}(f_1)$, the expected frequency shift of the resonant mode frequencies would be:

$$\Delta f_n = n\Delta f_1 \tag{3-5}$$

However, the actual frequency shift includes the relative permittivity dispersion. Therefore, one can define a deviation term for analyzing the dispersion behaviour of the relative permittivity profile pattern as follows;

$$\Delta f_{n\,dev} = n\Delta f_1 - \Delta f_n \tag{3-6}$$

Considering a fairly constant relative permittivity for the air, the shift deviation term for the n_{th} resonant mode ($\Delta f_{n,dev}$) is described by:

$$\Delta f_{n\,dev} = \frac{nC}{2\pi r}\left(\frac{\sqrt{\varepsilon_{eff}(f_1)} - \sqrt{\varepsilon_{eff}(f_n)}}{\sqrt{\varepsilon_{eff}(f_1)\,\varepsilon_{eff}(f_n)}}\right) \tag{3-7}$$

So the relative permittivity decrement in the testing material profile emanates in deviation term through (3-8). For example, Fig. 3.5 shows the shift deviation caused by the difference between the invariant relative permittivity profile of the model with $\varepsilon_s = \varepsilon_\infty = \varepsilon_{s\,Methanol}$ and methanol's Debye model on a set of resonant modes. The corresponding deviation values can be perceived along the material spectrum by performing an arbitrary sampling distribution on the material's relative permittivity profile. Then, the samples with a high level of shift deviation are predicted as suitable candidates for future design plans. Any changes along the relative permittivity spectrum of the MUT can be mapped in terms of the shift deviation. By increasing the number of resonant mode frequencies or sample points in the specified probing range, the resolution of the deviation curves can be improved, and the interpolated curve becomes smoother. The deviation-based spectroscopy is completed through this approach, and the acquired results can be used to determine the convenient frequencies.

3.2.1.4 Pre-Experimental Characterization

In practice, the sensor design and the test setup impact the effective relative permittivity observed by the sensor, which needs to be considered in the pre-experimental characterization. We designed a simple microstrip ring resonator on Rogers RO3003 ($\varepsilon_r = 3$ and $\tan\delta = 0.0013$) as shown in Fig. 3.6. The values of the geometrical parameters are $r_{in} =$ 20 mm and ring width of 1.9 mm on the 760 μm substrate coupled through a 0.5 mm gap to the 50Ω microstrip line. The 3D schematic of the sensor used for full-wave HFSS simulations together with the fabricated version of the sensor is shown in (a) and (b), respectively.

The sensor in Fig. 3.6 is used, and a small polymer container with $\varepsilon_r \approx 4.1$ (assumed a constant relative permittivity value at the utilized frequency range by this project) was attached and fixed on the top of the resonator. The container dielectric property is calibrated, and its effect on sensor response is included during the individual subcomponent's measurements. The pre-defined volume of the liquids under the test is set to 6.4 mL, adjusted by a dispenser with 1μL precision, thoroughly covers the surface of the ring resonator.

A complete set of simulations is performed that correlates expected resonant mode frequencies with the associated substrate and MUT permittivities. This helps to understand and distinguish the impact of the effective relative permittivity resulting from the substrate and the MUT in the system calibration. A full-wave HFSS simulation is performed for obtaining the analytic values of each resonant mode, and the results are exhibited in a 3D plot of resonance frequency resonant modes in Fig. 3.7. The designed unloaded ring resonator operates at its first resonant modes of $f_1 = 1.42$ GHz, $f_2 = 2.84$ GHz and $f_3 = 4.26$ GHz. It could be seen from Fig. 3.7 that the device resonance frequencies at all the resonant modes have a high dependency on the substrate permittivity. It also presents the dependency of the results to the relative permittivity of MUT that is located on top of the resonator. Here, we are modelling this pattern by utilizing exponential fitting with an averaged relative error of 1.8% in MATLAB as follows;

$$f_n = a + be^{(-\beta {\varepsilon_{mut_n}}^{P1} - \alpha {\varepsilon_{sub_n}}^{P2})} \tag{3-8}$$

where ε_{sub_n} and ε_{mut_n} are the relative permittivity of the substrate and material under the test respectively at the associated resonant mode, and coefficients, a, b, α, β, $P1$, and $P2$ can accept a different range of values after being compared and calibrated with the valid model or measurements. This equation can be written as follows:

$$\varepsilon_{mut_n} = \left(\frac{\ln\left(\frac{f_n - a}{b}\right) + \alpha {\varepsilon_{sub}}^{P2}}{-\beta}\right)^{1/P1} \tag{3-9}$$

Equation (3-9) can be applied as a proposed formula in our discrete microwave spectroscopy to correlate the relative permittivity to the resonant mode frequencies and used here as a powerful tool for sensor analysis.

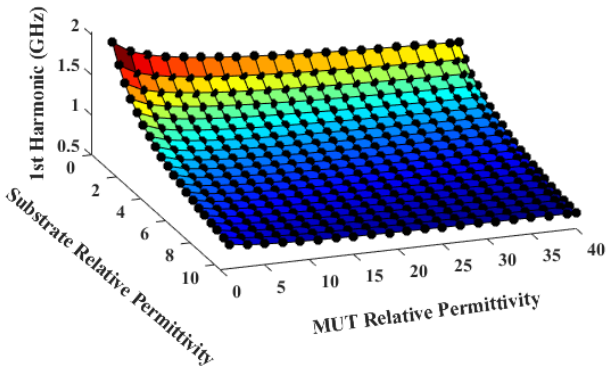

(a)

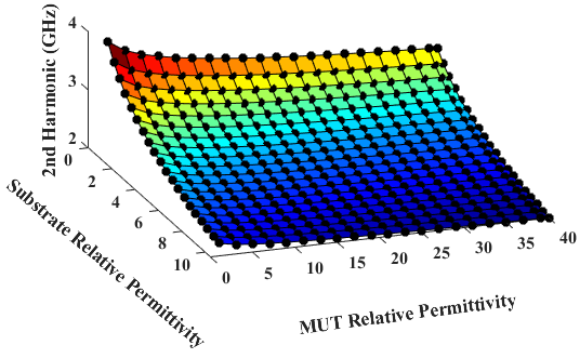

(b)

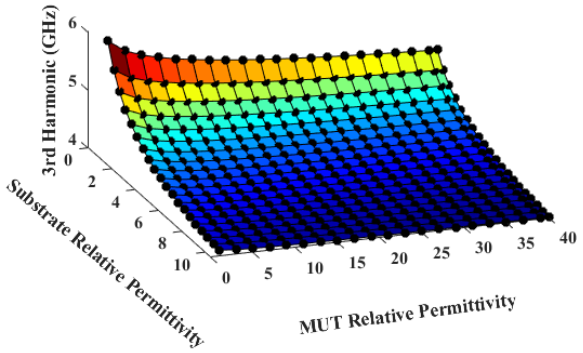

(c)

Fig. 3.7. The plot of the (a) first, (b) second, and (c) third resonant mode of the full-wave simulation ring resonator model for different substrate and MUTs relative permittivity values [45].

3.2.2 Volumetric Fraction Analysis

After understanding the impact of the resonator substrate on the overall effective permittivity, it is time to formulate the relative permittivity of the mixture to be able to correlate the sub resonant mode frequency shifts with the mixture subcomponents.

3.2.2.1 Mixture Equations and Preferences

Any change in relative permittivity of the components can alter the mixture properties and its relative permittivity profile. There are many types of equations addressing mixtures model such as Maxwell-Garnett [30]–[34], Kraszewski [35], Lichtenecker [36] and/or other extended formulations [37] that relates the impacts of volume fractions of the components to the final mixture relative permittivity through the superposition effect. Amongst these, Maxwell-Garnett is one of the approaches commonly used to predict the final mixture relative permittivity using sub-components volume fraction and their relative permittivity [38]. However, it is more suitable for binary mixtures rather than multivariable mixtures [39]. The permittivity and their molecular interactions are responsible for determining the permittivity values [40], [41]. The Lichtenecker and Kraszewski equations present the linear approximation and less complexity in the formulation compared to the other analysis, which is preferred in computation. In comparison, Lichtenecker has been even further simplified by the ternary solvent formulation presented in [42] and thus is used in this chapter. Based on this analysis, the total relative permittivity can be related to the subcomponents relative permittivity as follows:

$$\ln \varepsilon_{n_{mix}} = \sum_{i=1}^{N} V_i \ln (\varepsilon_{ni}) \tag{3-10}$$

where V_i is the volume fraction of the mixture components, $\varepsilon_{n_{mix}}$ and ε_{ni} present the dielectric constant of the mixture and its components at f_n (resonant mode frequencies) respectively. To highlight again, *n* is referred to as the resonant mode numbers, and *i* corresponds with the mixture component index. Using (3-10) in (3-11), one can get:

$$\ln\left(\frac{\ln\left(\frac{f_{n_{mix}}-a}{b}\right)+\alpha{\varepsilon_{sub}}^{P2}}{-\beta}\right)^{1/P1} = \sum_{i=1}^{N} V_i \ln\left(\frac{\ln\left(\frac{f_{ni}-a}{b}\right)+\alpha{\varepsilon_{sub}}^{P2}}{-\beta}\right)^{1/P1} \quad (3\text{-}11)$$

Therefore, the matrix presentation of the equations can be written as:

$$\begin{bmatrix} \ln \varepsilon_{1_{mix}} \\ \vdots \\ \ln \varepsilon_{n_{mix}} \end{bmatrix}_{n\times 1} = \begin{bmatrix} \ln(\varepsilon_{11}) & \cdots & \ln(\varepsilon_{1i}) \\ \vdots & \ddots & \vdots \\ \ln(\varepsilon_{n1}) & \cdots & \ln(\varepsilon_{ni}) \end{bmatrix}_{n\times i} \begin{bmatrix} V_1 \\ \vdots \\ V_i \end{bmatrix}_{i\times 1} \quad (3\text{-}12)$$

where $\ln(\varepsilon_{ni})$ presents the relative permittivity of the subcomponent *i* at the n^{th} resonant mode.

In addition, considering the total volume of the mixture as 1, we have,

$$\sum_{i=1}^{N} V_i = 1 \quad (3\text{-}13)$$

Here, to minimize the number of required resonant modes for the sampling, equation (3-13) can be the complementary relation. So, in extended format, (3-12) and (3-13) can be integrated and rewritten in the form of (3-14), which is a completed form of the system of equations for obtaining the volumetric concentrations of the mixture components,

$$\underbrace{\begin{bmatrix} \ln \varepsilon_{1_{mix}} \\ \vdots \\ \ln \varepsilon_{n_{mix}} \\ 1 \end{bmatrix}_{i\times 1}}_{\substack{Mixture \\ Matrix(MM)}} = \underbrace{\begin{bmatrix} \ln(\varepsilon_{11}) & \cdots & \ln(\varepsilon_{1i}) \\ \vdots & \ddots & \vdots \\ \ln(\varepsilon_{n1}) & \cdots & \ln(\varepsilon_{ni}) \\ 1 & \cdots & 1 \end{bmatrix}_{i\times i}}_{\substack{Sensor\ Calibration \\ Matrix(SCM)}} \times \underbrace{\begin{bmatrix} V_1 \\ \vdots \\ V_i \end{bmatrix}_{i\times 1}}_{\substack{Volume\ Fraction \\ Matrix(VFM)}} \quad (3\text{-}14)$$

So, for the number of unknown volume fractions, (*i*), the linear system of equations will need at least *(i-1)* resonant modes data for solving and getting the volume percentages of the components. The final form of matrix equation can also be presented as the following generalized format:

$$VFM = SCM^{-1} \times MM \quad (3\text{-}15)$$

3.2.2.2 Volumetric Analysis of the Mixture

Here, the volume fraction matrix contains the volumetric information of the mixture components. The sensor calibration matrix is achieved by testing the sensor for each mixture component individually as MUT. The prepared dataset evaluates and records the sensor response for each of the mixture components separately in each test as each material impacts the sensor resonant modes differently. The final step is to examine the same resonant mode's reaction while perturbing the sensor by the resultant mixture. The achieved data from each frequency reflects each component's contribution in the final mixture characteristics. For example, the components with higher volume fractions create dominant influence comparing the materials with small portions. The mixture matrix includes all the essential information for solving the equations based on mixture properties.

For the best performance, the resonant modes should be chosen from the frequency range that the mixture components have the most dispersion. This helps to avoid non-orthogonal equations. Here, we chose the second, f_2 = 2.84 GHz, and third, f_3 = 4.26 GHz, resonant modes for the data acquisition process, and the main resonance frequency at 1.42 GHz for the bare resonator. These are the main criteria for designing the resonator.

3.2.3 Validation of Sensor Performance

S_{21} was measured and plotted for the first three resonant modes to validate the sensor's performance and capability to monitor the relative permittivity profile properties. The measured results and quality factor of 6.4 mL methanol, ethanol, and propanol loading microstrip ring resonator are illustrated in Fig. 3.8 and Table 3.1, respectively. The dataset achieved from the resonant modes is used for filling in the sensor calibration matrix (SCM) in (3-16) by assigning a relative permittivity for each measured frequency. This process is described with further details in section 3.2.1 through acquiring the relative permittivity values on the sensor calibration curve. Considering the Debye model of the liquid components, distinct shift levels occur for resonant modes while loading the resonator with different liquids. The accuracy of the measured results will

be validated through analyzing and comparing the corresponding resonance shifts profile pattern and the loss factor, respectively. All measurements were performed using the Copper-Mountain-Technologies© C2420 4-Port 20 GHz vector network analyzer, with a calibration frequency range from 500MHz to 5GHz with 8001 measurement points, under the temperature of 23℃ in lab condition. First, the loss based patterning and analysis is performed and compared with ε_r'' curve pattern. To fulfill the expectations, the resonance amplitude variations should follow the same trend as the loss factor amplitude Fig. 3.9 presents the measured insertion loss of the system while loading the resonator with different scenarios and compares it with absorption curves in the Debye model. The higher resonant modes can experience even increasing or decreasing loss profiles. For the higher frequencies, methanol loss is higher than the loss of ethanol and propanol. In other words, methanol exhibits the rising trend for higher resonant modes while the propanol loss spectrum presents a descending pattern.

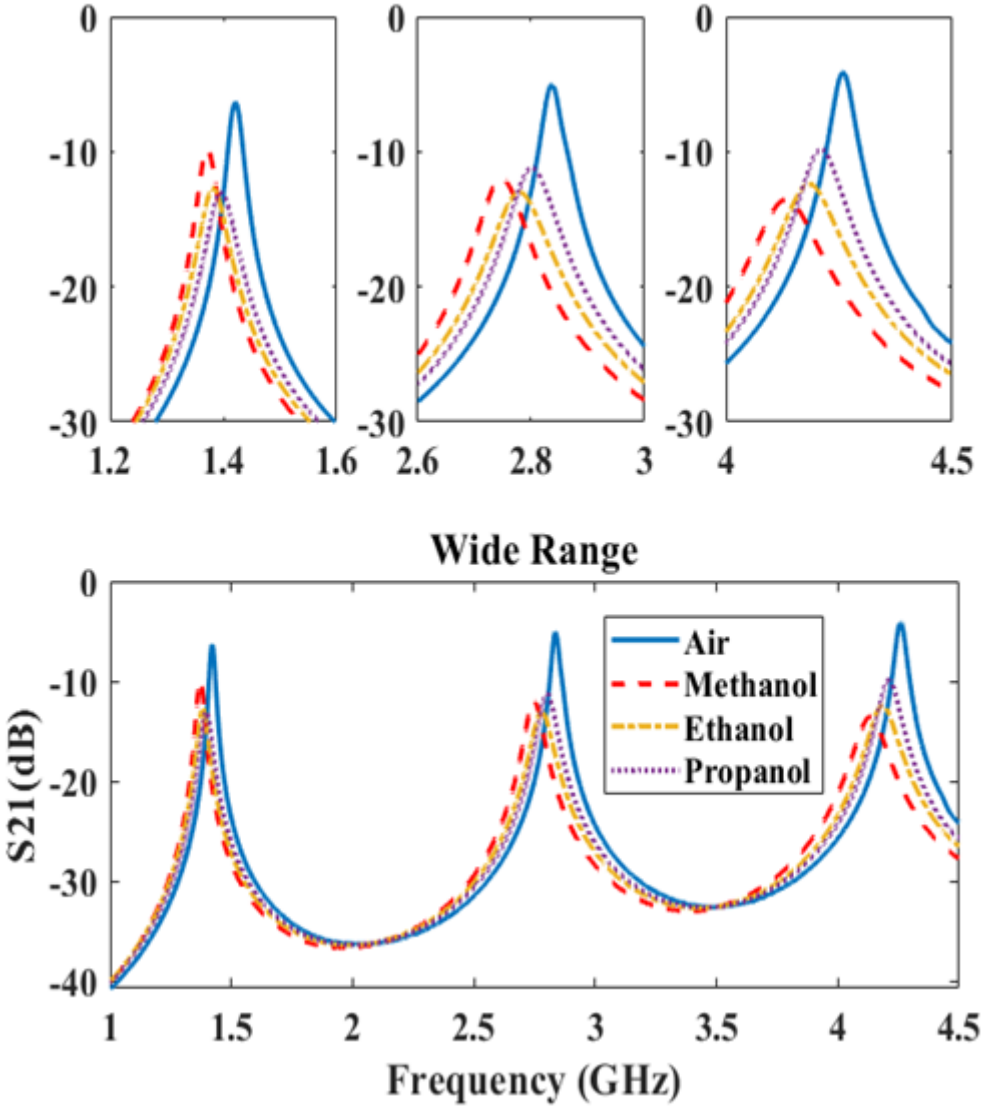

Fig. 3.8. The spectrum of three measured resonant modes of the ring resonator while loading the sensor with different scenarios [45].

Table 3.1. The measured quality factors for different resonant modes.

	Q_m	Q_e	Q_p	Q_{Air}
1st Resonant mode	44	32	30	60
2nd Resonant mode	37	33	40	82
3rd Resonant mode	33	37	50	90

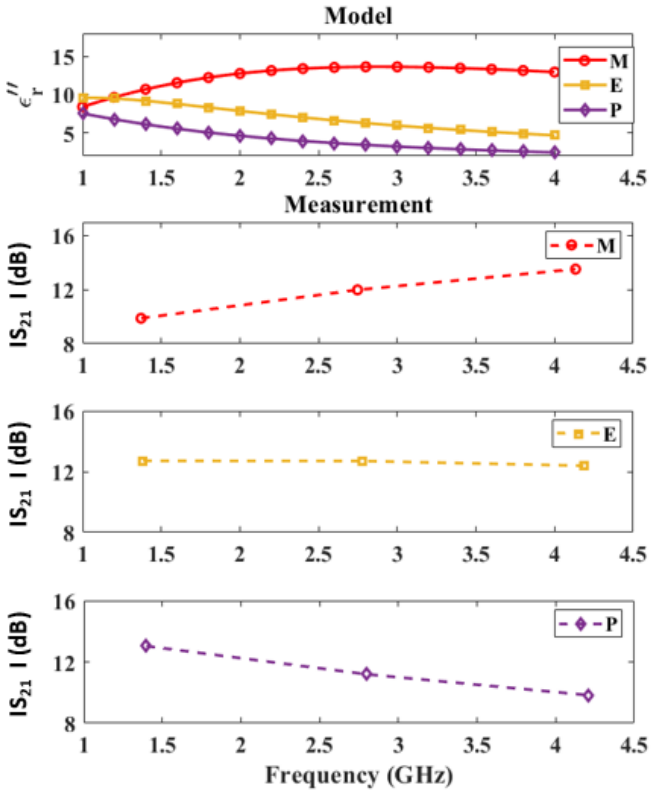

Fig. 3.9. The plot of absorption curves and measured insertion loss of the sensor for methanol (M), ethanol (E) and propanol (P) [45].

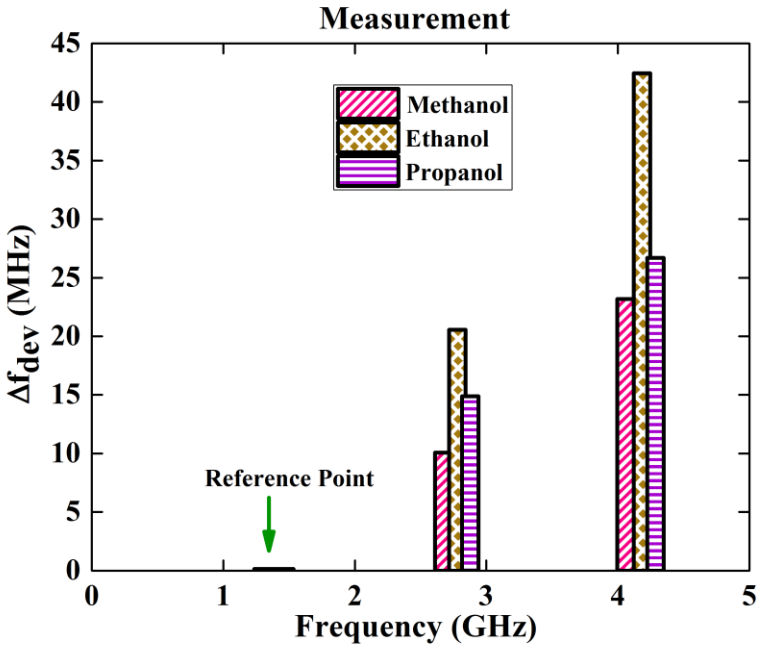

Fig. 3.10. The measured shift deviation spectrum of the resonant modes for different MUT loadings calculated by equation 8 [45].

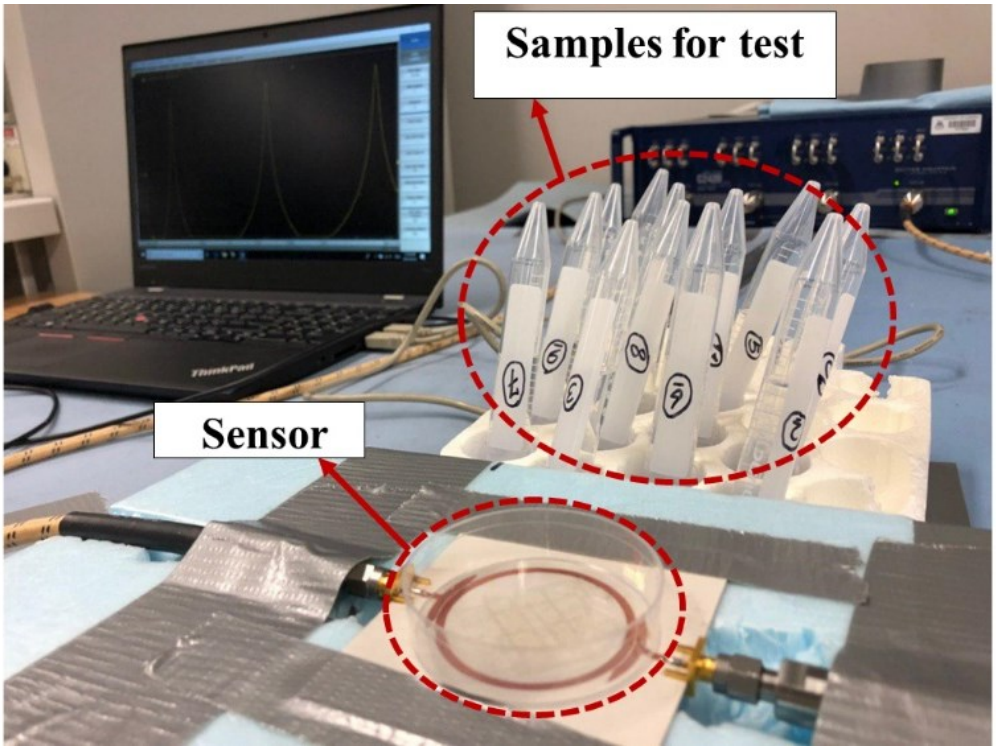

Fig. 3.11. The experiment setup for measuring and characterizing the volumetric ratios of different mixture components [45].

For ethanol, the absorption curve is mostly uniform and invariant for selected ranges of frequencies. These characteristics result in the same amplitude variations for all specified resonant modes in the band. Second, the relative permittivity impact on the sensor functionality is investigated.

Using equation (3-7), Fig. 3.10 presents and compares the shifting deviations of the corresponding resonant modes for different measured loading scenarios.

This shifting deviation is a critical factor for getting a meaningful response out of our system of equations. The information in Fig. 3.10 provides enough data for monitoring the variability of the material's relative permittivity profile. Therefore, the resonant mode shift deviations represent the level of nonlinearity and the permittivity variation at each frequency.

3.2.4 Sensing Experiments and Discussion

The complete experiment setup for the sensor calibration process and mixture measurements are shown in Fig. 3.11. The mixture samples were prepared before the experiment, including different methanol, ethanol, and propanol volume percentages.

3.2.4.1 Sensor Calibration Matrix and Mixture Matrix Formation

Before any mixture measurements, the proposed microwave sensor should be loaded by the pure materials chosen as mixture components to form the sensor calibration matrix (SCM). Without loss of generality, the parameters in the proposed resonant mode-based equation (3-9) in section 3.2.1 are characterized at the measured frequencies through intersecting with Debye models. This process is for assigning the corresponded relative permittivity values for each measured data. Then, the sensor calibration curves are formatted as depicted in Fig. 3.12.

Using intersecting points, labelling of each measured frequency with the corresponding relative permittivity is completed, which forms the sensor calibration matrix. For the present sensor with the proposed experiment setup, the calculated coefficients with MATLAB software after the intersection process are shown in Table 3.2.

Table 3.2. Calculated coefficients of the Eq. 3-9 after the intersection.

	a	b	α	β	$P1$	$P2$
1st Resonant mode	0.76	4.8	0.85	0.53	0.031	0.5
2nd Resonant mode	1	4.66	0.4	0.241	0.06	0.5
3rd Resonant mode	1.5	4.47	0.19	0.157	0.09	0.5

3.2.4.2 Multicomponent Matrix Measurement

The sensor calibration matrix is formed, and now the system of equations is ready for the mixture characterization. The linear system of the equation is presented in equation (3-15). Resonant mode-based data achieved from mixture subcomponents will be used to obtain the percentage of the mixture subcomponents after the total mixture measurement.

Fig. 3.13 shows the mixture data achieved from 8 different mixtures utilized for this experiment. The summarized experimental steps can be clarified as follows;

- Measuring the S-parameters of the sensor loaded by each subcomponent individually.
- Using the measured resonant modes and obtaining the corresponding relative permittivity values through MATLAB-based intersection. (Calibrating the sensor model curves and establishing the sensor calibration curves as Table 3.2)
- Generating the sensor calibration matrix using the relative permittivity values on the intersection points of the sensor calibration curves.
- Measuring S-parameters for the favourite mixture as load, analyzing the related mix relative permittivity by the achieved sensor calibration curves. (Mixture Matrix)
- Finalizing the system of equations and calculating the volumetric data of the subcomponents.

Using the 2nd and 3rd resonant mode-based measurements, the volumetric fraction data is extracted and illustrated in Table 3.3. The expected falling and raising trend of amplitudes validate the quality of measures while comparing the resonant mode-based measurement results in Fig. 3.13 with volumetric specifications in Table 3.3.

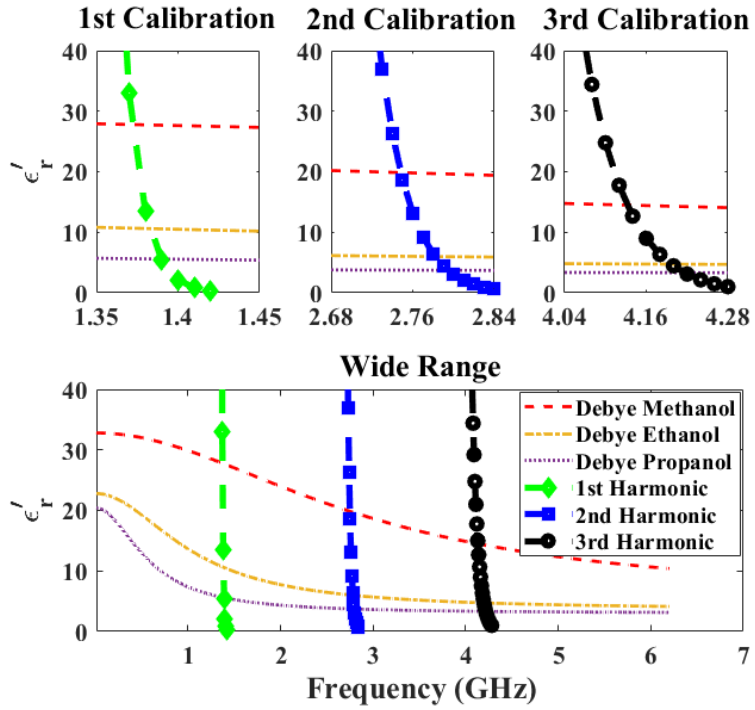

Fig. 3.12. The sensor calibration curves intersection with the Debye model at measured frequencies for characterizing the parameters in equation (3-9) and achieving the sensor calibration matrix in equation (3-15) [45].

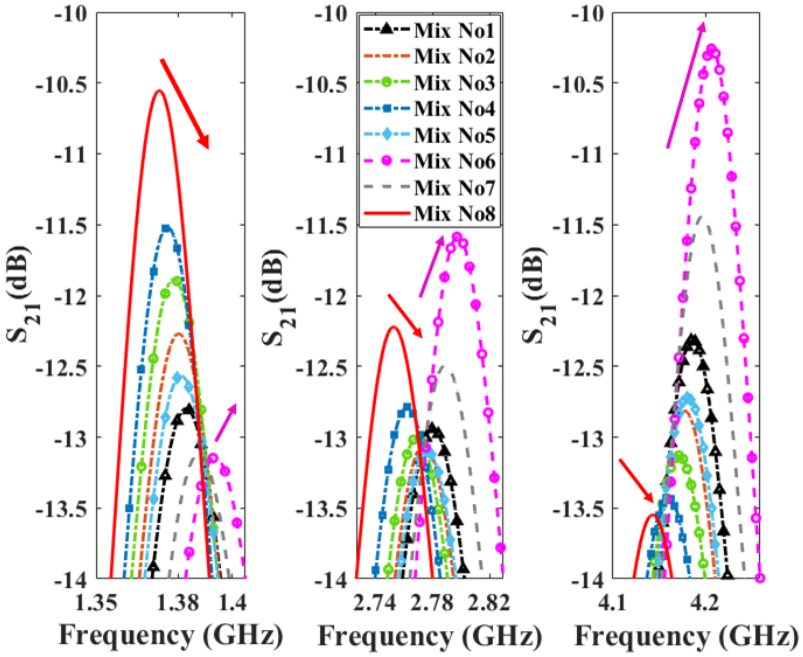

Fig. 3.13. Different resonant mode shifts regarding the mixture-based measurements extracted for each resonance from different types of mixtures [45].

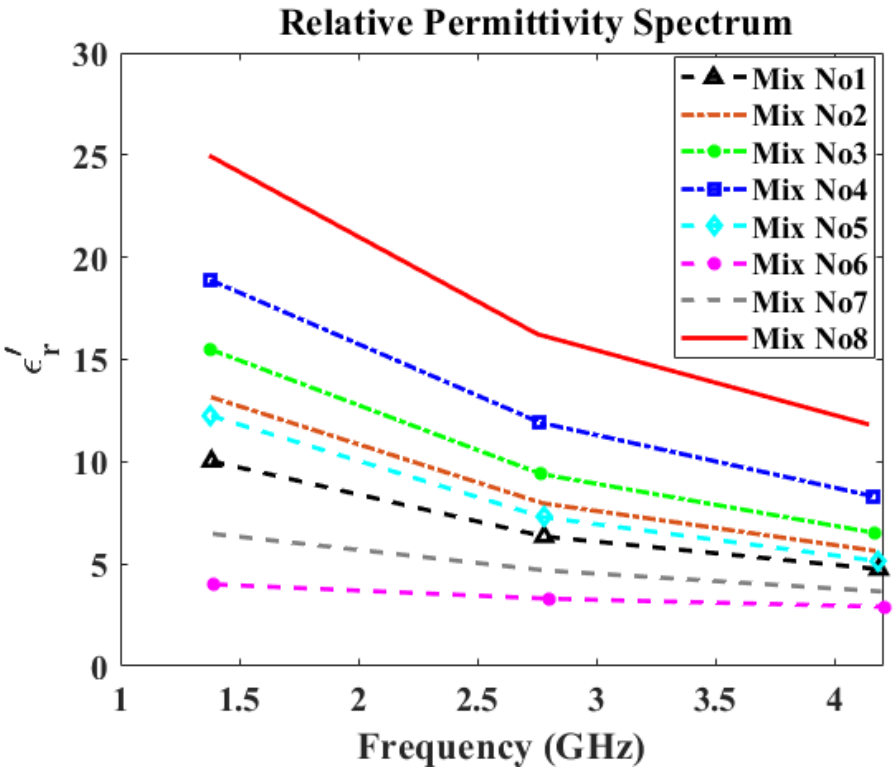

Fig. 3.14. The experimentally achieved spectrum of the relative permittivity for different mixtures at each resonant mode [45].

Using the proposed formula in (10), the relative permittivity spectrum of each mixture calculated for different resonant modes is also exhibited in Fig. 3.14. As an example, for mixture number 6 shown in Table 3.3, 80 % of the mixture volume is propanol, which follows a decreasing loss pattern in Fig. 3.9.

The resonant mode spectrum of the ring is tracking the same decreasing insertion loss scheme of propanol with minimum resonance shift as the dominant component of the mixture. In contrast, mixture number 8 methanol is the dominant subcomponent of the mixture with a volume fraction of 80 %. The resonant mode response of the mixture exhibits an increase of the loss factor and, consequently, decreases the amplitude in the S_{21} profile.

To verify the validity of the proposed measurement, Table 3.3 presents the initially mixed subcomponents compared with its measurement results extracted for three repetitions of each

experiment. The corresponding standard deviations (SD) for each set of tests are also calculated and presented in the same table. It could be seen that the measured volume fractions match well with the initially assigned subcomponents to the mixtures. The small error values of less than 6% are achieved according to the proposed method, mainly attributed to the experimental errors such as material preparation, and accuracy of the initial mixture models used. Moreover, the sensor's sensitivity to the volume error of the mixture is also investigated. It is about 150 KHz for 5% variation in the volume of the mixture, which is negligible and is only about 0.3% of error in the calculation of ethanol.

Table 3.3. A comparison between the extracted and actual components of each experiment.

	Experiment							
Volume Fraction	Mix 1	Mix 2	Mix 3	Mix 4	Mix 5	Mix 6	Mix 7	Mix 8
Methanol Assigned Vol. %	20	40	40	60	20	0	20	80
Ethanol Assigned Vol. %	40	20	40	20	60	20	0	20
Propanol Assigned Vol. %	40	40	20	20	20	80	80	0
Measured Methanol Vol. %	19.5	38.8	39.5	58.5	20.5	1.3	19.2	82
Measured Ethanol Vol. %	42.5	22.7	41.3	22	58.7	21.7	3.9	16.7
Measured Propanol Vol. %	38	38.5	19.2	19.5	20.8	77	76.9	1.3
Standard Deviation (SD) of	0.79 %	0.67 %	1.9 %	5.6 %	3.59 %	1.18 %	3.4 %	3.5 %
Measurements for 3	1.63 %	1.8 %	0.48 %	3.1 %	2.41 %	1.84 %	1.34 %	3.6 %
Repetitions of Experiment	1.06 %	1.1 %	0.43 %	2.57 %	1.92 %	1.14 %	2.05 %	0.16 %

3.3 A Model-Free Approach for Multivariable Biofuel Analysis using Artificial Intelligence Assisted Non-Contact Microwave Sensor

As mentioned before, one of the most complicated issues in the field of microwave resonator-based sensors is multivariable component analysis. A new methodology for providing new independent features for assessing the volumetric fraction of water, ethanol, and gasoline in E85 biofuel samples is developed as complementary work. For this part of the project, Dr. Masoud Baghelani helped with conceptualization, methodology, and MATLAB analysis, while Navid Hosseini contributed with sensor design, fabrication and HFSS analysis. The innovative features are derived from a multi-resonant modes measurement of frequency and amplitude fluctuations of the resonator transmission response due to dispersion and uniqueness of permittivity spectrum of various materials. After 66% of the test samples have been trained, an artificial neural network is created for model-free processing of the data from the test samples. The experimental results demonstrate the sensor's ability to selectively monitor all components of a multivariable mixture simultaneously. During this research, a big step forward is being made by increasing microwave resonator-based sensors' selectivity by introducing additional independent features derived from the sensors' higher mode responses to the new materials.

The theory underlying this technique, as before, is based on inherent dispersion in the relative permittivity spectrum of materials, which is caused by the various relaxation times of different materials in the same environment. This procedure extracts all of the resonator's available properties in a broad-spectrum range for the first three resonant modes, such as frequency shifts, resonance amplitude, and quality factor of each resonant mode of the resonator according to each sample. The data is collected across many samples and used to train a feed-forward artificial neural network for data processing. Following the artificial neural network's training, the network can interpret unknown mixture samples using the features acquired from the resonator measurement. Promising findings with meagre error rates back up our technique for a multivariable sensing application.

3.3.1 Sensor Designing Process

The sensor used in this study is a planar microstrip split-ring resonator that works at the fundamental resonance frequency, permittivity of the materials of interest varies in the higher resonant modes. This research introduces new characteristics such as frequency shifts for different resonant modes of resonators and changes in transmission amplitude and quality aspects (Q).

The Debye model for ethanol, gasoline, and water is shown in Fig. 3.15. Because of the differences in their relaxation times, their permittivity spectrums are altering at various frequencies. [43], [44].

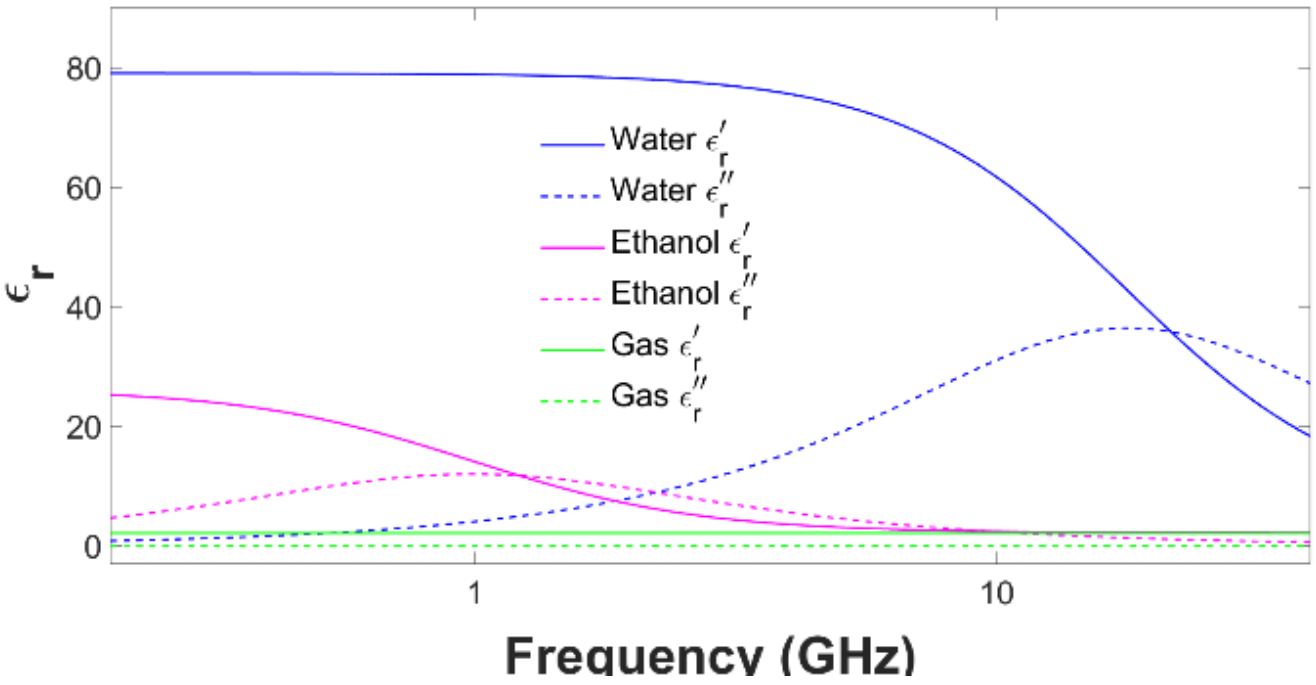

Fig. 3.15. Debye models for ethanol, water and gasoline [52].

In the case of biofuels, it can be shown in Fig. 3.15 that any resonance frequency between 500MHz and 1GHz provides the proper resonant modes, with varied permittivities in the spectrum of the material. The sensor's fundamental frequency is 970 MHz, and three initial resonant modes are selected for feature extraction to get a higher number of features for better neural network training. In the data analysis phase of this project, these traits will be investigated further.

The resonator's transmission response, including the first three resonant modes, is shown in Fig. 3.16 (b), which was simulated using the High-Frequency Structure Simulator (HFSS). Due to the constant permittivity of their ambient material, the resonator shows a roughly similar field distribution profile. All frequency shifts due to loading the resonator with different permittivities are measured using the following relations [45].

$$f_n = \frac{nC}{l_{eff}\sqrt{\varepsilon_{eff,air}(f_n)}} \tag{3-16}$$

$$\Delta f_n = f_n - \frac{nC}{l_{eff}\sqrt{\varepsilon_{eff,air}(f_n)}} \tag{3-17}$$

Where [4]

$$\varepsilon_{eff,air} \approx \frac{\varepsilon_{r,sub}+1}{2} + \frac{\varepsilon_{r,sub}-1}{2}\left(\frac{1}{\sqrt{1+\frac{12h}{W}}}\right) \tag{3-18}$$

Where n is the number of resonant modes, $\varepsilon_{eff,mut}(f_n)$ is the effective permittivity of the whole system after introduction of the material under the test (MUT) to the sensor, c is the speed of light in the free space, $\varepsilon_{r,sub}$ is the relative permittivity of the substrate material, l_{eff} is the effective length of the resonator and h and W are the thickness of the substrate and the width of the copper trace of the resonator, respectively. Furthermore, because the quality factor is an additional feature for data analysis in this study, a straightforward definition would be beneficial. [44]:

$$Q = 2\pi f_0 \frac{average energy stored}{energy loss/\sec.} = \frac{f_0}{BW_{-3dB}} \tag{3-19}$$

Where f_0 is the resonance frequency of interest, and BW_{-3dB} is the 3dB bandwidth of the resonator transmission response. Furthermore, attenuation, which may predict based on various loss processes, can be given in microstrip resonators. [46]:

$$\alpha = \alpha_C + \alpha_D + \alpha_G + \alpha_R \tag{3-20}$$

Where α is the overall attenuation and α_C, α_D, α_G, and α_R are attenuations due to metal loss, dielectric loss tangent, dielectric conductivity loss, and radiation loss, respectively which could be described as follows [5]:

$$\alpha_C = 8.686 \times \frac{R^{'}}{2Z_0} \ (dB/meter) \tag{3-21}$$

$$\alpha_D = 8.686 \times \tan(\delta) \frac{2\pi f_0 C^{'} Z_0}{2} \ (dB/meter) \tag{3-22}$$

$$\alpha_G = 8.686 \times \frac{G^{'} Z_0}{2} \ (dB/meter) \tag{3-23}$$

Where R' is the RF resistance per unit length of the metal layer (here copper), Z_0 is the characteristic impedance of the structure (~50Ω), tan(δ) is the loss tangent of the dielectric materials ambient to the resonator structure, C′ is the capacitance of the transmission line, and G′ is the conductivity of the dielectric materials around the resonator. The radiation loss has been considered to have only a minimal influence on the total attenuation of these devices. [48].

Because a precise closed-form formulation of the resonance frequency versus MUT permittivity is not easily accessible and can only be retrieved through curve fitting by matching the data with the Debye model, an artificial neural network (ANN) is used to handle the data as a black box.

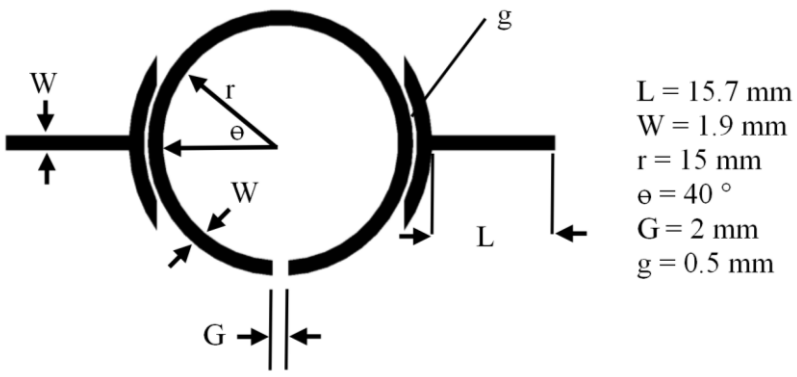

(a)

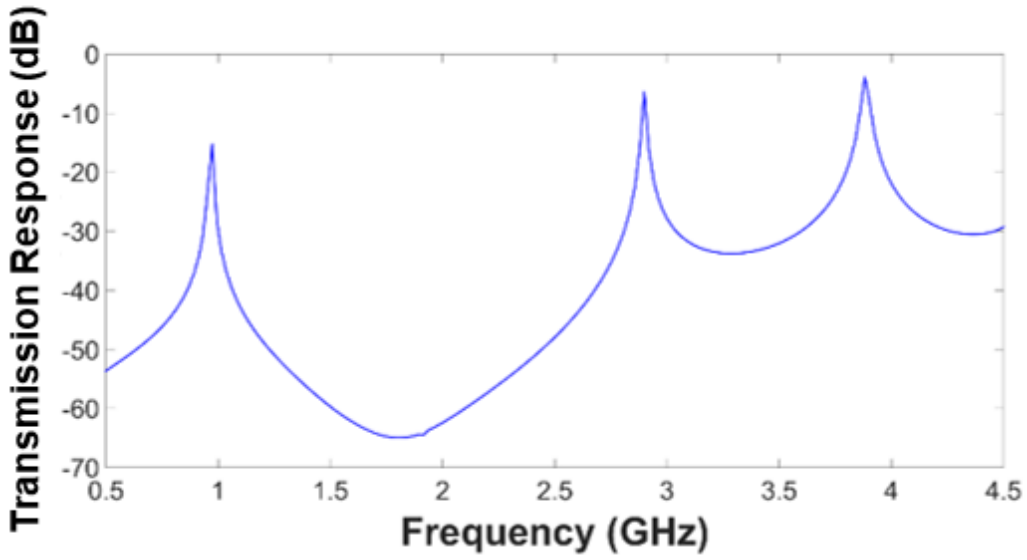

(b)

Fig. 3.16. (a) The schematic of the designed resonator and (b) its multi-resonance transmission response, including its first three resonant modes [52].

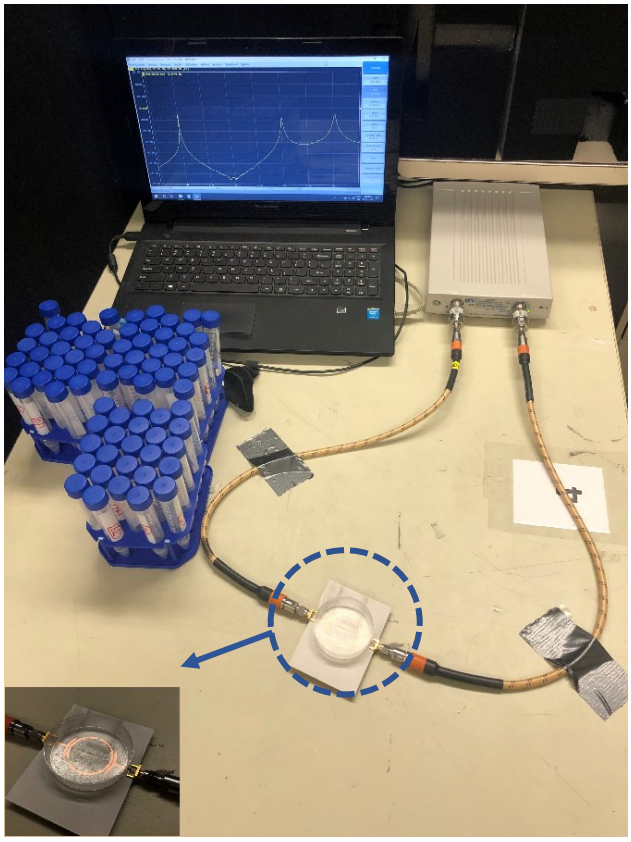

Fig. 3.17. The experimental setup for testing the samples [52].

3.3.2 Experimental results

Table 3.4. A comparison between the simulation and experimental results for the case of an unloaded resonator. Numbers represent the resonant modes.

Sensor Specifications	Simulation	Experiment
Q at the 1st resonant mode	105.4	160.95
Q at the 2nd resonant mode	219.6	125.20
Q at the 3rd resonant mode	184.8	109.89
Δf at the 1st resonant mode (MHz)	973.5	997.9
Δf at the 2nd resonant mode (MHz)	2899	3005

Δf at the 3rd resonant mode (MHz)	3882	4022
Amplitude variation at the 1st resonant mode (dB)	-15.1	-8.5
Amplitude variation at the 2nd resonant mode (dB)	-6.3	-8.0
Amplitude variation at the 3rd resonant mode (dB)	-3.8	-4.7

The setup shown in Fig. 3.17 is used for both network training and tests. As mentioned, the sensor is a split ring resonator intended to resonate at around 970 MHz as the fundamental mode, allowing higher modes to occur at the necessary frequencies if the materials of interest have sufficient dispersion in their permittivity spectrums.

The low-loss double-sided EL-7876 silicone transfer adhesive tape secures the polymer container to the substrate. A Copper Mountain Technologies S5085 2-Port VNA with a frequency range of 500MHz to 4.5GHz and 8001 measurement points was employed for the measurements. A 1µl precision dispenser is used to prepare samples. All samples have a capacity of 10 ml, which covers the sensor's top plane based on the container's volume. The container is dried out using a room temperature blower after each test. The resonator's resonance frequency with the empty container is returned to the same place as before each experiment.

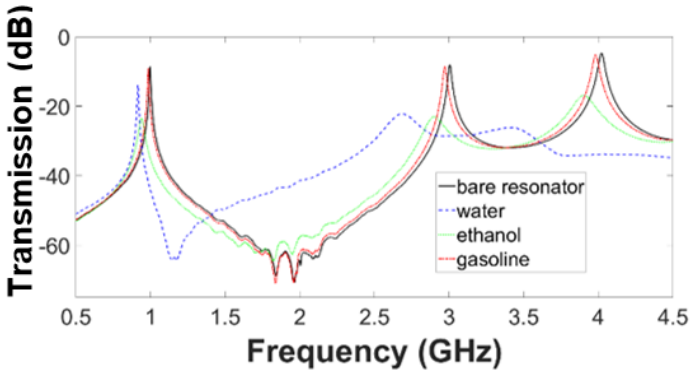

Fig. 3.18. Transmission response of the unloaded resonator with the empty container and its responses in case of the container filled with water, ethanol, and gasoline, respectively [52].

Table 3.4 compares the simulation findings in Fig. 3.16 (b) with the experimental results in Fig. 3.18 for the bare resonator situation. The inconsistencies might be the consequence of the container's dielectric characteristics being unknown, along with the soldering effect, which is all calibrated and included in sensor response. The mismatch between simulation and experimental data does not produce any errors because the data processing given in section 3.3.3 is purely based on the experimental results. For the first three resonant modes of the sensor, the transmission response (S21) for each of the materials of interest (ethanol, gasoline, and water) is shown in Fig. 3.18, which includes the container dielectric properties as well. The unloaded quality factors (Q) at all of its resonant modes are shown in Fig. 3.18. Table 3.5 shows the Q of the resonator for all of the materials.

3.3.3 Model-Free Analysis of Biofuel Sensor using Artificial Neural Network

A multi-layer perceptron (MLP) is a feed-forward neural network with one input layer, one output layer, and single or multi hidden layers between them. We will not go through all of the technical intricacies of this well-known artificial neural network for brevity, including the learning process, which can be found in standard textbooks [49]. The retrieved features from the samples

are linked to the input layer. The hidden layers activation function is commonly a sigmoid function, which can be described as:

$$y(v) = \frac{1}{1-e^{-v}} \tag{3-24}$$

Where,

$$v = \sum_{i=1}^{m} w_i \times x_i \tag{3-25}$$

where x_i is the i^{th} feature and w_i is a coefficient called weight calculated during the neural network's learning process (Fig. 3.19 contains more details). For pattern recognition applications, the neural network's output layer is commonly a hard-limit function. Because this project aims to determine the proportion of each subcomponent in an unknown combination, the rectified linear unit (ReLU) may be a better option. [50].

Table 3.5. Different specifications of the data extracted from Fig. 3.18. All Δf and amplitude changes are expressed in absolute values and determined in comparison to unloaded resonator data.

Specification	Bare resonator	Ethanol	Gasoline	Water
Q at the 1st resonant mode	160.95	29.18	153.95	147.72
Q at the 2nd resonant mode	125.20	21.31	123.88	13.17
Q at the 3rd resonant mode	109.89	26.73	104.78	12.15
Δf at the 1st resonant mode (MHz)	0	58.1	12.6	82
Δf at the 2nd resonant mode (MHz)	0	106	34	319
Δf at the 3rd resonant mode (MHz)	0	119	40	601
Amplitude variation at the 1st resonant mode (dB)	0	14.88	0.37	5.25
Amplitude variation at the 2nd resonant mode (dB)	0	12.15	0.44	21.43
Amplitude variation at the 3rd resonant mode (dB)	0	14.94	0.56	14.16

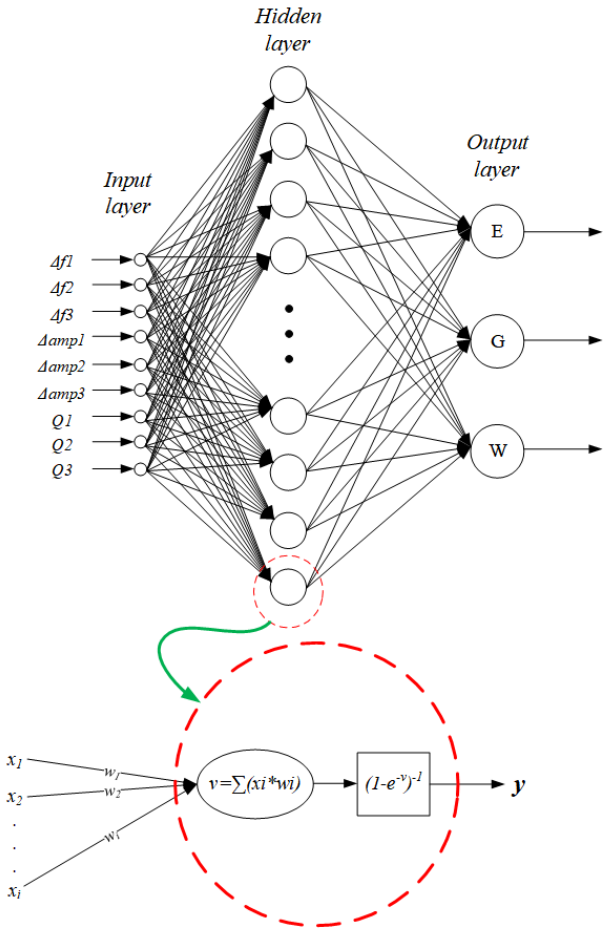

Fig. 3.19. A multi-layer perceptron network was used, with 9 input neurons for each of the nine extracted characteristics, 42 neurons in the hidden layer, and three ReLU neurons in the output layer, each allocated to one subcomponent volumetric data [52].

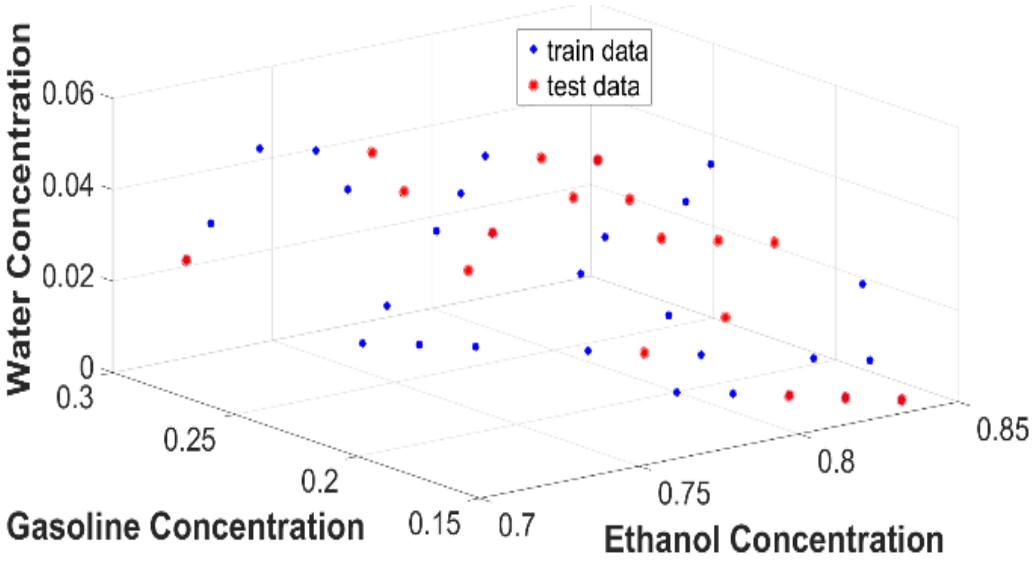

Fig. 3.20. Sample space for training and test the sensor system including the artificial neural network [52].

Sixty samples with the following volumetric variation ranges for E85 biofuel are given to train and test the neural network [51]:

$$\begin{cases} 51 < V_E < 85 \\ 15 < V_G < 49 \\ 0 < V_W < 6 \\ V_E + V_G + V_W = 100 \end{cases} \tag{3-26}$$

VE, VG, and VW are the volume fractions of ethanol, gasoline, and water. As illustrated in Fig. 3.20. The samples are generated at random but picked so that they cover the problem volume with a somewhat uniform distribution. 40 samples are chosen randomly for training the network, with the remaining 20 being evaluated for testing. The transmission response of some of the samples is shown in Fig. 3.21. Table 3.6 lists the samples as well as the concentrations of each component. According to Fig. 3.21, the inclusion of each material resulted in the extraction of 9 characteristics from the sensor's transmission response, including frequency shift, amplitude, and quality factor at the resonance frequency for all three resonant modes. The values obtained from the resonator with the empty container are used to normalize the above parameters. Normalization of features is critical in the neural network learning process since high values, such as frequency changes of several MHz, can overload the network and limit the influence of other information, such as quality factor fluctuations that are millions of times smaller.

Table 3.6. Achieved results from the processing of the sensor's data by the artificial neural network. It could be seen that the maximum absolute error in determining water concentration is 1.4%, with the maximum relative error of as low as 0.36%.

Sample number	Actual ethanol concentration (%)	Results of ethanol concentration from the sensor (%)	Actual gasoline concentration (%)	Results of gasoline concentration from the sensor (%)	Actual water concentration (%)	Results of water concentration from the sensor (%)
1	81	80.60	18	18.30	1	1.1
2	82	82.62	18	17.23	0	0.05
3	78	77.90	17	17.13	5	4.97
4	81	80.01	19	20.06	0	0.02
5	72	72.73	27	26.64	1	0.64
6	78	77.90	17	17.13	5	4.97
7	74	75.72	24	22.49	2	1.73
8	77	76.64	19	19.14	4	4.23
9	70	68.46	24	24.94	6	6.27
10	78	78.65	16	14.96	6	5.89
11	75	74.02	22	22.52	3	3.49
12	70	69.08	28	29.19	2	1.72
13	79	80.09	19	17.82	2	2.09
14	83	84.31	16	14.81	1	0.87
15	84	83.69	16	16.26	0	0.05
16	80	79.44	20	20.65	0	0.00
17	74	71.98	23	24.55	3	3.46
18	76	79.81	19	18.61	5	6.4
19	82	83.59	17	15.43	1	0.97
20	71	71.08	26	25.89	3	3.04

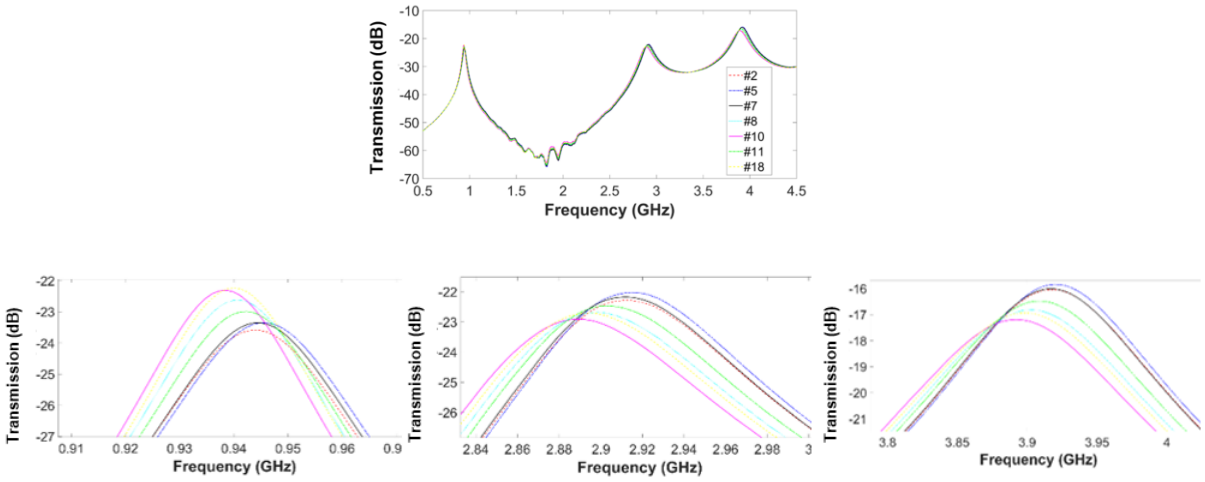

Fig. 3.21. Transmission response of some of the test samples as outlined in Table III and their zoomed versions around the three first resonant modes [52].

Table 3.6 summarises the results of the data analysis utilizing the neural network. The hidden layer's size is chosen to get the lowest error with a total of 42 neurons. In the computation of volumetric concentration of all the materials, the total mean squared error (MSE) is roughly 0.13%. It is also worth noting that when the artificial neural network has been trained, it becomes a collection of basic computations with fixed coefficients. As a result, the network's reaction to new characteristics indicating a new unknown sample will be rapidly available due to the fast computation speed of current computers and processors. The artificial neural network also allows for model-free data processing without the need for complex sensor environment modelling.

3.4 Conclusion

The extraction of new independent characteristics for real-time non-contact multivariable selective sensing applications has been produced using a unique approach based on multi-resonant modes analysis of the microwave split ring resonator. Because the permittivity spectrum of different materials is dispersed and unique, and the resonator's different resonant modes fall within the variation range of different components in the mixture, the shift in the resonance frequency and amplitude of the resonator's transmission response become independent, allowing detection of

multiple variations in the mixture. Then, an artificial neural network has been built for model-free analysis of the generated information to avoid sophisticated modelling and inaccuracies from curve-fitting predictions. The findings demonstrate the developed system's capacity to measure multivariable volumetric percentages for biofuel analysis applications. The limitations of the technique, its accuracy, and performed approximations were explained in Chapter 6.

3.5 References

[1] H. F. Cook, “Dielectric behaviour of human blood at microwave frequencies,” Nature, vol. 168, no. 4267, p. 247, 1951.

[2] H. Choi, J. Nylon, S. Luzio, J. Beutler, and A. Porch, “Design of continuous non-invasive blood glucose monitoring sensor based on a microwave split ring resonator,” in 2014 IEEE MTT-S International Microwave Workshop Series on RF and Wireless Technologies for Biomedical and Healthcare Applications (IMWS-Bio2014), 2014, pp. 1–3.

[3] A. Rohman, D. L. Setyaningrum, and S. Riyanto, “FTIR spectroscopy combined with partial least square for analysis of red fruit oil in ternary mixture system,” Int. J. Spectrosc., vol. 2014, 2014.

[4] A. Kondyli and W. Schrader, “High-resolution GC/MS studies of a light crude oil fraction,” J. mass Spectrom., vol. 54, no. 1, pp. 47–54, 2019.

[5] J. J. Pitt, “Principles and applications of liquid chromatography-mass spectrometry in clinical biochemistry,” Clin. Biochem. Rev., vol. 30, no. 1, p. 19, 2009.

[6] D. Havelka, O. Krivosudský, and M. Cifra, “Grounded coplanar waveguide-based 0.5–50 GHz sensor for dielectric spectroscopy,” in 2017 47th European Microwave Conference (EuMC), 2017, pp. 950–953.

[7] N. Bonanos, P. Pissis, and J. R. Macdonald, “Impedance spectroscopy of dielectrics and electronic conductors,” Charact. Mater., pp. 1–14, 2002.

[8] A. Fendri, H. Ghariani, and O. Kanoun, “Dielectric spectroscopy for assessment of water content in edible oils,” in 2017 14th International Multi-Conference on Systems, Signals & Devices (SSD), 2017, pp. 728–732.

[9] M. Nakamura, T. Tajima, K. Ajito, and H. Koizumi, “Selectivity-enhanced glucose measurement in multicomponent aqueous solution by broadband dielectric spectroscopy,” in 2016 IEEE MTT-S International Microwave Symposium (IMS), 2016, pp. 1–3.

[10] M. A. Suster, D. Maji, N. Vitale, U. Gurkan, and P. Mohseni, “An RF/microwave microfluidic sensor for miniaturized dielectric spectroscopy based on sensor transmission characteristics,” in 2015 IEEE Sensors, 2015, pp. 1–4.

[11] A. P. Saghati, J. S. Batra, J. Kameoka, and K. Entesari, “A metamaterial-inspired wideband microwave interferometry sensor for dielectric spectroscopy of liquid chemicals,” IEEE Trans. Microw. Theory Tech., vol. 65, no. 7, pp. 2558–2571, 2017.

[12] M. Abdolrazzaghi, M. H. Zarifi, C. F. A. Floquet, and M. Daneshmand, “Contactless Asphaltene Detection Using an Active Planar Microwave Resonator Sensor,” Energy & Fuels, vol. 31, no. 8, pp. 8784–8791, 2017.

[13] M. Nosrati, Z. Abbasi, M. Baghelani, S. Bhadra, and M. Daneshmand, “Locally Strong-Coupled Microwave Resonator Using PEMC Boundary for Distant Sensing Applications,” IEEE Trans. Microw. Theory Tech., 2019.

[14] M. A. Karimi, M. Arsalan, and A. Shamim, “Design and dynamic characterization of an orientation insensitive microwave water-cut sensor,” IEEE Trans. Microw. Theory Tech., vol. 66, no. 1, pp. 530–539, 2017.

[15] W.-T. S. Chen and R. R. Mansour, “Miniature gas sensor and sensor array with single-and dual-mode RF dielectric resonators,” IEEE Trans. Microw. Theory Tech., vol. 66, no. 8, pp. 3697–3704, 2018.

[16] Z. Abbasi, P. Shariaty, M. Nosrati, Z. Hashisho, and M. Daneshmand, “Dual-Band Microwave Circuits for Selective Binary Gas Sensing System,” IEEE Trans. Microw. Theory Tech., 2019.

[17] M. H. Zarifi, T. Thundat, and M. Daneshmand, “High resolution microwave microstrip resonator for sensing applications,” Sensors Actuators A Phys., vol. 233, pp. 224–230, 2015.

[18] M. Daneshmand and M. H. Zarifi, “Apparatus and method for high resolution complex permittivity sensing using high Q microwave sensors for lossy or non-lossy mediums and samples.” Google Patents, 08-Jan-2019.

[19] G. Gennarelli, S. Romeo, M. R. Scarfi, and F. Soldovieri, “A microwave resonant sensor for concentration measurements of liquid solutions,” IEEE Sens. J., vol. 13, no. 5, pp. 1857–1864, 2013.

[20] S. O. Nelson and A. W. Kraszewski, “Sensing pulverized material mixture proportions by resonant cavity measurements,” IEEE Trans. Instrum. Meas., vol. 47, no. 5, pp. 1201–1204, 1998.

[21] A. Megriche, A. Belhadj, and A. Mgaidi, “Microwave dielectric properties of binary solvent wateralcohol, alcohol-alcohol mixtures at temperatures between-35° C and+ 35° C and dielectric relaxation studies,” Mediterr. J. Chem., vol. 1, no. 4, pp. 200–209, 2012.

[22] M. Abdolrazzaghi, M. Daneshmand, and A. K. Iyer, “Strongly enhanced sensitivity in planar microwave sensors based on metamaterial coupling,” IEEE Trans. Microw. Theory Tech., vol. 66, no. 4, pp. 1843–1855, 2018.

[23] K. M. Chew, R. Sudirman, N. Seman, and C. Y. Yong, “Relaxation frequency and relaxation time estimation for phantom modeling by proposed fitting linear models,” in 2012 IEEE-EMBS Conference on Biomedical Engineering and Sciences, 2012, pp. 911–915.

[24] M. Y. Onimisi and J. T. Ikyumbur, “Comparative analysis of dielectric constant and loss factor of pure butan-1-ol and ethanol,” Am. J. Condens. Matter Phys., vol. 5, no. 3, pp. 69–75, 2015.

[25] S. Mashimo, T. Umehara, and H. Redlin, “Structures of water and primary alcohol studied by microwave dielectric analyses,” J. Chem. Phys., vol. 95, no. 9, pp. 6257–6260, 1991.

[26] T. Sato, A. Chiba, and R. Nozaki, “Dynamical aspects of mixing schemes in ethanol–water mixtures in terms of the excess partial molar activation free energy, enthalpy, and entropy of the dielectric relaxation process,” J. Chem. Phys., vol. 110, no. 5, pp. 2508–2521, 1999.

[27] N. Hosseini, M. Baghelani, and M. Daneshmand, “Discrete Microwave Spectroscopy using Planar Resonator,” in 2019 IEEE Canadian Conference of Electrical and Computer Engineering (CCECE), 2019, pp. 1–4.

[28] A. Talai, F. Steinhäußer, A. Bittner, U. Schmid, R. Weigel, and A. Koelpin, “A permittivity characterization method by detuned ring-resonators for bulk materials up to 110 GHz,” in 2014 44th European Microwave Conference, 2014, pp. 124–127.

[29] J. L. Zamora, D. R. Vargas, Y. K. Hernández-Gómez, and G. A. Álvarez-Botero, “Improvement the permittivity determination in glyphosate-water mixture using CSRR as sensor,” in 2018 IEEE International Instrumentation and Measurement Technology Conference (I2MTC), 2018, pp. 1–5.

[30] V. A. Markel, “Introduction to the Maxwell Garnett approximation: tutorial,” JOSA A, vol. 33, no. 7, pp. 1244–1256, 2016.

[31] B. Salski and M. Celuch, “On the equivalence between the Maxwell-Garnett mixing rule and the Debye relaxation formula,” IEEE Trans. Microw. Theory Tech., vol. 60, no. 8, pp. 2352–2358, 2012.

[32] A. H. Sihvola and I. V Lindell, “Chiral Maxwell-Garnett mixing formula,” Electron. Lett., vol. 26, no. 2, pp. 118–119, 1990.

[33] B. Salski and M. Celuch, “The debye rigorous equivalent of the Maxwell-Garnett mixing rule for effective modeling of carbon suspensions under MW irradiation,” in 2011 IEEE MTT-S International Microwave Symposium, 2011, pp. 1–4.

[34] M. H. Nisanci, F. de Paulis, M. Y. Koledintseva, J. L. Drewniak, and A. Orlandi, “From Maxwell Garnett to Debye model for electromagnetic simulation of composite dielectrics—PART II: Random cylindrical inclusions,” IEEE Trans. Electromagn. Compat., vol. 54, no. 2, pp. 280–289, 2011.

[35] A. Kraszewski, “Prediction of the dielectric properties of two-phase mixtures,” J. Microw. Power, vol. 12, no. 3, pp. 216–222, 1977.

[36] K. Lichtenecker, “Die Herleitung des logarithmischen Mischungsgesetzes aus allgemeinen Prinzipien der stationaren Stromung,” phys. Z, vol. 32, pp. 255–260, 1931.

[37] E. M. Cheng, M. F. B. A. Malek, M. Ahmed, K. Y. You, K. Y. Lee, and H. Nornikman, “The use of dielectric mixture equations to analyze the dielectric properties of a mixture of rubber tire dust and rice husks in a microwave absorber,” Prog. Electromagn. Res., vol. 129, pp. 559–578, 2012.

[38] A. Sihvola, “Mixing rules with complex dielectric coefficients,” Subsurf. Sens. Technol. Appl., vol. 1, no. 4, pp. 393–415, 2000.

[39] T. P. Leão, E. Perfect, and J. S. Tyner, “Evaluation of lichtenecker’s mixing model for predicting effective permittivitty of soils at 50 MHZ,” Trans. ASABE, vol. 58, no. 1, pp. 83–91, 2015.

[40] D. Havelka, O. Krivosudský, J. Průša, and M. Cifra, “Rational design of sensor for broadband dielectric spectroscopy of biomolecules,” Sensors Actuators B Chem., vol. 273, pp. 62–69, 2018.

[41] M. Cifra, J. Průša, D. Havelka, and O. Krivosudský, “Water models in molecular dynamics simulation prediction of dielectric properties of biomaterials,” IEEE J. Electromagn. RF Microwaves Med. Biol., vol. 3, no. 2, pp. 97–104, 2018.

[42] A. Jouyban, S. Soltanpour, and H.-K. Chan, “A simple relationship between dielectric constant of mixed solvents with solvent composition and temperature,” Int. J. Pharm., vol. 269, no. 2, pp. 353–360, 2004.

[43] D. El Khaled, N. Novas, J. A. Gázquez, R. M. García, and F. Manzano-Agugliaro, "Alcohols and alcohols mixtures as liquid biofuels: A review of dielectric properties," Renew. Sustain. Energy Rev., vol. 66, pp. 556–571, 2016.

[44] F. Motasemi, M. T. Afzal, A. A. Salema, J. Mouris, and R. M. Hutcheon, "Microwave dielectric characterization of switchgrass for bioenergy and biofuel," Fuel, vol. 124, pp. 151–157, 2014.

[45] N. Hosseini, M. Baghelani and M. Daneshmand, "Selective Volume Fraction Sensing Using Resonant-Based Microwave Sensor and Its Harmonics," *IEEE T. Microw. Theory*, doi: 10.1109/TMTT.2020.2990139.

[46] D. M. Pozar, Microwave engineering. John Wiley & Sons, 2009.

[47] S. L. Van Berkel, "Characterization of printed transmission lines at high frequencies.", 2015. available at: https://repository.tudelft.nl/islandora/object/uuid:dc192664-0720-486d-9423-e0b6d93f1de7

[48] A. Sabban, and K.C.Gupta, "Characterization of radiation loss from microstrip discontinuities using a multiport network modeling approach," IEEE T. Microw. Theory, vol. 39, no.4, pp.705-712. Apr. 1991.

[49] S. Haykin, Neural Networks and Learning Machines, 3/E. Pearson Education India, 2010.

[50] A. F. Agarap, "Deep learning using rectified linear units (relu)," arXiv Prepr. arXiv1803.08375, 2018.

[51] K. Moriarty, "Handbook for Handling, Storing, and Dispensing E85 and Other Ethanol-Gasoline Blends (Book)," National Renewable Energy Lab.(NREL), Golden, CO (United States), 2013.

[52] M. Baghelani, N. Hosseini and M. Daneshmand, "Artificial Intelligence Assisted Non-Contact Microwave Sensor for Multivariable Biofuel Analysis," in IEEE TRANSACTIONS on Industrial Electronics, doi: 10.1109/TIE.2020.3032870.

Chapter 4 Novel Miniaturized Asymmetric CPW Split Ring Resonator Design for Monitoring Water and Brine Concentration in Crude Oil

This chapter proposes a novel modified split-ring resonator (SRR) for expanded field distribution and miniaturized dimensions. A resonant mode-based multivariable analysis is performed using the same style SRR. The proposed design is based on an asymmetric coplanar waveguide type SRR and demonstrates a smaller radius of 0.035×λ with a resonance of 1.57 GHz at its first resonant mode. The proposed structure has the potential of higher sensitivity, requires smaller sample volume, and is miniaturized compared to the conventional ring resonators. The long but narrow overlap gaps evident in the proposed miniaturized SRR create capacitive and inductive contributions for a better sensing performance regime and optimized for superior efficiency and miniaturization capability. For sensitivity evaluation, a coplanar SRR prototype operating at the same resonance is compared with the proposed miniaturized coplanar SRR to underscore its superior performance profile.

4.1 Introduction

Every material has an identifiable and unique set of electrical properties that directly dependent on its dielectric characteristics. These dielectric properties affect the electromagnetic (EM) field profile near the resonator. Every material has an identifiable and unique set of electrical properties that directly dependent on its dielectric characteristics. These dielectric properties affect the electromagnetic (EM) field profile near the resonator. In turn, the electrical characteristics (namely: resonance location, signal power level and Q-factor (Q), etc.) of the resonator change relative to the dielectric properties. Printed planar microwave sensors are recently becoming promising alternatives for enhanced sensitivity and accurate material characterization. Different

application-specific planar microwave resonators with enhanced performance profiles optimized for accurate material characterization have been reported in the literature [1-7]. They have been identified as attractive candidates due to contact-less capability, low-power consumption, cheap, ease of integration with available monolithic microwave integrated circuits and CMOS. power level and Q-factor (Q), etc.) of the resonator change relative to the dielectric properties. Printed planar microwave sensors are recently becoming promising alternatives for enhanced sensitivity and accurate material characterization. Different application-specific planar microwave resonators with enhanced performance profiles optimized for accurate material characterization have been reported in the literature [1-7] and have been identified as attractive candidates due to contact-less capability, low-power consumption, low-cost, ease of integration with available monolithic microwave integrated circuits and CMOS. They have numerously been deployed as displacement and/or velocity sensors [8–12], rotational sensor [13], 2D displacement and alignment sensor [14-15], differential sensor [16-18], concentration measurements [19-20], and dielectric constant and/or loss tangent measurements [20, 21-26]. Nonetheless, some suffer from low resolution, low range, poor sensitivity, etc., whereas nearly all do not bear direct overlaps with our focus. Despite these shortcomings, split-ring resonator (SRR) has been very popular since 1999 when reported by Pendry *et al.* due to its small form factor at resonance [27-28]. Indiscriminate positioning of the samples at optimized positions so-called "hot-spots" as reported in [30] to optimize enough EM interaction for high sensitivity would be arbitrary, inconsistent, and unreliable at best. The passband resonators have been known to exhibit localized EM fields at gaps and coupling spaces (hotspots), and thus demonstrate optimal detection capabilities at these locations. These scenarios created a poor sensitivity regime when the sample is loaded elsewhere other than the gaps and coupling spaces. The situation could worsen if the sample volume is overtly small such as obtainable in microfluidic applications for biomedical specimens, cell growth and recognition, and particle sensing. Unlike the passband resonator, traditional notch band resonators have their EM distributions across their aperture. However, they are also bedevilled with poor coupling coefficients, lower signal amplitude, a significant difference in EM properties due to poor coupling with attendant low sensitivity regime [30 – 32] and limited field distribution patterns for sample

characterization. This could create low-quality material characterization, unreliable obtained results and misleading sensor profiling.

Instead, our proposed miniaturized SRR with extended overlap gaps across its surface could extend considerable *E*-field across the aperture surface. It will undoubtedly increase the average field intensity interacting with the sample, enhance sensing capability and thus be adaptable for smaller sample volume. Such attainable sensitivity to a small sample size could benefit in the biomedical application and often depends on sample size and sample location. Therefore, this chapter presents a novel miniaturized coplanar waveguide SRR (MSRR) with three objectives. The first is to increase the average field strength and expanded *E*-field distribution for better sample interaction. The second is to create a larger field concentration area for smaller sample volume and finally to miniaturize the resonator footprint for compact capability.

4.2 Operational Principles and Sensor Implementation

Like every other planar ring resonator, SRR defines a simple resonator that supports the odd and even degenerate modes depending on its asymmetrical geometry relative to its input and output excitations. For the odd modes, most of the *E*-field is concentrated at the gap area, and any higher index medium in the gap vicinity will experience a substantial *E*-field interaction when capacitively loaded. This, in turn, shifts the resultant resonance due to the medium. The order of capacitance created by the amount of the charge enclosed relative to resonance within the gap areas can be evaluated in terms of C_{eq} perturbation using the circuit-based formulation of Eq. (4-1). Alternatively, the geometric-based representation of the resonance can be shown as Eq. (4-2), where ω_n is the angular resonance of *n*-th resonant modes, *R* is the radius of the SRR, and *n* is the number of resonant modes, also f_r and ω_n present the resonant modes.

$$f_r = \frac{1}{2\pi\sqrt{L_{eq}C_{eq}}} \tag{4-1}$$

$$\omega_n = \frac{nC}{2R(\varepsilon_{eff})^{0.5}} \qquad n = 1, 3, 5, \ldots \tag{4-2}$$

where L_{eq}, C_{eq}, and ε_{eff} describe the effective inductance, capacitance, and permittivity of the structure. Typically, a half-wavelength SRR with its equivalent circuit depicted in Fig. 4.1(a) will exhibit optimal out-of-phase *E*-field concentration at the gap region with marginal *E*-field concentration at the inductive side opposite to the gap as shown in Fig. 4.1(b). Therefore, extending E-field distributions across the aperture surface requires the gap to be modified and extended across the surface. The cross of this work is to leverage the field intensity within the gap area by opening the gap and replicating it as much as possible across the cross-section of the SRR to concentrate optimal E-field distributions and increase the electrical length miniaturization.

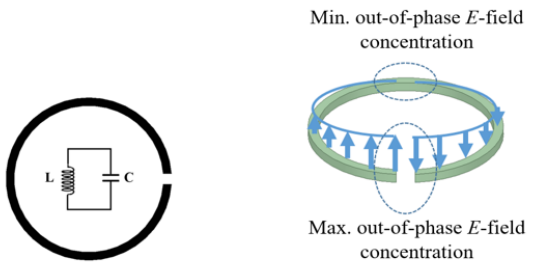

Fig. 4.1. The asymmetric coplanar waveguide-based SRR. (a) Geometry and parameters, (b) First mode E-Field concentration [72].

4.3 Proposed Structure

To create a wider field concentrated area than the conventional SRR, we propose the resonator design shown in Fig. 4.2(a). The structure is based on a half wavelength conductor with an extended capacitive coupling gap for the first resonance mode. The half-wavelength conductor is turned in fractal shape to create a circular ring enclosing i.) an extended inductive segment and ii.) an extended capacitive segment. The duo's effect concentrates on field distributions across the resonator aperture to extend the *E*-field profile across the MSRR surface and create an expanded field area. The inductive segment decreases the ring's physical length while maintaining the same area in favour of miniaturization. Besides, the performance profile of the MSRR is enhanced owing

to capacitive and inductive contributions arisen by the inductive and capacitive segments of the structure, thus yielding a reasonable Q. The inductive segment is essentially for miniaturization and consists of four non-concentric numbers of rings with radii R_1- R_4, as depicted in the inset of Fig. 4.2, (a) and highlighted with a blue circle. The inductive segment has four distinct gaps and forms associated parallel capacitances (C_1 - C_4). Total capacitance $C_T = \sum(C_i)$ where i = 1,…,4 and $C = \varepsilon A/g_i$, A is the cross-sectional area of the gap, with the size of g_i. The equivalent circuit of C_T and the component's RL circuit are as shown in the inset of Fig. 4.2(b). The C_T is marginal and can be ignored, as it affects the resonance less. The amount of coupled E-field contribution due to C_T is meagre at notch area (area with minimum E field concentration), making the inductor-like segment highly inductive and confining the magnetic coupling between the inductor rings.

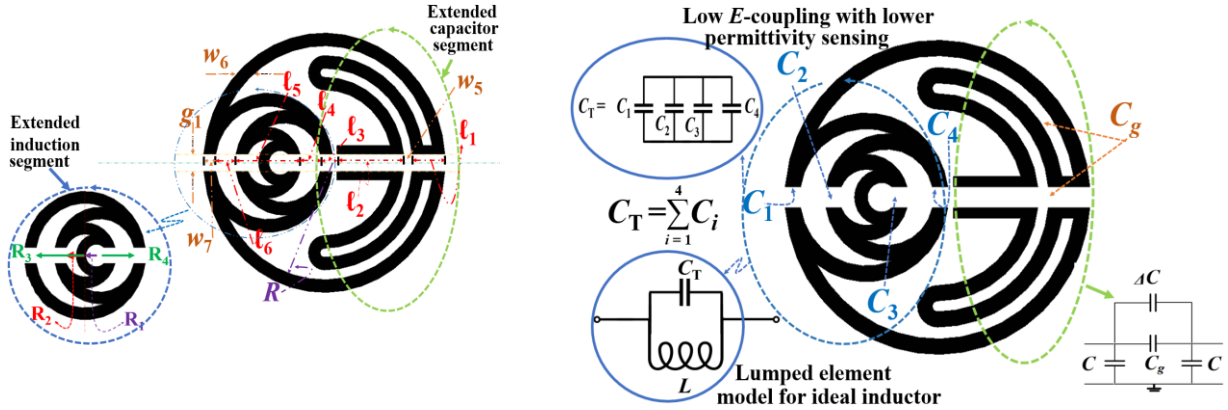

Fig. 4.2. The MSRR. (a) Geometry and parameters, (b) Structure and the respective lumped element equivalent [72].

At the electrically blind spot (notch) area, the inductive segment effectively confined the magnetic field within its vicinity. Since both E- and H-field is orthogonally polarized, the E-field coupling is further extended across a larger area of the entire MSRR to yield more considerable E-field strength. Higher field penetration for better sensitivity is achieved together with device miniaturization, a significant parameter in many applications.

It could also provide a useful H-field for sensitivity measurement of magnetic samples based on their relative permeabilities. The capacitive segment (extended capacitive edges) highlighted with the green ring in Fig. 4.2(b) is folded over to create three layers of capacitive contributions circumferentially parallel to the main ring to form a fractal-like loop shape. The insets of Fig.

4.2(b) are the lumped element equivalent circuits of the capacitive structure. The effects of capacitances are considerable than that of the inductance segment and thus becomes more capacitive with effective capacitance C_g. The impact of C_g on the resonance frequency is remarkable when loaded with the sample. Hence, the resonance frequency of the MSSR is highly influenced by the capacitive segment and reasonably by the inductive contribution of the *RL* circuit of Fig. 4.2(b). This is supported by Eq. (4-2).

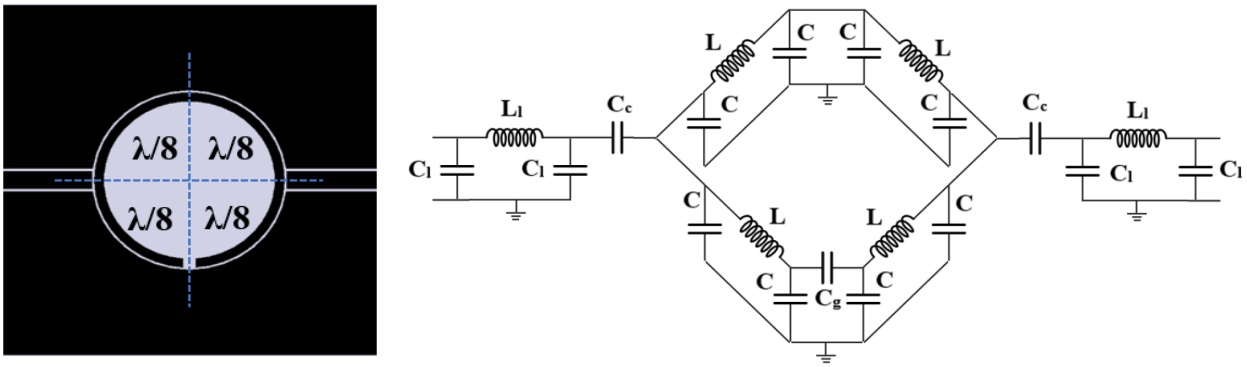

(a) (b)

Fig. 4.3. Basic design modelling. (a) SRR, (b) Extended, the modified equivalent circuit of SRR [72].

4.4 Coplanar Waveguide MSRR Design Techniques

The proposed resonator is the extended version of coplanar waveguide-based SRR. The equivalent circuit model of SRR with f1 = 2.16 GHz is designed as proper sized sensor to start the analysis. The same equivalent circuit is modified to reflect the miniaturized MSRR layout schematic shown in Fig. 4.3(b). The SRR, on its first mode can be considered as four cascaded λ/8-TL segments to form the λ/2 size cavity as shown in Fig. 4.3(a). The characteristic impedance of each line segment [33] and their electrical length are calculated and plugged into Eq. (4-3). The calculated capacitance, C, and inductance, L, were imported into Agilent ADS software to generate the final circuit.

$$C = \frac{2}{\omega Z_0} tan\left(\frac{\theta}{2}\right), L = \frac{Z_0}{2\omega} tan\left(\frac{\theta}{2}\right) \quad (4\text{-}3)$$

The L_1 and C_1, the equivalent capacitance and inductance values of feeding lines, were evaluated based on the electrical length, θ, of the coupling feedline, whereas coupling capacitance (Cc) between the feedline and MSSR is minimal and insignificant to affect the SRR resonance. For our designs, the electrical length of the coplanar feed lines is set at 25 degrees with W_1 = 1.55 mm and l_1 = 7.36 mm. Using Eq. (4-3), we determine C_1 = 0.56 pF and L_1 = 0.47 nH for the feed lines and C = 0.4 pF and L = 2.4 nH for λ/8-TL segments at resonance frequency of 2.16 GHz. We also chose Cg = 0.2 pF and Cc = 0.1 pF as the minimum capacitor values that are not contributing to the resonance of the SRR. Because of the asymmetric property of the SRR, the expected impedance of the line is slightly higher than the double-ground coplanar lines. For the resonator of the same diameter, the same circuit topology is extended with the addition of ΔC_i in both gap areas ($C_g^{'} = C_g + \Delta C_g$) and C component of the lines together with inductance variation, ΔL that can be modelled through the Ceq and Leq using Eq. (4-1) with the following relations;

$$C_{eq} = F(Cg', C + \Delta C), \; L_{eq} = G(L + \Delta L), \quad (4\text{-}4)$$

Where C_{eq} a function F of ($C_g^{'}$, $C + \Delta C$) and L_{eq} a function G of ($L + \Delta L$) are the perturbed parameters of the SRR. The equivalent circuit of Fig. 4.3 can be mapped and extended to the updated MSRR model using the defined ΔC_i and ΔL parameters in Eq. (4-4) as geometrical modifications without losing the generality.

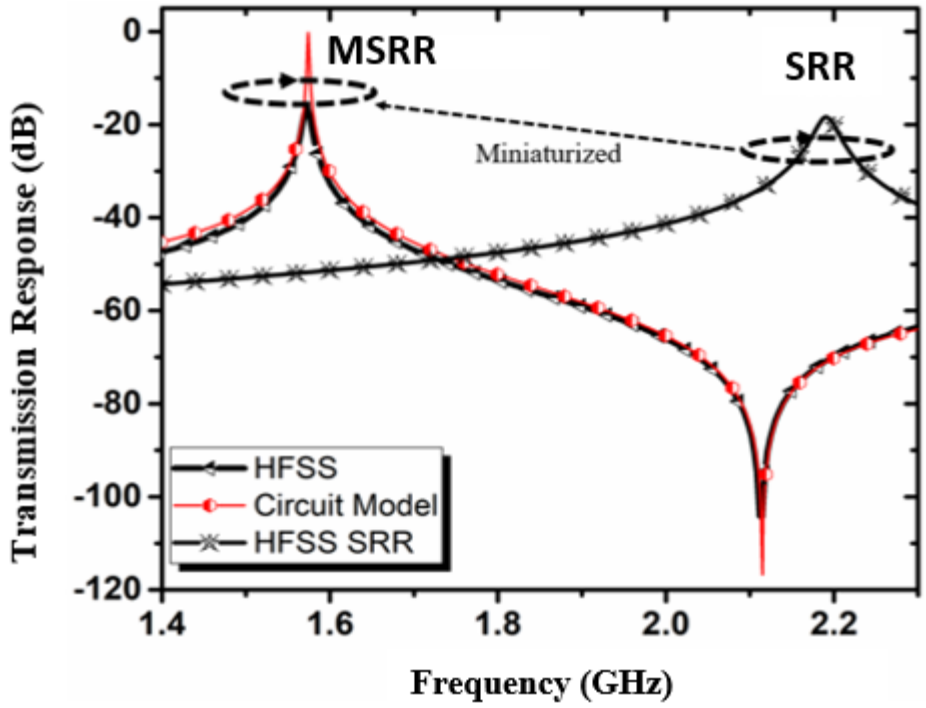

Fig. 4.4. |S21| of MSRR model for both HFSS and the equivalent circuit analysis [72].

The resulting equivalent circuit of the proposed MSRR is modelled using Agilent ADS, and the corresponding Momentum simulation is further investigated using Ansys HFSS based on the parameters of Table 4.1. Fig. 4.4 compares the two results where both responses agree well and validate the correctness of the model. The ΔC and ΔL values were extracted to be 0.22 pF and 0.7 nH. Also, 0.1 pF is extracted for ΔC_g as C_g augmentation at the miniaturized resonance frequency of 1.57 GHz using the ADS model with the same feeding and coupling parameters. The Figure also compares the HFSS response of the conventional SSR against the proposed MSRR. Instead of 2.17 GHz, the MSRR now resonates at 1.57GHz.

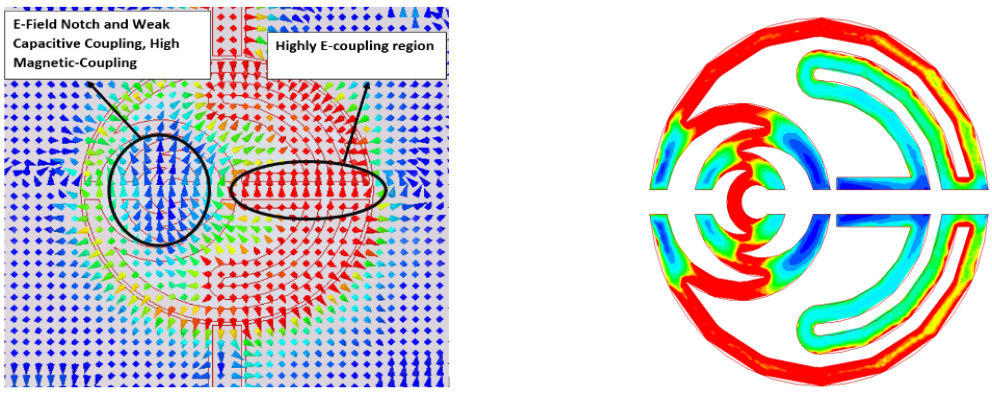

(a) (b)

Fig. 4.5. Field distributions across the MSRR surface. (a) Low and high E-Field profiling, (b) Current distributions [72].

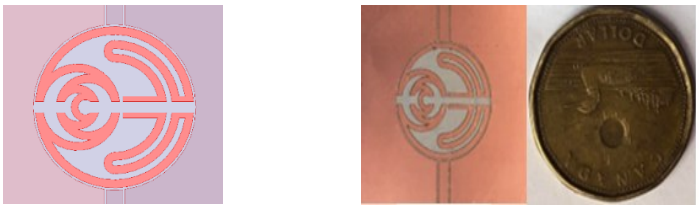

(a) (b)

Fig. 4.6. The MSRR design. (a) The simulation, (b) The prototype [72].

Table 4.1. The design parameters of MSRR.

Parameter	Value (mm)	Parameter	Value (mm)	Parameter	Value (mm)
l_1	2.0	W_5	0.5	R_1	0.69
l_2	4.0	W_6	0.7	R_2	1.32
l_3	1.0	W_7	0.75	R_3	3.27
l_4	1.23			R_4	2.28
l_5	4.0			R	6.77
l_6	1.23				

Fig. 4.5(a) profile the *E*-field distribution over the surface of MSRR and shows vigorous field intensity (red) over the capacitive segment, moderate value (greenish-yellow) at the inductive and nominal weak field in-between (blue). This is more evident in Fig. 4.5(b) and more apparent that the field distribution is more than 95% of the entire surface.

4.5 Sensor Design Characterization

The prototype is etched on a RO3003 microwave laminate with dielectric permittivity (ε_r) of 3, substrate thickness (h) of 0.76 mm, loss tangent of 0.0013 and metallization thickness (t) of 35 µm

as depicted in Fig. 4.6(b). The effect of the inductive and capacitive segments on the resonator performance is parametrized by removing each in turn. In Fig. 4.7(b), the impact of eliminating the capacitive component is depicted, whereas removing the inductive segment is shown in Fig. 4.7(a). It's evident that the resonance shifted much higher (220 MHz) as the capacitive component is removed and reasonable otherwise. The resonance without the inductive segment occurred at 1.69 GHz and otherwise at 1.57 GHz, constituting about a 6.51% reduction alone. This behaviour is supported by the resonance Equation of Eq. (4-2), such that resonance shift is a function of the variant of the inductive component or the capacitive or both.

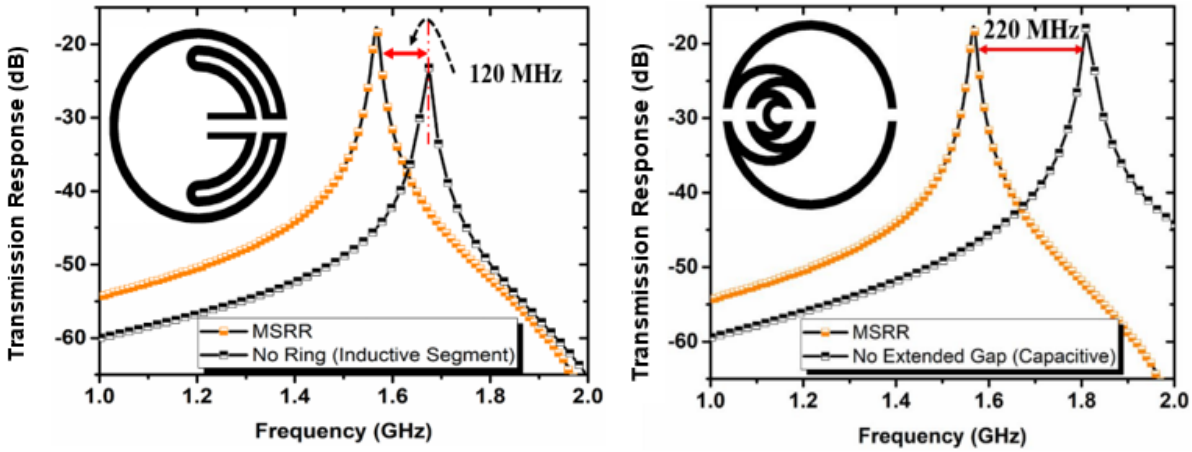

Fig. 4.7. The Simulated results for MSRR geometrical parameters. (a) Inductive perturbation effect, (b) Capacitive perturbation influence [72].

4.6 Experiments and Measurements

The prototype is measured using Blue Copper Mountain 100 KHz – 20 GHz network analyzer (VNA – EB362C), and the result is as shown in Fig. 4.8. The simulated and measured |S21| agreed substantially with resonance at about 1.57 GHz. The Q has been enhanced considerably, and the size has been miniaturized to about 55% compared to SRR at the same resonance.

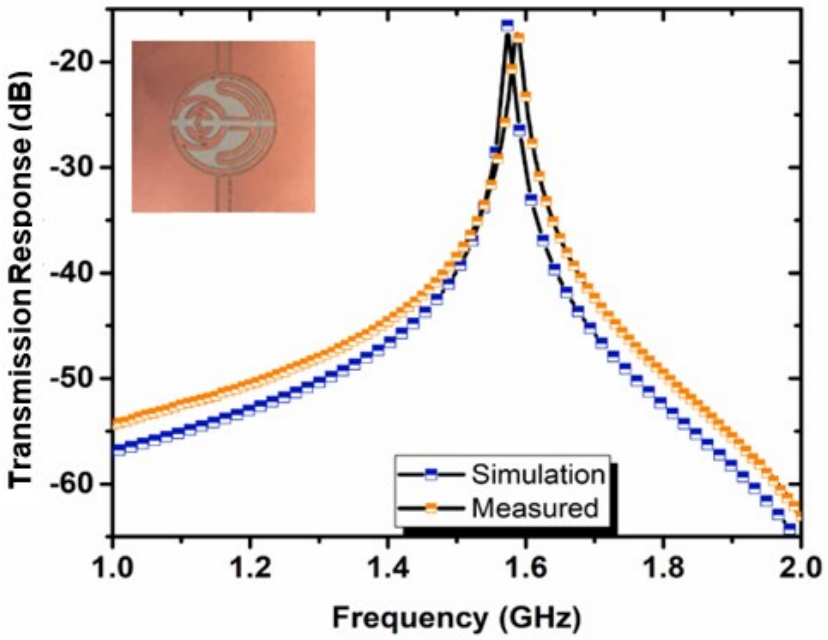

Fig. 4.8. The S-parameter results of the resonator in comparison with full-wave simulation results [72].

Preliminary performance characterization of the proposed resonator as a sensor is done using Ansys HFSS to determine the sensor's capabilities in terms of available *E*-field coverage and observe if the bottom plane can be leveraged for sensing applications. It is also done to identify various locations that have optimum or extended field distributions. Fig. 4.9(a) demonstrates our selected locations, whereas Fig. 4.9(b) demonstrated the simulated response due to the location-based Teflon loading of the resonator. The percent resonance response ($\Delta f_r/f_{r\_unloaded}$ (%)) is 2% for location (Y = 0, X = 7) and 3% for location (Y = 0, X = 2) and nothing substantial for (Y = 0, X = 12).

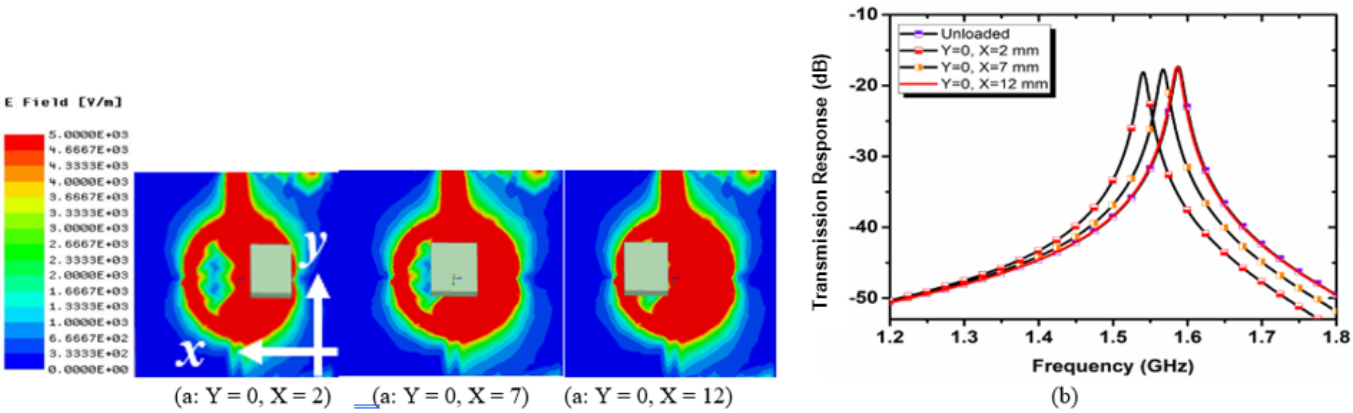

Fig. 4.9. Simulated location-based sensitivity analysis of the MSRR. (a) E-Field distribution for different sample relocating, (b) |S21| vs. Freq [72].

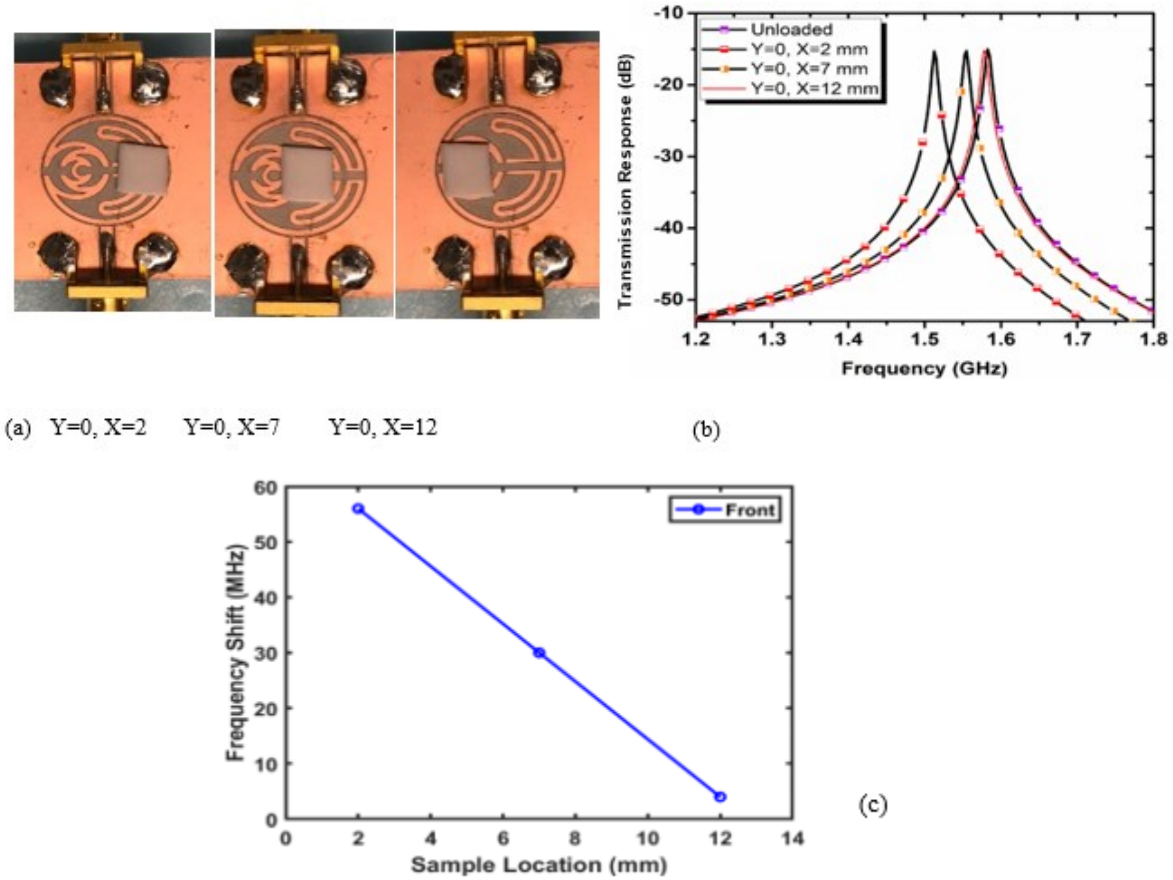

Fig. 4.10. Location-based sensitivity analysis of the MSRR. (a) Prototype, (b) |S21| vs. Freq and (c) Δfreq. vs. location [72].

Subsequently, we repeated Fig. 4.9(a) experimentally as shows in Fig. 4.10(a) using Blue Copper Mountain 100 KHz – 20 GHz network analyzer. Fig. 4.10(b) is the location-based sensitivity metric and measure the $|S_{21}|$ of the resonator versus frequency upon interactions with the sample placed in its vicinity. It identifies three locations with sensitivity levels of 3 MHz, 30 MHz and 56 MHz, corresponding respectively with areas (Y=0, X=12), (Y=0, X=7) and (Y=0, X=2). Alternatively, Fig. 4.10(c) succinctly relates the sensitivity capability of the resonator with the sample locations where sensitivity is substantial at locations (Y=0, X=2), (Y=0, X=7) and almost non-existence at (Y=0, X=12). The response exactly duplicates the simulated result of Fig. 4.9(b) with better performance at the blind spot (Y = 0, X = 12) as depicted.

We further conducted a full-sensitivity analysis of the sensor to benchmark the sensor's performance metrics. We opined that doing so will provide a robust platform to correctly compare its performance with asymmetric coplanar SRR at the same frequency. Five samples with geometric progression in size are considered to examine the sensitivity level of the fabricated sensor. The sample size is normalized to give standardized data points such that an arbitrary sample size of 6.75 × 6.0 (S_1) sq.mm of Teflon is cautiously taken experimentally. This sample size is firstly to get a coverage ratio (sample size/resonator area) of 25% of the resonator aperture size following the procedure shown in Fig. 4.11. This will be the first sample (S_1). The same process is then repeated for a 113% coverage ratio to realize the sensor's full coverage, as demonstrated in the figure. Therefore, any term between these data points can be determined by multiply the preceding sample (between first and final samples) with a relation $S_n = S_1 \times (1.44)^{n-1}$, where n is the n-th sample in the data points, and S_n is the n-th sample area with scale ratio of 1.44. The values are as stated in Table 4.2 (column 1).

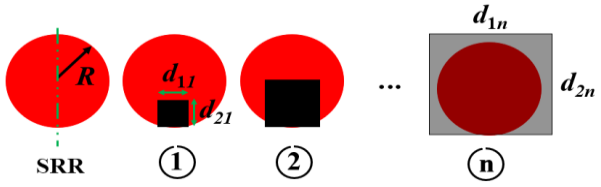

Fig. 4.11. Location-based sensitivity characterization of the proposed sensor [72].

Table 4.2. The measured resonance shifts for different loading scenarios on both planes.

MSRR			SRR	
Size (mm^2)	Front Plane	Back Plane	Front Plane	Back Plane
	Freq. (GHz)		Freq. (GHz)	
6.8 × 6.0	1.53	1.543	1.556	1.564
8.1 × 7.2	1.497	1.527	1.548	1.561
9.7 × 8.6	1.479	1.510	1.541	1.559
11.7 × 10.4	1.469	1.505	1.533	1.557
14.0 × 12.4	1.465	1.495	1.530	1.555

Both SRR and the proposed resonator are subsequently loaded on both planes (sides) with these sample sizes and the responses monitored. The resonance values are documented in Table 4.2 (columns 2 & 3). The response against frequency for both resonators are depicted in Fig. 4.12(a), whereas our predictive model plot is shown in Fig. 4.12(b). The data were quantified using computer-aided polynomial curve fittings to approximately predicts the resonance response with respect to sample size in terms of its area when the sample is loaded in the vicinity of the resonator. This is done to do a proper average-based calibration of the proposed coplanar-based MSRR for expanded *E*-field distribution.

Table 4.3. Coefficients of the fitted curve.

Fitted Coefficinet	Front Plane	Back Plane
P_0	-0.6287	-0.1567
P_1	1.834	1.379
P_2	-0.0088	-0.0077
P_3	1.3×10^{-5}	1.622×10^{-5}

The predictive polynomial for front-plane loaded is as stated in Eq. (4-5), where the values of p_0, p_1, p_2, and p_3 are as indicated in Table 4.3. The same polynomial is valid for the backplane loaded but with the reported values of p_0, p_1, p_2, and p_3 as stated in column 2 of Table 4.3. The data for both sides of the MSRR traces a curvilinear model and is substantially well fitted by Eq. (4-5) with a confidence level of 95% and empirically quantifies approximately the resonance shift for any sample size.

$$\Delta f_r(A) = \sum_{i=0}^{n} p_i A^i \tag{4-5}$$

where A is the sample physical area, Δf_r is the resonance shift per sample, p is the coefficient of the fitted curve based on our measurements.

The polynomial data-fitting program demonstrated considerable resonance shift when front-plane loaded, followed by the moderate response when backplane loaded, as shown in Fig. 4.12(b). Our observation is reported in Table 4.4. Our proposed resonator demonstrates enhanced sensitivity of about 250% for the smallest sample size of 50 sq.mm compared to the conventional SRR of the same sample size and a factor of 200% for the largest sample size when front-plane loaded. Ours also demonstrated a superior sensitivity factor of more than 80% when backplane loaded at any sample size. In addition, a smaller sample volume could be utilized and detected with a high degree of sensitivity for a given sensitivity. The graphs for MSSR show significantly enhanced sensitivity, and thus, the measurements verify the second and third objectives of the proposed resonator design. Lastly, considering the sensor size reduction, the proposed resonator has significant advantages compared to the conventional SRR. The effective area of the proposed (153 sq.mm) is miniaturized by 55.6% compared to the conventional SRR of area 346 sq.mm at the same resonance.

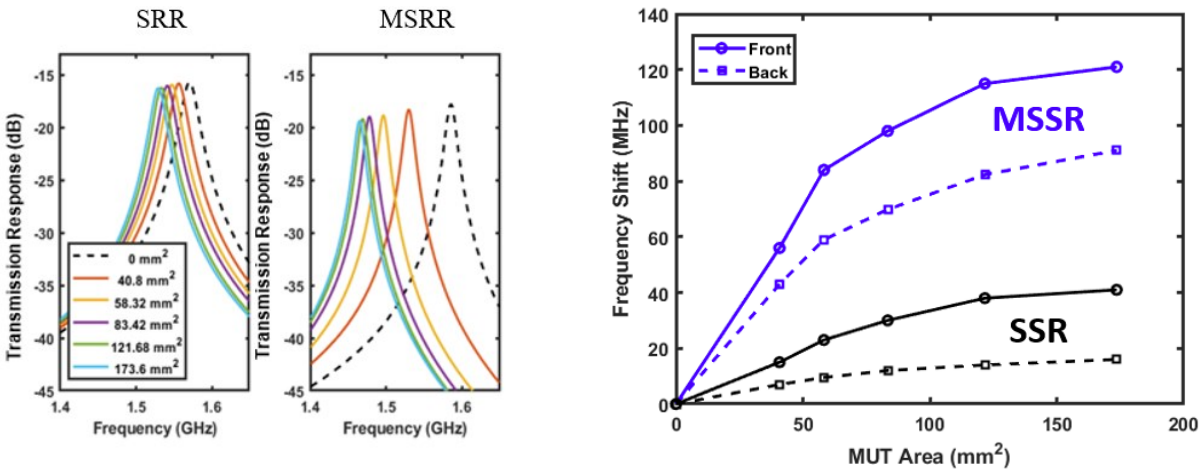

(a) (b)

Fig. 4.12. Measured size-based sensitivity comparison. (a) |S21| vs. Freq., (b) Freq. Shift vs. sample size [72].

Table 4.4. Sensitivity analysis performance based on Fig. 4.12(b).

Front Plane				Back Plane		
Sample Size (mm^2)	MSRR Δf (MHz)	SRR Δf (MHz)	MSRR/SRR Δf (MHz)	MSRR Δf (MHz)	SRR Δf (MHz)	MSRR/SRR Δf (MHz)
50	70	20	2.5	53	9	4.9
100	105	34	2	74	12	5.1
150	120	40	2	88	18	3.9

4.7 Design Validation

Regarding the nature of the experiment in this section, which is monitoring the humidity level, Teflon is not a proper candidate. Therefore, the device's efficiency is validated by loading both sides of the resonator with a 3M transparent water-soluble wave solder tape 5414 Poly-vinyl alcohol (PVA) film having a thickness of 20 µm as shown in Fig. 4.13. Two samples 0.05λ × 0.05λ sq.m and strip of 0.045λ × 0.015λ sq.m moisture-responsive 3M samples are separately loaded on the resonator (like Fig. 4.9(a)), and the frequency shift is observed for both planes as shown in Fig. 4.14. The percent shift is 4% (62.5 MHz) for 0.045λ × 0.015λ sq.m sample and 8%

(112.5 MHz) for 0.05λ × 0.05λ sq.m respectively. The achieved *Q* factor is also substantial *Q* (= 360). Thus, the backside is functional and can be leveraged for sensing and be adaptable for detecting liquid ingress at the interface between the resonator substrate and the pipeline in some specific pipeline integrity monitoring [34]-[36].

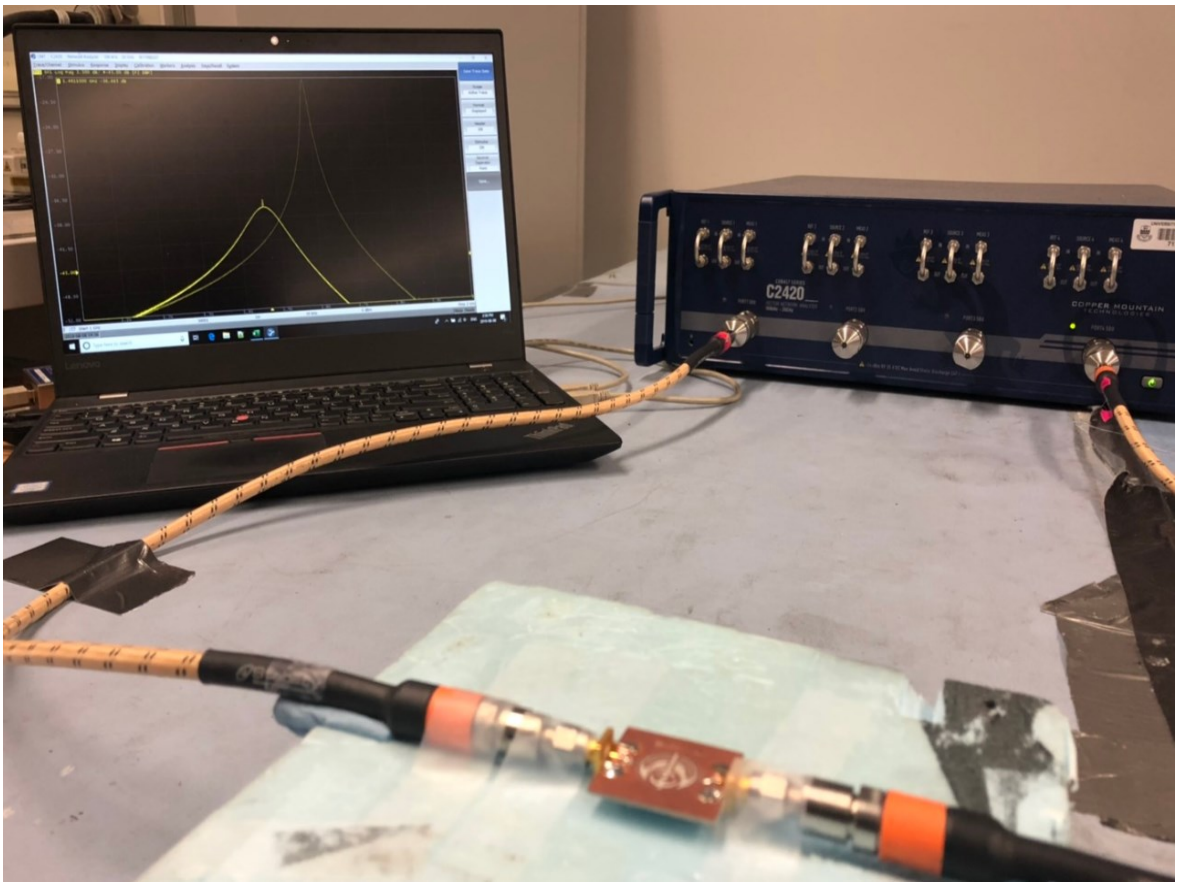

Fig. 4.13. Loading the resonator with PVA [72].

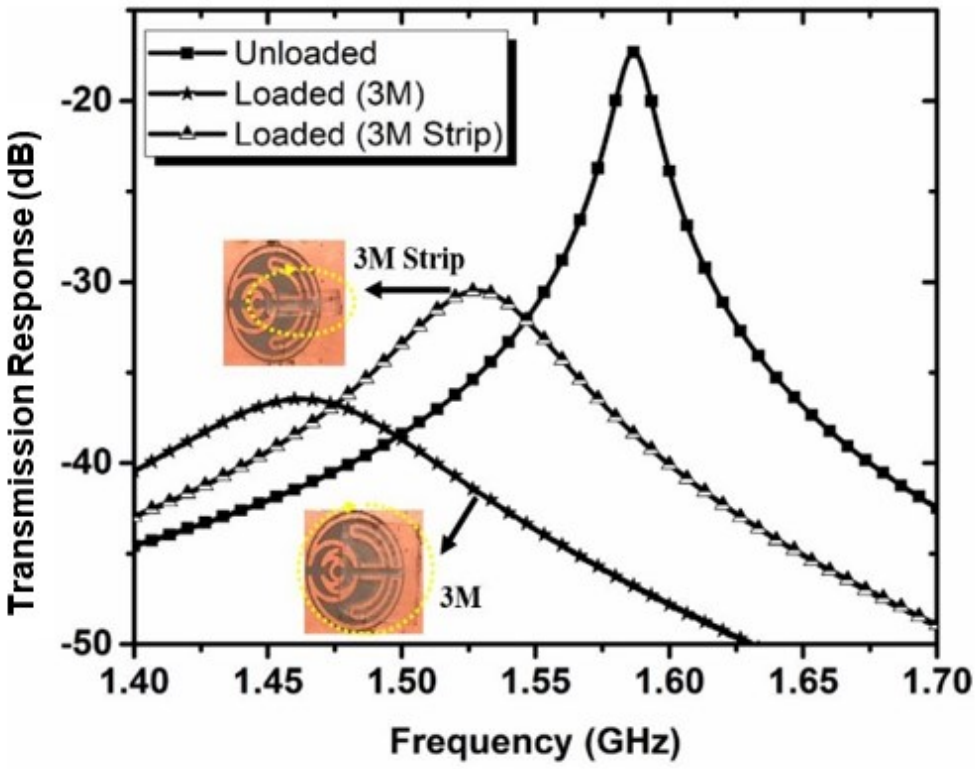

Fig. 4.14. Sensitivity measurement using the proposed resonator [72].

Using the above 3M samples, we conducted two more measurements for liquid characterization. In the first experiment, 0.05λ × 0.05λ sq.m moisture-responsive 3M sample is loaded on the resonator and drops of water at 50 ml/hr. is dropped at the resonator's center for 2 minutes using a benchtop pre-calibrated syringe pump from Cole Parmer. In the second experiment, 3M strip of 0.045λ × 0.015λ sq.m sample is used, and water is loaded the same way as the first experiment but is moved along the strip (Y = 0, X = 2 to 12) as shown with the yellow arrow of inset of Fig. 4.15(b). Fig. 4.15 depicts the response of the proposed resonator as moisture sensors. In Fig. 4.15(a), the resonance frequency shifts down as drops of water increase (in the range 0.5 – 3 ml) until the 3M is saturated and resonance becomes constant at about 600 MHz. In the second experiment shown in Fig. 4.15(b), the frequency also shifts down as the water increases. However, the rate (the slope of the curve) is much faster at the first couple of drops correlating with x=0 in Fig. 4.10.

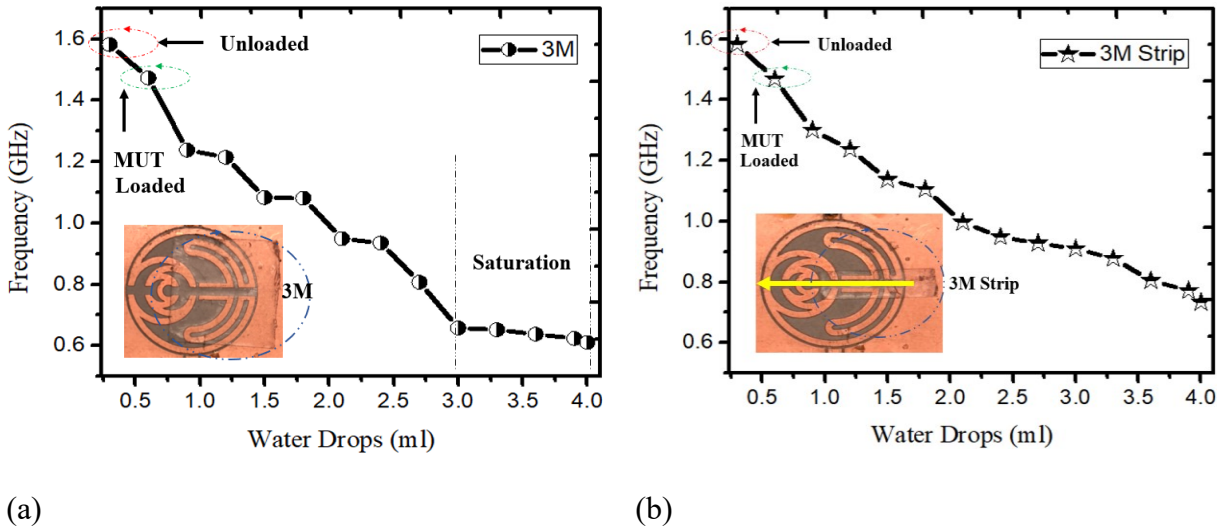

(a) (b)

Fig. 4.15. Moisture-responsive test using 3M sample. (a) 0.05λ × 0.05λ, (b) 0.045λ × 0.015λ [72].

Table 4.5. Performance profile comparison with other planar resonators.

Ref.	Resonatgor	F_{res} (GHz)	S_{21} (dB)	Q	Size (mm)	$\Delta f / f_0$ (%)	Field Pattern
[37]	SRR	3	-70	-	0.16 λ×0.16 λ	0.7	EL
[38,42]	SSRR	2.22	-14.55, -8.92	267, 653	0.5 λ×0.74 λ	5.4	EL
[29]	SRR	5	-15.22	110	0.11 λ×0.1 λ	0.4	EL
[39]	Double SRR	1.85	-17.27	-	0.07 λ×0.09 λ	1.63	-
[40]	SRR	4.5	-	-	0.2 λ×0.08 λ	2.4	EL
[41]	Meander MTM	2.15	-15.34	-	0.14 λ×0.03 λ	7	-
[43]	λ/2	2.4	-	-	0.5 λ×0.2 λ	1.04	GP
	Propsed Work	1.57	-20	360	0.7 λ×0.7 λ	7.2	Ex.
	EL = Edge Localized			GL= Gap Localized		Ex. = Extended	

Table 4.5 compares our proposed resonator sensor with other resonators reported in the literature in terms of performance to underscore its core advantages. Apart from our resonators' extended field pattern capability, the miniaturization potential is considerable at 1.57 GHz

resonance. Compared to the other works, the Q = 360 is also significant for its size, with superior sensitivity of 7.2.

4.8 Monitoring of Water and Brine Concentrations in Crude Oil using MSRR

The measurement results of water content in crude oil are critical for the oil industry. Water content in crude oil might cause serious damage to production plants, refineries, transportation, and even impact price, in addition to diminishing the efficiency of oil storage. [44]. It is also used as a defining element for reservoir oil levels over time [45]. Although all oil research and development facilities have off-line procedures with complex and costly gear, real-time techniques are not being created as quickly as needed. [46], [47]. As a result, most oil firms collect samples and process them in their laboratories, which takes time. Aside from the high cost of labs, the timely nature of the process is the primary impediment to creating real-time feedback control systems for optimizing associated operations for maximum efficiency. [48].

Another challenge with water-based enhanced oil recovery systems is salinity management. Lowering the salinity of the water has also been demonstrated to increase the rate of oil recovery. [49], [50]. Furthermore, greater salinity in crude oil may raise the expense of maintaining desalting equipment in refineries, in addition to the associated environmental issues [51]. As a result, what's needed is a low-cost sensor system that can monitor the water content and salt concentration of crude oil in real-time.

The microwave cavity-based sensor wrapped around the pipe [52], [53], microwave probe penetrated within the pipe [54], capacitance-based approaches [55], and even image processing approaches [56] have all been introduced in the literature for real-time monitoring of the water content in crude oil. Although these approaches have certain appealing advantages, they generally only examine water and oil, and they are based on binary sensing or liquid separation. This is especially true of practically all microwave cavity-based sensors. Different fields ranging from oil and gas industries to biological and chemical sensing have been examined using diverse technology designs [57]–[65].

Most completed investigations for water content monitoring in crude oil based on microwave sensors consider distilled water in crude oil for meeting a single variable sensing requirement, owing to this ostensibly inherent difficulty [66], [67]. A large quantity of salt is dissolved in water in real-world applications, and brackish water is extracted with crude oil instead of clean distilled water.

This section applies the multivariable analysis technique for monitoring simultaneous changes in water, brine, and crude oil concentrations in a combination in real-time where Dr. Masoud Bghalni contributed with methodology, validation, and resources. At the same time Navid Hoseini performed the sensor design, fabrication, HFSS and MATLAB analysis. The suggested approach is based on the different actual dielectric permittivity and conductivity of various materials as a function of frequency.

4.8.1 Design Principles and Technical Approaches

As shown in Fig. 4.16, the extended microstrip split-ring resonator is the basic design of the suggested water-brine-crude oil sensor. The microstrip type sensor is used for this experiment to have a sharper resonance response for the loaded resonator. The resonator's wideband transmission response (S21) simulated using HFSS is shown in Fig. 4.16(c). The resonator's sensing operation is based on a change in the resonance frequency due to a change in the effective permittivity of the loaded resonator.

The field concentration inside the substrate and around the split area showing the fringing field are shown in Fig. 4.17. The total effective real permittivity of the resonator changes as the real permittivity of MUT changes with variations in its components' concentration, leading to a shift in the resonance frequency.

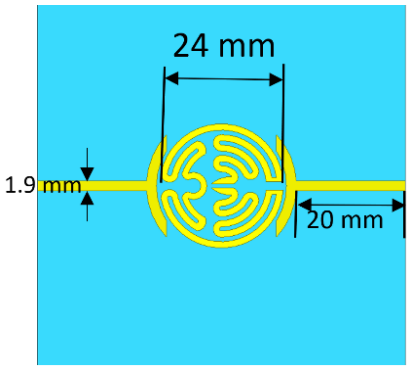

(a)

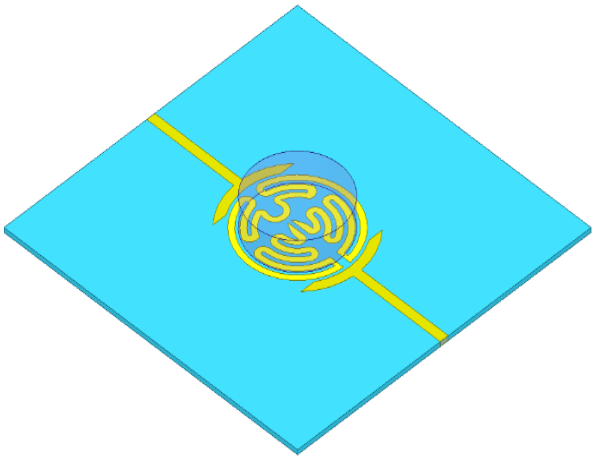

(b)

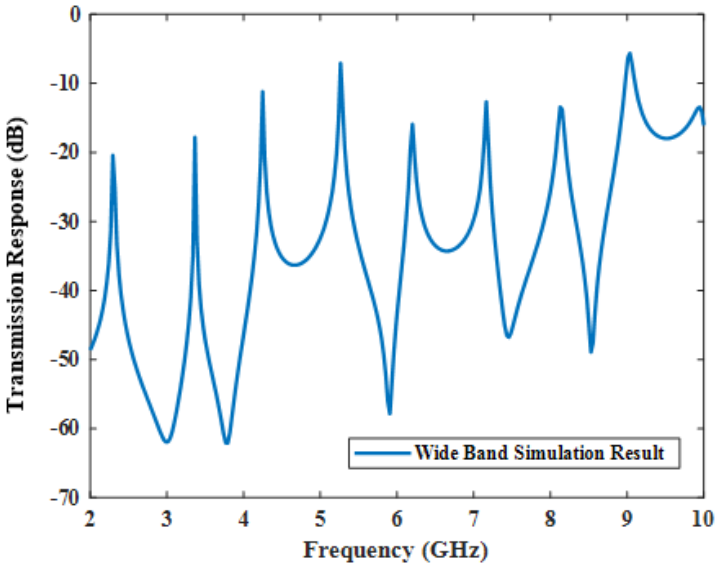

(c)

Fig. 4.16. (a) top view of the designed resonator alongside the dimensions, (b) isometric view of the resonator with the liquid container attached to its top surface, (c) wideband transmission analysis of the resonator sensor, including the higher resonant mode response [71].

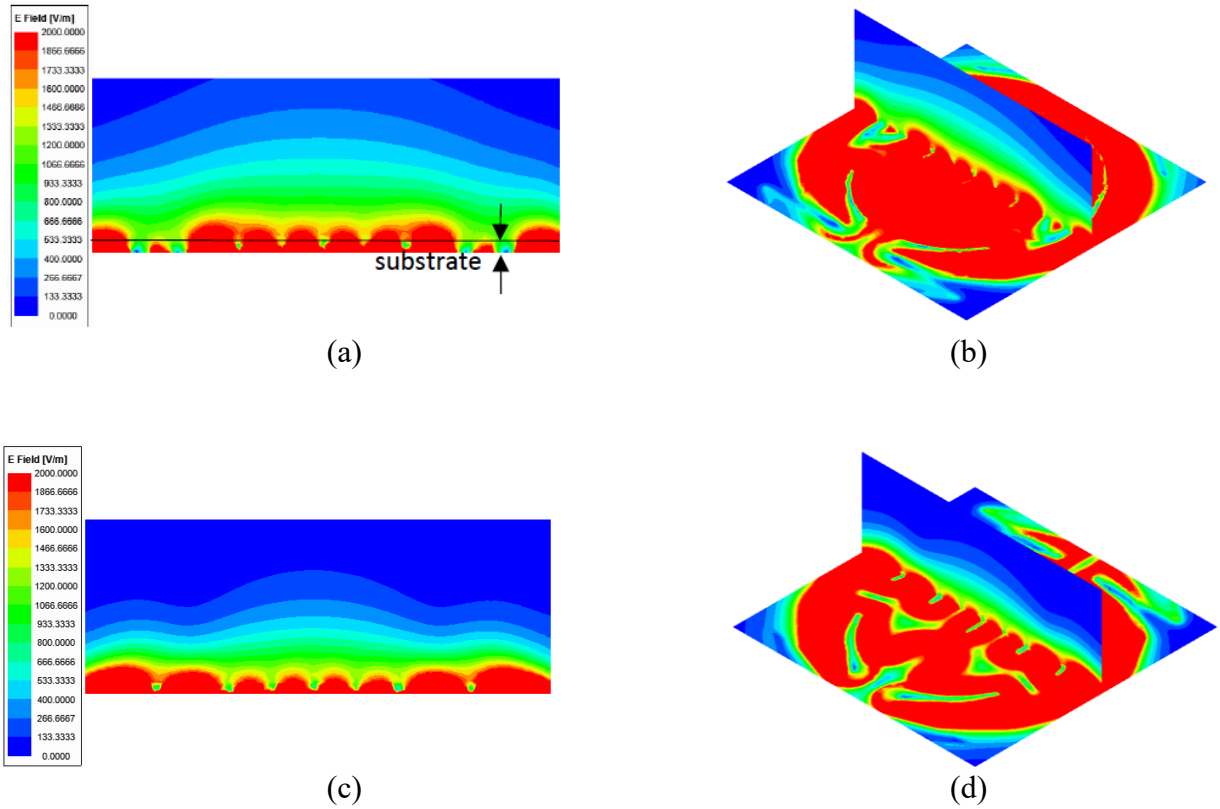

Fig. 4.17. Field concentration of the resonator inside the substrate as well as on top of the resonator constructing the fringing E-field. (a) side-view at 2.3GHz, (b) perspective view at 2.3GHz, (c) side-view at 3.37GHz, and (d) perspective view at 3.37GHz [71].

Due to modern electronics readout circuitry, frequency shift measurement is more reliable at high frequencies. That is why most microwave resonator-based sensors use the resonance frequency change as the primary signal processing characteristic. The resonant frequency shift for the provided sensor's fundamental resonance vs changes in the actual permittivity of MUT is shown in Fig. 4.18. It can be observed that even for slight differences in the real permittivity of MUT, the resulting shift in the resonance frequency is considerable.

Although the field concentration inside the substrate is more significant than in other areas for both of the given modes, the close-to-surface field is still strong, implying a high sensitivity. Furthermore, the resonator hotspot is extended over most of the resonator surface, boosting the entire system's sensitivity compared to a basic traditional split ring resonator with only a tiny spot at the sensitive area due to the resonator's unique design.

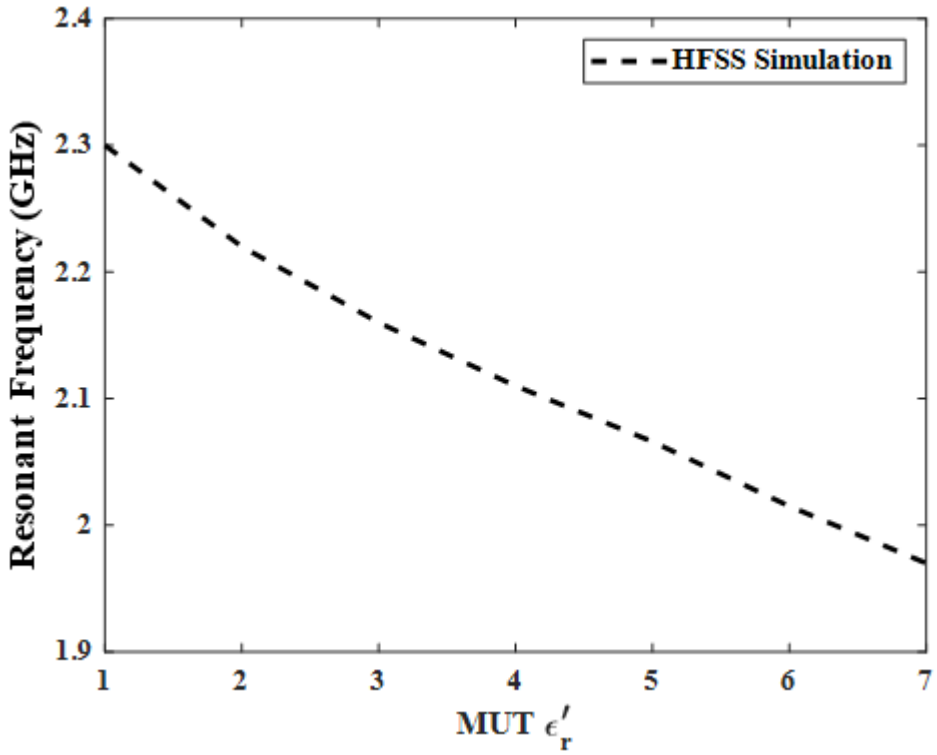

Fig. 4.18. Resonance frequency variation of the structure versus the real permittivity of MUT [71].

Because crude oil may include a large amount of salinity in addition to water, the proposed technology for this application should be able to sense three factors at once. Monitoring three variables with a predetermined overall volume necessitates at least two characteristics while considering the shift in the fundamental mode is insufficient to solve the problem.

When salt is added to a combination of water and crude oil, the conductivity of the mixture increases dramatically, increasing the insertion loss in the sensor's transmission response at the resonance frequency. However, due to a high percentage of salt in water, and the mixture's real permittivity variations, the resonance frequency shifts. As a result, using the amplitude variation to measure the brine concentration results in considerable response inaccuracies.

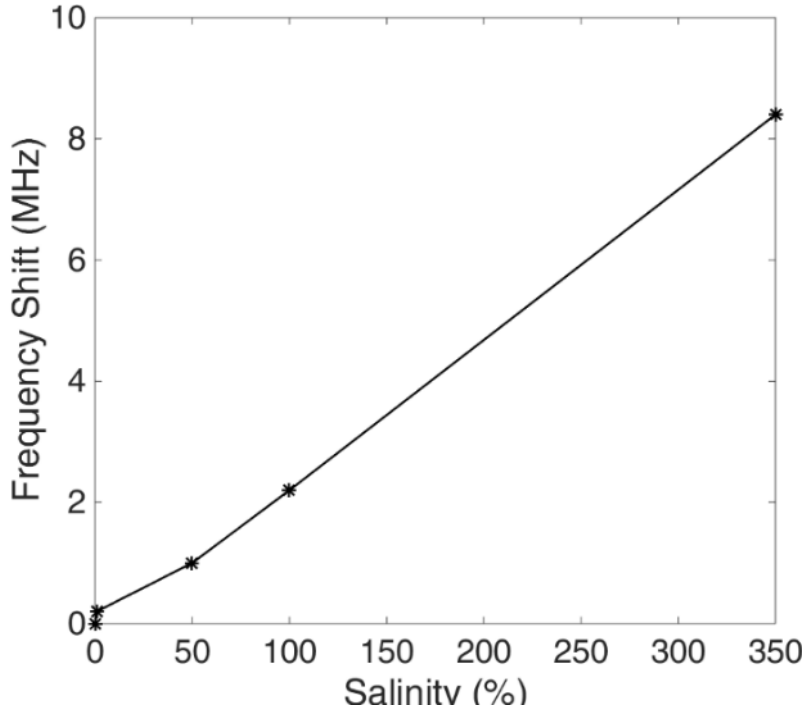

(a)

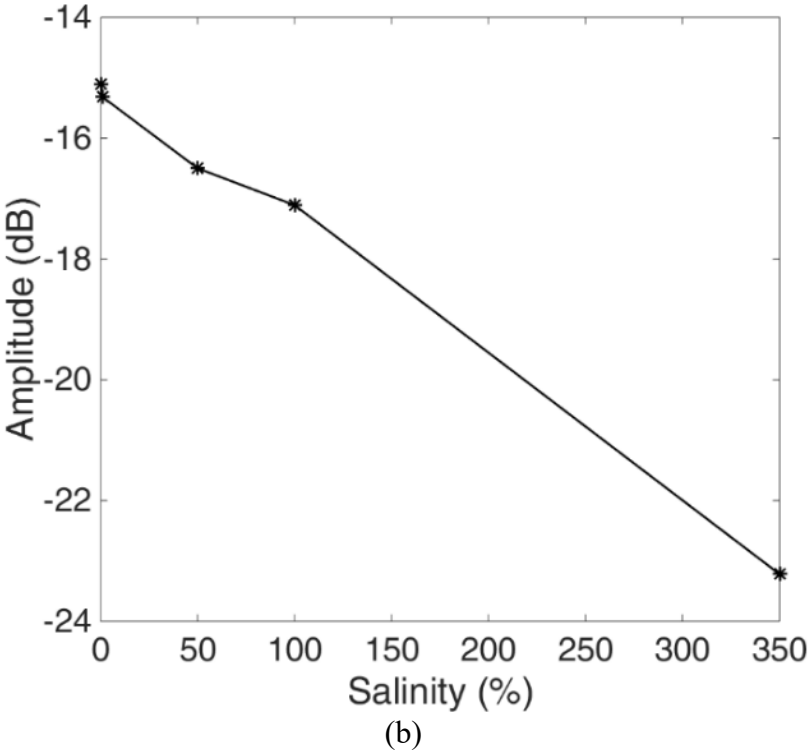

(b)

Fig. 4.19. Impact of brine concentration in (a) frequency shift, and (b) amplitude variation of the first resonant mode. It could be seen that in addition to the significant shift in the amplitude, a considerable shift in the resonance frequency is also expectable [71].

The frequency and amplitude shifts due to salt concentration variations in distilled water are depicted in Fig. 4.19, demonstrating the major influence of the brine contribution to the frequency shift. As a result, that is vital to provide novel sensing characteristics for accurate signal analysis of the structure. Salinity can be defined in the following way:

$$\text{Salinity } \left(\frac{g}{Kg}\right) = \frac{Salt\ Concentration\ (g)}{Weight\ of\ Water\ (Kg)} \tag{4-6}$$

This study utilizes the proposed technique for getting the needed additional feature by employing higher resonant modes of the resonator. The dispersion and uniqueness of the real permittivity spectrum vs frequency of different materials are the concepts behind the nonlinear frequency shifts and amplitude variations. The Debye model [68]–[70] depicts the real permittivity of water, brine, and oil vs frequency.

According to the theory, the difference between the spectrums of the materials begins to change at specified frequencies, resulting in various frequency shifts at different modes for the same materials. Only the sensor's fundamental mode should be chosen so that its higher resonance modes fall in the dispersive spectrum. As a result, the first resonance mode (at 2.3 GHz) and 4 (at 5.2 GHz) have been chosen for performing the sensing task. According to Fig. 4.20, a large nonlinearity occurs at the shifts of these resonant modes, resulting in high-frequency separation for better precision sensing. Fig. 4.21 shows the field distribution for the 4th mode. By comparing Fig. 4.21 and Fig. 4.17, it can be observed that the field distributions for both modes are comparable, which generate a similar field penetration into the samples, implying that the fourth resonant mode has a similar sensitivity to the first one.

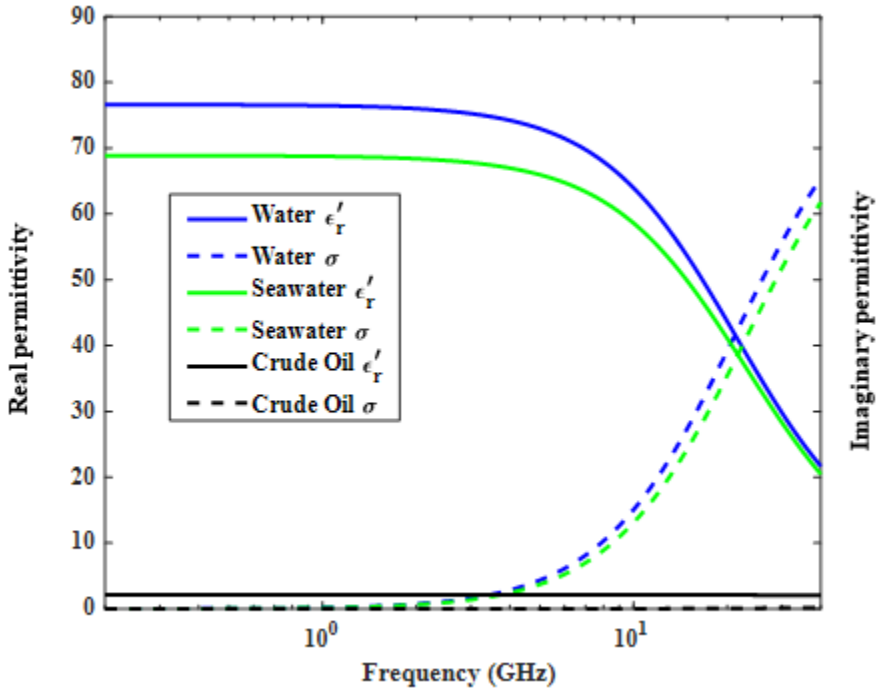

Fig. 4.20. Real and imaginary parts of dielectric permittivity of distilled water, seawater with the salinity of 35 (g/Kg), and crude oil versus frequency according to literature [71].

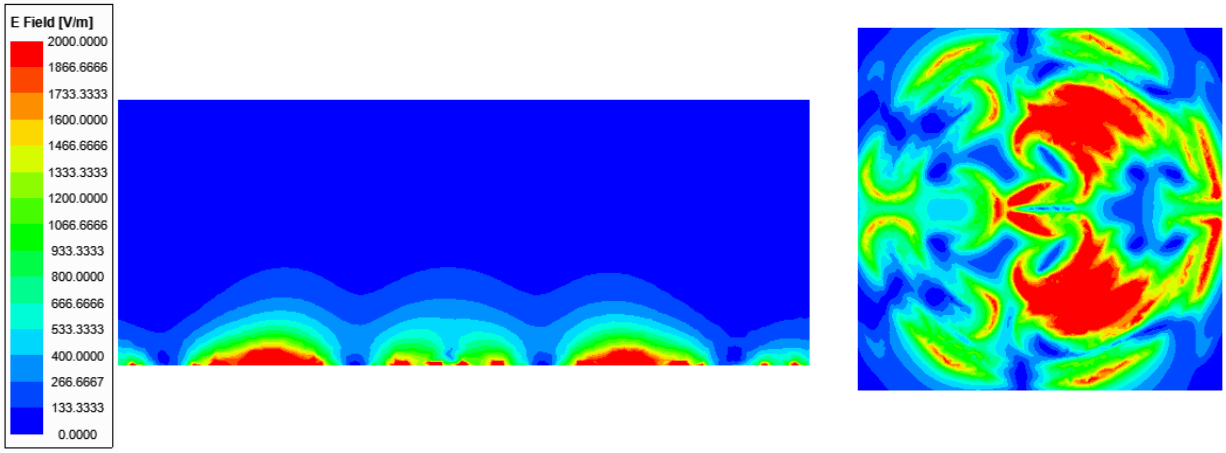

(a) (b)

Fig. 4.21. (a) Side-view and (b) top view of the field distribution for the 4th resonant modes of the resonator. It could be seen that the resonator presents strong field distribution even at higher resonant modes resulting in a significant sensitivity [71].

Data analysis for determining the volumetric concentration of each of the components will result from the solution of the following set of equations:

$$\begin{cases} V_W + V_S + V_O = 1 \\ \Delta f_{W,1} \times V_W + \Delta f_{S,1} \times V_S + \Delta f_{O,1} \times V_O = \Delta f_{y,1} \\ \Delta f_{W,4} \times V_W + \Delta f_{S,4} \times V_S + \Delta f_{O,4} \times V_O = \Delta f_{y,4} \end{cases} \quad (4\text{-}7)$$

Where V_W, V_S, and V_O are volumetric concentrations of water, brine, and oil of the sample under the test, respectively. $\Delta f_{x,1}$ and $\Delta f_{x,4}$ are the frequency shift of the sensor as the result of the introduction of the material x to the resonator (material x could be water, brine, oil, or the sample under the test at first and fourth resonant modes, respectively). The first portion of equation (4-7) is derived based on the unity of the overall volume. The permittivity's contribution in each mode's final shift is the second and third sections of equation (4-7). Because the materials' dielectric permittivity changes over the frequency spectrum, their contribution correspondingly changes for each resonant mode.

4.8.2 Results and Discussions

The experimental setup for assessing the performance of the proposed sensor is shown in Fig. 4.22. A Copper Mountain Technologies C2420 4-Port 20 GHz Vector Network Analyzer with a measurement range of 1.5GHz – 10GHz, 10001 points, and IF bandwidth of 3KHz is used to assess the sensor's transmission response as a consequence of the introduction of all the samples. To improve the overall precision of the measurements, all of the samples are made with a 10µl precision dispenser. The planar microwave resonator is built on a Rogers 5880 substrate with ε_r=2.2, tan δ=0.0009, and 0.787mm thickness. A double-sided low loss tape is used to secure a 10-milt container with $\varepsilon_r \approx 4.1$ and a wall thickness of around 0.5mm on top of the resonator, which its dielectric properties effect is included during the individual measurements. The sample volume is set so that the samples cover all the container's bottom surfaces.

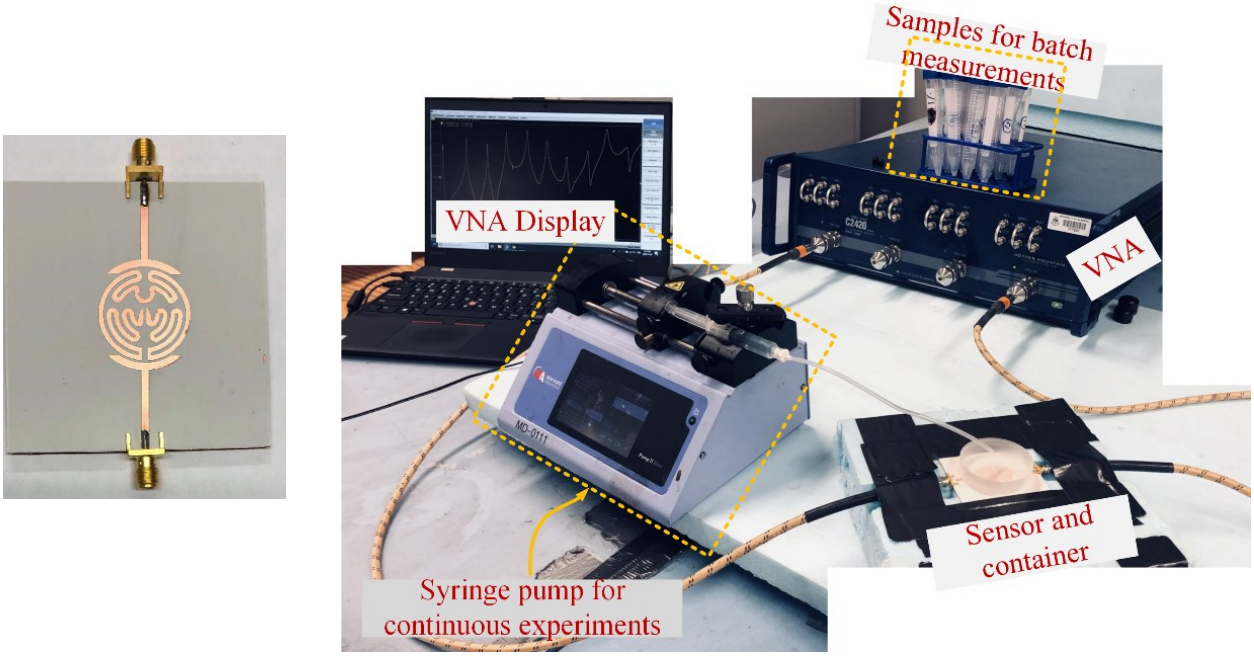

(a) (b)

Fig. 4.22. The fabricated resonator (a) and the experimental setup (b). For the illustrated setup in Fig.7(b) both setups for batch and continuous experiments are presented for the sake of being concise. The syringe pump is only used for the continuous experiment [71].

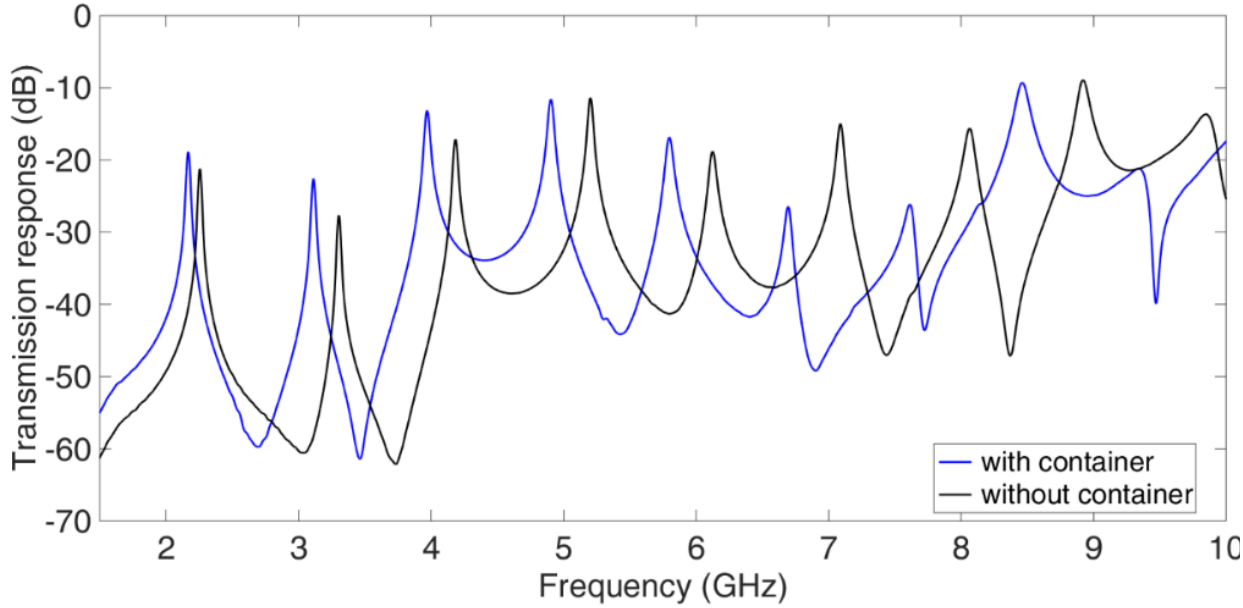

Fig. 4.23. The impact of the attachment of the container to the response of the sensor [71].

The effect of placing the container on top of the sensor is seen in Fig. 4.23. It can be observed that the inclusion of the container will cause some fluctuation in the spectrum of the microwave sensor's transmission response, which was not taken into account in the simulations. A time-based study is used to assess the stability of the measurement setup, in which the sensor's response is evaluated over time with simply an empty container on top.

The response sampling system created in LabVIEW® will detect any variations in the experimental setup as well as the lab environment, such as temperature changes, cable movements, or even very slight detachments in the adhesive layers. The stability analysis tests, which included both amplitude and frequency monitoring, are shown in Fig. 4.24. It can be observed that the frequency is fully steady throughout the test time, implying that the setup and lab environment was relatively steady during the experiments. However, there are some differences in the amplitude response. As the total amplitude change is less than 0.04dB and the VNA's amplitude measurement precision is in the range of 0.1dB, the amplitude variations might be regarded as VNA measurement mistakes.

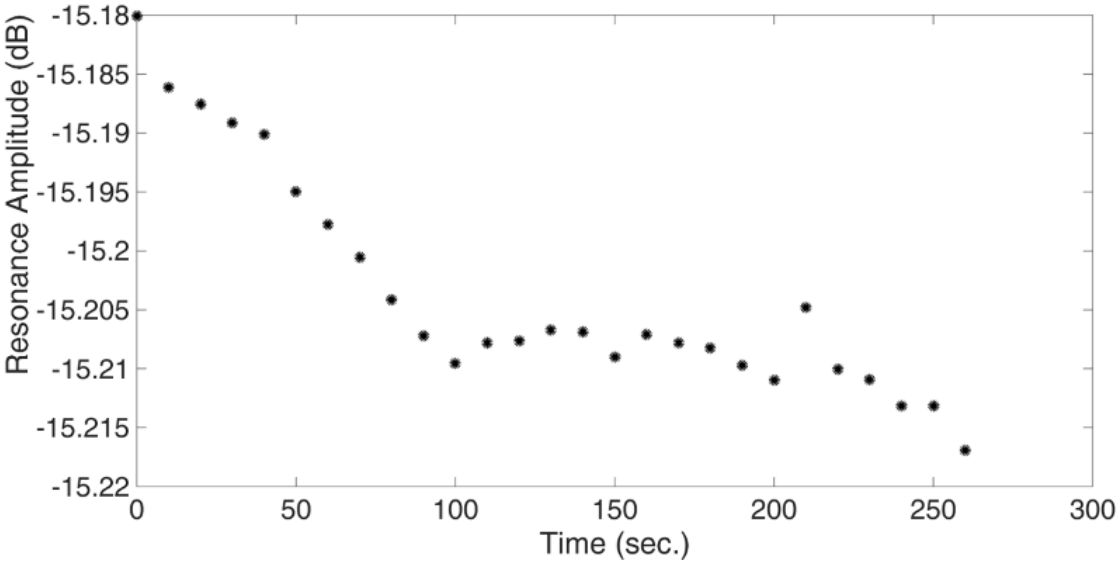

(a)

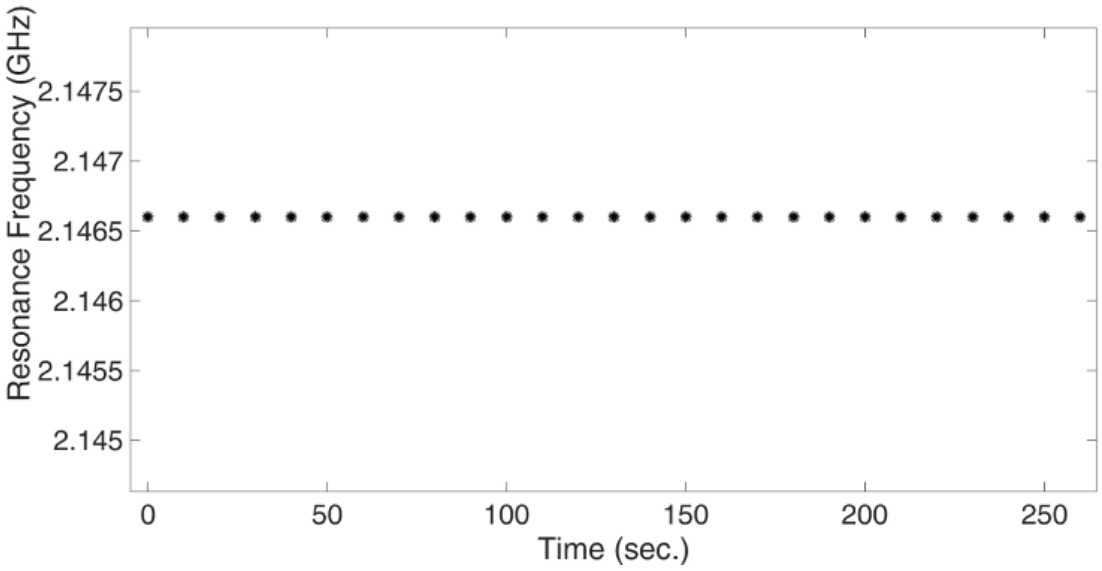

(b)

Fig. 4.24. Stability analysis of the experimental setup. (a) amplitude, (b) frequency. These results imply that both amplitude and frequency response of the setup are extremely stable [71].

Fig. 4.25 (a-c) shows a set of experimental findings demonstrating the influence of salinity fluctuation on the amplitude and frequency response of the microwave sensor. It can be shown that, in addition to the change in amplitude response, a significant frequency shift of over 20 MHz occurs with 35 (g/Kg) of salinity, which is more than double the predicted from models. This disparity between simulation and experiment results might be due to differences in simulation and experimental setups caused by unknown parameters such as the precision of the container real permittivity, $\varepsilon_r \approx 4.1$ and its unknown dielectric loss, as well as other environmental variations, or it might be due to an inaccurate calculation of the brine real permittivity in the simulation.

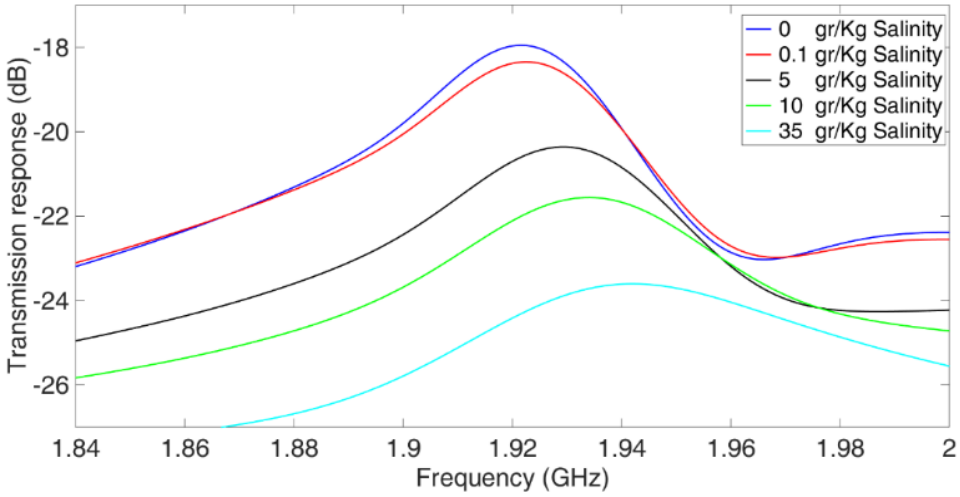

(a)

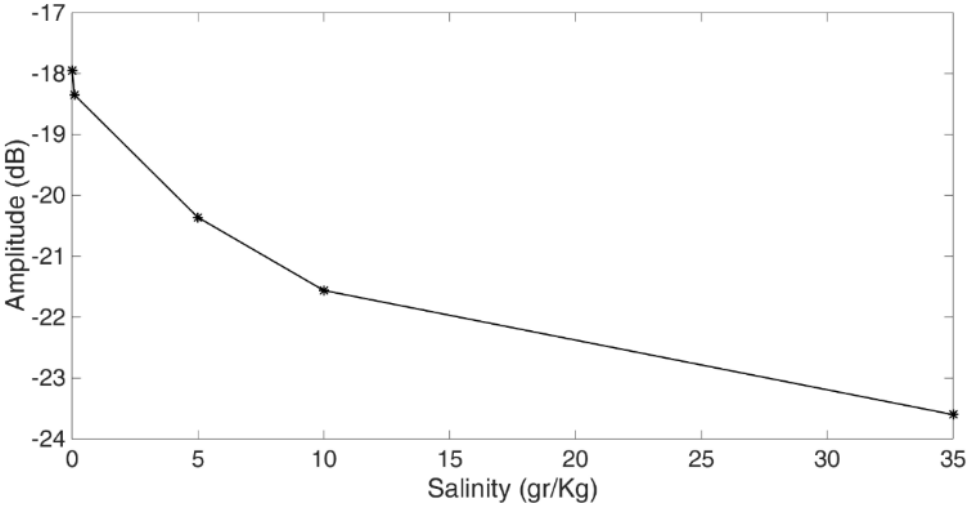

(b)

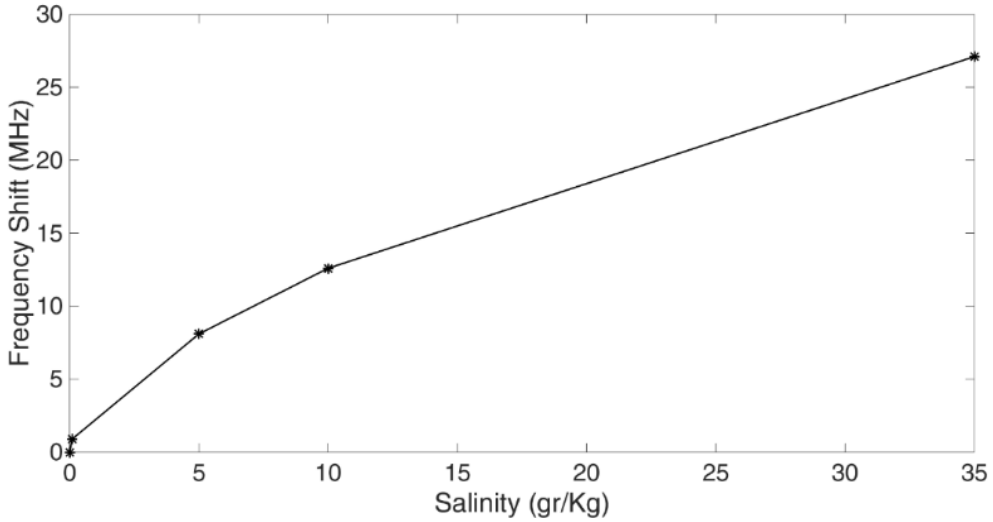

(c)

Fig. 4.25. Impact of the water salinity on sensor. (a) Transmission response between DI water and water with various levels of salinity. (b) Resonance amplitude versus the level of salinity. (c) Resonance frequency variation versus the level of salinity [71].

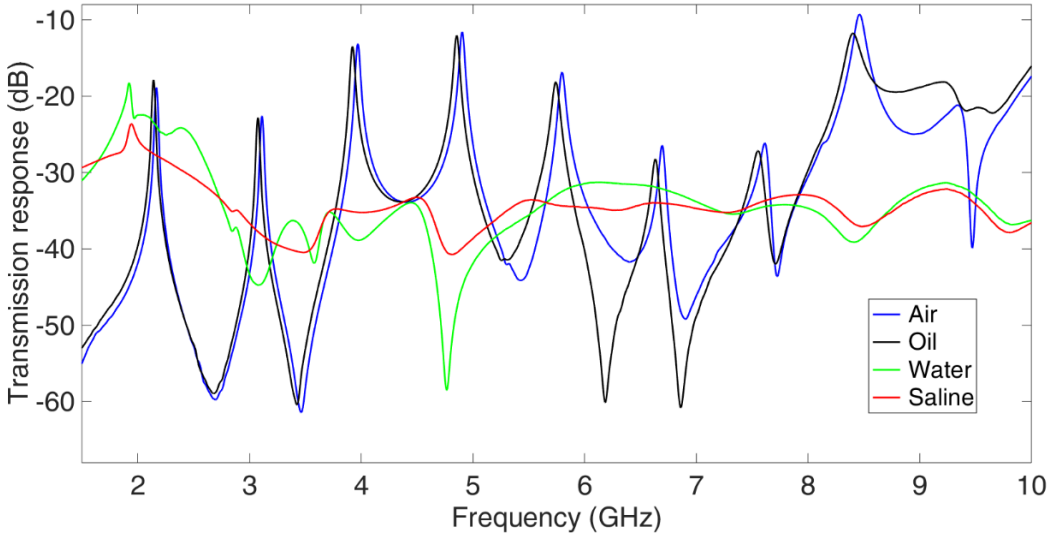

Fig. 4.26. The response of the sensor to samples with oil, water, brine (with 35 (g/Kg) of salinity), and the empty container (air) [71].

Fig. 4.26 shows the sensor's experimental transmission response with the three materials of interest within the container. It can be noticed that the sensor's response is too muted for data processing due to the substantial dielectric loss of the water and brine samples. Due to the tremendous dielectric loss of water, the overall response of the water and brine samples is not suitable for data processing, as shown. Therefore, the continued application of the sensing mechanism necessitates the use of samples with superior response in terms of measurement clarity.

Instead of pure water and brine samples, two samples from the generated mixes to test the proposed approach listed in Table 4.6 are used to achieve this purpose. Samples 10 and 12 are being evaluated for improved outcomes. These samples had 90% oil contents and 10% water and 10% salinity, respectively. Because the major purpose of this research is to evaluate the water content of oil, all of the experiments must have a minimum oil concentration of 90%. Because all of the samples are two-phase mixes, considering those two samples gives a more potent analogy with the other samples. All brine samples in the studies are water with a 35 (g/Kg) salinity, classified as a separate liquid from water. To better understand the pieces, sample number 12 has 35 g of salt, 1 millilitre of water, and 9 millilitres of oil in the 10-millilitre sample, which is said to have 10% brine and 90% brine % oil. The sensor's response to oil and samples 10 and 12 are shown in Fig. 4.27.

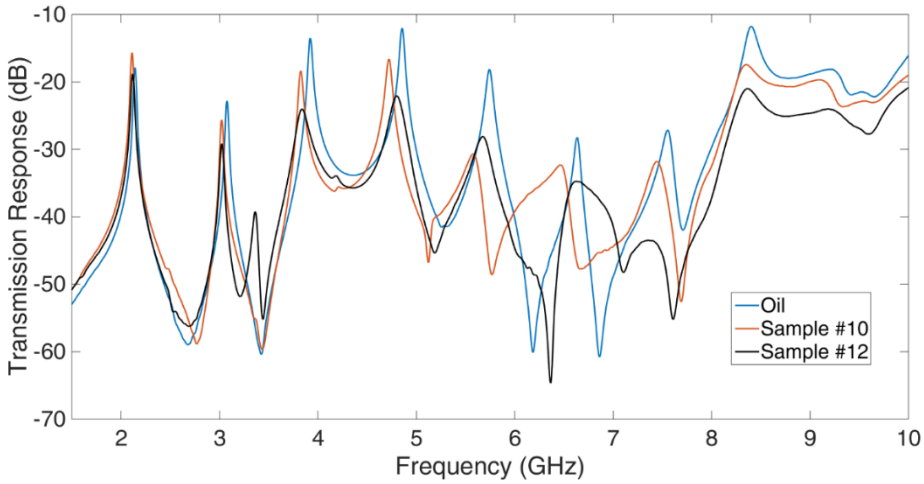

(a)

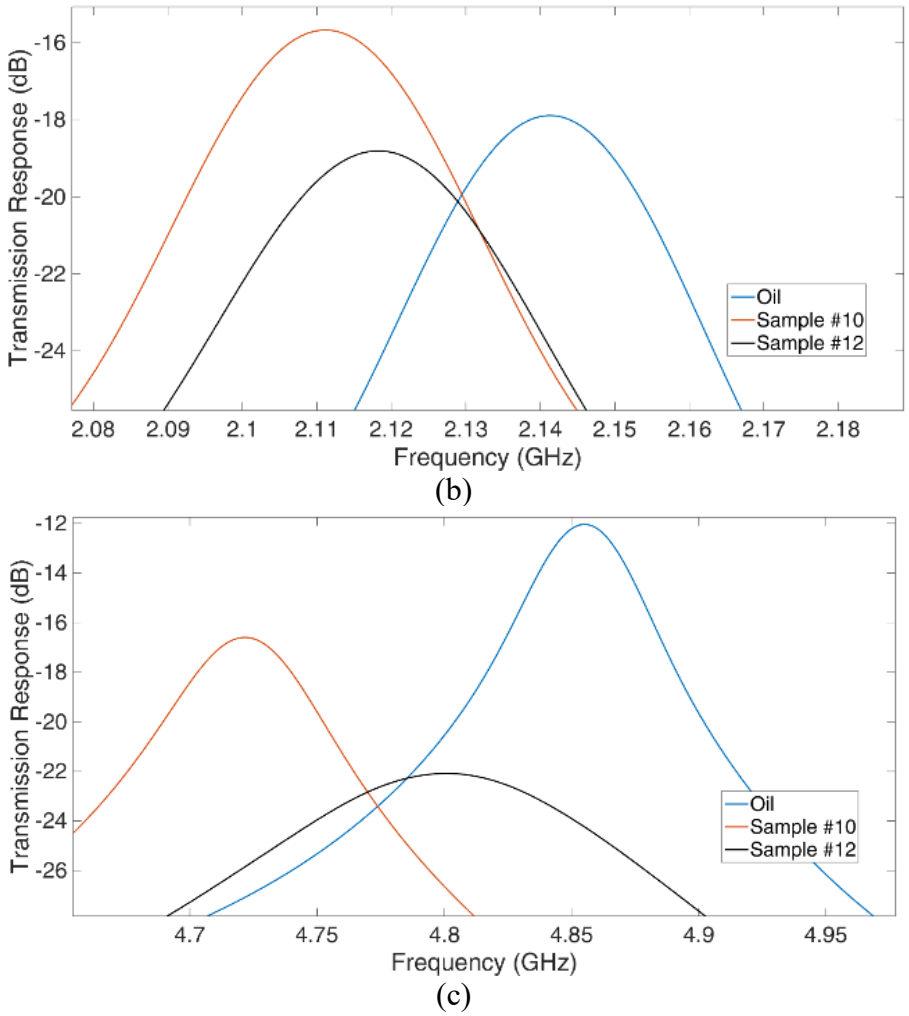

Fig. 4.27. (a) The spectrum of the sensor's response to oil, sample number 10 and sample number 12 and (b) zoomed around the 1st resonant mode, and (c) zoomed around the 4th resonant mode [71].

According to these concerns, the updated version of equation (4-7) could be rewritten as follows:

$$\begin{cases} V_{Sam10} + V_{Sam12} + V_O = 1 \\ \Delta f_{Sam10,1} \times V_{Sam10} + \Delta f_{Sam12,1} \times V_{Sam12} + \Delta f_{O,1} \times V_O = \Delta f_{y,1} \\ \Delta f_{Sam10,4} \times V_{Sam10} + \Delta f_{Sam12,4} \times V_{Sam12} + \Delta f_{O,4} \times V_O = \Delta f_{y,4} \end{cases} \quad (4\text{-}8)$$

Where $\Delta f_{Samx,i}$ is the resultant frequency shift of the i^{th} resonant mode due to the introduction of the sample number x. One additional step is necessary for this scenario to get water, oil, and 35 (g/Kg) brine concentrations. Consider the instance when each material's total volumetric

concentrations are Vsam10=0.5, Vsam12=0.2, and Voil=0.3. Because the water content of sample #10 is 10%, only 10% of the 0.5 is water (i.e. VW=0.05). The brine concentration is computed as VS=0.02, and the oil concentration is computed as VO=0.93 in the same way for Vsam12=0.2. Table 4.6 shows the results of the computations based on the stated multi-mode observations.

The measurement results show that the suggested approach can achieve low Mean Square Error (MSE) rates even in multi-phase settings. Water content has the maximum measured error of 0.87 percent, whereas 35 (g/Kg) brine has the most significant recorded error of 0.54 percent. In all the samples, Table 4.7 shows the frequency changes in both frequencies of interest.

Another series of studies are being carried out to identify the addition of brine solution with a salt content of 35 (g/Kg) in the oil samples. A syringe pump is used to inject the brine into the container, pre-filled with 7ml of oil. The injection rate is 0.5 millilitres per minute, and the experiment lasts 140 seconds. As shown in Fig. 4.28, the sensor response to permittivity change demonstrates that the sensor could be applied to detect water pollution with great precision. The fundamental drawback of this design is that it cannot operate at high water and brine concentrations. Due to their substantial dielectric losses, these materials' resonance frequencies are mostly subdued. This is not a severe concern for the current application because the approach is designed to identify modest amounts of water and brine in oil samples.

Table 4.6. Summary of the samples used for multivariable analysis and verification of the proposed approach.

Sample #	Actual Oil content (%)	Measured Oil content (%)	Actual Brine content (%)	Measured Brine content (%)	Actual Water content (%)	Measured Water content (%)	MSE (Overall)
1	99	98.53	0	0.07	1	1.39	1.26E-5
2	99	97.77	0.28	0.40	0.72	1.59	7.61E-5
3	99	98.60	1	1.40	0	0.00	1.06E-5
4	97	97.29	0	0.39	3	2.32	2.33E-5
5	97	97.71	0.85	0.74	2.15	1.55	2.92E-5
6	97	97.37	3	2.46	0	0.17	1.52E-5
7	95	95.33	0	0.10	5	4.57	1.01E-5
8	95	95.58	1.43	1.24	3.57	3.18	7.31E-5
9	95	94.63	5	4.94	0	0.43	1.08E-5
11	90	90.02	2.85	2.85	7.15	7.13	1.34E-6
10	**90**	---	**0**	---	**10**	---	Used as the data analysis samples
12	**90**	---	**10**	---	**0**	---	

Table 4.7. Frequency shifts due to introducing the samples to the sensor.

Sample number	Frequency shift at the first resonant mode (MHz)	Frequency shift at the fourth resonant mode (MHz)
1	32	64
2	34	68
3	30	59
4	37	76
5	35	70
6	34	69
7	45	98
8	43	92
9	43	90
10	**69**	**155**
11	65	145
12	**58**	**124**
Oil	**26**	**49**

4.9 Conclusion

Miniaturized planar microwave resonator for extended average field distributions with a good performance in reasonable Q and enhanced sensitivity is reported. The otherwise footprint size of the conventional SRR of radius 0.084λg is folded over several times to form long capacitive and inductive contributions, increasing the field distributions to form E-field expanded across at least 90% of the entire resonator's surface. This is done to improve the sensitivity (by increasing field penetration to the sample), adaptable for smaller sample volume due to the extended average E-field and reduce the physical (while sustaining the electrical) size to about 55%. The performance of the sensor is analyzed based on sample location and sample size. It is also adapted for liquid application and characterized for moisture sensors.

For multi-phase multivariable liquid mixture analysis, the same miniaturized split ring resonator has been redesigned and tested. While the liquids are not emulsified and in a two-phase state, the provided sensor can concurrently identify water concentration and its amount of saltiness in oil. The fundamental idea behind this study was based on the change of real permittivity of different materials over the frequency spectrum and real permittivity sampling by measuring the frequency shift of the primary resonance and its higher modes. This method uses two resonant modes of a split ring resonator for data processing, and high accuracy results are obtained. The findings open the path for the commercialization of microwave resonator-based sensors, allowing them to overcome their selectivity issue.

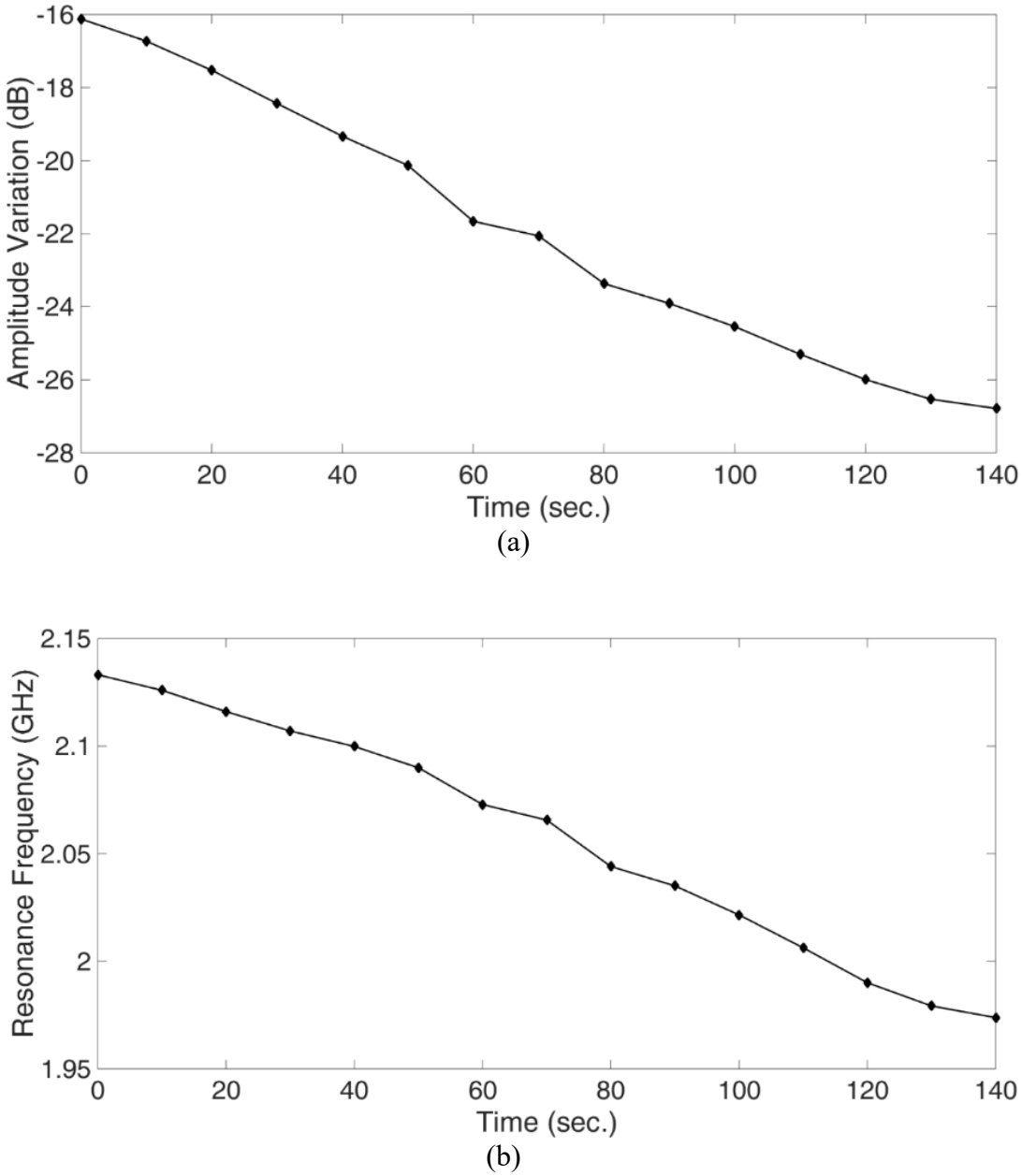

Fig. 4.28. Continuous analysis of the response of the (a) amplitude, and (b) frequency, of the sensor [71].

4.10 References

[1] M. H. Zarifi, M. Rahimi, M. Daneshmand, T. Thundat, 2016. Microwave ring resonator-based non-contact interface sensor for oil sands applications, Sensors and Actuators B: Chemical, vol 224, pp 632-639, https://doi.org/10.1016/j.snb.2015.10.061

[2] M. Schüßeler, C. Mandel, M. Puentes, and R.Jakoby, 2012. Metamaterial inspired microwave sensors, IEEE Microw. Mag., vol. 13, no. 2, pp. 57–68, https://doi.org/ 10.1109/MMM.2011.2181448

[3] H.-J. Lee, and J.-G. Yook, 2008. Biosensing using split-ring resonators at microwave regime, Appl. Phys. Lett, vol. 92, no. 25, pp. 4103, https://doi.org/10.1063/1.2946656

[4] R. Joffe, E. O. Kamenetskii, and R. Shavit, 2013. Novel microwave nearfield sensors for material characterization, biology, and nanotechnology, J. Appl. Phys., vol. 113, no. 6, pp. 63912, https://doi.org/10.1063/1.4791713

[5] M. H. Zarifi, M. Daneshmand, 2016. Liquid sensing in aquatic environment using high quality planar microwave resonator, Sensors and Actuators B: Chemical, vol. 225, pp. 517-521, https://doi.org/10.1016/j.snb.2015.11.063

[6] M. H. Zarifi, P. Shariaty, Zaher Hashisho, Mojgan Daneshmand, 2017. A non-contact microwave sensor for monitoring the interaction of zeolite 13X with CO2 and CH4 in gaseous streams, Sensors and Actuators B: Chemical, vol. 238, pp. 1240-1247, https://doi.org/10.1016/j.snb.2016.09.047

[7] M. H. Zarifi and M. Daneshmand, 2016. Wide dynamic range microwave planar coupled ring resonator for sensing applications, Appl. Phys. Lett. 108, 232906, https://doi.org/10.1063/1.4953465

[8] A. K, Jha, N, Delmonte, A, Lamecki, M, Mrozowski, M, Bozzi, 2019. Design of microwave-based angular displacement sensor, IEEE Microw. Wireless Compon. Lett., vol. 29, no4, pp. 306-308. https://doi.org/ 10.1109/LMWC.2019.2899490

[9] J. Naqui and F. Martín, 2013. Transmission lines loaded with bisymmetric resonators and their application to angular displacement and velocity sensors, IEEE Trans. Microw. Theory Techn., vol. 61, no. 12, pp. 4700–4713. https://doi.org/ 10.1109/TMTT.2013.2285356

[10] J. Naqui, J. Coromina, A. Karami-Horestani, C. Fumeaux, and F. Martín, 2015. Angular displacement and velocity sensors based on coplanar waveguides (CPWs) loaded with S-shaped split ring resonator (S-SRR), Sensors, vol. 15, pp. 9628–9650. https://doi.org/ 10.3390/s150509628.

[11] A.K. Horestani, C. Fumeaux, S.F. Al-Sarawi, and D. Abbott, 2013. Displacement sensor based on diamond-shaped tapered split ring resonator, IEEE Sens. J., vol. 13, pp. 1153–1160. https://doi.org/ 10.1109/JSEN.2012.2231065

[12] J. Naqui and F. Martín, 2014. Angular displacement and velocity sensors based on electric-LC (ELC) loaded microstrip lines," IEEE Sensors J., vol. 14, no. 4, pp. 939–940. https://doi.org/ 10.1109/JSEN.2013.2295518

[13] A.K. Horestani, D. Abbott, and C. Fumeaux, 2013. Rotation sensor based on horn-shaped split ring resonator," IEEE Sens. J., vol. 13, pp. 3014–3015. https://doi.org/ 10.1109/JSEN.2013.2264804

[14] A. K. Horestani, J. Naqui, Z. Shaterian, D. Abbott, C. Fumeaux, and F. Martín 2014. Two-dimensional alignment and displacement sensor based on movable broadside-coupled split

ring resonators, Sensors and Actuators A, vol. 210, pp. 18–24. https://doi.org/ 10.1016/j.sna.2014.01.030

[15] A.K. Horestani, J. Naqui, D. Abbott, C. Fumeaux, and F. Martín, 2014. Two-dimensional displacement and alignment sensor based on reflection coefficients of open microstrip lines loaded with split ring resonators," Elec. Lett., vol. 50, pp. 620–622. https://doi.org/ 10.1049/el.2014.0572

[16] P. Vélez, J. Muñoz-Enano, M. Gil, J. Mata-Contreras, and F. Martín, 2019. Differential microfluidic sensors based on dumbbell-shaped defect ground structures in microstrip technology: analysis, optimization, and applications", Sensors, vol. 19, pp. 3189. https://doi.org/ 10.3390/s19143189

[17] A. Ebrahimi, J. Scott and K. Ghorbani, 2018. Differential sensors using microstrip lines loaded with two split ring resonators," IEEE Sensors J., vol. 18, pp. 5786-5793. https://doi.org/ 10.1109/JSEN.2018.2840691

[18] A. Ebrahimi, J. Scott, K. Ghorbani, 2018. Transmission Lines Terminated with LC Resonators for Differential Permittivity Sensing, IEEE Microw. Wireless Compon. Lett., vol. 28, no. 12, pp. 1149-1151. https://doi.org/ 10.1109/LMWC.2018.2875996

[19] P. Vélez, J. Muñoz-Enano, K. Grenier, J. Mata-Contreras, D. Dubuc, F. Martín, 2019. Split ring resonator (SRR) based microwave fluidic sensor for electrolyte concentration measurements, IEEE Sensors J., vol. 19, no. 7, pp. 2562-2569. https://doi.org/ 10.1109/JSEN.2018.2890089

[20] P. Vélez, K. Grenier, J. Mata-Contreras, D. Dubuc and F. Martín, 2018. Highly-Sensitive Microwave Sensors Based on Open Complementary Split Ring Resonators (OCSRRs) for Dielectric Characterization and Solute Concentration Measurement in Liquids, IEEE Access, vol. 6, pp. 48324-48338. https://doi.org/10.1109/ACCESS.2018.2867077

[21] C.-S. Lee and C.-L. Yang, 2014. Complementary split-ring resonators for measuring dielectric constants and loss tangents, IEEE Microw. Wireless Compon. Lett., vol. 24, no. 8, pp. 563−565. https://doi.org/ 10.1109/LMWC.2014.2318900

[22] A. Ebrahimi, W. Withayachumnankul, S. Al-Sarawi, D. Abbott, 2014. High-sensitivity metamaterial-inspired sensor for microfluidic dielectric characterization, IEEE Sensors J., vol. 14, no. 5, pp. 1345−1351. https://doi.org/10.1109/JSEN.2013.2295312

[23] C.-L. Yang, C.-S. Lee, K.-W. Chen, and K.-Z. Chen, 2016. Noncontact measurement of complex permittivity and thickness by using planar resonators, IEEE Trans. Microw. Theory Techn., vol. 64, no.1, pp. 247−257. https://doi.org/ 10.1109/TMTT.2015.2503764

[24] L. Su, J. Mata-Contreras, P. Vélez, A. Fernández-Prieto and F. Martín, 2018. Analytical method to estimate the complex permittivity of oil Samples, Sensors, vol.18no. 4, pp. 984. https://doi.org/10.3390/s18040984

[25] M. S. Boybay and O. M. Ramahi, 2012. Material characterization using complementary split-ring resonators, IEEE Trans. Instrum. Meas., vol. 61, no. 11, pp. 3039−3046. https://doi.org/ 10.1109/TIM.2012.2203450

[26] P. Vélez, L. Su, K. Grenier, J. Mata-Contreras, D. Dubuc, and F. Martín, 2017. Microwave microfluidic sensor based on a microstrip splitter/combiner configuration and split ring resonators (SRR) for dielectric characterization of liquids, IEEE Sensors J., vol. 17, pp. 6589-6598. https://doi.org/10.1109/JSEN.2017.2747764

[27] J. B. Pendry, A. J. Holden, D. J. Robbins, and W. J. Stewart, 1999. Magnetism from conductors and enhanced nonlinear phenomena, IEEE Trans. Microwave Theory Tech., vol. 47, pp. 2075-2084, https://doi.org/ 10.1109/22.798002

[28] P. Gay-Balmaz and O.J.F. Martin, 2002. Electromagnetic resonances in individual and coupled split-ring resonators, J. Appl. Phys., vol. 92, pp. 2929-2936, https://doi.org/10.1063/1.1497452

[29] M. Abdolrazzaghi, M. H. Zarifi, and M. Daneshmand, 2016. Sensitivity enhancement of split ring resonator based liquid sensors," 2016 IEEE SENSORS, Orlando, FL, pp. 1-3. https://doi.org/ 0.1109/ICSENS.2016.7808957

[30] M. H. Zarifi, A. Gholidoust, M. Abdolrazzaghi, P. Shariaty, Z. Hashisho, M. Daneshmand, 2018. Sensitivity enhancement in planar microwave active-resonator using metal organic framework for CO2 detection, Sensors and Actuators B: Chemical, vol. 255, no. 2, pp. 1561-1568, https://doi.org/10.1016/j.snb.2017.08.169

[31] M. H. Zarifi, P. Shariaty, M. Abdolrazzaghi, Z. Hashisho, M. Daneshmand, 2016. Particle size characterization using a high-resolution planar resonator sensor in a lossy medium, Sensors and Actuators B: Chemical, vol. 234, pp. 332-337, https://doi.org/10.1016/j.snb.2016.04.130

[32] M. Abdolrazzaghi, M. Daneshmand and A. K. Iyer, 2018. Strongly Enhanced Sensitivity in Planar Microwave Sensors Based on Metamaterial Coupling, in IEEE Trans. Microwave Theory Tech., vol. 66, no. 4, pp. 1843-1855, https://doi.org/ 10.1109/TMTT.2018.2791942

[33] M. Nosrati and M. Daneshmand, 2017. Substrate Integrated Waveguide L-Shaped Iris for Realization of Transmission Zero and Evanescent-Mode Pole, in IEEE Trans. Microwave Theory Tech., vol. 65, no. 7, pp. 2310-2320. https://doi.org/10.1109/TMTT.2017.2679011.

[34] M. H. Zarifi et al., 2018. A Microwave Ring Resonator Sensor for Early Detection of Breaches in Pipeline Coatings, IEEE Transactions on Industrial Electronics, vol. 65, no. 2, pp. 1626-1635. https://doi.org/10.1109/TIE.2017.2733449

[35] M. H. Zarifi, S. Deif, M. Daneshmand, 2017. Wireless passive RFID sensor for pipeline integrity monitoring, Sensors and Actuators A: Physical, vol. 261, pp.24-29. https://doi.org/10.1016/j.sna.2017.04.006.

[36] S. Deif, B. Leier, M. Snow, M. Daneshmand, 2018. Microwave Sensor Array for Corrosion Prediction in Steel Tank Bottoms, 2018 12th International Pipeline Conference, American Soc. of Mechanical Engineer, pp.1-6, https://doi.org/10.1115/IPC2018-78224

[37] N. Hosseini, M. Baghelani and M. Daneshmand, 2019. "Discrete Microwave Spectroscopy using Planar Resonator," IEEE Canadian Conference of Electrical and Computer Engineering (CCECE), Edmonton, AB, Canada, 2019, pp. 1-4. doi: 10.1109/CCECE.2019.8861771

[38] R. A. Alahnomi, Z. Zakaria, E. Ruslan, S. R. Ab Rashid and A. A. Mohd Bahar, 2017. High-Q Sensor Based on Symmetrical Split Ring Resonator with Spurlines for Solids Material Detection," in IEEE Sensors Journal, vol. 17, no. 9, pp. 2766-2775. https://doi.org/10.1109/JSEN.2017.2682266

[39] G. Galindo-Romera, F. Javier Herraiz-Martínez, M. Gil, J. J. Martínez-Martínez and D. Segovia-Vargas, 2016. Submersible Printed Split-Ring Resonator-Based Sensor for Thin-Film Detection and Permittivity Characterization, in IEEE Sensors Journal, vol. 16, no. 10, pp.3587-3596. https://doi.org/10.1109/JSEN.2016.2538086.

[40] V. Sekar, W. J. Torke, S. Palermo and K. Entesari, 2012. A Self-Sustained Microwave System for Dielectric-Constant Measurement of Lossy Organic Liquids, *IEEE Transactions on Microwave Theory and Techniques*, vol. 60, no. 5, pp. 1444-1455.**https://doi.org/**doi: 10.1109/TMTT.2012.2187066

[41] N. Wiwatcharagoses, K. Y. Park, J. A. Hejase, L. Williamson, and P. Chahal, 2011. Microwave artificially structured periodic media microfluidic sensor," in Proc. IEEE 61st Electron. Compon. Technol. Conf. (ECTC), pp. 1889–1893. **https://doi.org/**doi: 10.1109/ECTC.2011.5898773

[42] R. A. Alahnomi, Z. Zakaria, E. Ruslan, A. A. Mohd Bahar, and S. R. Ab Rashid, 2016. High sensitive microwave sensor based on symmetrical split ring resonator for material characterization. Microw. Opt. Technol. Lett., vol. 58, pp. 2106-2110. https://doi.org/10.1002/mop.29979.

[43] C. Liu and Y. Pu, 2008. A microstrip resonator with slotted ground plane for complex permittivity measurements of liquids, IEEE Microw. Wireless Compon. Lett., vol. 18, no. 4, pp. 257–259. **https://doi.org/**doi: 10.1109/LMWC.2008.918894

[44] E. Dykesteen, "Handbook of Multiphase Metering," *Nor. Soc. Oil Gas Meas. NFOGM, Revis.*, vol. 2, 2005.

[45] Z. Aghaeifar, S. Strand, T. Puntervold, T. Austad, and F. M. Sajjad, "Smart Water injection strategies for optimized EOR in a high temperature offshore oil reservoir," *J. Pet. Sci. Eng.*, vol. 165, pp. 743–751, 2018.

[46] A. Fakhru'l-Razi, A. Pendashteh, L. C. Abdullah, D. R. A. Biak, S. S. Madaeni, and Z. Z. Abidin, "Review of technologies for oil and gas produced water treatment," *J. Hazard. Mater.*, vol. 170, no. 2–3, pp. 530–551, 2009.

[47] S. K. Panda, M. A. Mohammed, A. Cadix, M. Alaboalirat, C. Poix-Davaine, and E. Duran, "Size exclusion chromatography reveals a key parameter of demulsifiers for enhanced water separation from crude oil emulsions," *Fuel*, vol. 257, p. 115881, 2019.

[48] A. G. Ryder, "Assessing the maturity of crude petroleum oils using total synchronous fluorescence scan spectra," *J. Fluoresc.*, vol. 14, no. 1, pp. 99–104, 2004.

[49] P. Rostami, M. F. Mehraban, M. Sharifi, M. Dejam, and S. Ayatollahi, "Effect of water salinity on oil/brine interfacial behaviour during low salinity waterflooding: A mechanistic study," *Petroleum*, vol. 5, no. 4, pp. 367–374, 2019.

[50] T. E. Chávez-Miyauchi, A. Firoozabadi, and G. G. Fuller, "Nonmonotonic elasticity of the crude oil–brine interface in relation to improved oil recovery," *Langmuir*, vol. 32, no. 9, pp. 2192–2198, 2016.

[51] Y. Guoxiang, L. Ü. Xiaoping, P. Fei, H. Pingfang, and S. Xuan, "Pretreatment of crude oil by ultrasonic-electric united desalting and dewatering," *Chinese J. Chem. Eng.*, vol. 16, no. 4, pp. 564–569, 2008.

[52] H. Moghadas, M. Daneshmand, and P. Mousavi, "A passive non-contact microwave loop resonance sensor for liquid interface," *Sensors Actuators B Chem.*, vol. 241, pp. 96–98, 2017.

[53] S. Winecki *et al.*, "Improved oil recovery sensor," *Sensors Actuators A Phys.*, vol. 295, pp. 308–316, 2019.

[54] P. Sharma, L. Lao, and G. Falcone, "A microwave cavity resonator sensor for water-in-oil measurements," *Sensors Actuators B Chem.*, vol. 262, pp. 200–210, 2018.

[55] S. I. M. Sheikh, E. E. M. Hassan, and S. Iqbal, “Capacitance Based Monitoring of a Three-phase Crude-Oil Flow,” *IEEE Trans. Instrum. Meas.*, 2019.

[56] Q. Liu, B. Chu, J. Peng, and S. Tang, “A Visual Measurement of Water Content of Crude Oil Based on Image Grayscale Accumulated Value Difference,” *Sensors*, vol. 19, no. 13, p. 2963, 2019.

[57] M. Baghelani, Z. Abbasi, and M. Daneshmand, “Noncontact high sensitivity chipless tag microwave resonator for bitumen concentration measurement at high temperatures,” *Fuel*, vol. 265, p. 116916, 2020.

[58] M. Abdolrazzaghi, and Daneshmand, M.," A phase-Noise reduced microwave oscillator sensor with enhanced limit of detection using active filter," IEEE Microwave and Wireless Components Letters, 28(9), pp.837-839, 2018.

[59] S. Kiani, P. Rezaei, and M. Navaei. "Dual-sensing and dual-frequency microwave SRR sensor for liquid samples permittivity detection." Measurement (2020): 107805.

[60] Z. Abbasi, M. Baghelani, M. Nosrati, A. Sanati-Nezhad, and M. Daneshmand, “Real-Time Non-Contact Integrated Chipless RF Sensor for Disposable Microfluidic Applications,” *IEEE J. Electromagn. RF Microwaves Med. Biol.*, 2019.

[61] M. Nosrati, Z. Abbasi, M. Baghelani, S. Bhadra, and M. Daneshmand, “Locally Strong-Coupled Microwave Resonator Using PEMC Boundary for Distant Sensing Applications,” *IEEE Trans. Microw. Theory Tech.*, vol. 67, no. 10, pp. 4130–4139, 2019.

[62] M. Abdolrazzaghi, and M. Daneshmand," Dual active resonator for dispersion coefficient measurement of asphaltene nano-particles," IEEE Sensors Journal, 17(22), pp.7248-7256, 2017.

[63] T.-G. Kang, J.-K. Park, B.-H. Kim, J. J. Lee, H. H. Choi, H.-J. Lee, and J.-G. Yook. "Microwave characterization of conducting polymer PEDOT: PSS film using a microstrip line for humidity sensor application." Measurement 137 (2019): 272-277.

[64] N. Hosseini, M. Baghelani, and M. Daneshmand, “Discrete Microwave Spectroscopy using Planar Resonator,” in *2019 IEEE Canadian Conference of Electrical and Computer Engineering (CCECE)*, 2019, pp. 1–4.

[65] N. Hosseini, M. Baghelani, and M. Daneshmand," Selective Volume Fraction Sensing Using Resonant-Based Microwave Sensor and Its Harmonics," IEEE Trans. Microw. Theory Tech., May 2020, DOI: 10.1109/TMTT.2020.2990139

[66] M. A. Karimi, M. Arsalan, and A. Shamim, “Low cost and pipe conformable microwave-based water-cut sensor,” *IEEE Sens. J.*, vol. 16, no. 21, pp. 7636–7645, 2016.

[67] G. Andria, F. Attivissimo, A. Di Nisio, A. Trotta, S. M. Camporeale, and P. Pappalardi. "Design of a microwave sensor for measurement of water in fuel contamination." Measurement 136 (2019): 74-81.

[68] P. S. Mun, H. N. Ting, Y. B. Chong, and T. A. Ong, “Dielectric properties of glycosuria at 0.2-50 GHz using microwave spectroscopy,” *J. Electromagn. Waves Appl.*, vol. 29, no. 17, pp. 2278–2292, 2015.

[69] L. M. Middelburg *et al.*, “Multi-domain spectroscopy for composition measurement of water-containing bio-ethanol fuel,” *Fuel Process. Technol.*, vol. 167, pp. 127–135, 2017.

[70] W. J. Ellison *et al.*, “A comparison of ocean emissivity models using the Advanced Microwave Sounding Unit, the Special Sensor Microwave Imager, the TRMM Microwave

Imager, and airborne radiometer observations," *J. Geophys. Res. Atmos.*, vol. 108, no. D21, 2003.

[71] M. Baghelani, N. Hosseini, M. Daneshmand, "Non-contact real-time water and brine concentration monitoring in crude oil based on multi-variable analysis of microwave resonators," Measurement. 2021 Jun 1;177:109286.

[72] N. Hosseini, SS. Olokede, M. Daneshmand, "A novel miniaturized asymmetric CPW split ring resonator with extended field distribution pattern for sensing applications," Sensors and Actuators A: Physical. 2020 Apr 1;304:111769.

Chapter 5 Selective Non-Contact Alcohol Concentration Measurement during Fermentation Process using Microwave Split-Ring Resonator Based Sensor

Real-time fermentation process monitoring is crucial in process control attaining high-quality products in many food industries. Although microwave resonators offer non-contact, high sensitivity, real-time sensing capabilities at meagre cost with reusable structures, the lack of selectivity, even in controlled environments, limits their applications to single variable systems or binary sensing. Since fermentation is a more complex process with at least three variables that could change simultaneously, the traditional microwave sensing techniques fail to measure each component's volumetric fraction. This chapter presents a novel approach enabling microwave resonators to perform volumetric fraction analysis of complex dynamically varying liquids while keeping all the aforementioned interesting characteristics for microwave resonator-based sensors. Multiple simulation and experimental results verify the capabilities of the proposed technique in real-time monitoring of ethanol, water, and sugar concentrations during the fermentation process.

5.1 Introduction

Alcoholic fermentation is an anaerobic process of converting different types of sugar into ethanol. The fermentation process has many applications expanded from food and beverage industries to biofuels [1], [2]. Due to the importance of the fermentation process monitoring the quality of the final product and the speed of the process determining the overall cost, there is an increasing demand for real-time fermentation monitoring methods [3], [4]. Primarily, it is crucial if the monitoring system is capable of instantaneous real-time measurement without causing any interruption in the fermentation process and setup. As the significant product of the fermentation process, ethanol monitoring is the most critical parameter followed by the concentration of sugar in the final product.

According to the importance of monitoring the fermentation process, several methods have been presented in literature based on various technologies. Those techniques are expanded from measuring the CO2 production [5], density monitoring [6] to using advanced laboratory-based techniques such as Fourier Transform-Infra Red spectroscopy (FTIR) [7] and gas chromatography [8]. Although some of the mentioned methods, especially the laboratory-based techniques, could be very accurate, they require a significant amount of time to analyze the samples and are not real-time monitoring. Therefore, those methods fail to provide real-time data as sensing signal feedback to the fermentation process control. Fiber optic-based techniques are also developed and presented as real-time monitoring systems, but they are expensive and require a highly complex data analysis process [9]. Researchers also focused on biosensors as alternative candidates for real-time monitoring purposes, but they are suffering from fouling problems due to the prolonged process of fermentation [10].

Due to their high sensitivity, moderate to high-quality factor, being inherently non-invasive and non-intrusive, and their capability of real-time sensing, microwave planar resonators have been used for various sensing applications expanded from oil and gas [11]–[14], to biomedical sensing [11]–[20]. Their extremely low-cost, simple fabrication process, extremely high durability without saturation make them exciting candidates for many more sensing applications [21]–[28]. Their high sensitivity enables their utilization in high-precision applications with real-time demand. The fundamental feature behind this technology is the variation of their resonance frequency due to changes in the dielectric constant. Although having all the mentioned remarkable characteristics, this technology suffers from the lack of enough features addressing the selectivity of the sensors or the feasibility of their usage in multivariable environments. With the shift as their only independent feature, microwave resonator-based sensors are only capable of operating in binary sensing or as single variable sensors in highly controlled environments [17], [18], [29]–[31].

This chapter presents a method based on microwave resonator sensors for multivariable real-time non-invasive measurement of ethanol, water, and sugar during the fermentation process by introducing new features to these sensors. The presented method for alcohol, water, and sugar analysis is based on the uniqueness of the dielectric constant of different materials and their

nonlinear behaviour over the frequency spectrum. Therefore, a spectrum sampling using higher resonant modes of a split-ring microwave resonator is accomplished, providing the new independent features adequate for multivariable analysis of the mentioned materials during the fermentation process.

The chapter is organized as follows; after an introduction in section 5.1, materials and methods, including the sensor theory and design, fundamentals of multivariable analysis using the sensor and modelling and simulation are given in section 5.2. Experimental setup and numerous experiments verifying our approach and data analysis are given in section 5.3, followed by a conclusion in section 5.4.

5.2 Materials and Methods

5.2.1 Microwave Resonator Design

A planar split-ring resonator (SRR) is designed and fabricated with high sensitivity to detect the permittivity changes of the surrounding materials. The total size of the device is 6×10 cm^2 fabricated on Rogers substrate. Using the laminator machine, the layout of the circuit is printed on the substrate. The substrate is then immersed in ammonium persulfate from MG Chemicals Inc. and water solution, acting as an etching bath, for about 45 minutes. As a copper etchant, ammonium persulfate is a highly soluble salt in water, and its etching capability is boosted by applying the heat and turbulence produced by a bubble maker simultaneously into the solution. During the etching process, because of the high ratio of the line width (~1.9mm) to the copper thickness (~35μm), the masked area of the copper is not etched. As seen from the trapezoidal schematic of the proposed resonator, the fabricated structure is matched to a 50-ohm microstrip transmission line with a 1.91 mm width. It creates a bandstop filter through side coupling to the high impedance section of the line. The notches on transmission coefficient are taking place for different SRR resonant modes, f_{even} and f_{odd}, which can be expressed as follows [32]:

$$f_{even} = \frac{n \cdot c}{L\sqrt{\varepsilon_{eff}}}, \qquad f_{odd} = \frac{(2n-1) \cdot c}{2L\sqrt{\varepsilon_{eff}}} \tag{5-1}$$

where L denotes the length of the SRR, and ε_{eff} presents the effective permittivity of the resonator's ambient. The U-shape complementary SRR is defined and coupled to the gaping area of the trapezoidal SRR to enhance the E-field coupling for the higher resonant modes and better Q-factor as a result. Sensor miniaturization, getting higher sensitivity through boosting electric field profile on the sample, and better-quality factor are the main parameters of the design. The miniaturization technique is realized by extending the SRR edges, which carry the maximum E-field intensity, as were shown in Fig. 5.1b. Also, the complimentary small SRR shown in Fig. 5.1c provides higher effective capacitance between the larger SRR edges and more miniaturization. The detailed response of the sensor for each step design was explained in Fig. 5.1. We have started with a traditional SRR structure with a split part. The simulation is performed through variation of the dielectric permittivity of the material inside the container from 1 (unloaded response) to an arbitrary material with ϵ_r=10. It could be seen in Fig. 5.1 that (in a step-by-step fashion), the additional lines and structures improved the overall sensitivity of the resonator by 100%.

(a) Classic SRR

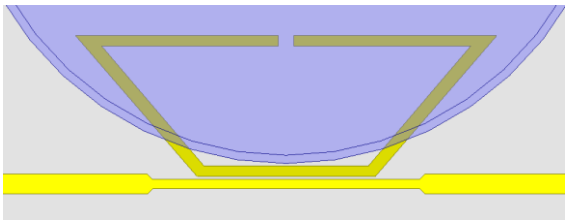

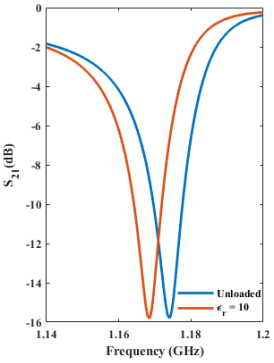

$\Delta f = 8\ MHz$

(b) Miniaturized SRR

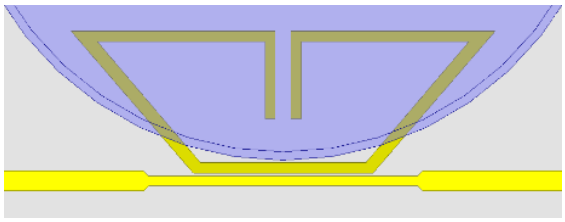

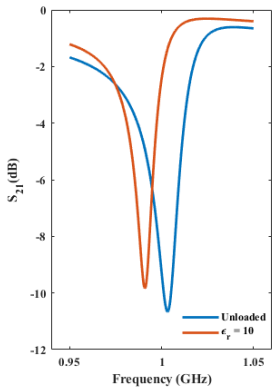

$\Delta f = 12\ MHz$

(c) Final Prototype

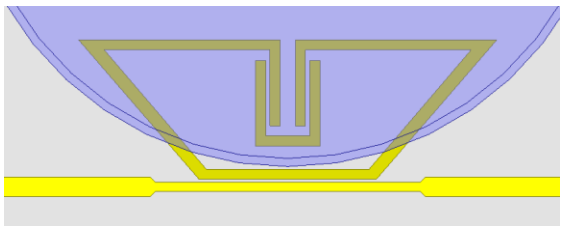

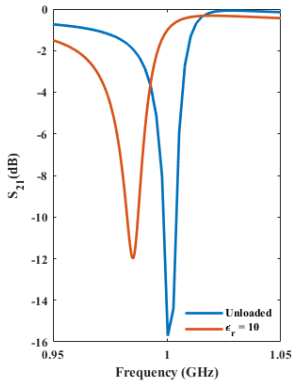

$\Delta f = 16\ MHz$

Fig. 5.1. The step-by-step design responses for the sample with ε_r=10 covering the top plane of the device. It could be seen that the impact of the complementary part improved the sensitivity of the structure by 100% [44].

The operating frequency can be changed and controlled by altering the length of the SRR. The proposed structure is etched on a dielectric substrate Rogers RO3003 with a relative permittivity of 3, loss tangent tanδ = 0.0013, and lamination thickness of 760 um which is designed for giving the first operational frequency at 1GHz with following values of geometrical parameters: L_1 = 41 mm, L_2 = 17.4 mm, L_3 = 18 mm, LS_1 = 8.4 mm, LS_2 = 6.3 mm, W_1 = 1.2 mm, W_2 = 0.9 mm, and g = 1.5 mm, as were shown in Fig. 5.2.

(a)

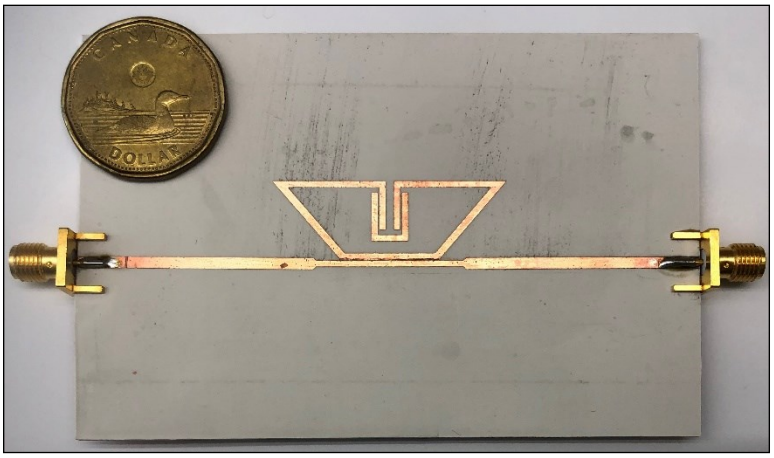

(b)

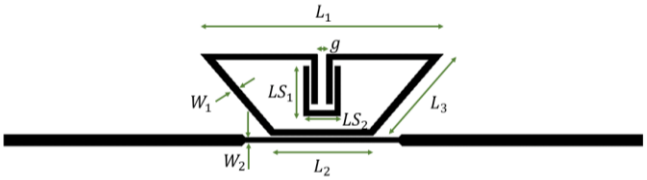

Fig. 5.2. (a) Photograph and (b) layout of the designed SRR coupled to the high impedance section of the transmission line [44].

To inspect the most sensitive regions on the sensor and select the optimized area for positioning the sample, a full-wave microwave simulation is performed using Ansys HFSS software to map and plot the electric-field pattern for each operating frequency. The odd and even modes generate different electric-field distributions shown in Fig. 5.3. Although the electric-field plot exhibits highly concentrated coupled fields at the gap area happening for the odd modes, the even mode, 2GHz, still accumulates a satisfactory electric field for sensing the materials around. Since the higher concentration of electric field results in the more sensitive regions, the mentioned area of the resonator is the best region for achieving the highest sensitivity.

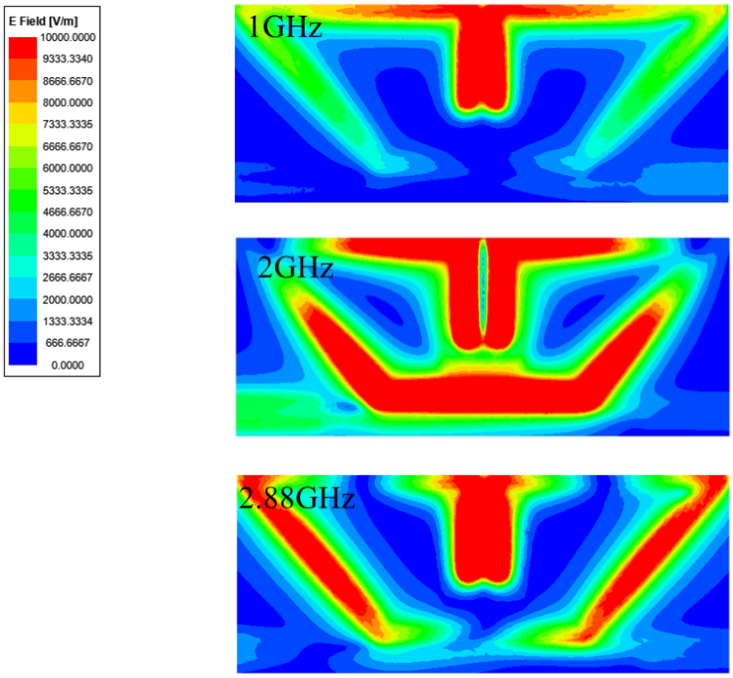

Fig. 5.3. HFSS simulation of the electric field distribution around the SRR shown for different resonant modes [44].

5.2.2 Basic Materials and Modeling

A class of materials presents the individual permittivity spectrum for a specific range of frequencies. For the low-frequency ranges, the polar molecules can be aligned with the external E-field yielding the static permittivity. In contrast, for the higher frequencies these molecules cannot follow the subjected field alternations and the overall permittivity decreases. One of the simplest models is the well-known Debye equation defining a single relaxation frequency convenient for fast computational methods [33].

Fig. 5.4 refers to the Debye presentation of absorption and conductivity curves for distilled water, saturated glucose solution, and ethanol for the wide range of frequencies. As can be seen, the curves have distinct falling edges, resulting from diverse relaxation times for each spectrum. For example, ethanol dielectric constant, with lower relaxation frequency, decreases at lower frequencies compared with water and its glucose solution. Some Debye parameters such as static and high-frequency permittivity values can be found within the academic literature [34]–[36],[33]. The diversity of the permittivity patterns introduces the nonlinearity into the frequency shift

relation, which defines the new features utilized for multivariable sensing explained in the following section.

As previously explained in section 5.2.1, SRRs are the resonators that generate multiple resonant modes in their operational band, which can be easily perturbed through their integration with external materials. These resonant mode frequencies are dependent features of the rings as they iterate themselves and their operational frequencies. To convert these elements into unique and independent features, the variant permittivity profile of the specimens can be used and parameterized. The frequency-dependent permittivities can impact the linear behaviour of the resonant modes considering the relation explained in Eq. (5-1). Here, the denominator of the Eq. (5-1) is not a constant number anymore and varies from one resonant mode to another depending on ε_{eff} values. This inherent feature can be applied to define new independent parameters from a single sensor response.

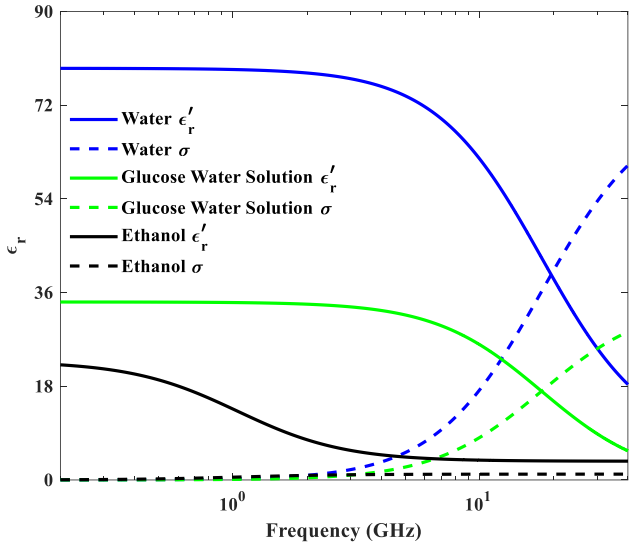

Fig. 5.4. Frequency dependence of the real relative permittivty, εr' and σ for water, saturated glucose-water mixture and ethanol at 23° C [44].

5.2.3 Multivariable Sensing

The main challenge for performing multivariable sensing is the limited number of output parameters from the sensing system that restrict possible unknown characterizations. The majority of the multivariable experiments seek more assisting parameters and independent features for

finalizing their solution. In microwave sensing approaches using the resonance-based method, the resonance frequency shift is a beneficial parameter for measurements. Developing the frequency shift of the resonances as a function of real relative permittivity variations defines the multiple independent features enabling the multivariable analysis. This can be realized by forming a system of equations for each independent resonant mode and solving them for volumetric unknowns or sub-component concentrations, as shown in previous chapters. During this chapter, we applied the same analogy using a different kind of frequency response. We will evaluate the method using notch-band frequency response for different types of sub-component characterizations.

As mentioned in section 5.2.2, the impact of the materials on the effective permittivity of the sensor is more significant for sensitive areas on the SRR surface. For achieving the highest effect on the resonator's resonant modes, a container including the liquid samples is positioned on the gap area of the sensor where boosted E-field concentration is located, as shown in Fig. 5.5. On the other hand, the variant permittivity profile of various materials shown in Fig. 5.4 perturbs and shapes the resultant mixture differently, enabling the multivariable sensing for the label-free analysis of mixtures. For example, the water-ethanol mixture's relaxation frequency is decreasing by adding ethanol, as the ethanol relaxation enforces the resultant solution relaxation frequency to the lower values [36]. So different volumetric percentages or concentrations of components yield the different permittivity patterns and specific resonant mode responses of the resonator, which is the crucial parameter for selective sensing of the mixtures. The resonance frequencies of the sensor should be designed to operate within the variant profile of the sub-component for sampling the permittivity variations of the final mixture [21], [22].

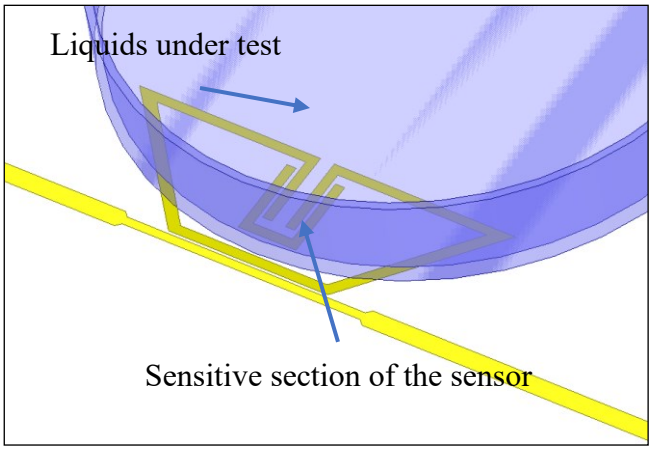

Fig. 5.5. Configuration of the resonator structure loaded with the container covered the gap areas of the sensor [44].

5.2.4 Theoretical Analysis

The individual samples of water, saturated glucose, and ethanol are tested with the same volume inside the container presented in Fig. 5.5. Each sample creates different resonant mode shifts by affecting the resonator capacitance by defining different effective permittivities illustrated in Eq. (5-1). The corresponding shifts from the HFSS simulator are shown in Fig. 5.6 in which the amount of the shifts follows the permittivity values reported in Fig. 5.4.

The relation between the resonant mode shifts and permittivity variations should be explored for the sensor calibration process. For example, referring to Eq (5-1) for the even resonant modes, the relation between the n^{th} resonant mode shifts and the effective permittivity can be calculated using the following relation [37].

Considering the constant relative permittivity for the air, if the relative permittivity of the samples is invariant over the operational frequencies, the n^{th} resonant mode shift would be n times of the fundamental frequency shift, and all resonant mode-based features are dependent. Between each resonant mode and its corresponding shift, the variant permittivity profile imposes the nonlinearity on the frequency shift function, which yields the multiple independent features used for multivariable sensing. As an example, defined ΔF as the shift of an arbitrary resonant mode, and having $\Delta F(H_1) = \Delta f_1$ correspondingly, the general relations can be written as:

$$\varepsilon_{eff}(f_n) \neq \varepsilon_{eff}(f_1), \qquad \Delta F(nH_1) = \Delta f_n \neq n\Delta f_1 \tag{5-2}$$

where H_1 is the first resonant mode frequency for the unloaded sensor. So, using these independent features, multiple equations can be written in a matrix form as follow [21], [22]:

$$\sum_{k=1}^{i} V_k = 1 \tag{5-3}$$

$$\underbrace{\begin{bmatrix} \Delta f_{1,mix} \\ \vdots \\ \Delta f_{n,mix} \\ 1 \end{bmatrix}_{i\times 1}}_{Mixture\ output} = \underbrace{\begin{bmatrix} \Delta f_{11} & \cdots & \Delta f_{1i} \\ \vdots & \ddots & \vdots \\ \Delta f_{n1} & \cdots & \Delta f_{ni} \\ 1 & & 1 \end{bmatrix}_{i\times i}}_{Calibration\ matrix} \times \underbrace{\begin{bmatrix} V_1 \\ \vdots \\ V_i \end{bmatrix}_{i\times 1}}_{Volumetric\ data} \tag{5-4}$$

where V_k is the volume fraction of kth material. Thus, by knowing the nth resonant mode shift as a result of ith material loading, Δf_{ni}, each component's the volumetric fraction could be calculated correspondingly. Considering what we have in Eq. (5-4), at least two independent features are required to characterize the multivariable mixture of water, saturated glucose solution, and ethanol as three sub-components of the solvent. For the present chapter, two linearly independent resonant modes shifts in the resonance frequency are utilized to complete the analysis. Considering what we have in Fig. 5.6, including pre-experimental analysis, Eq. (5-4) can be rewritten as follows.

$$\begin{aligned} &V_E + V_G + V_W = 1 \\ &\Delta f_{1,mix} = \Delta f_{1,E}\, V_E + \Delta f_{1,G} V_G + \Delta f_{1,W}\, V_W \\ &\Delta f_{2,mix} = \Delta f_{2,E}\, V_E + \Delta f_{2,G} V_G + \Delta f_{2,W}\, V_W \end{aligned} \tag{5-5}$$

where V_E, V_G, and V_W present the volume fraction of the ethanol, saturated glucose solution, and water as subcomponents of the mixture. $\Delta f_{n,mix}$ refers to the nth resonant mode shift caused by mixture as load, while other Δf_n in the right side of the Eq. (5-5) represent different sub-components responses measured separately.

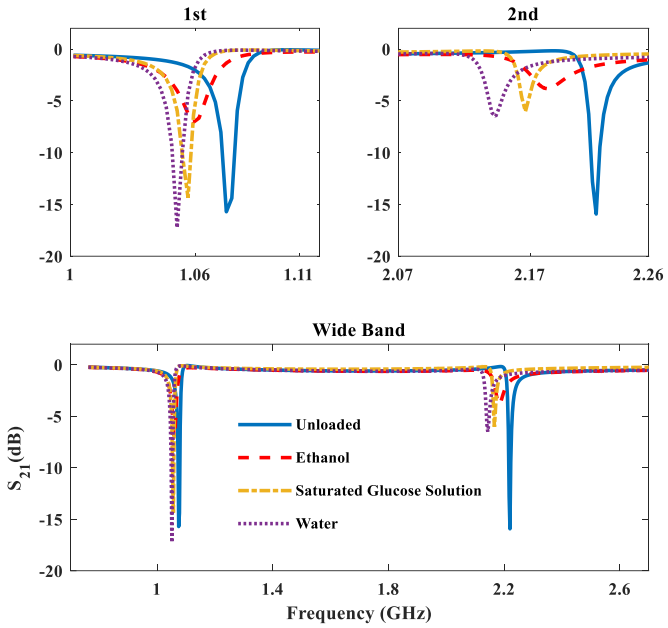

Fig. 5.6. S21 results of the simulations for different loading scenarios presented for individual resonant mode shifts [44].

5.3 Results and Discussion

Fig. 5.7 shows the detailed photograph of the experimental setup, including the sensor loaded by the ABS polymer container with $\varepsilon_r \approx 4.1$, 7 mm depth, and 5.7 cm diameter on its top plane. The container is positioned so that it covers the most sensitive section of the sensor surface. The relative permittivity of the container is around 4 which its effect is included in our measurements during the sensor calibration process. To validate the sensor performance, the transmission coefficient is measured and compared with full-wave simulation results completed by HFSS, as illustrated in Fig. 5.8. Several combinations of water-saturated glucose solution and ethanol as mixture sub-components are prepared for the experiments. The sub-components are highly soluble in each other, and the resultant unsaturated mixtures are prepared by shaking and giving adequate time to rest. All final mixture volume is assigned to be 10 ml for each sample. Measurements are performed using a Copper Mountain S5065 2-port 6.5 GHz vector network analyzer. The difference in S_{21} amplitude between the simulation and measurement results is the small dimensions and effective permittivity uncertainties. Using equation (5-4) and considering three volumetric percentages as unknown, at least two resonant mode data are required to complete the shift sampling process. For

implementing the measurements, 1st and 2nd resonant modes are chosen to be used in the data acquisition process, including the permittivity variation impact on the frequencies of the resonant modes.

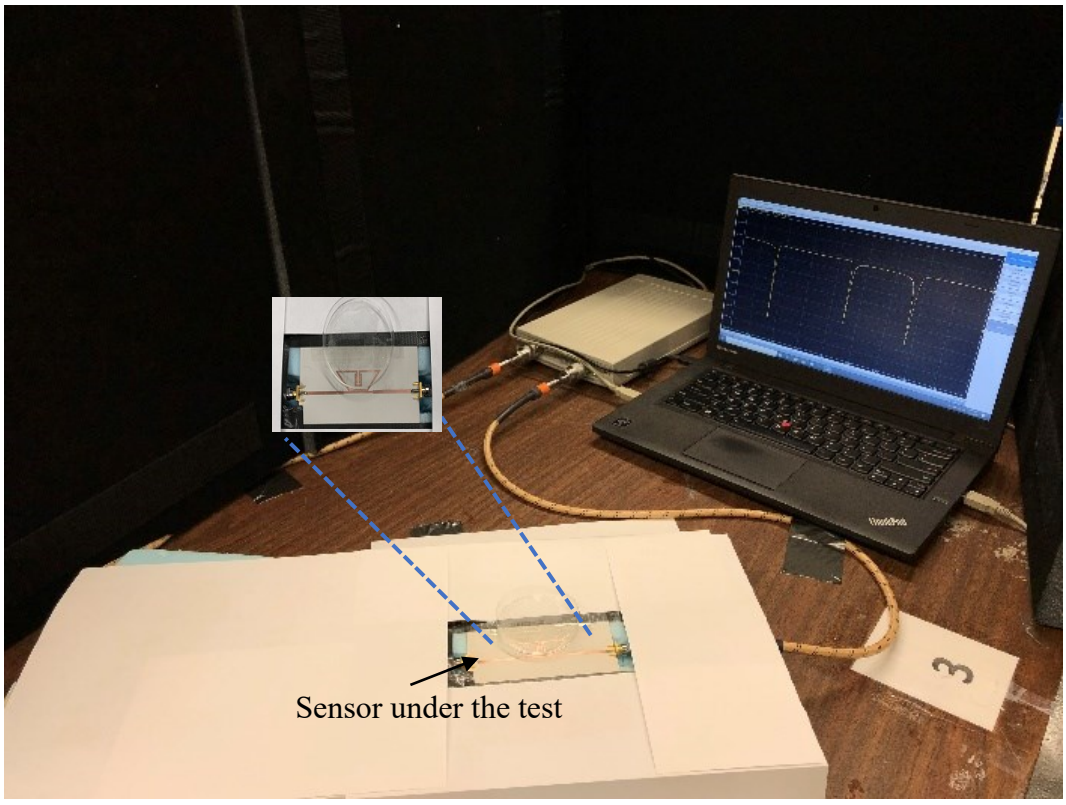

Fig. 5.7. Picture of the experiment setup for evaluating the sensor operation under the load [44].

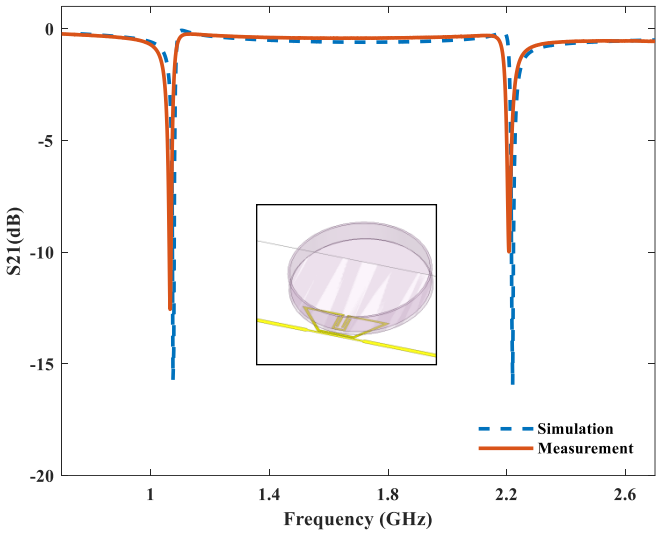

Fig. 5.8. Simulated and measurement the results of the transmission coefficient for the unloaded sensor in its operational band [44].

All the frequency shifts are analyzed with respect to the unloaded sensor response. Before starting the main phase of the experiments, the system's real-time behaviour is explored and studied. Fig. 5.9 refers to the real-time observation of the sensor response while increasing the DI water concentration in ethanol. For performing this, first, the empty container mounted the top plane of the sensor is loaded with 10 ml ethanol. Ethanol occupies 56 % of the container volume, then using the standard infuse pump II elite programmable syringe pump, DI water concentration is rising from 0 to 30 % of the final solution volume.

It takes about 960 seconds for the pump to infuse the 4 ml DI water into the ethanol while the infusion rate is set to 0.25 ml/min. A gradual increase in the amount of water in the solution raises the whole effective permittivity of the sensor. It pushes the resonance location back, as can be seen in Fig. 5.9. First, the sensor's responses are captured for individual components of the mixture, including water, ethanol, and saturated glucose solution, as depicted in Fig. 5.10. The solid blue line represents the performance of the sensor for the unloaded container. The interaction between the electromagnetic fields and different liquids alters the sensor response and shifts the resonance frequency of each resonant mode accordingly. Considering what we have for the Debye model

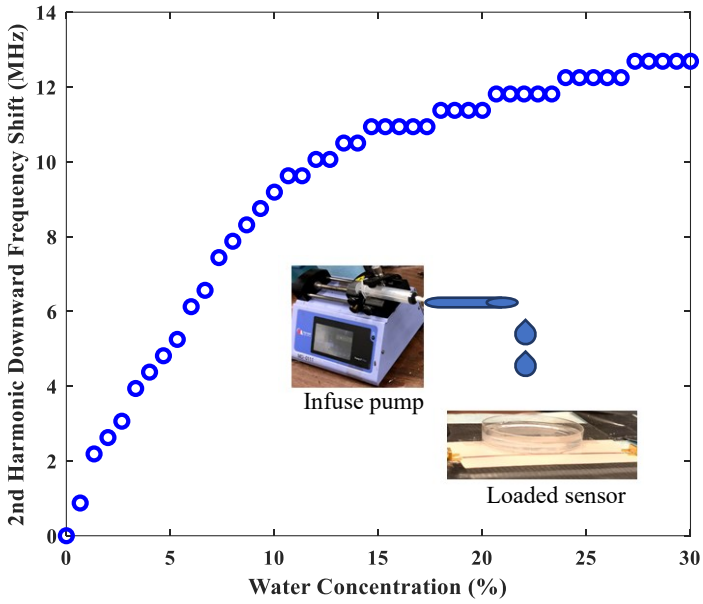

Fig. 5.9. Time-based variations of the sensor response for the different water concentrations in ethanol [44].

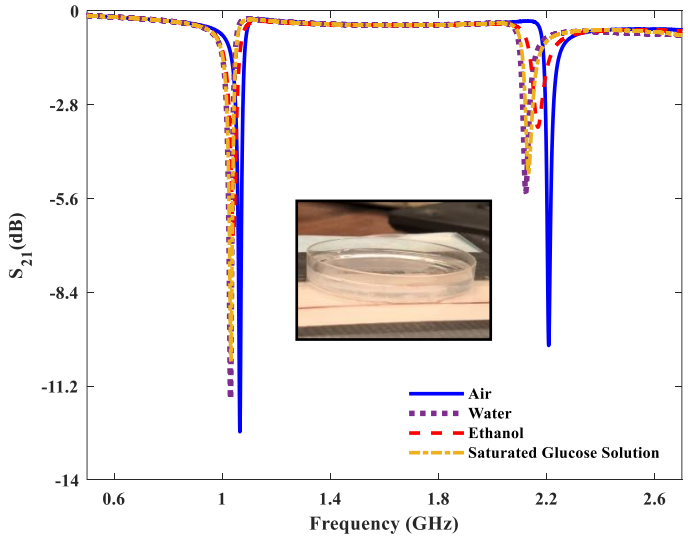

Fig. 5.10. Measurement results of different resonant mode shifts by water, ethanol, and saturated glucose solution in lab temperature [44].

of the liquids, water as a high permittivity load perturbs the resonance frequency shift more than the other solvents. These shifts in the resonance frequency values for the 1st and 2nd resonant modes are measured in all sub-components, reported in Table 5.1. Then, using equations (5-6) and the data illustrated in Table 5.1, the amount of 1st and 2nd resonant mode shifts are calculated and compared with exact measured shifts achieved from each mixture. Table 5.2 contains a comparison

between the calculated and measured values for different loading scenarios. There is a good agreement between the formula-based calculations and the exact measurement data. The information described in Table 5.1 and Table 5.2 is used to solve the equation system shown in Eq. (5-4). The nonlinear shifts occurring from variant permittivity profiles of different materials provide linearly independent equations (5-4). Once the calibration matrix is formed, the volumetric analysis can be performed for different component combinations.

Table 5.1. The 1st and 2nd resonant mode shifts were measured for different loading scenarios.

	Water	Ethanol	Saturated Glucose Solution
Δf_1 (MHz)	34.56	23.62	32.81
Δf_2 (MHz)	84.87	39.81	74.37

Table 5.2. A comparison between the calculated and measured results of Δf for individual experiments.

	Resonant mode Shifts (MHz)							
Sampling Resonant mode	Mix 1	Mix 2	Mix 3	Mix 4	Mix 5	Mix 6	Mix 7	Mix 8
Calculated $\Delta f_{1,\,mix}$ (MHz)	32.7	33.05	32.59	32.13	31.32	31.67	30.86	31.21
Measured $\Delta f_{1,\,mix}$ (MHz)	32.81	33.25	32.81	32.37	31.5	31.93	31.48	31.51
Calculated $\Delta f_{2,\,mix}$ (MHz)	74.75	76.84	75.11	73.39	69.56	71.66	67.83	69.93
Measured $\Delta f_{2,\,mix}$ (MHz)	74.37	77	75.25	73.5	69.56	72.62	69.12	70.87

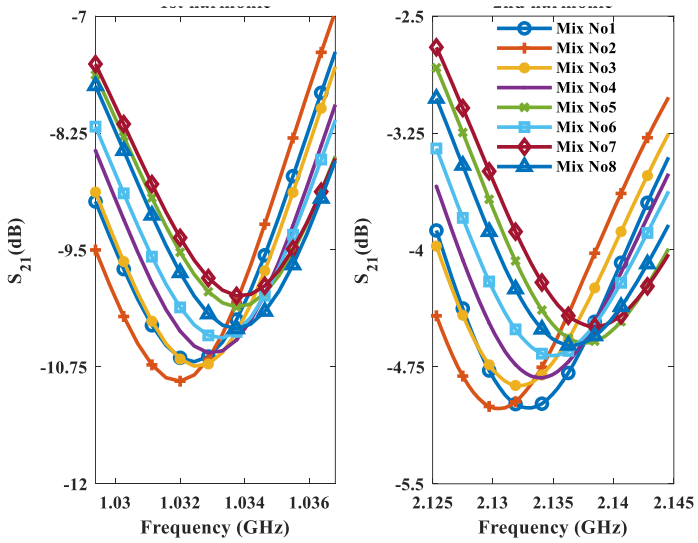

Fig. 5.11. The first and second resonant mode measurement results shift for different combinations of water, glucose solution, and ethanol as sub-components [44].

Table 5.3 recapitulates the measured and pre-assigned volumetric values for each mixture type. To monitor the efficiency of the method, sub-components with different volumetric percentages are combined and mixed. As shown in Fig. 5.11, different mixtures, having various permittivity values, impact the resonant mode frequencies in different manners. The dielectric profile behavior of the mixtures can be associated with the Debye of the components. This phenomenon can be witnessed in resonant mode shifts of the sensor loaded with Mix 7 and 8. On the other hand, each resonant mode shift will increase accordingly for the mixtures with higher water concentrations. Loading the sensor container with Mix 2, with the highest relative permittivity average, the greatest shifts will appear for each resonant mode frequency. As the final step, the average error of all measurements is calculated and presented in Table 5.3 using the pre-assigned values of sub-components volumes for each experiment. The average error is calculated as follows:

$$Average\_error = \frac{\sum_{i=1}^{3}\left(\frac{|Expected\_value - Calculated\_value|}{Expected\_value}\right)}{3} \tag{5-6}$$

Table 5.3. A comparison between the extracted and actual components of each experiment.

	Volumetric Percentages (%)							
Mixture Components	Mix 1	Mix 2	Mix 3	Mix 4	Mix 5	Mix 6	Mix 7	Mix 8
Water Assigned Vol. %	20	40	40	40	20	40	20	40
Glucose Sol. Assigned Vol.%	75	55	50	45	60	40	55	35
Ethanol Assigned Vol. %	5	5	10	15	20	20	25	25
Measured Water Vol. %	19	44	42.9	43.5	20	39.4	22.3	34.5
Measured Glucose Sol.Vol.%	75.3	50.4	46.5	45.3	60.4	43.6	55.7	44
Measured Ethanol Vol. %	5.7	5.6	10.6	11.2	19.6	17	22	21.5
Average error	0.0647	0.1010	0.0675	0.1157	0.0088	0.0850	0.0825	0.1781

Table 5.4. State of Art comparison for different mixture sensing and sensors

References	Sensing Elements	Operational Frequency (GHz)	Multivariable Analysis	Application
[38]	double-ring resonator	4.5	No	glucose-acetate
[39]	Planar SRR	0.5 – 2.2	No	NaCl, KCL, $MgCl_2$, $CaCL_2$, Na_2CO_3
[40]	Planar Resonator	2.5, 3.5, 4.5	No	water, methanol, ethanol, chloroform
[41]	IDE-SRR	≈ 1	No	water-methanol, water-tetrahydrofuran
[42]	CPW-SRR	19.4	No	glucose-water, NaCl-water
[43]	SRR	2	No	glucose-water
This work	Planar SRR	1.1, 2.2	Yes	ethanol-water-glucose Sol

Different mixture sensing techniques and the corresponding microwave sensors are stated and compared in Table 5.4. In most works, split-ring resonators were chosen as a proper candidate for performing the measurements because of their efficiency and simplicity. Our work has the advantage of using multi-resonant modes compared to the single resonant studies mentioned in Table 5.4.

5.4 Conclusion

A split-ring resonator microwave sensor has been presented with an extended sensing region for non-contact fermentation process monitoring. Contrary to the traditional microwave resonator-based techniques considering a single resonance for measuring in binary (single variable) environments, the presented sensing mechanism was based on utilizing multiple resonant mode resonances, enabling multivariable analysis. The main idea behind the proposed technique is based on the uniqueness and dispersion of dielectric permittivity of different materials. By wisely selecting the resonant modes for analysis, volumetric fractions of each component in the mixture could be achieved through a simple set of equations. An average error of 0.0878 has been achieved in analyzing the fermentation process at various stages. This work could pave the way to

employing microwave sensors with sophisticated characteristics such as low-cost, and non-contact sensing for complex applications such as food processing technologies.

5.5 References

[1] H. S. Son, Y. S. Hong, W. M. Park, M. A. Yu, and C. H. Lee, "A novel approach for estimating sugar and alcohol concentrations in wines using refractometer and hydrometer," *J. Food Sci.*, vol. 74, no. 2, pp. C106–C111, 2009.

[2] C. Lamy, A. Lima, V. LeRhun, F. Delime, C. Coutanceau, and J.-M. Léger, "Recent advances in the development of direct alcohol fuel cells (DAFC)," *J. Power Sources*, vol. 105, no. 2, pp. 283–296, 2002.

[3] S. Piermarini, G. Volpe, M. Esti, M. Simonetti, and G. Palleschi, "Real time monitoring of alcoholic fermentation with low-cost amperometric biosensors," *Food Chem.*, vol. 127, no. 2, pp. 749–754, 2011.

[4] G. McLeod *et al.*, "A comparison of variate pre-selection methods for use in partial least squares regression: a case study on NIR spectroscopy applied to monitoring beer fermentation," *J. Food Eng.*, vol. 90, no. 2, pp. 300–307, 2009.

[5] I. S. Daoud and B. A. Searle, "On-line monitoring of brewery fermentation by measurement of CO2 evolution rate," *J. Inst. Brew.*, vol. 96, no. 5, pp. 297–302, 1990.

[6] A. Ktenioudaki, F. Butler, U. Gonzales-Barron, U. Mc Carthy, and E. Gallagher, "Monitoring the dynamic density of wheat dough during fermentation," *J. Food Eng.*, vol. 95, no. 2, pp. 332–338, 2009.

[7] L. Wynne, S. Clark, M. J. Adams, and N. W. Barnett, "Compositional dynamics of a commercial wine fermentation using two-dimensional FTIR correlation analysis," *Vib. Spectrosc.*, vol. 44, no. 2, pp. 394–400, 2007.

[8] H.-W. Lee *et al.*, "Development of novel on-line capillary gas chromatography-based analysis method for volatile organic compounds produced by aerobic fermentation," *J. Biosci. Bioeng.*, vol. 127, no. 1, pp. 121–127, 2019.

[9] J. Fernández-Novales, M.-I. López, M.-T. Sánchez, J.-A. García, and J. Morales, "A feasibility study on the use of a miniature fiber optic NIR spectrometer for the prediction of volumic mass and reducing sugars in white wine fermentations," *J. Food Eng.*, vol. 89, no. 3, pp. 325–329, 2008.

[10] J. Shi, D. Feng, and Y. Li, "Biosensors in fermentation applications," *Ferment. Process.*, p. 145, 2017.

[11] M. Baghelani, Z. Abbasi, and M. Daneshmand, "Noncontact high sensitivity chipless tag microwave resonator for bitumen concentration measurement at high temperatures," *Fuel*, vol. 265, p. 116916, 2020.

[12] M. Baghelani, Z. Abbasi, M. Daneshmand, and P. E. Light, "Non-invasive continuous-time glucose monitoring system using a chipless printable sensor based on split ring microwave resonators," *Sci. Rep.*, vol. 10, no. 1, pp. 1–15, 2020.

[13] M. Baghelani, N. Hosseini, and M. Daneshmand, "Artificial Intelligence Assisted Non-Contact Microwave Sensor for Multivariable Biofuel Analysis," *IEEE Trans. Ind. Electron.*, 2020.

[14] P. Sharma, L. Lao, and G. Falcone, "A microwave cavity resonator sensor for water-in-oil measurements," *Sensors Actuators B Chem.*, vol. 262, pp. 200–210, 2018.

[15] Z. Abbasi, M. Baghelani, M. Nosrati, A. Sanati-Nezhad, and M. Daneshmand, "Real-time non-contact integrated chipless RF sensor for disposable microfluidic applications," *IEEE*

J. Electromagn. RF Microwaves Med. Biol., 2019.

[16] N. Chudpooti *et al.*, "In-Situ Self-Aligned NaCl-Solution Fluidic-Integrated Microwave Sensors for Industrial and Biomedical Applications," *IEEE Access*, vol. 8, pp. 188897–188907, 2020.

[17] A. Ebrahimi, F. J. Tovar-Lopez, J. Scott, and K. Ghorbani, "Differential microwave sensor for characterization of glycerol–water solutions," *Sensors Actuators B Chem.*, vol. 321, p. 128561, 2020.

[18] A. Ebrahimi, J. Scott, and K. Ghorbani, "Microwave reflective biosensor for glucose level detection in aqueous solutions," *Sensors Actuators A Phys.*, vol. 301, p. 111662, 2020.

[19] P. Vélez, J. Munoz-Enano, K. Grenier, J. Mata-Contreras, D. Dubuc, and F. Martín, "Split ring resonator-based microwave fluidic sensors for electrolyte concentration measurements," *IEEE Sens. J.*, vol. 19, no. 7, pp. 2562–2569, 2018.

[20] A. Ebrahimi, W. Withayachumnankul, S. F. Al-Sarawi, and D. Abbott, "Microwave microfluidic sensor for determination of glucose concentration in water," in *2015 IEEE 15th Mediterranean Microwave Symposium (MMS)*, 2015, pp. 1–3.

[21] N. Hosseini, S. S. Olokede, and M. Daneshmand, "A novel miniaturized asymmetric CPW split ring resonator with extended field distribution pattern for sensing applications," *Sensors Actuators, A Phys.*, vol. 304, Apr. 2020, doi: 10.1016/j.sna.2019.111769.

[22] N. Hosseini, M. Baghelani, and M. Daneshmand, "Selective Volume Fraction Sensing Using Resonant- Based Microwave Sensor and its Harmonics," *IEEE Trans. Microw. Theory Tech.*, Sep. 2020, doi: 10.1109/TMTT.2020.2990139.

[23] M. Baghelani, N. Hosseini, and M. Daneshmand, "Selective measurement of water content in multivariable biofuel using microstrip split ring resonators," in *IEEE MTT-S International Microwave Symposium Digest*, 2020, vol. 2020-Augus, doi: 10.1109/IMS30576.2020.9223908.

[24] M. Benlamri *et al.*, "Planar microwave resonator with electrodeposited ZnO thin film for ultraviolet detection," *Semicond. Sci. Technol.*, vol. 35, no. 2, p. 25003, 2019.

[25] Z. Li, Z. Meng, A. Haigh, P. Wang, and A. Gibson, "Characterisation of water in honey using a microwave cylindrical cavity resonator sensor," *J. Food Eng.*, vol. 292, p. 110373.

[26] K. Nakagawa and S. Kono, "Monitoring of primary drying in the freeze-drying process using an open-ended coaxial microwave resonator," *J. Food Eng.*, p. 110163, 2020.

[27] Z. Abbasi, H. Niazi, M. Abdolrazzaghi, W. Chen, and M. Daneshmand, "Monitoring pH Level Using High-Resolution Microwave Sensor for Mitigation of Stress Corrosion Cracking in Steel Pipelines," *IEEE Sens. J.*, vol. 20, no. 13, pp. 7033–7043, 2020.

[28] P. Velez, K. Grenier, J. Mata-Contreras, D. Dubuc, and F. Martín, "Highly-sensitive microwave sensors based on open complementary split ring resonators (OCSRRs) for dielectric characterization and solute concentration measurement in liquids," *IEEE Access*, vol. 6, pp. 48324–48338, 2018.

[29] A. Ebrahimi, J. Scott, and K. Ghorbani, "Ultrahigh-sensitivity microwave sensor for microfluidic complex permittivity measurement," *IEEE Trans. Microw. Theory Tech.*, vol. 67, no. 10, pp. 4269–4277, 2019.

[30] M. Abdolrazzaghi and M. Daneshmand, "Exploiting Sensitivity Enhancement in Microwave Planar Sensors Using Intermodulation Products With Phase Noise Analysis," *IEEE Trans. Circuits Syst. I Regul. Pap.*, 2020.

[31] A. A. M. Bahar, Z. Zakaria, S. R. Ab Rashid, A. A. M. Isa, and R. A. Alahnomi, "High-efficiency microwave planar resonator sensor based on bridge split ring topology," *IEEE Microw. Wirel. components Lett.*, vol. 27, no. 6, pp. 545–547, 2017.

[32] L. Wang, X. Q. Lin, F. Cheng, Y. Fan, and Z. B. Zhu, "Electric split-ring resonator based on double-sided parallel-strip line," *IEEE Antennas Wirel. Propag. Lett.*, vol. 12, pp. 69–71, 2013.

[33] M. Y. Onimisi and J. T. Ikyumbur, "Comparative analysis of dielectric constant and loss factor of pure butan-1-ol and ethanol," *Am. J. Condens. Matter Phys.*, vol. 5, no. 3, pp. 69–75, 2015.

[34] T. Ikyumbur, M. Onimisi, S. Abdu, E. Hemba, and Z. Kirji, "Optimization in the computation of dielectric constant of methanol using Debye relaxation method," *Br. J. Appl. Sci. Technol*, vol. 19, pp. 1–10, 2017.

[35] S. Mashimo, T. Umehara, and H. Redlin, "Structures of water and primary alcohol studied by microwave dielectric analyses," *J. Chem. Phys.*, vol. 95, no. 9, pp. 6257–6260, 1991, doi: 10.1063/1.461546.

[36] T. Sato, A. Chiba, and R. Nozaki, "Dynamical aspects of mixing schemes in ethanol–water mixtures in terms of the excess partial molar activation free energy, enthalpy, and entropy of the dielectric relaxation process," *J. Chem. Phys.*, vol. 110, no. 5, pp. 2508–2521, 1999.

[37] N. Hosseini, M. Baghelani, and M. Daneshmand, "Discrete Microwave Spectroscopy using Planar Resonator," 2019, doi: 10.1109/CCECE.2019.8861771.

[38] S. Mohammadi, A. V. Nadaraja, D. J. Roberts, and M. H. Zarifi, "Real-time and hazard-free water quality monitoring based on microwave planar resonator sensor," *Sensors Actuators A Phys.*, vol. 303, p. 111663, 2020.

[39] S. Harnsoongnoen and A. Wanthong, "A non-contact planar microwave sensor for detection of high-salinity water containing NaCl, KCl, CaCl2, MgCl2 and Na2CO3," *Sensors Actuators B Chem.*, vol. 331, p. 129355, 2021.

[40] A. A. Abduljabar, H. Hamzah, and A. Porch, "Multi-resonators, microwave microfluidic sensor for liquid characterization," *Microw. Opt. Technol. Lett.*, vol. 63, no. 4, pp. 1042–1047, 2021.

[41] X. Bao *et al.*, "Integration of interdigitated electrodes in split-ring resonator for detecting liquid mixtures," *IEEE Trans. Microw. Theory Tech.*, vol. 68, no. 6, pp. 2080–2089, 2020.

[42] S. Mohammadi *et al.*, "Gold Coplanar Waveguide Resonator Integrated With a Microfluidic Channel for Aqueous Dielectric Detection," *IEEE Sens. J.*, vol. 20, no. 17, pp. 9825–9833, 2020.

[43] N. Sharafadinzadeh, M. Abdolrazzaghi, and M. Daneshmand, "Highly sensitive microwave split ring resonator sensor using gap extension for glucose sensing," in *2017 IEEE MTT-S International Microwave Workshop Series on Advanced Materials and Processes for RF and THz Applications (IMWS-AMP)*, 2017, pp. 1–3, doi: 10.1109/IMWS-AMP.2017.8247400.

[44] N. Hosseini, and M. Baghelani, "Selective real-time non-contact multi-variable water-alcohol-sugar concentration analysis during fermentation process using microwave split-ring resonator based sensor." Sensors and Actuators A: Physical 325 (2021): 112695.

Chapter 6 Conclusion and Future Work

This chapter includes the conclusion, limitations of the proposed multivariable sensing approach, and a brief review of the future directions and possible potentials.

6.1 Conclusion

A new multi-resonant mode data analysis technique has been developed to measure and extract the volume fraction of the components in an arbitrary mixture. The multi-resonant mode of the resonator can generate new independent features for performing multivariable sensing which is based on the distinctive permittivity spectrum of different materials.

Since relative permittivity variation is reflected in the resonance frequency shift, the shift in various modes of a single microwave ring resonator has been employed in developing a set of mathematically independent equations. The volumetric fraction of each material could then be extracted from the solution of these equations. In the model-based technique, A new analytic microwave spectroscopy formula has been derived and offered to be used in the mixture equation to generate a linear system of equations. The formula is based on analyzing patterns of the operational frequency of the resonator simulated by full-wave EM simulator HFSS.

Several component combinations yielding orthogonal mixture types were tested and examined through a simple ring resonator, and a series of agreeable results are obtained. Results for measuring the volumetric fraction of methanol, ethanol, and propanol as proof of concept have shown promising precision with maximum error as low as 6%, mainly originating from the materials preparation and experimental errors for mixtures with three variables.

For simplifying the proposed approach, both AI-based process and frequency-based methodology have been developed. Also, for more accurate measurements, new types of planar resonators have been designed and presented. The overall achievements of this study can be summarized as follows;

- Developing the model-based and model-free analysis for selective volumetric sensing using:
    - Permittivity-based closed-form formula
    - AI-assisted multivariable approach (model-free)
- Designing and developing the novel passive sensors for multivariable analysis mentioned as:
    - Miniaturized split ring resonator (MSRR)
    - Split ring resonator (SRR) with notch-band response
- Applying and testing the method for different kinds of mixtures including:
    - Ethanol-Methanol-Propanol
    - Water-Ethanol-Gasoline (Biofuel)
    - Water-Brine-Crude Oil (Crude oil impurities)
    - Glucose-Water-Ethanol (Fermentation)

Throughout the thesis, different kinds of resonators with various geometries and layouts have been designed and proposed. For proof of concept, I started with the ring resonator in Chapter 3, as one of the simplest forms of planar resonator, which includes multi-resonant modes in its operational frequency band. Then, to have a better sensing profile, SRR has been suggested. For the sake of device miniaturization and having a higher sensitivity level, novel types of planer resonators have been designed and utilized during Chapters 4 and 5.

6.1.1 Considerations and Limitations

Besides the significant features of the model-based analysis, there are some concerns and considerations that should be taken into account, such as accuracy of the permittivity spectrum from a database, temperature effect and setup stability, approximation of the Litcheneker formula , electric field profile, and the peak distortion of the resonances.

Besides the considerations that have been mentioned, the ratios of different sub-component and the maximum number of materials for characterization are limited to parameters such as minimum detectable frequency shift, averaged relative error of the calculations, and the variant band of the permittivity profile

It should be mentioned that the container's relative permittivity spectrum, the air gap, and the loss effect of the adhesive tape on sensor response are all calibrated during the individual component loadings on the resonator. Considering the negligible deviations of the container permittivity over the multi-modes of the resonator, one can relate the resonant frequency shifts to the subcomponent permittivity variations. The complementary and alternative remedy for these issues is to use the frequency-based formulation instead of the permittivity-based approach. Chapters 4 and 5 of the thesis show how unsaturated resonator modes are considered to change linearly with permittivity values. Then these resonant modes are directly plugged into the system of equations for the final solution.

6.2 Future Directions

The potential research works that can be developed based on multi-feature analysis for multivariable systems can be presented through developing the transient analysis for the multivariable approach.

This can lead to the industrialization of the technique using CMOS technology which requires designing and layout the demanded hardware tape-out (pulse generator, ADC). The pulse generator was considered as one of the basic and potential sources used in the transient method that will be clarified in the next section.

The other potential research topic can be wireless sensing. This can be initiated through designing semi-active RFID tags for wireless selective sensing, which demands designing UHF antenna modules for the tag accompanied and integrated with sensor interface (ADC).

6.2.1 Transient Analysis

Since the vector network analyzers (VNA) are usually expensive and non-portable instrumentation tools, so exciting the multi-mode structure with a tunable pulse generator can be investigated for the industrialization purpose of the proposed technique. This results in applying both low-cost and portable measuring devices and probes. The output transient signal can be digitized using an 8-bit analog to digital converter (ADC) and stored for the fast Fourier transform process. For proof of concept, the accuracy of the transient approach has been compared with the frequency-based method. This comparison is performed through exciting the same multi-mode system by both impulse and multi-frequency signals, as shown in Fig. 6.1.

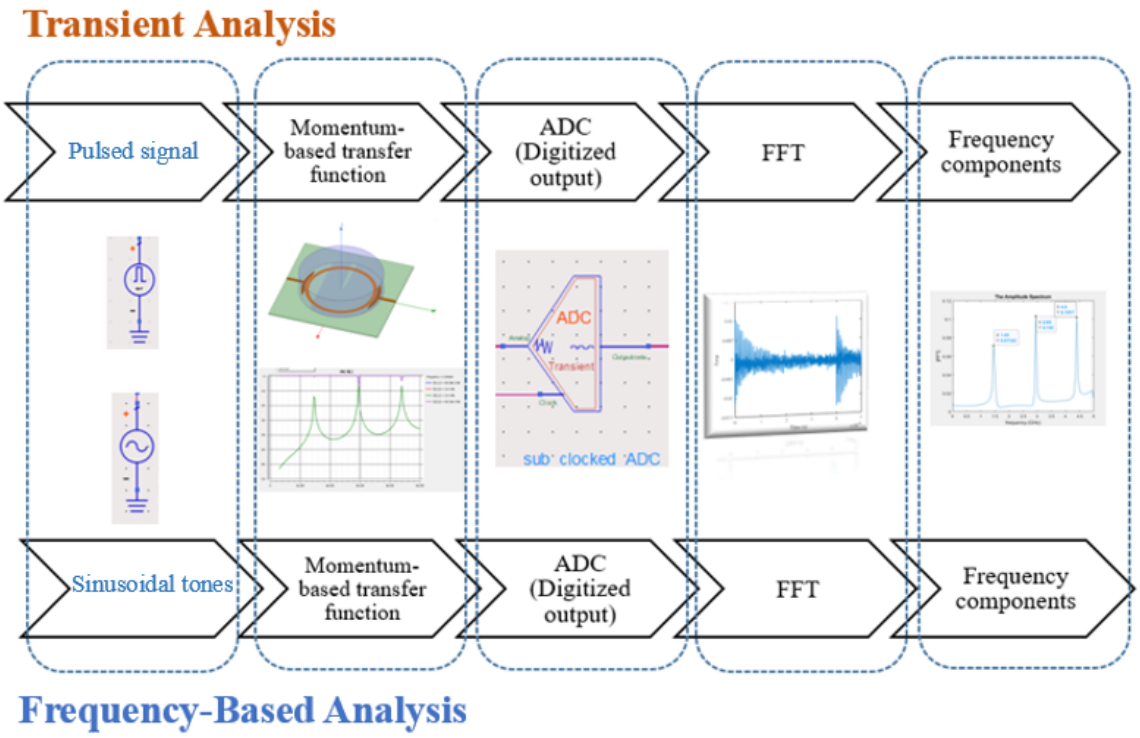

Fig. 6.1. A comparison between the frequency-based and transient-based methods.

Fig. 6.2 shows the simulation setup for performing the analysis. First, using the frequency response of the multi-mode resonator, the device under the test is excited by the pulse generator (transient analysis). The multi-tone sine waves are considered input around the second and third resonant modes as the next step (frequency-based analysis). The frequency components of both cases are shown in Fig. 6.2(b) and (c). The preliminary results present a satisfactory correlation between both of the methods. This can pave the way for using transient analysis as an efficient alternative for multivariable sensing.

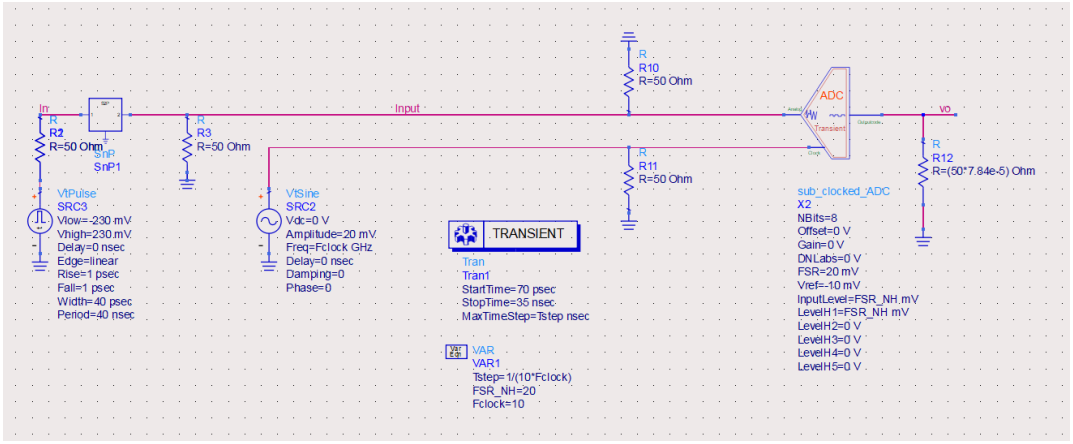

(a)

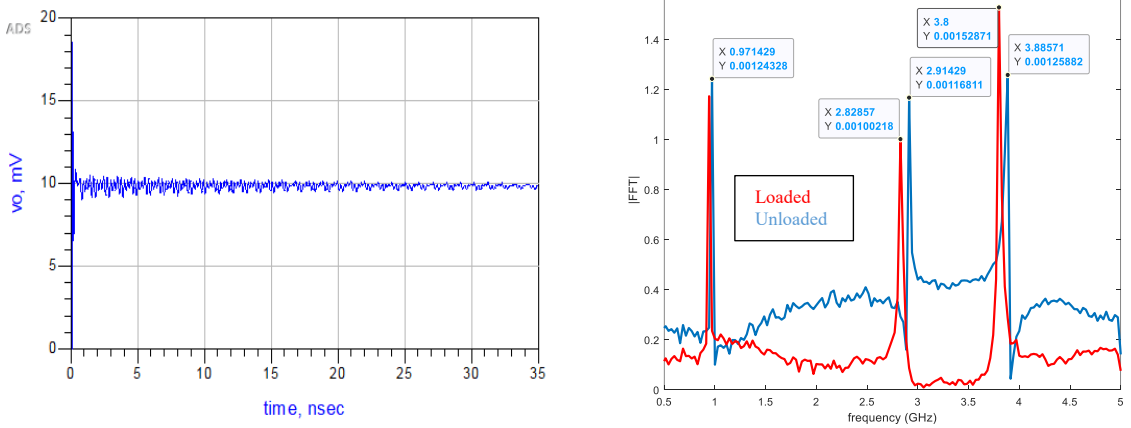

(b)

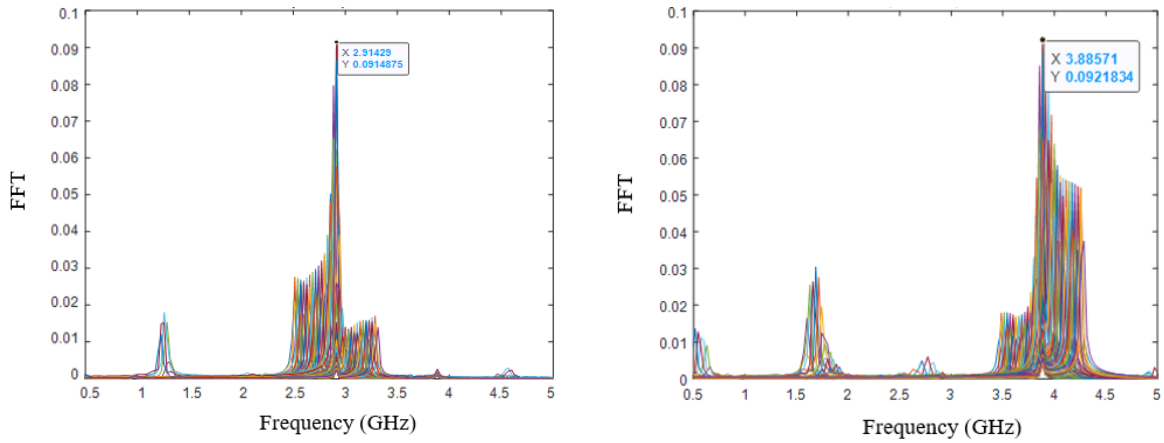

(c)

Fig. 6.2. The ADS Simulation setup (a) compares the frequency components of the impulse response (b) and frequency sweep response around the 2nd and 3rd resonant modes.

Bibliography

H. F. Cook, “Dielectric behaviour of human blood at microwave frequencies,” *Nature*, vol. 168, no. 4267, p. 247, 1951.

H. Choi, J. Nylon, S. Luzio, J. Beutler, and A. Porch, “Design of continuous non-invasive blood glucose monitoring sensor based on a microwave split ring resonator,” in *2014 IEEE MTT-S International Microwave Workshop Series on RF and Wireless Technologies for Biomedical and Healthcare Applications (IMWS-Bio2014)*, 2014, pp. 1–3.

A. Rohman, D. L. Setyaningrum, and S. Riyanto, “FTIR spectroscopy combined with partial least square for analysis of red fruit oil in ternary mixture system,” *Int. J. Spectrosc.*, vol. 2014, 2014.

A. Kondyli and W. Schrader, “High-resolution GC/MS studies of a light crude oil fraction,” *J. mass Spectrom.*, vol. 54, no. 1, pp. 47–54, 2019.

J. J. Pitt, “Principles and applications of liquid chromatography-mass spectrometry in clinical biochemistry,” *Clin. Biochem. Rev.*, vol. 30, no. 1, p. 19, 2009.

D. Havelka, O. Krivosudský, and M. Cifra, “Grounded coplanar waveguide-based 0.5–50 GHz sensor for dielectric spectroscopy,” in *2017 47th European Microwave Conference (EuMC)*, 2017, pp. 950–953.

N. Bonanos, P. Pissis, and J. R. Macdonald, “Impedance spectroscopy of dielectrics and electronic conductors,” *Charact. Mater.*, pp. 1–14, 2002.

A. Fendri, H. Ghariani, and O. Kanoun, “Dielectric spectroscopy for assessment of water content in edible oils,” in *2017 14th International Multi-Conference on Systems, Signals & Devices (SSD)*, 2017, pp. 728–732.

M. Nakamura, T. Tajima, K. Ajito, and H. Koizumi, “Selectivity-enhanced glucose measurement in multicomponent aqueous solution by broadband dielectric spectroscopy,” in *2016 IEEE MTT-S International Microwave Symposium (IMS)*, 2016, pp. 1–3.

M. A. Suster, D. Maji, N. Vitale, U. Gurkan, and P. Mohseni, “An RF/microwave microfluidic sensor for miniaturized dielectric spectroscopy based on sensor transmission characteristics,” in *2015 IEEE SENSORS*, 2015, pp. 1–4.

A. P. Saghati, J. S. Batra, J. Kameoka, and K. Entesari, “A metamaterial-inspired wideband microwave interferometry sensor for dielectric spectroscopy of liquid chemicals,” *IEEE Trans. Microw. Theory Tech.*, vol. 65, no. 7, pp. 2558–2571, 2017.

M. Abdolrazzaghi, M. H. Zarifi, C. F. A. Floquet, and M. Daneshmand, “Contactless Asphaltene Detection Using an Active Planar Microwave Resonator Sensor,” *Energy & Fuels*, vol. 31, no. 8, pp. 8784–8791, 2017.

M. Nosrati, Z. Abbasi, M. Baghelani, S. Bhadra, and M. Daneshmand, “Locally Strong-Coupled Microwave Resonator Using PEMC Boundary for Distant Sensing Applications,” *IEEE Trans. Microw. Theory Tech.*, 2019.

M. A. Karimi, M. Arsalan, and A. Shamim, “Design and dynamic characterization of an orientation insensitive microwave water-cut sensor,” *IEEE Trans. Microw. Theory Tech.*, vol. 66, no. 1, pp. 530–539, 2017.

W.-T. S. Chen and R. R. Mansour, “Miniature gas sensor and sensor array with single-and

dual-mode RF dielectric resonators," *IEEE Trans. Microw. Theory Tech.*, vol. 66, no. 8, pp. 3697–3704, 2018.
Z. Abbasi, P. Shariaty, M. Nosrati, Z. Hashisho, and M. Daneshmand, "Dual-Band Microwave Circuits for Selective Binary Gas Sensing System," *IEEE Trans. Microw. Theory Tech.*, 2019.
M. H. Zarifi, T. Thundat, and M. Daneshmand, "High resolution microwave microstrip resonator for sensing applications," *Sensors Actuators A Phys.*, vol. 233, pp. 224–230, 2015.
M. Daneshmand and M. H. ZARIFI, "Apparatus and method for high resolution complex permittivity sensing using high Q microwave sensors for lossy or non-lossy mediums and samples." Google Patents, Jan. 08, 2019.
S. Harnsoongnoen, U. Charoen-In, and A. Wanthong, "Determination of glucose concentration with resonant coplanar microwave sensor," in *2017 International Electrical Engineering Congress (iEECON)*, 2017, pp. 1–3.
L. Benkhaoua, M. T. Benhabiles, S. Mouissat, and M. L. Riabi, "Miniaturized quasi-lumped resonator for dielectric characterization of liquid mixtures," *IEEE Sens. J.*, vol. 16, no. 6, pp. 1603–1610, 2015.
X. Zhang, C. Ruan, and K. Chen, "High-sensitivity microwave sensor for liquid characterization using a complementary circular spiral resonator," *Sensors*, vol. 19, no. 4, p. 787, 2019.
T. Chretiennot, D. Dubuc, and K. Grenier, "A microwave and microfluidic planar resonator for efficient and accurate complex permittivity characterization of aqueous solutions," *IEEE Trans. Microw. Theory Tech.*, vol. 61, no. 2, pp. 972–978, 2012.
N. Hosseini, M. Baghelani, and M. Daneshmand, "Discrete Microwave Spectroscopy using Planar Resonator," in *2019 IEEE Canadian Conference of Electrical and Computer Engineering (CCECE)*, 2019, pp. 1–4, doi: 10.1109/CCECE.2019.8861771.
M. Baghelani, N. Hosseini, and M. Daneshmand, "Selective measurement of water content in multivariable biofuel using microstrip split ring resonators," in *IEEE MTT-S International Microwave Symposium Digest*, 2020, vol. 2020-Augus, doi: 10.1109/IMS30576.2020.9223908.
G. Pandey, R. Kumar, and R. J. Weber, "Design and implementation of a self-calibrating, compact micro strip sensor for in-situ dielectric spectroscopy and data transmission," in IEEE Sensors*, 2013 IEEE*, 2013, pp. 1–4.
C. Schröder and O. Steinhauser, "Using fit functions in computational dielectric spectroscopy," *J. Chem. Phys.*, vol. 132, no. 24, p. 244109, 2010.
A. Talai, F. Steinhäußer, A. Bittner, U. Schmid, R. Weigel, and A. Koelpin, "A permittivity characterization method by detuned ring-resonators for bulk materials up to 110 GHz," in *2014 44th European Microwave Conference*, 2014, pp. 124–127.
X. Bao, I. Ocket, J. Bao, D. Kil, L. Brancato, and B. Nauwelaers, "Broadband dielectric spectroscopy measurements of liquids combining interdigital capacitor and coplanar waveguide," in *2017 47th European Microwave Conference (EuMC)*, 2017, pp. 946–949.
D. Havelka, O. Krivosudský, and M. Cifra, "Grounded coplanar waveguide-based 0.5–50 GHz sensor for dielectric spectroscopy," in *2017 47th European Microwave Conference (EuMC)*, 2017, pp. 950–953.
A. Fendri, H. Ghariani, and O. Kanoun, "Dielectric spectroscopy for assessment of water content in edible oils," in *2017 14th International Multi-Conference on Systems, Signals & Devices (SSD)*, 2017, pp. 728–732.

M. Nakamura, T. Tajima, K. Ajito, and H. Koizumi, “Selectivity-enhanced glucose measurement in multicomponent aqueous solution by broadband dielectric spectroscopy,” in *2016 IEEE MTT-S International Microwave Symposium (IMS)*, 2016, pp. 1–3.
M. A. Suster, D. Maji, N. Vitale, U. Gurkan, and P. Mohseni, “An RF/microwave microfluidic sensor for miniaturized dielectric spectroscopy based on sensor transmission characteristics,” in IEEE Sensors, 2015, pp. 1–4.
A. P. Saghati, J. S. Batra, J. Kameoka, and K. Entesari, “A metamaterial-inspired wideband microwave interferometry sensor for dielectric spectroscopy of liquid chemicals,” *IEEE Trans. Microw. Theory Tech.*, vol. 65, no. 7, pp. 2558–2571, 2017.
M. S. Venkatesh and G. S. V Raghavan, “An overview of dielectric properties measuring techniques,” *Can. Biosyst. Eng.*, vol. 47, no. 7, pp. 15–30, 2005.
Z. Lu, M. Lanagan, E. Manias, and D. D. Macdonald, “Two-port transmission line technique for dielectric property characterization of polymer electrolyte membranes,” *J. Phys. Chem. B*, vol. 113, no. 41, pp. 13551–13559, 2009.
S. Liu, I. Ocket, M. Cauwe, D. Schreurs, and B. Nauwelaers, “Sensitivity analysis of broadband on-wafer dielectric spectroscopy of yeast cell suspensions up to 110 GHz,” *IEEE Microw. Wirel. Components Lett.*, vol. 25, no. 3, pp. 199–201, 2015.
J. C. Booth *et al.*, “Quantitative permittivity measurements of nanoliter fluid volumes from 50 MHz to 40 GHz with microfluidic channels,” in *CPEM 2010*, 2010, pp. 353–354.
J. Mateu, N. Orloff, M. Rinehart, and J. C. Booth, “Broadband permittivity of liquids extracted from transmission line measurements of microfluidic channels,” in *2007 IEEE/MTT-S International Microwave Symposium*, 2007, pp. 523–526.
D. K. Ghodgaonkar, V. V Varadan, and V. K. Varadan, “Free-space measurement of complex permittivity and complex permeability of magnetic materials at microwave frequencies,” *IEEE Trans. Instrum. Meas.*, vol. 39, no. 2, pp. 387–394, 1990.
W. J. Ellison and J.-M. Moreau, “Open-ended coaxial probe: Model limitations,” *IEEE Trans. Instrum. Meas.*, vol. 57, no. 9, pp. 1984–1991, 2008.
I. M. Woodhead, I. Platt, J. H. Christie, and S. Krenek, “A broadband spectroscopic sensor probe,” *Int. J. Smart Sens. Intell. Syst.*, vol. 1, no. 2, pp. 459–469, 2008.
A. I. Mekhannikov, A. V Myl’nikov, and L. P. Maslennikova, “Calibration of a coaxial antenna-probe for microwave dielectric measurements,” *Meas. Tech.*, vol. 50, no. 4, pp. 425–428, 2007.
M. S. Boybay and O. M. Ramahi, “Material characterization using complementary split-ring resonators,” *IEEE Trans. Instrum. Meas.*, vol. 61, no. 11, pp. 3039–3046, 2012.
A. Ebrahimi, W. Withayachumnankul, S. Al-Sarawi, and D. Abbott, “High-sensitivity metamaterial-inspired sensor for microfluidic dielectric characterization,” *IEEE Sens. J.*, vol. 14, no. 5, pp. 1345–1351, 2013.
M. H. Zarifi and M. Daneshmand, “Liquid sensing in aquatic environment using high quality planar microwave resonator,” *Sensors Actuators B Chem.*, vol. 225, pp. 517–521, 2016.
M. Abdolrazzaghi, M. H. Zarifi, and M. Daneshmand, “Sensitivity enhancement of split ring resonator based liquid sensors,” in *2016 IEEE SENSORS*, 2016, pp. 1–3.
M. H. Zarifi, A. Sohrabi, P. M. Shaibani, M. Daneshmand, and T. Thundat, “Detection of volatile organic compounds using microwave sensors,” *IEEE Sens. J.*, vol. 15, no. 1, pp. 248–254, 2014.
P. Debye, “Zur theorie der spezifischen wärmen,” *Ann. Phys.*, vol. 344, no. 14, pp. 789–

839, 1912.
K. M. Chew, R. Sudirman, N. Seman, and C. Y. Yong, “Relaxation frequency and relaxation time estimation for phantom modeling by proposed fitting linear models,” in *2012 IEEE-EMBS Conference on Biomedical Engineering and Sciences*, 2012, pp. 911–915.
P. Q. Mantas, “Dielectric response of materials: extension to the Debye model,” *J. Eur. Ceram. Soc.*, vol. 19, no. 12, pp. 2079–2086, 1999.
Y. Feldman, A. Puzenko, Y. Ryabov, W. T. Coffey, and Y. P. Kalmykov, “Dielectic Relaxation Phenomena in Complex Materials,” *Adv. Chem. Phys.*, vol. 133, no. A, p. 1, 2006.
C. Cametti, “Dielectric and conductometric properties of highly heterogeneous colloidal systems,” *Riv. del Nuovo Cim. della Soc. Ital. di Fis.*, vol. 32, no. 5, pp. 185–260, 2009.
R. Hilfer, “Analytical representations for relaxation functions of glasses,” *J. Non. Cryst. Solids*, vol. 305, no. 1–3, pp. 122–126, 2002.
A. Khamzin, R. Nigmatullin, and I. Popov, “Justification of the empirical laws of the anomalous dielectric relaxation in the framework of the memory function formalism,” *Fract. Calc. Appl. Anal.*, vol. 17, no. 1, pp. 247–258, 2014.
R. Metzler and J. Klafter, “The random walk’s guide to anomalous diffusion: a fractional dynamics approach,” *Phys. Rep.*, vol. 339, no. 1, pp. 1–77, 2000.
K. S. Cole and R. H. Cole, “Dispersion and absorption in dielectrics I. Alternating current characteristics,” *J. Chem. Phys.*, vol. 9, no. 4, pp. 341–351, 1941.
K. S. Cole and R. H. Cole, “Dispersion and absorption in dielectrics II. Direct current characteristics,” *J. Chem. Phys.*, vol. 10, no. 2, pp. 98–105, 1942.
S. Havriliak and S. Negami, “A complex plane analysis of α-dispersions in some polymer systems,” in *Journal of Polymer Science Part C: Polymer Symposia*, 1966, vol. 14, no. 1, pp. 99–117.
V. A. Markel, “Introduction to the Maxwell Garnett approximation: tutorial,” *JOSA A*, vol. 33, no. 7, pp. 1244–1256, 2016.
B. Salski and M. Celuch, “On the equivalence between the Maxwell-Garnett mixing rule and the Debye relaxation formula,” *IEEE Trans. Microw. Theory Tech.*, vol. 60, no. 8, pp. 2352–2358, 2012.
A. H. Sihvola and I. V Lindell, “Chiral Maxwell-Garnett mixing formula,” *Electron. Lett.*, vol. 26, no. 2, pp. 118–119, 1990.
B. Salski and M. Celuch, “The debye rigorous equivalent of the Maxwell-Garnett mixing rule for effective modeling of carbon suspensions under MW irradiation,” in *2011 IEEE MTT-S International Microwave Symposium*, 2011, pp. 1–4.
M. H. Nisanci, F. de Paulis, M. Y. Koledintseva, J. L. Drewniak, and A. Orlandi, “From Maxwell Garnett to Debye model for electromagnetic simulation of composite dielectrics—PART II: Random cylindrical inclusions,” *IEEE Trans. Electromagn. Compat.*, vol. 54, no. 2, pp. 280–289, 2011.
A. Sihvola, “Mixing rules with complex dielectric coefficients,” *Subsurf. Sens. Technol. Appl.*, vol. 1, no. 4, pp. 393–415, 2000.

H. F. Cook, “Dielectric behaviour of human blood at microwave frequencies,” Nature, vol. 168, no. 4267, p. 247, 1951.

H. Choi, J. Nylon, S. Luzio, J. Beutler, and A. Porch, “Design of continuous non-invasive blood glucose monitoring sensor based on a microwave split ring resonator,” in 2014 IEEE MTT-S International Microwave Workshop Series on RF and Wireless Technologies for Biomedical and Healthcare Applications (IMWS-Bio2014), 2014, pp. 1–3.

A. Rohman, D. L. Setyaningrum, and S. Riyanto, “FTIR spectroscopy combined with partial least square for analysis of red fruit oil in ternary mixture system,” Int. J. Spectrosc., vol. 2014, 2014.

A. Kondyli and W. Schrader, “High-resolution GC/MS studies of a light crude oil fraction,” J. mass Spectrom., vol. 54, no. 1, pp. 47–54, 2019.

J. J. Pitt, “Principles and applications of liquid chromatography-mass spectrometry in clinical biochemistry,” Clin. Biochem. Rev., vol. 30, no. 1, p. 19, 2009.

D. Havelka, O. Krivosudský, and M. Cifra, “Grounded coplanar waveguide-based 0.5–50 GHz sensor for dielectric spectroscopy,” in 2017 47th European Microwave Conference (EuMC), 2017, pp. 950–953.

N. Bonanos, P. Pissis, and J. R. Macdonald, “Impedance spectroscopy of dielectrics and electronic conductors,” Charact. Mater., pp. 1–14, 2002.

A. Fendri, H. Ghariani, and O. Kanoun, “Dielectric spectroscopy for assessment of water content in edible oils,” in 2017 14th International Multi-Conference on Systems, Signals & Devices (SSD), 2017, pp. 728–732.

M. Nakamura, T. Tajima, K. Ajito, and H. Koizumi, “Selectivity-enhanced glucose measurement in multicomponent aqueous solution by broadband dielectric spectroscopy,” in 2016 IEEE MTT-S International Microwave Symposium (IMS), 2016, pp. 1–3.

M. A. Suster, D. Maji, N. Vitale, U. Gurkan, and P. Mohseni, “An RF/microwave microfluidic sensor for miniaturized dielectric spectroscopy based on sensor transmission characteristics,” in 2015 IEEE Sensors, 2015, pp. 1–4.

A. P. Saghati, J. S. Batra, J. Kameoka, and K. Entesari, “A metamaterial-inspired wideband microwave interferometry sensor for dielectric spectroscopy of liquid chemicals,” IEEE Trans. Microw. Theory Tech., vol. 65, no. 7, pp. 2558–2571, 2017.

M. Abdolrazzaghi, M. H. Zarifi, C. F. A. Floquet, and M. Daneshmand, “Contactless Asphaltene Detection Using an Active Planar Microwave Resonator Sensor,” Energy & Fuels, vol. 31, no. 8, pp. 8784–8791, 2017.

M. Nosrati, Z. Abbasi, M. Baghelani, S. Bhadra, and M. Daneshmand, “Locally Strong-Coupled Microwave Resonator Using PEMC Boundary for Distant Sensing Applications,” IEEE Trans. Microw. Theory Tech., 2019.

M. A. Karimi, M. Arsalan, and A. Shamim, “Design and dynamic characterization of an orientation insensitive microwave water-cut sensor,” IEEE Trans. Microw. Theory Tech., vol. 66, no. 1, pp. 530–539, 2017.

W.-T. S. Chen and R. R. Mansour, “Miniature gas sensor and sensor array with single-and dual-mode RF dielectric resonators,” IEEE Trans. Microw. Theory Tech., vol. 66, no. 8, pp. 3697–3704, 2018.

Z. Abbasi, P. Shariaty, M. Nosrati, Z. Hashisho, and M. Daneshmand, “Dual-Band Microwave Circuits for Selective Binary Gas Sensing System,” IEEE Trans. Microw. Theory Tech., 2019.

M. H. Zarifi, T. Thundat, and M. Daneshmand, “High resolution microwave microstrip resonator for sensing applications,” Sensors Actuators A Phys., vol. 233, pp. 224–230, 2015.

M. Daneshmand and M. H. ZARIFI, “Apparatus and method for high resolution complex permittivity sensing using high Q microwave sensors for lossy or non-lossy mediums and samples.” Google Patents, 08-Jan-2019.

G. Gennarelli, S. Romeo, M. R. Scarfi, and F. Soldovieri, “A microwave resonant sensor for concentration measurements of liquid solutions,” IEEE Sens. J., vol. 13, no. 5, pp. 1857–1864, 2013.

S. O. Nelson and A. W. Kraszewski, “Sensing pulverized material mixture proportions by resonant cavity measurements,” IEEE Trans. Instrum. Meas., vol. 47, no. 5, pp. 1201–1204, 1998.

A. Megriche, A. Belhadj, and A. Mgaidi, “Microwave dielectric properties of binary solvent wateralcohol, alcohol-alcohol mixtures at temperatures between-35° C and+ 35° C and dielectric relaxation studies,” Mediterr. J. Chem., vol. 1, no. 4, pp. 200–209, 2012.

M. Abdolrazzaghi, M. Daneshmand, and A. K. Iyer, “Strongly enhanced sensitivity in planar microwave sensors based on metamaterial coupling,” IEEE Trans. Microw. Theory Tech., vol. 66, no. 4, pp. 1843–1855, 2018.

K. M. Chew, R. Sudirman, N. Seman, and C. Y. Yong, “Relaxation frequency and relaxation time estimation for phantom modeling by proposed fitting linear models,” in 2012 IEEE-EMBS Conference on Biomedical Engineering and Sciences, 2012, pp. 911–915.

M. Y. Onimisi and J. T. Ikyumbur, “Comparative analysis of dielectric constant and loss factor of pure butan-1-ol and ethanol,” Am. J. Condens. Matter Phys., vol. 5, no. 3, pp. 69–75, 2015.

S. Mashimo, T. Umehara, and H. Redlin, “Structures of water and primary alcohol studied by microwave dielectric analyses,” J. Chem. Phys., vol. 95, no. 9, pp. 6257–6260, 1991.

T. Sato, A. Chiba, and R. Nozaki, “Dynamical aspects of mixing schemes in ethanol–water mixtures in terms of the excess partial molar activation free energy, enthalpy, and entropy of the dielectric relaxation process,” J. Chem. Phys., vol. 110, no. 5, pp. 2508–2521, 1999.

N. Hosseini, M. Baghelani, and M. Daneshmand, “Discrete Microwave Spectroscopy using Planar Resonator,” in 2019 IEEE Canadian Conference of Electrical and Computer Engineering (CCECE), 2019, pp. 1–4.

A. Talai, F. Steinhäußer, A. Bittner, U. Schmid, R. Weigel, and A. Koelpin, “A permittivity characterization method by detuned ring-resonators for bulk materials up to 110 GHz,” in 2014 44th European Microwave Conference, 2014, pp. 124–127.

J. L. Zamora, D. R. Vargas, Y. K. Hernández-Gómez, and G. A. Álvarez-Botero, “Improvement the permittivity determination in glyphosate-water mixture using CSRR as sensor,” in 2018 IEEE International Instrumentation and Measurement Technology Conference (I2MTC), 2018, pp. 1–5.

V. A. Markel, “Introduction to the Maxwell Garnett approximation: tutorial,” JOSA A, vol. 33, no. 7, pp. 1244–1256, 2016.

B. Salski and M. Celuch, “On the equivalence between the Maxwell-Garnett mixing rule and the Debye relaxation formula,” IEEE Trans. Microw. Theory Tech., vol. 60, no. 8, pp. 2352–2358, 2012.

A. H. Sihvola and I. V Lindell, “Chiral Maxwell-Garnett mixing formula,” Electron. Lett., vol. 26, no. 2, pp. 118–119, 1990.

B. Salski and M. Celuch, “The debye rigorous equivalent of the Maxwell-Garnett mixing rule for effective modeling of carbon suspensions under MW irradiation,” in 2011 IEEE MTT-S International Microwave Symposium, 2011, pp. 1–4.

M. H. Nisanci, F. de Paulis, M. Y. Koledintseva, J. L. Drewniak, and A. Orlandi, “From Maxwell Garnett to Debye model for electromagnetic simulation of composite dielectrics—PART II: Random cylindrical inclusions,” IEEE Trans. Electromagn. Compat., vol. 54, no. 2, pp. 280–289, 2011.

A. Kraszewski, “Prediction of the dielectric properties of two-phase mixtures,” J. Microw. Power, vol. 12, no. 3, pp. 216–222, 1977.

K. Lichtenecker, “Die Herleitung des logarithmischen Mischungsgesetzes aus allgemeinen Prinzipien der stationaren Stromung,” phys. Z, vol. 32, pp. 255–260, 1931.

E. M. Cheng, M. F. B. A. Malek, M. Ahmed, K. Y. You, K. Y. Lee, and H. Nornikman, “The use of dielectric mixture equations to analyze the dielectric properties of a mixture of rubber tire dust and rice husks in a microwave absorber,” Prog. Electromagn. Res., vol. 129, pp. 559–578, 2012.

A. Sihvola, “Mixing rules with complex dielectric coefficients,” Subsurf. Sens. Technol. Appl., vol. 1, no. 4, pp. 393–415, 2000.

T. P. Leão, E. Perfect, and J. S. Tyner, “Evaluation of lichtenecker’s mixing model for predicting effective permittivitty of soils at 50 MHZ,” Trans. ASABE, vol. 58, no. 1, pp. 83–91, 2015.

D. Havelka, O. Krivosudský, J. Průša, and M. Cifra, “Rational design of sensor for broadband dielectric spectroscopy of biomolecules,” Sensors Actuators B Chem., vol. 273, pp. 62–69, 2018.

M. Cifra, J. Průša, D. Havelka, and O. Krivosudský, “Water models in molecular dynamics simulation prediction of dielectric properties of biomaterials,” IEEE J. Electromagn. RF Microwaves Med. Biol., vol. 3, no. 2, pp. 97–104, 2018.

A. Jouyban, S. Soltanpour, and H.-K. Chan, “A simple relationship between dielectric constant of mixed solvents with solvent composition and temperature,” Int. J. Pharm., vol. 269, no. 2, pp. 353–360, 2004.

D. El Khaled, N. Novas, J. A. Gázquez, R. M. García, and F. Manzano-Agugliaro, "Alcohols and alcohols mixtures as liquid biofuels: A review of dielectric properties," Renew. Sustain. Energy Rev., vol. 66, pp. 556–571, 2016.

F. Motasemi, M. T. Afzal, A. A. Salema, J. Mouris, and R. M. Hutcheon, "Microwave dielectric characterization of switchgrass for bioenergy and biofuel," Fuel, vol. 124, pp. 151–157, 2014.

N. Hosseini, M. Baghelani and M. Daneshmand, "Selective Volume Fraction Sensing Using Resonant-Based Microwave Sensor and Its Harmonics," *IEEE T. Microw. Theory*, doi: 10.1109/TMTT.2020.2990139.

D. M. Pozar, Microwave engineering. John Wiley & Sons, 2009.

S. L. Van Berkel, "Characterization of printed transmission lines at high frequencies.", 2015. available at:

https://repository.tudelft.nl/islandora/object/uuid:dc192664-0720-486d-9423-e0b6d93f1de7

A. Sabban, and K.C.Gupta, "Characterization of radiation loss from microstrip discontinuities using a multiport network modeling approach," IEEE T. Microw. Theory, vol. 39, no.4, pp.705-712. Apr. 1991.

S. Haykin, Neural Networks and Learning Machines, 3/E. Pearson Education India, 2010.

A. F. Agarap, "Deep learning using rectified linear units (relu)," arXiv Prepr. arXiv1803.08375, 2018.

K. Moriarty, "Handbook for Handling, Storing, and Dispensing E85 and Other Ethanol-Gasoline Blends (Book)," National Renewable Energy Lab.(NREL), Golden, CO (United States), 2013.

M. Baghelani, N. Hosseini and M. Daneshmand, "Artificial Intelligence Assisted Non-Contact Microwave Sensor for Multivariable Biofuel Analysis," in IEEE Transactions on Industrial Electronics, doi: 10.1109/TIE.2020.3032870.

M. H. Zarifi, M. Rahimi, M. Daneshmand, T. Thundat, 2016. Microwave ring resonator-based non-contact interface sensor for oil sands applications, Sensors and Actuators B: Chemical, vol 224, pp 632-639, https://doi.org/10.1016/j.snb.2015.10.061

M. Schüßeler, C. Mandel, M. Puentes, and R.Jakoby, 2012. Metamaterial inspired microwave sensors, IEEE Microw. Mag., vol. 13, no. 2, pp. 57–68, https://doi.org/ 10.1109/MMM.2011.2181448

H.-J. Lee, and J.-G. Yook, 2008. Biosensing using split-ring resonators at microwave regime, Appl. Phys. Lett, vol. 92, no. 25, pp. 4103, https://doi.org/10.1063/1.2946656

R. Joffe, E. O. Kamenetskii, and R. Shavit, 2013. Novel microwave nearfield sensors for material characterization, biology, and nanotechnology, J. Appl. Phys., vol. 113, no. 6, pp. 63912, https://doi.org/10.1063/1.4791713

M. H. Zarifi, M. Daneshmand, 2016. Liquid sensing in aquatic environment using high quality planar microwave resonator, Sensors and Actuators B: Chemical, vol. 225, pp. 517-521, https://doi.org/10.1016/j.snb.2015.11.063

M. H. Zarifi, P. Shariaty, Zaher Hashisho, Mojgan Daneshmand, 2017. A non-contact microwave sensor for monitoring the interaction of zeolite 13X with CO2 and CH4 in gaseous streams, Sensors and Actuators B: Chemical, vol. 238, pp. 1240-1247, https://doi.org/10.1016/j.snb.2016.09.047

M. H. Zarifi and M. Daneshmand, 2016. Wide dynamic range microwave planar coupled ring resonator for sensing applications, Appl. Phys. Lett. 108, 232906, https://doi.org/10.1063/1.4953465

A. K, Jha, N, Delmonte, A, Lamecki, M, Mrozowski, M, Bozzi, 2019. Design of microwave-based angular displacement sensor, IEEE Microw. Wireless Compon. Lett., vol. 29, no4, pp. 306-308. https://doi.org/ 10.1109/LMWC.2019.2899490

J. Naqui and F. Martín, 2013. Transmission lines loaded with bisymmetric resonators and their application to angular displacement and velocity sensors, IEEE Trans. Microw. Theory Techn., vol. 61, no. 12, pp. 4700–4713. https://doi.org/ 10.1109/TMTT.2013.2285356

J. Naqui, J. Coromina, A. Karami-Horestani, C. Fumeaux, and F. Martín, 2015. Angular displacement and velocity sensors based on coplanar waveguides (CPWs) loaded with S-

shaped split ring resonator (S-SRR), Sensors, vol. 15, pp. 9628–9650. https://doi.org/ 10.3390/s150509628.

A.K. Horestani, C. Fumeaux, S.F. Al-Sarawi, and D. Abbott, 2013. Displacement sensor based on diamond-shaped tapered split ring resonator, IEEE Sens. J., vol. 13, pp. 1153–1160. https://doi.org/ 10.1109/JSEN.2012.2231065

J. Naqui and F. Martín, 2014. Angular displacement and velocity sensors based on electric-LC (ELC) loaded microstrip lines," IEEE Sensors J., vol. 14, no. 4, pp. 939–940. https://doi.org/ 10.1109/JSEN.2013.2295518

A.K. Horestani, D. Abbott, and C. Fumeaux, 2013. Rotation sensor based on horn-shaped split ring resonator," IEEE Sens. J., vol. 13, pp. 3014–3015. https://doi.org/ 10.1109/JSEN.2013.2264804

A. K. Horestani, J. Naqui, Z. Shaterian, D. Abbott, C. Fumeaux, and F. Martín 2014. Two-dimensional alignment and displacement sensor based on movable broadside-coupled split ring resonators, Sensors and Actuators A, vol. 210, pp. 18–24. https://doi.org/ 10.1016/j.sna.2014.01.030

A.K. Horestani, J. Naqui, D. Abbott, C. Fumeaux, and F. Martín, 2014. Two-dimensional displacement and alignment sensor based on reflection coefficients of open microstrip lines loaded with split ring resonators," Elec. Lett., vol. 50, pp. 620–622. https://doi.org/ 10.1049/el.2014.0572

P. Vélez, J. Muñoz-Enano, M. Gil, J. Mata-Contreras, and F. Martín, 2019. Differential microfluidic sensors based on dumbbell-shaped defect ground structures in microstrip technology: analysis, optimization, and applications", Sensors, vol. 19, pp. 3189. https://doi.org/ 10.3390/s19143189

A. Ebrahimi, J. Scott and K. Ghorbani, 2018. Differential sensors using microstrip lines loaded with two split ring resonators," IEEE Sensors J., vol. 18, pp. 5786-5793. https://doi.org/ 10.1109/JSEN.2018.2840691

A. Ebrahimi, J. Scott, K. Ghorbani, 2018. Transmission Lines Terminated with LC Resonators for Differential Permittivity Sensing, IEEE Microw. Wireless Compon. Lett., vol. 28, no. 12, pp. 1149-1151. https://doi.org/ 10.1109/LMWC.2018.2875996

P. Vélez, J. Muñoz-Enano, K. Grenier, J. Mata-Contreras, D. Dubuc, F. Martín, 2019. Split ring resonator (SRR) based microwave fluidic sensor for electrolyte concentration measurements, IEEE Sensors J., vol. 19, no. 7, pp. 2562-2569. https://doi.org/ 10.1109/JSEN.2018.2890089

P. Vélez, K. Grenier, J. Mata-Contreras, D. Dubuc and F. Martín, 2018. Highly-Sensitive Microwave Sensors Based on Open Complementary Split Ring Resonators (OCSRRs) for Dielectric Characterization and Solute Concentration Measurement in Liquids, IEEE Access, vol. 6, pp. 48324-48338. https://doi.org/10.1109/ACCESS.2018.2867077

C.-S. Lee and C.-L. Yang, 2014. Complementary split-ring resonators for measuring dielectric constants and loss tangents, IEEE Microw. Wireless Compon. Lett., vol. 24, no. 8, pp. 563−565. https://doi.org/ 10.1109/LMWC.2014.2318900

A. Ebrahimi, W. Withayachumnankul, S. Al-Sarawi, D. Abbott, 2014. High-sensitivity metamaterial-inspired sensor for microfluidic dielectric characterization, IEEE Sensors J., vol. 14, no. 5, pp. 1345−1351. https://doi.org/10.1109/JSEN.2013.2295312

C.-L. Yang, C.-S. Lee, K.-W. Chen, and K.-Z. Chen, 2016. Noncontact measurement of complex permittivity and thickness by using planar resonators, IEEE Trans. Microw. Theory Techn., vol. 64, no.1, pp. 247−257. https://doi.org/ 10.1109/TMTT.2015.2503764

L. Su, J. Mata-Contreras, P. Vélez, A. Fernández-Prieto and F. Martín, 2018. Analytical method to estimate the complex permittivity of oil Samples, Sensors, vol.18no. 4, pp. 984. https://doi.org/10.3390/s18040984

M. S. Boybay and O. M. Ramahi, 2012. Material characterization using complementary split-ring resonators, IEEE Trans. Instrum. Meas., vol. 61, no. 11, pp. 3039−3046. https://doi.org/ 10.1109/TIM.2012.2203450

P. Vélez, L. Su, K. Grenier, J. Mata-Contreras, D. Dubuc, and F. Martín, 2017. Microwave microfluidic sensor based on a microstrip splitter/combiner configuration and split ring resonators (SRR) for dielectric characterization of liquids, IEEE Sensors J., vol. 17, pp. 6589-6598. https://doi.org/10.1109/JSEN.2017.2747764

J. B. Pendry, A. J. Holden, D. J. Robbins, and W. J. Stewart, 1999. Magnetism from conductors and enhanced nonlinear phenomena, IEEE Trans. Microwave Theory Tech., vol. 47, pp. 2075-2084, https://doi.org/ 10.1109/22.798002

P. Gay-Balmaz and O.J.F. Martin, 2002. Electromagnetic resonances in individual and coupled split-ring resonators, J. Appl. Phys., vol. 92, pp. 2929-2936, https://doi.org/10.1063/1.1497452

M. Abdolrazzaghi, M. H. Zarifi, and M. Daneshmand, 2016. Sensitivity enhancement of split ring resonator based liquid sensors," 2016 IEEE SENSORS, Orlando, FL, pp. 1-3. https://doi.org/ 0.1109/ICSENS.2016.7808957

M. H. Zarifi, A. Gholidoust, M. Abdolrazzaghi, P. Shariaty, Z. Hashisho, M. Daneshmand, 2018. Sensitivity enhancement in planar microwave active-resonator using metal organic framework for CO2 detection, Sensors and Actuators B: Chemical, vol. 255, no. 2, pp. 1561-1568, https://doi.org/10.1016/j.snb.2017.08.169

M. H. Zarifi, P. Shariaty, M. Abdolrazzaghi, Z. Hashisho, M. Daneshmand, 2016. Particle size characterization using a high-resolution planar resonator sensor in a lossy medium, Sensors and Actuators B: Chemical, vol. 234, pp. 332-337, https://doi.org/10.1016/j.snb.2016.04.130

M. Abdolrazzaghi, M. Daneshmand and A. K. Iyer, 2018. Strongly Enhanced Sensitivity in Planar Microwave Sensors Based on Metamaterial Coupling, in IEEE Trans. Microwave Theory Tech., vol. 66, no. 4, pp. 1843-1855, https://doi.org/ 10.1109/TMTT.2018.2791942

M. Nosrati and M. Daneshmand, 2017. Substrate Integrated Waveguide L-Shaped Iris for Realization of Transmission Zero and Evanescent-Mode Pole, in IEEE Trans. Microwave Theory Tech., vol. 65, no. 7, pp. 2310-2320. https://doi.org/10.1109/TMTT.2017.2679011.

M. H. Zarifi et al., 2018. A Microwave Ring Resonator Sensor for Early Detection of Breaches in Pipeline Coatings, IEEE Transactions on Industrial Electronics, vol. 65, no. 2, pp. 1626-1635. https://doi.org/10.1109/TIE.2017.2733449

M. H. Zarifi, S. Deif, M. Daneshmand, 2017. Wireless passive RFID sensor for pipeline integrity monitoring, Sensors and Actuators A: Physical, vol. 261, pp.24-29. https://doi.org/10.1016/j.sna.2017.04.006.

S. Deif, B. Leier, M. Snow, M. Daneshmand, 2018. Microwave Sensor Array for Corrosion Prediction in Steel Tank Bottoms, 2018 12th International Pipeline Conference, American Soc. of Mechanical Engineer, pp.1-6, https://doi.org/10.1115/IPC2018-78224

N. Hosseini, M. Baghelani and M. Daneshmand, 2019. "Discrete Microwave Spectroscopy using Planar Resonator," IEEE Canadian Conference of Electrical and Computer Engineering (CCECE), Edmonton, AB, Canada, 2019, pp. 1-4. doi: 10.1109/CCECE.2019.8861771

R. A. Alahnomi, Z. Zakaria, E. Ruslan, S. R. Ab Rashid and A. A. Mohd Bahar, 2017. High-Q Sensor Based on Symmetrical Split Ring Resonator with Spurlines for Solids Material Detection," in IEEE Sensors Journal, vol. 17, no. 9, pp. 2766-2775. https://doi.org/10.1109/JSEN.2017.2682266

G. Galindo-Romera, F. Javier Herraiz-Martínez, M. Gil, J. J. Martínez-Martínez and D. Segovia-Vargas, 2016. Submersible Printed Split-Ring Resonator-Based Sensor for Thin-Film Detection and Permittivity Characterization, in IEEE Sensors Journal, vol. 16, no. 10, pp.3587-3596. https://doi.org/10.1109/JSEN.2016.2538086.

V. Sekar, W. J. Torke, S. Palermo and K. Entesari, 2012. A Self-Sustained Microwave System for Dielectric-Constant Measurement of Lossy Organic Liquids, *IEEE Transactions on Microwave Theory and Techniques*, vol. 60, no. 5, pp. 1444-1455.**https://doi.org/**doi: 10.1109/TMTT.2012.2187066

N. Wiwatcharagoses, K. Y. Park, J. A. Hejase, L. Williamson, and P. Chahal, 2011. Microwave artificially structured periodic media microfluidic sensor," in Proc. IEEE 61st Electron. Compon. Technol. Conf. (ECTC), pp. 1889–1893. **https://doi.org/**doi: 10.1109/ECTC.2011.5898773

R. A. Alahnomi, Z. Zakaria, E. Ruslan, A. A. Mohd Bahar, and S. R. Ab Rashid, 2016. High sensitive microwave sensor based on symmetrical split ring resonator for material characterization. Microw. Opt. Technol. Lett., vol. 58, pp. 2106-2110. https://doi.org/10.1002/mop.29979.

C. Liu and Y. Pu, 2008. A microstrip resonator with slotted ground plane for complex permittivity measurements of liquids, IEEE Microw. Wireless Compon. Lett., vol. 18, no. 4, pp. 257–259. **https://doi.org/**doi: 10.1109/LMWC.2008.918894

E. Dykesteen, "Handbook of Multiphase Metering," *Nor. Soc. Oil Gas Meas. NFOGM, Revis.*, vol. 2, 2005.

Z. Aghaeifar, S. Strand, T. Puntervold, T. Austad, and F. M. Sajjad, "Smart Water injection strategies for optimized EOR in a high temperature offshore oil reservoir," *J. Pet. Sci. Eng.*, vol. 165, pp. 743–751, 2018.

A. Fakhru'l-Razi, A. Pendashteh, L. C. Abdullah, D. R. A. Biak, S. S. Madaeni, and Z. Z. Abidin, "Review of technologies for oil and gas produced water treatment," *J. Hazard. Mater.*, vol. 170, no. 2–3, pp. 530–551, 2009.

S. K. Panda, M. A. Mohammed, A. Cadix, M. Alaboalirat, C. Poix-Davaine, and E. Duran, "Size exclusion chromatography reveals a key parameter of demulsifiers for enhanced water separation from crude oil emulsions," *Fuel*, vol. 257, p. 115881, 2019.

A. G. Ryder, "Assessing the maturity of crude petroleum oils using total synchronous fluorescence scan spectra," *J. Fluoresc.*, vol. 14, no. 1, pp. 99–104, 2004.

P. Rostami, M. F. Mehraban, M. Sharifi, M. Dejam, and S. Ayatollahi, "Effect of water salinity on oil/brine interfacial behaviour during low salinity waterflooding: A mechanistic study," *Petroleum*, vol. 5, no. 4, pp. 367–374, 2019.

T. E. Chávez-Miyauchi, A. Firoozabadi, and G. G. Fuller, “Nonmonotonic elasticity of the crude oil–brine interface in relation to improved oil recovery,” *Langmuir*, vol. 32, no. 9, pp. 2192–2198, 2016.

Y. Guoxiang, L. Ü. Xiaoping, P. Fei, H. Pingfang, and S. Xuan, “Pretreatment of crude oil by ultrasonic-electric united desalting and dewatering,” *Chinese J. Chem. Eng.*, vol. 16, no. 4, pp. 564–569, 2008.

H. Moghadas, M. Daneshmand, and P. Mousavi, “A passive non-contact microwave loop resonance sensor for liquid interface,” *Sensors Actuators B Chem.*, vol. 241, pp. 96–98, 2017.

S. Winecki *et al.*, “Improved oil recovery sensor,” *Sensors Actuators A Phys.*, vol. 295, pp. 308–316, 2019.

P. Sharma, L. Lao, and G. Falcone, “A microwave cavity resonator sensor for water-in-oil measurements,” *Sensors Actuators B Chem.*, vol. 262, pp. 200–210, 2018.

S. I. M. Sheikh, E. E. M. Hassan, and S. Iqbal, “Capacitance Based Monitoring of a Three-phase Crude-Oil Flow,” *IEEE Trans. Instrum. Meas.*, 2019.

Q. Liu, B. Chu, J. Peng, and S. Tang, “A Visual Measurement of Water Content of Crude Oil Based on Image Grayscale Accumulated Value Difference,” *Sensors*, vol. 19, no. 13, p. 2963, 2019.

M. Baghelani, Z. Abbasi, and M. Daneshmand, “Noncontact high sensitivity chipless tag microwave resonator for bitumen concentration measurement at high temperatures,” *Fuel*, vol. 265, p. 116916, 2020.

M. Abdolrazzaghi, and Daneshmand, M.," A phase-Noise reduced microwave oscillator sensor with enhanced limit of detection using active filter," IEEE Microwave and Wireless Components Letters, 28(9), pp.837-839, 2018.

S. Kiani, P. Rezaei, and M. Navaei. "Dual-sensing and dual-frequency microwave SRR sensor for liquid samples permittivity detection." Measurement (2020): 107805.

Z. Abbasi, M. Baghelani, M. Nosrati, A. Sanati-Nezhad, and M. Daneshmand, “Real-Time Non-Contact Integrated Chipless RF Sensor for Disposable Microfluidic Applications,” *IEEE J. Electromagn. RF Microwaves Med. Biol.*, 2019.

M. Nosrati, Z. Abbasi, M. Baghelani, S. Bhadra, and M. Daneshmand, “Locally Strong-Coupled Microwave Resonator Using PEMC Boundary for Distant Sensing Applications,” *IEEE Trans. Microw. Theory Tech.*, vol. 67, no. 10, pp. 4130–4139, 2019.

M. Abdolrazzaghi, and M. Daneshmand," Dual active resonator for dispersion coefficient measurement of asphaltene nano-particles," IEEE Sensors Journal, 17(22), pp.7248-7256, 2017.

T.-G. Kang, J.-K. Park, B.-H. Kim, J. J. Lee, H. H. Choi, H.-J. Lee, and J.-G. Yook. "Microwave characterization of conducting polymer PEDOT: PSS film using a microstrip line for humidity sensor application." Measurement 137 (2019): 272-277.

N. Hosseini, M. Baghelani, and M. Daneshmand, “Discrete Microwave Spectroscopy using Planar Resonator,” in *2019 IEEE Canadian Conference of Electrical and Computer Engineering (CCECE)*, 2019, pp. 1–4.

N. Hosseini, M. Baghelani, and M. Daneshmand," Selective Volume Fraction Sensing Using Resonant-Based Microwave Sensor and Its Harmonics," IEEE Trans. Microw. Theory Tech., May 2020, DOI: 10.1109/TMTT.2020.2990139

M. A. Karimi, M. Arsalan, and A. Shamim, “Low cost and pipe conformable microwave-based water-cut sensor,” *IEEE Sens. J.*, vol. 16, no. 21, pp. 7636–7645, 2016.

G. Andria, F. Attivissimo, A. Di Nisio, A. Trotta, S. M. Camporeale, and P. Pappalardi. "Design of a microwave sensor for measurement of water in fuel contamination." Measurement 136 (2019): 74-81.

P. S. Mun, H. N. Ting, Y. B. Chong, and T. A. Ong, “Dielectric properties of glycosuria at 0.2-50 GHz using microwave spectroscopy,” *J. Electromagn. Waves Appl.*, vol. 29, no. 17, pp. 2278–2292, 2015.

L. M. Middelburg *et al.*, “Multi-domain spectroscopy for composition measurement of water-containing bio-ethanol fuel,” *Fuel Process. Technol.*, vol. 167, pp. 127–135, 2017.

W. J. Ellison *et al.*, “A comparison of ocean emissivity models using the Advanced Microwave Sounding Unit, the Special Sensor Microwave Imager, the TRMM Microwave Imager, and airborne radiometer observations,” *J. Geophys. Res. Atmos.*, vol. 108, no. D21, 2003.

M. Baghelani, N. Hosseini, M. Daneshmand, “Non-contact real-time water and brine concentration monitoring in crude oil based on multi-variable analysis of microwave resonators,” Measurement. 2021 Jun 1;177:109286.

N. Hosseini, SS. Olokede, M. Daneshmand, “A novel miniaturized asymmetric CPW split ring resonator with extended field distribution pattern for sensing applications,” Sensors and Actuators A: Physical. 2020 Apr 1;304:111769.

H. S. Son, Y. S. Hong, W. M. Park, M. A. Yu, and C. H. Lee, “A novel approach for estimating sugar and alcohol concentrations in wines using refractometer and hydrometer,” *J. Food Sci.*, vol. 74, no. 2, pp. C106–C111, 2009.

C. Lamy, A. Lima, V. LeRhun, F. Delime, C. Coutanceau, and J.-M. Léger, “Recent advances in the development of direct alcohol fuel cells (DAFC),” *J. Power Sources*, vol. 105, no. 2, pp. 283–296, 2002.

S. Piermarini, G. Volpe, M. Esti, M. Simonetti, and G. Palleschi, “Real time monitoring of alcoholic fermentation with low-cost amperometric biosensors,” *Food Chem.*, vol. 127, no. 2, pp. 749–754, 2011.

G. McLeod *et al.*, “A comparison of variate pre-selection methods for use in partial least squares regression: a case study on NIR spectroscopy applied to monitoring beer fermentation,” *J. Food Eng.*, vol. 90, no. 2, pp. 300–307, 2009.

I. S. Daoud and B. A. Searle, “On-line monitoring of brewery fermentation by measurement of CO2 evolution rate,” *J. Inst. Brew.*, vol. 96, no. 5, pp. 297–302, 1990.

A. Ktenioudaki, F. Butler, U. Gonzales-Barron, U. Mc Carthy, and E. Gallagher, “Monitoring the dynamic density of wheat dough during fermentation,” *J. Food Eng.*, vol. 95, no. 2, pp. 332–338, 2009.

L. Wynne, S. Clark, M. J. Adams, and N. W. Barnett, “Compositional dynamics of a commercial wine fermentation using two-dimensional FTIR correlation analysis,” *Vib. Spectrosc.*, vol. 44, no. 2, pp. 394–400, 2007.

H.-W. Lee *et al.*, “Development of novel on-line capillary gas chromatography-based analysis method for volatile organic compounds produced by aerobic fermentation,” *J. Biosci. Bioeng.*, vol. 127, no. 1, pp. 121–127, 2019.

J. Fernández-Novales, M.-I. López, M.-T. Sánchez, J.-A. García, and J. Morales, “A

feasibility study on the use of a miniature fiber optic NIR spectrometer for the prediction of volumic mass and reducing sugars in white wine fermentations," *J. Food Eng.*, vol. 89, no. 3, pp. 325–329, 2008.

J. Shi, D. Feng, and Y. Li, "Biosensors in fermentation applications," *Ferment. Process.*, p. 145, 2017.

M. Baghelani, Z. Abbasi, and M. Daneshmand, "Noncontact high sensitivity chipless tag microwave resonator for bitumen concentration measurement at high temperatures," *Fuel*, vol. 265, p. 116916, 2020.

M. Baghelani, Z. Abbasi, M. Daneshmand, and P. E. Light, "Non-invasive continuous-time glucose monitoring system using a chipless printable sensor based on split ring microwave resonators," *Sci. Rep.*, vol. 10, no. 1, pp. 1–15, 2020.

M. Baghelani, N. Hosseini, and M. Daneshmand, "Artificial Intelligence Assisted Non-Contact Microwave Sensor for Multivariable Biofuel Analysis," *IEEE Trans. Ind. Electron.*, 2020.

P. Sharma, L. Lao, and G. Falcone, "A microwave cavity resonator sensor for water-in-oil measurements," *Sensors Actuators B Chem.*, vol. 262, pp. 200–210, 2018.

Z. Abbasi, M. Baghelani, M. Nosrati, A. Sanati-Nezhad, and M. Daneshmand, "Real-time non-contact integrated chipless RF sensor for disposable microfluidic applications," *IEEE J. Electromagn. RF Microwaves Med. Biol.*, 2019.

N. Chudpooti *et al.*, "In-Situ Self-Aligned NaCl-Solution Fluidic-Integrated Microwave Sensors for Industrial and Biomedical Applications," *IEEE Access*, vol. 8, pp. 188897–188907, 2020.

A. Ebrahimi, F. J. Tovar-Lopez, J. Scott, and K. Ghorbani, "Differential microwave sensor for characterization of glycerol–water solutions," *Sensors Actuators B Chem.*, vol. 321, p. 128561, 2020.

A. Ebrahimi, J. Scott, and K. Ghorbani, "Microwave reflective biosensor for glucose level detection in aqueous solutions," *Sensors Actuators A Phys.*, vol. 301, p. 111662, 2020.

P. Vélez, J. Munoz-Enano, K. Grenier, J. Mata-Contreras, D. Dubuc, and F. Martín, "Split ring resonator-based microwave fluidic sensors for electrolyte concentration measurements," *IEEE Sens. J.*, vol. 19, no. 7, pp. 2562–2569, 2018.

A. Ebrahimi, W. Withayachumnankul, S. F. Al-Sarawi, and D. Abbott, "Microwave microfluidic sensor for determination of glucose concentration in water," in *2015 IEEE 15th Mediterranean Microwave Symposium (MMS)*, 2015, pp. 1–3.

N. Hosseini, S. S. Olokede, and M. Daneshmand, "A novel miniaturized asymmetric CPW split ring resonator with extended field distribution pattern for sensing applications," *Sensors Actuators, A Phys.*, vol. 304, Apr. 2020, doi: 10.1016/j.sna.2019.111769.

N. Hosseini, M. Baghelani, and M. Daneshmand, "Selective Volume Fraction Sensing Using Resonant- Based Microwave Sensor and its Harmonics," *IEEE Trans. Microw. Theory Tech.*, Sep. 2020, doi: 10.1109/TMTT.2020.2990139.

M. Baghelani, N. Hosseini, and M. Daneshmand, "Selective measurement of water content in multivariable biofuel using microstrip split ring resonators," in *IEEE MTT-S International Microwave Symposium Digest*, 2020, vol. 2020-Augus, doi: 10.1109/IMS30576.2020.9223908.

M. Benlamri *et al.*, "Planar microwave resonator with electrodeposited ZnO thin film for

ultraviolet detection," *Semicond. Sci. Technol.*, vol. 35, no. 2, p. 25003, 2019.

Z. Li, Z. Meng, A. Haigh, P. Wang, and A. Gibson, "Characterisation of water in honey using a microwave cylindrical cavity resonator sensor," *J. Food Eng.*, vol. 292, p. 110373.

K. Nakagawa and S. Kono, "Monitoring of primary drying in the freeze-drying process using an open-ended coaxial microwave resonator," *J. Food Eng.*, p. 110163, 2020.

Z. Abbasi, H. Niazi, M. Abdolrazzaghi, W. Chen, and M. Daneshmand, "Monitoring pH Level Using High-Resolution Microwave Sensor for Mitigation of Stress Corrosion Cracking in Steel Pipelines," *IEEE Sens. J.*, vol. 20, no. 13, pp. 7033–7043, 2020.

P. Velez, K. Grenier, J. Mata-Contreras, D. Dubuc, and F. Martín, "Highly-sensitive microwave sensors based on open complementary split ring resonators (OCSRRs) for dielectric characterization and solute concentration measurement in liquids," *IEEE Access*, vol. 6, pp. 48324–48338, 2018.

A. Ebrahimi, J. Scott, and K. Ghorbani, "Ultrahigh-sensitivity microwave sensor for microfluidic complex permittivity measurement," *IEEE Trans. Microw. Theory Tech.*, vol. 67, no. 10, pp. 4269–4277, 2019.

M. Abdolrazzaghi and M. Daneshmand, "Exploiting Sensitivity Enhancement in Microwave Planar Sensors Using Intermodulation Products With Phase Noise Analysis," *IEEE Trans. Circuits Syst. I Regul. Pap.*, 2020.

A. A. M. Bahar, Z. Zakaria, S. R. Ab Rashid, A. A. M. Isa, and R. A. Alahnomi, "High-efficiency microwave planar resonator sensor based on bridge split ring topology," *IEEE Microw. Wirel. components Lett.*, vol. 27, no. 6, pp. 545–547, 2017.

L. Wang, X. Q. Lin, F. Cheng, Y. Fan, and Z. B. Zhu, "Electric split-ring resonator based on double-sided parallel-strip line," *IEEE Antennas Wirel. Propag. Lett.*, vol. 12, pp. 69–71, 2013.

M. Y. Onimisi and J. T. Ikyumbur, "Comparative analysis of dielectric constant and loss factor of pure butan-1-ol and ethanol," *Am. J. Condens. Matter Phys.*, vol. 5, no. 3, pp. 69–75, 2015.

T. Ikyumbur, M. Onimisi, S. Abdu, E. Hemba, and Z. Kirji, "Optimization in the computation of dielectric constant of methanol using Debye relaxation method," *Br. J. Appl. Sci. Technol*, vol. 19, pp. 1–10, 2017.

S. Mashimo, T. Umehara, and H. Redlin, "Structures of water and primary alcohol studied by microwave dielectric analyses," *J. Chem. Phys.*, vol. 95, no. 9, pp. 6257–6260, 1991, doi: 10.1063/1.461546.

T. Sato, A. Chiba, and R. Nozaki, "Dynamical aspects of mixing schemes in ethanol–water mixtures in terms of the excess partial molar activation free energy, enthalpy, and entropy of the dielectric relaxation process," *J. Chem. Phys.*, vol. 110, no. 5, pp. 2508–2521, 1999.

N. Hosseini, M. Baghelani, and M. Daneshmand, "Discrete Microwave Spectroscopy using Planar Resonator," 2019, doi: 10.1109/CCECE.2019.8861771.

S. Mohammadi, A. V. Nadaraja, D. J. Roberts, and M. H. Zarifi, "Real-time and hazard-free water quality monitoring based on microwave planar resonator sensor," *Sensors Actuators A Phys.*, vol. 303, p. 111663, 2020.

S. Harnsoongnoen and A. Wanthong, "A non-contact planar microwave sensor for detection of high-salinity water containing NaCl, KCl, CaCl2, MgCl2 and Na2CO3," *Sensors Actuators B Chem.*, vol. 331, p. 129355, 2021.

A. A. Abduljabar, H. Hamzah, and A. Porch, “Multi-resonators, microwave microfluidic sensor for liquid characterization,” *Microw. Opt. Technol. Lett.*, vol. 63, no. 4, pp. 1042–1047, 2021.

X. Bao *et al.*, “Integration of interdigitated electrodes in split-ring resonator for detecting liquid mixtures,” *IEEE Trans. Microw. Theory Tech.*, vol. 68, no. 6, pp. 2080–2089, 2020.

S. Mohammadi *et al.*, “Gold Coplanar Waveguide Resonator Integrated With a Microfluidic Channel for Aqueous Dielectric Detection,” *IEEE Sens. J.*, vol. 20, no. 17, pp. 9825–9833, 2020.

N. Sharafadinzadeh, M. Abdolrazzaghi, and M. Daneshmand, “Highly sensitive microwave split ring resonator sensor using gap extension for glucose sensing,” in *2017 IEEE MTT-S International Microwave Workshop Series on Advanced Materials and Processes for RF and THz Applications (IMWS-AMP)*, 2017, pp. 1–3, doi: 10.1109/IMWS-AMP.2017.8247400.

N. Hosseini, and M. Baghelani, "Selective real-time non-contact multi-variable water-alcohol-sugar concentration analysis during fermentation process using microwave split-ring resonator based sensor." Sensors and Actuators A: Physical 325 (2021): 112695.

Appendix A

The single Debye model at 23℃ temperature for different kinds of alcohols can be presented as below:

The methanol single Debye model

$$\varepsilon_r = 5.5 + \frac{27.3}{1+j2\pi f(55\times10^{-12})}$$

The ethanol single Debye model

$$\varepsilon_r = 3.6 + \frac{19.2}{1+j2\pi f(152\times10^{-12})}$$

And the propanol single Debye is

$$\varepsilon_r = 3 + \frac{17.4}{1+j2\pi f(275\times10^{-12})}$$

By combining Eq. (3-11) and Eq. (3-16) and substituting equations (3-17 to 19), the detailed equation of the volume fraction analysis for the three mentioned materials could be given as follows:

$$\begin{bmatrix} V_1 \\ \vdots \\ V_i \end{bmatrix}_{i\times1} = \begin{bmatrix} \ln\left(\frac{\ln\left(\frac{f_{11}-a}{b}\right)+\alpha{\varepsilon_{sub}}^{P2}}{-\beta}\right)^{1/P1} & \cdots & \ln\left(\frac{\ln\left(\frac{f_{1i}-a}{b}\right)+\alpha{\varepsilon_{sub}}^{P2}}{-\beta}\right)^{1/P1} \\ \vdots & \ddots & \vdots \\ \ln\left(\frac{\ln\left(\frac{f_{n1}-a}{b}\right)+\alpha{\varepsilon_{sub}}^{P2}}{-\beta}\right)^{1/P1} & \cdots & \ln\left(\frac{\ln\left(\frac{f_{ni}-a}{b}\right)+\alpha{\varepsilon_{sub}}^{P2}}{-\beta}\right)^{1/P1} \\ 1 & & 1 \end{bmatrix}^{-1}_{i\times i}$$

$$\times \begin{bmatrix} \ln\left(\frac{\left(\frac{{f_1}_{mix}-a}{b}\right)+\alpha {\varepsilon_{sub}}^{P2}}{-\beta}\right)^{1/P1} \\ \vdots \\ \ln\left(\frac{\left(\frac{{f_n}_{mix}-a}{b}\right)+\alpha {\varepsilon_{sub}}^{P2}}{-\beta}\right)^{1/P1} \\ 1 \end{bmatrix}_{i\times 1}$$

Appendix B

List of Contributions (2019-2021)

Journal papers

[J1] N. Hosseini, M. Baghelani and M. Daneshmand, "Selective Volume Fraction Sensing Using Resonant- Based Microwave Sensor and its Harmonics," in *IEEE Transactions on Microwave Theory and Techniques*, vol. 68, no. 9, pp. 3958-3968, Sept. 2020, doi: 10.1109/TMTT.2020.2990139.

[J2] M. Baghelani, N. Hosseini and M. Daneshmand, "Artificial Intelligence Assisted Non-Contact Microwave Sensor for Multivariable Biofuel Analysis," in *IEEE Transactions on Industrial Electronics*, doi: 10.1109/TIE.2020.3032870.

[J3] N. Hosseini, SS Olokede, M. Daneshmand. A novel miniaturized asymmetric CPW split ring resonator with extended field distribution pattern for sensing applications. Sensors and Actuators A: Physical. 2020 Apr 1;304:111769.

[J4] M. Baghelani, N. Hosseini and M. Daneshmand. Non-contact real-time water and brine concentration monitoring in crude oil based on multivariable analysis of microwave resonators. Measurement. 2021 Jun 1;177:109286.

[J5] N. Hosseini, M. Baghelani. Selective real-time non-contact multivariable water-alcohol-sugar concentration analysis during fermentation process using microwave split-ring resonator based sensor. Sensors and Actuators A: Physical. 2021 Jul 1;325:112695.

Conference papers

[C1] N. Hosseini, M. Baghelani and M. Daneshmand, "Discrete Microwave Spectroscopy using Planar Resonator," *2019 IEEE Canadian Conference of Electrical and Computer Engineering (CCECE)*, 2019, pp. 1-4, doi: 10.1109/CCECE.2019.8861771.

[C2] M. Baghelani, N. Hosseini and M. Daneshmand, "Selective Measurement of Water Content in Multivariable Biofuel Using Microstrip Split Ring Resonators," *2020 IEEE/MTT-S International Microwave Symposium (IMS)*, 2020, pp. 225-228, doi: 10.1109/IMS30576.2020.9223908.